Structuring Difference

The Additive Manufacture of Spatially & Functionally Differentiated Microstructures

Felicity Freeman

The University Of Sheffield.

A thesis presented for the degree of Doctor of Philosophy

Materials Science & Engineering
University of Sheffield

October 2018

Abstract

Additive manufacturing is an enabling technology for achieving spatially-differentiated functionally-graded materials at a resolution that could not be realised by conventional methods. This work covers the development of an in-situ magnetically and microstructurally graded material, built by selective laser melting from a single composition of 17-4PH stainless steel. The high solidification rates of additive manufacture are exploited to drive very fine austenite grain and cell sizes, suppressing the thermally-driven martensitic transformation and stabilising austenite. But additively manufactured parts are known to suffer from thermal strain, and the low stacking fault energy of metastable retained austenite makes it susceptible to deformation-driven transformation. Regions engineered to have low thermal strain remain fully austenitic and demonstrate paramagnetic behaviour, while other regions, tailored to have higher thermal strain, partially transform to ferromagnetic martensite. The magnetic properties are proportional to the phase composition, and therefore to thermal strain, and are shown to be controllable through the build parameters and geometry. The applications for this type of magnetically graded material include electrical machine architectures, and a SLM-built in-situ magnetically graded rotor is demonstrated in a synchronous motor.

What is this life if, full of care,
We have no time to stand and stare?

W. H. Davies

Acknowledgements

I would like to thank everyone who has been involved with this project for their help and support along the way. I cannot mention everyone by name, but a few people deserve special thanks.

Firstly I would like to thank my supervisor, Prof. Iain Todd, for encouraging me to find my own lines of research, for having confidence in my abilities, for helping to keep me motivated and for suggesting alternative ways of looking at the problem when I got stuck. I would also like to thank Dr. Al Lambourne (Rolls-Royce plc) for the idea of a magnetically graded material for electrical machine architectures and acknowledge his, and his colleagues, work designing and testing the rotor I made during this project.

Secondly, I must thank my colleagues, for their help and advice throughout this work. Specifically, Dr. Chris Smith for the long-term loan of a fridge magnet; Dr. Jo Sharp for assistance with electron microscopy; Dr. Mike Croucher for reviewing my Matlab models and making suggestions about more efficient coding approaches and Lova Chechik for operating the Aconity Mini and processing the pyrometer data.

I must also acknowledge the invaluable contribution made by Dr. Alex Lincoln (University of Manchester) for his time and expertise running the vibrating sample magnetometer used for magnetic characterisation, and showing me how to interpret the data.

Finally, I must thank my family and friends. My parents, Helen Byard and Bill Freeman, for supporting my decision to give up a perfectly good job in industry and become a student again. My partner, Ben Kelsey, for being patient when I talked about stainless steel all evening, for bringing me dinner when I worked late and would otherwise have forgotten to eat, and for making me go out running and climbing regularly to relax. And Charlotte Boig for making me laugh and providing last minute moral support when we both needed to finish writing up.

This work has been funded by the Engineering and Physical Sciences Research Council, award reference 1686001.

Some of the data contained within this work has been published in the journal **Materials & Design** under the title *Exploiting Thermal Strain to Achieve an In-Situ Magnetically Graded Material* [1].

Contents

List of Figures

List of Tables

Chapter 1

Introduction

Additive manufacture (AM) has been identified as a disruptive technology, with the potential to replace many of the conventional manufacturing techniques in use today. However, it is only recently gathering pace for volume manufacturing and is mostly focussed on high technology applications. It is defined by ASTM as 'the process of joining materials to make parts from 3D model data, usually layer upon layer, as opposed to subtractive manufacturing and formative manufacturing methodologies' [2].

One key advantage of AM is the ability to make a component to finished size, without the need for subsequent machining, and therefore to make a geometry that is unachievable through conventional methods. This has the potential to cut up-front manufacturing costs through reduced tooling, but also minimise waste by reduced levels of machining swarf. Further there is the possibility to reduce weight by turning multi-piece assemblies into single components, which has significant advantages for aerospace applications where specific fuel consumption is a strong driver in component design.

AM has many benefits, but as with every technology there are difficulties that must either be overcome or accommodated within the design.

High temperature gradients cause rapid cooling rates, resulting in a different microstructure from conventionally manufactured material and therefore different mechanical properties [5, 6]. These temperature gradients can also result in residual stresses which may deform the component [7, 8] or cause cracking.

Insufficient energy density can cause poor melting, leading to lack-of-fusion porosity, while

(a) **(b)**

Figure 1.1: a) Additively manufactured fuel nozzle for General Electric LEAP Engine [3]. A single AM part replaced an assembly of 20 conventionally manufactured components, with 25% reduction in weight. b) An orthopaedic implant built by electron-beam welding incorporating an optimised porous surface for improved integration with human bone [4]

excess energy density can cause keyhole melting with associated keyhole porosity [9]. AM components also experience in-situ heat treatment, caused by the heat affected zone from the processing of subsequent layers, which has the potential to modify the microstructure further [10].

While these are all issues which must be taken into account to achieve the desired outcome, if they can be sufficiently understood there is also the potential to exploit them to achieve even more from an AM product. This work explores the potential for some of these apparently undesirable characteristics to be used to control microstructure of the as-built product, with the aim of developing a magnetically graded material.

Chapter 5 covers the fabrication and analysis of a set of melt tracks, covering a range of build parameters, to be used in the validation of a Matlab model to predict melt pool geometry.

In Chapter 6, the evolution of the melt pool model is described, using the data from Chapter 5 for comparison. The process starts with the Rosenthal approach for a point heat source, moves to the Eagar solution for a Gaussian beam, and then modifies this to represent a pulsed laser moving through multiple hatches.

The role of austenite grain size on suppression of martensite start temperature in 17-4PH stainless steel is explored in Chapter 7, specifically assessing whether the effect can be exploited within an SLM build to achieve a microstructurally and magnetically graded material. The investigation includes consideration of existing data from literature, melt pool modelling and experimental observation.

Chapter 8 discusses the possibility of in-situ heat treatment affecting microstructure, the extent of recovery that can be expected during the build, and the impact on the likelihood of thermally-activated martensitic transformation.

In Chapter 9, the focus moves to deformation-driven martensitic transformation resulting from residual stress that can accrue during the build. This primarily uses spatially resolved data to assess martensite content in different regions of experimental samples, and compares that with the expected areas of increased strain.

Data presented in Chapter 7 identified the presence of two austenite phases, one of larger lattice parameter than expected. The origin of this phase is discussed in Chapter 10, considering both strain and compositional influences.

Chapter 11 looks at the application for a magnetically graded material, including manufacture and operation of a proof-of-concept magnetically graded rotor for a synchronous motor.

Chapter 2

Literature

2.1 Additive Manufacture

2.1.1 Metal Additive Manufacturing

Additive manufacture, originally called Rapid Prototyping, was first developed for polymer processing during the 1980's, using UV light to cure layers of photosensitive polymers [11]. AM systems for metal followed in the late 1990's, primarily as a powder manufacturing process. There are some metal AM systems which use wire-feed, but these are outside the scope of this project [12].

There are a variety of different names and acronyms in common usage for metal AM systems (Figure 2.1), depending on the exact nature of the process and the equipment manufacturer. Putting these to one side, the metal-powder AM systems can be classified at the top level as either *blown-powder* or *powder-bed*, and then further classified depending on the choice of electron-beam or laser-beam as the heat source. A more complete picture of the various metallic AM systems is shown in Figure 2.1 [2].

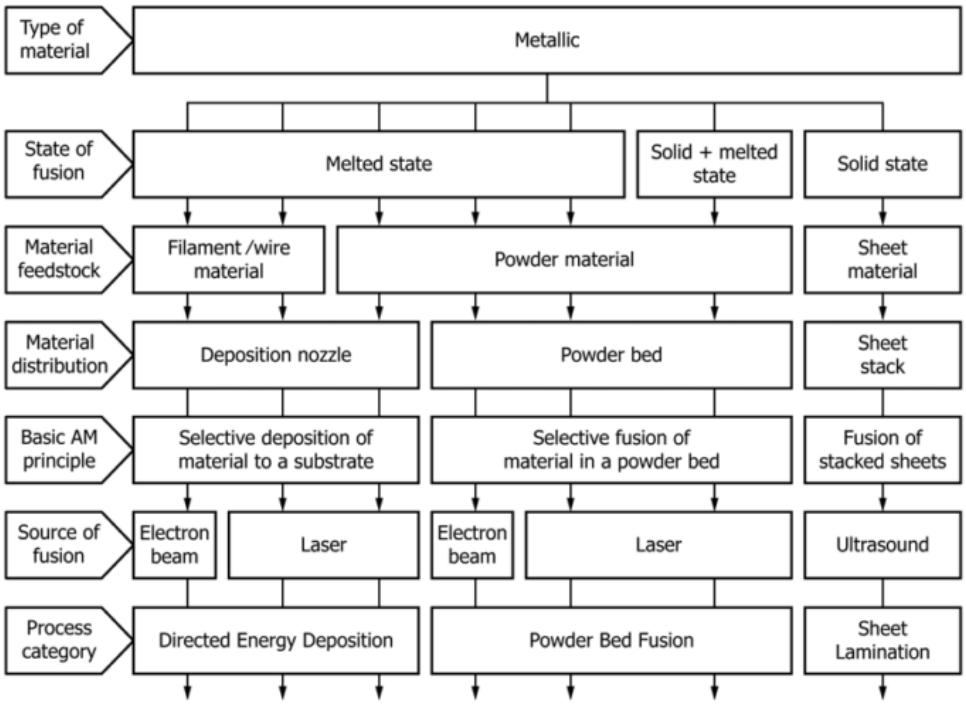

Figure 2.1: Flowchart of metal additive manufacturing processes [2].

Within the landscape described by Figure 2.1, the AM processes which will be referred to most frequently in this work are:

- Selective Laser Melting (SLM): A powder-bed method using a laser-beam heat source
- Electron Beam Welding (EBW): A powder-bed method using an electron-beam heat source
- Laser Engineered Net Shaping (LENS): A blown-powder method using a laser-beam heat source

The blown-powder systems have the laser mounted on a robot arm, surrounded by a number of nozzles that deliver a stream of metal powder into the focal point of the laser (Figure 2.2). As the beam moves across the surface it creates a melt pool, and metal powder is blown into this melt pool through the coaxial nozzles leaving a deposition track. This has the advantage of being able to build geometry free-form (e.g. for localised repair) but is comparatively expensive due to the robot arm and associated control equipment.

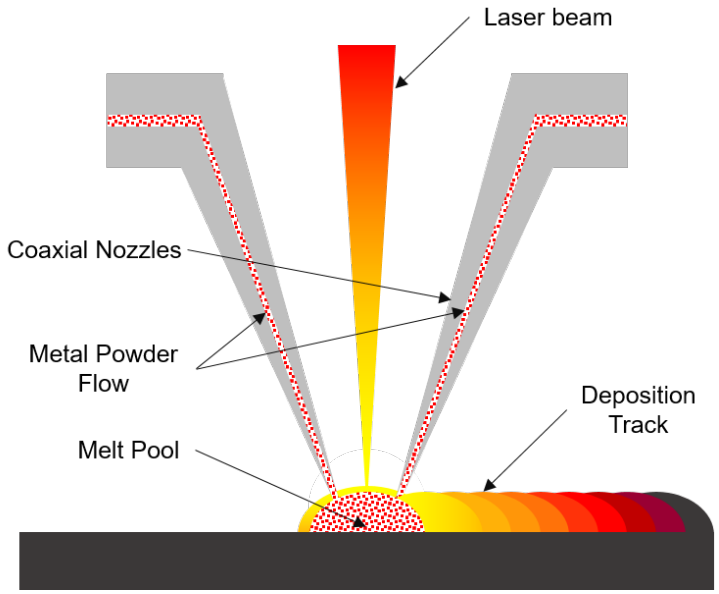

Figure 2.2: Schematic of blown-powder process.

The powder-bed systems have a fixed laser positioned directly above the build plate. A layer of powder is spread across the build plate and the laser moves across to melt the specific regions (Figure 2.3). When all melting is complete, the build plate moves down, a new layer of powder is added on top and the laser melts the next layer of geometry. The process is restricted to working in one build direction, which has some associated geometry constraints (e.g. overhangs require support), but the equipment is generally less expensive.

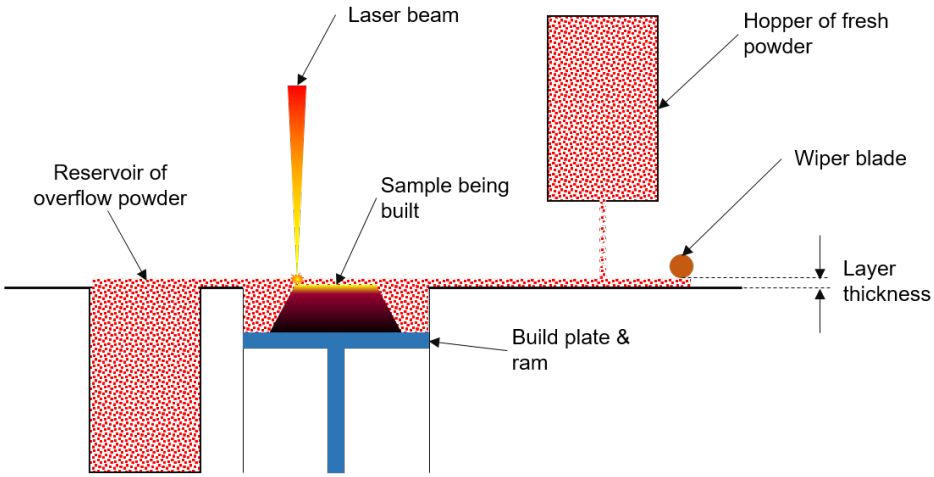

Figure 2.3: Schematic of powder-bed process.

2.1.2 Functional Grading

The game-changing aspect of AM is the opportunity for Functional Grading (FG) [13]. Functional grading can be simply regarded as concurrent design of material properties *and* geometry to meet the component requirements.

The convention when designing a component has been to prioritize form over material, an inefficient approach. This can result in the whole component being manufactured from a material that has properties only required by one small region.

FG allows a smarter approach, tailoring the material properties concurrently with the geometry, so that the design is fully optimised: maximal performance with minimal resources [14]. There are many examples in Nature where this resource efficient approach has been essential to achieving the desired outcome, and man-made functionally graded materials have been manufactured using both conventional and AM techniques.

One simple example from Nature is bamboo [15] (Figure 2.4). The stalk is a cylindrical shell built from longitudinal fibres within a matrix. The fibre packing density is higher at the outer edge of the stalk, increasing mechanical reinforcement in the area which will experience the highest loading.

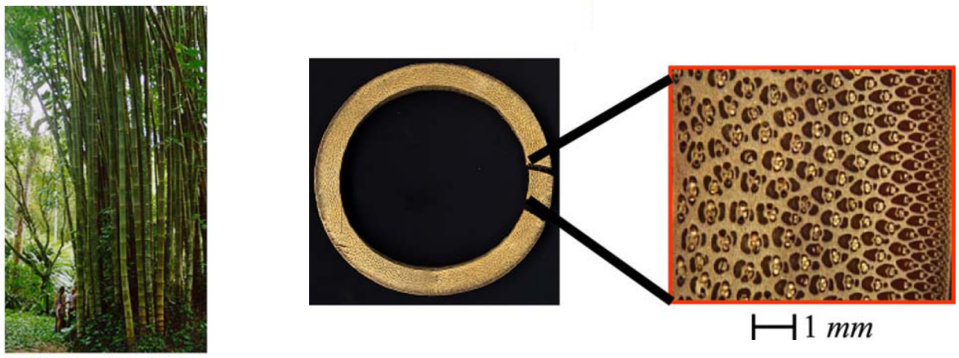

Figure 2.4: Structural hierarchy in bamboo [15].

Taking this further, functional grading can be considered at different length scales, where the critical aspect is the length scale over which the change is observable.

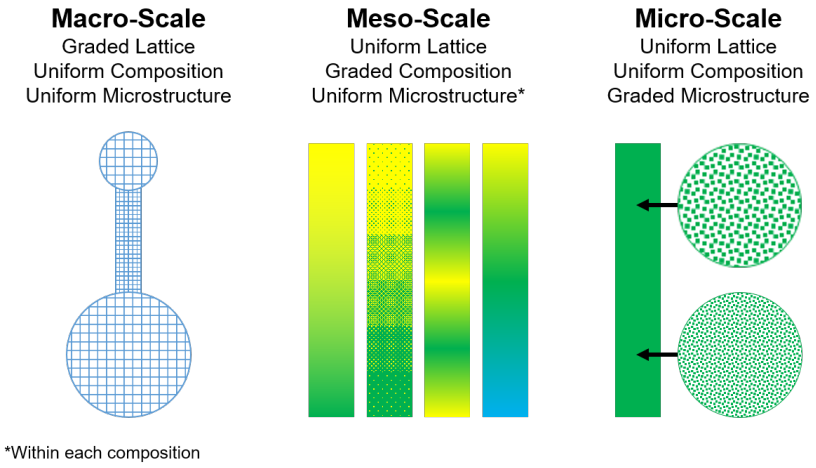

Figure 2.5: Functional grading length scales.

At the macro-scale, graded Ti-6Al-4V lattices have built by EBW, where the strut thickness was varied while keeping the unit cell size constant. The microstructure was uniform across the part, but the macro-structure changed and conferred a graduation in mechanical properties [16].

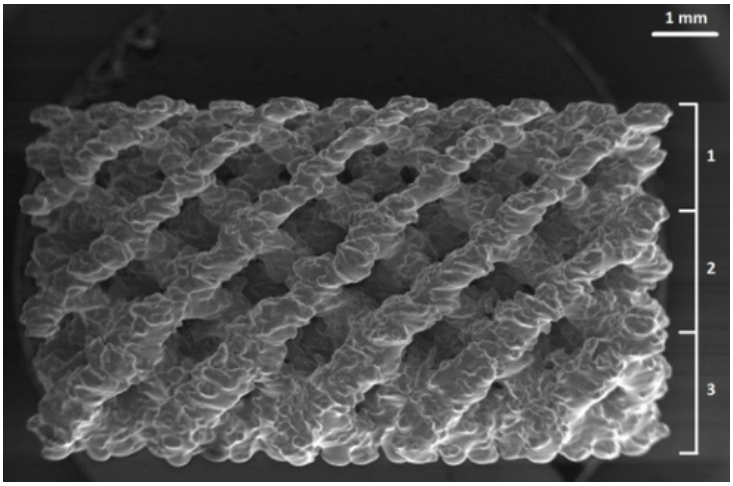

Figure 2.6: SEM image of graded lattice with 800 µm strut thickness at the base (Region 3), 500 µm strut thickness in the middle (Region 2) and 200 µm strut thickness at the top (Region 1) [16].

On the meso-scale are centrifugally cast aluminium metal matrix composites made from particle enriched slurries [17]. The centrifugal forces caused lighter particles to move towards the axis of rotation, while heavier particles moved away, resulting in graded particle enrichment along the sample length (Figure 2.7).

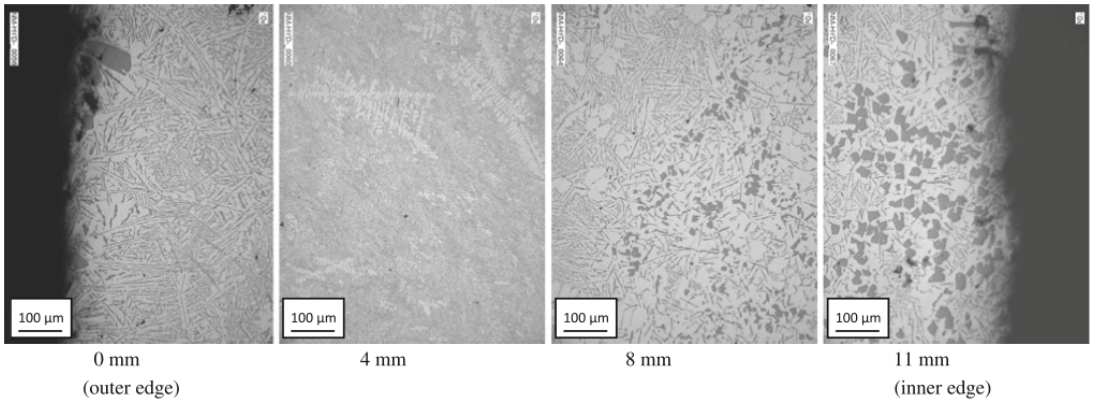

Figure 2.7: Optical micrographs of graded Al20%Si fabricated by centrifugal casting, with silicon enrichment at the inner periphery of the casting for improved hardness and wear resistance [17].

Compositionally graded examples within AM include functional grading of CTE, demonstrated by grading from Invar 36 to 304L [18] (Figure 2.8), and a built-in thermal barrier coating achieved by grading Waspaloy® with a proportion of zirconia [19] (Figure 2.9).

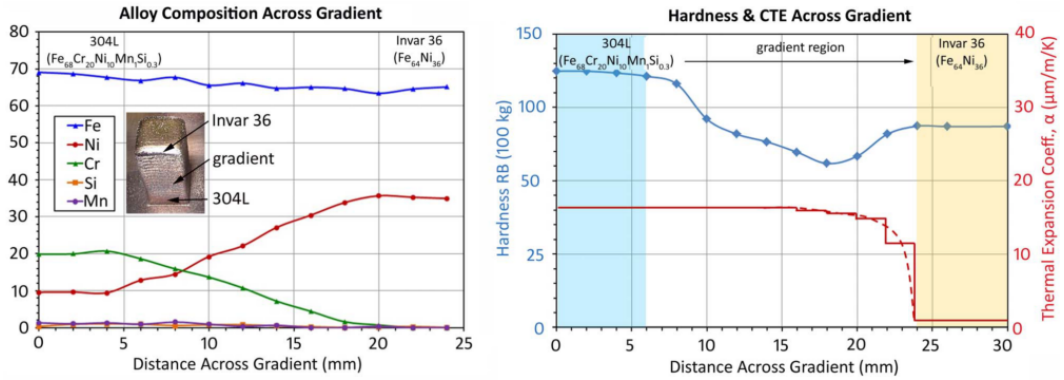

Figure 2.8: Compositional, hardness and CTE variation for 304L-Invar36 graded material [18]

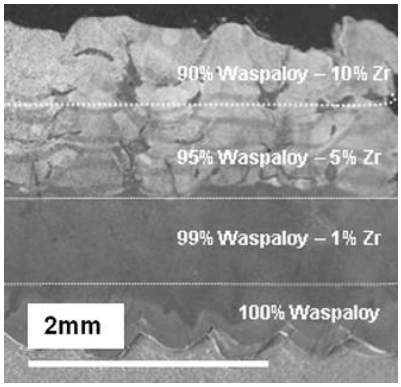

Figure 2.9: Cross-section of Waspaloy®-zirconia graded material [19]

Brittle intermetallics can be an issue with compositional grading, although it may be possible to avoid these with indirect gradient pathways [20] (Figure 2.10).

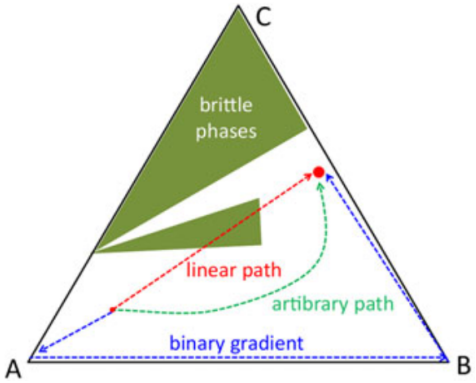

Figure 2.10: Schematic tertiary phase diagram showing paths of different compositional gradients which may encounter or avoid brittle intermetallic phases [20]

At the micro-scale are the microstructurally graded materials, where there is no (or minimal) compositional variation, but sufficient microstructural variation to deliver a change in functional properties.

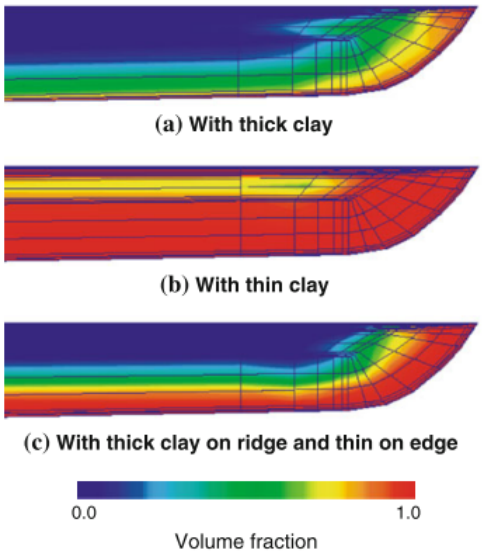

Figure 2.11: Computer simulation of effect of clay thickness on phase composition. The blades were manufactured using Japanese steel. The edge was given a thin layer of clay, resulting in a high cooling rate and hard martensitic structure. The ridge was given a thicker layer, reducing the cooling rate and giving a more ductile pearlite structure. [21]

This approach was exploited in traditional Japanese steel swords. The steel was obtained from iron sand by furnace melting, processed through a series of forging and folding stages,

which was then followed by coating the blade in clay and quenching. The thickness of the clay was varied to control the cooling rate, delivering a graded microstructure tailored to the specific requirements of different parts of the blade [21] (Figure 2.11).

Microstructural grading has also been demonstrated by additive manufacture. Samples of 316 stainless steel were built by SLM with either a 400 W laser to produce a fine grain structure, or a 1000 W laser to produce a coarse grain structure [22] (Figure 2.12).

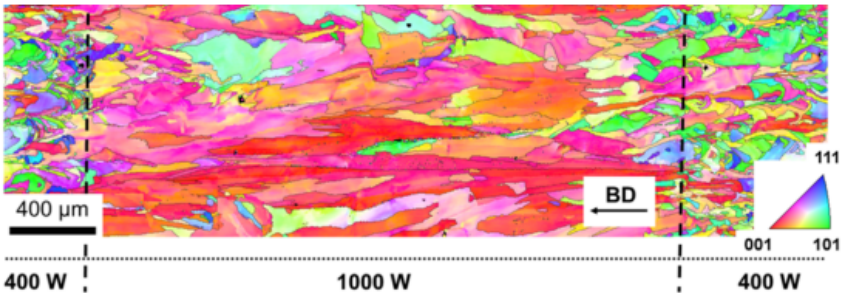

Figure 2.12: Grain-size graded 316L achieved by utilising two different laser powers. Central coarse-grained region build using 1000 W laser. Fine-grained ends built using 400 W laser. [22]

It should be possible to create a graded material for any functional property, provided that the materials and conditions exist for each extreme. The main constraint is achieving a well-bonded interface, often improved by blending more gradually [13], and avoiding brittle intermediate phases [20].

2.1.3 Applications of Magnetically Graded Materials

Magnetically graded materials are an enabling technology for a number of electrical machine architectures, including synchronous reluctance motors [23, 24], switched reluctance motors [25] and internal permanent magnet motors.

The stator of a synchronous reluctance motor consists of a series of windings, one set for each phase of current, arranged around a central axis (Figure 2.13a). When current is passed through these windings it sets up a magnetic field, whose strength is dependent on the magnitude of the current. Using 3-phase electricity, the current in each phase follows a sinusoidal and sequential pattern (Figure 2.13b), reaching a maximum in each phase in turn and causing the magnetic field to rotate.

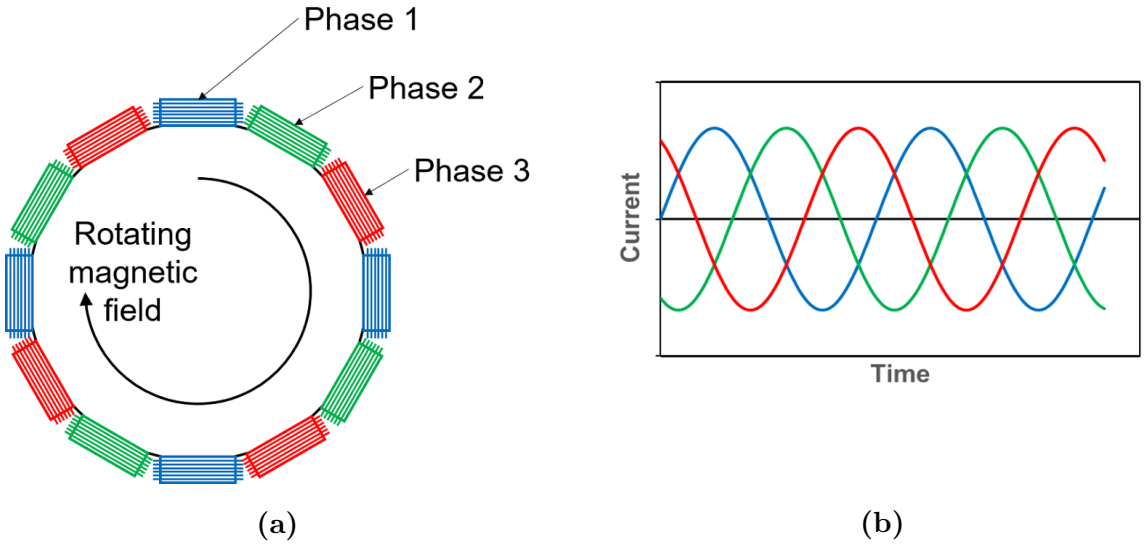

Figure 2.13: a) Schematic stator for a 4-pole synchronous reluctance motor. b) Schematic rotor for a synchronous reluctance motor.

The rotor is constructed from a series of ferromagnetic shells (Figure 2.14a). The magnetic flux locks into these shells, so that as the field rotates it pulls the rotor round at the same speed, *synchronous*. Ideally, the magnetic flux is fully contained within the shells, trapped by insulating material (air) around them. However, it is necessary for these shells to be supported, so they are connected together with a series of struts.

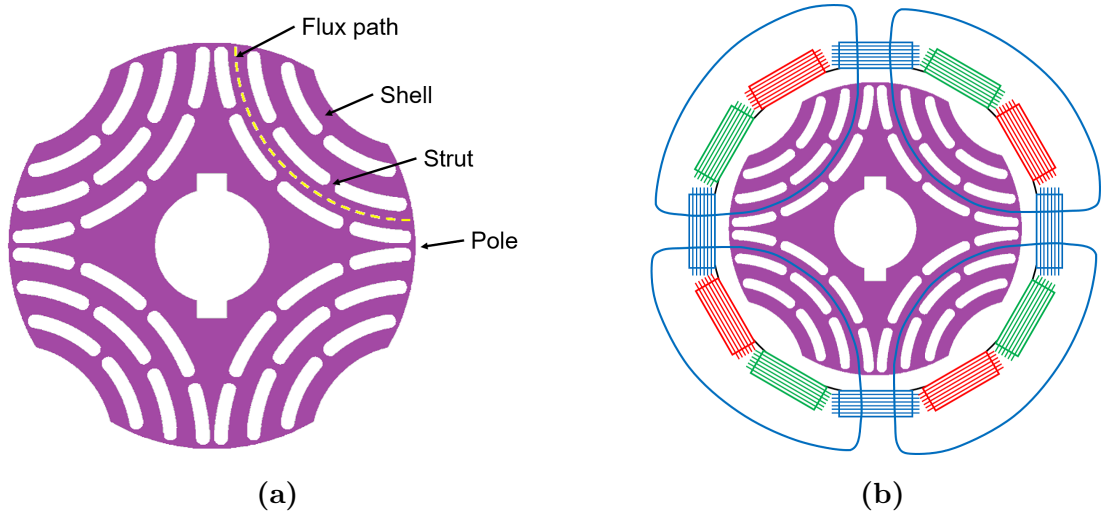

Figure 2.14: a) Schematic rotor for a synchronous reluctance motor. b) Schematic showing full motor with flux lines for one phase.

The rotors are currently cut from from thin sheets of electric steel, creating discs which

are glued together into a stack. This approach requires the whole geometry to be made from the same ferromagnetic material but, being ferromagnetic, the struts then act as flux leakage paths. Optimised designs minimise the strut thickness to reduce leakage, but they must balance magnetic efficiency with mechanical integrity. If these rotors could be made from a magnetically graded material, with ferromagnetic shells and paramagnetic struts, it would reduce flux leakage along the struts.

With the goal of direct manufacture of a magnetically graded rotor, a powder-metallurgy sintering approach has been patented [26]. This uses metal powder of two different compositions, one ferromagnetic and one paramagnetic. The die is filled with these powders, spatially differentiated to create regions with different magnetic behaviour, and sintered. The result is a magnetically graded disc, combining the two different powder compositions.

A similar method has been demonstrated in SLM, building samples with varying proportions of austenitic 316L (paramagnetic) and martensitic 17-4PH (ferromagnetic) [27]. The results showed a change in magnetic properties with changing proportion of the two alloys, and a concurrent change in microhardness, although the equipment used did not allow manufacture of a fully graded structure.

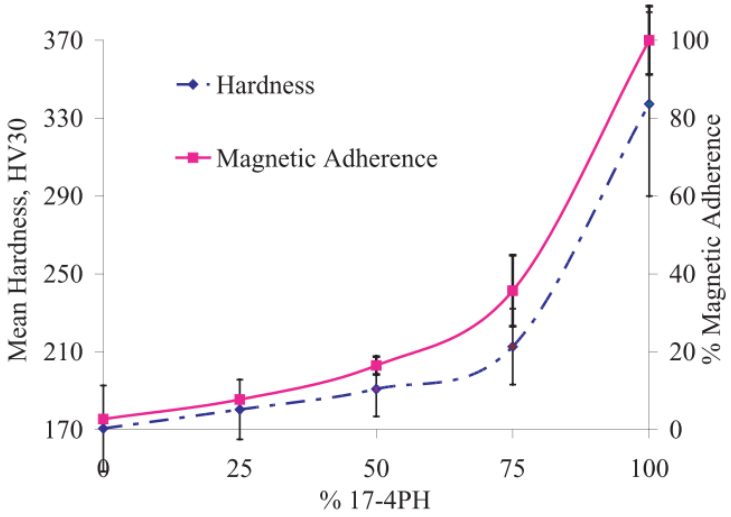

Figure 2.15: Change in magnetic properties and microhardness for SLM-built samples of 316L/17-4PH mixtures with increasing proportion of 17-4PH [27]. The 'magnetic adherence' metric was measured by attaching a small earth magnet to an elastic band, and then to a 20kN tensile testing machine fitted with a 50N load cell. The adherence was the force required to remove the magnet from the sample surface, expressed as a percentage of the highest force required across the samples in the study. Further detail can be found in [27].

The solid-state transformation between austenite and martensite has also been exploited to deliver magnetic grading within a single composition through thermo-mechanical processing. In one instance, a fully martensitic sample was annealed in a temperature gradient to drive varying levels of austenitisation [28] (Figure 2.16a). In the other, a wedge of austenitic steel was rolled to drive varying levels of deformation-driven martensitic transformation [29] (Figure 2.16b).

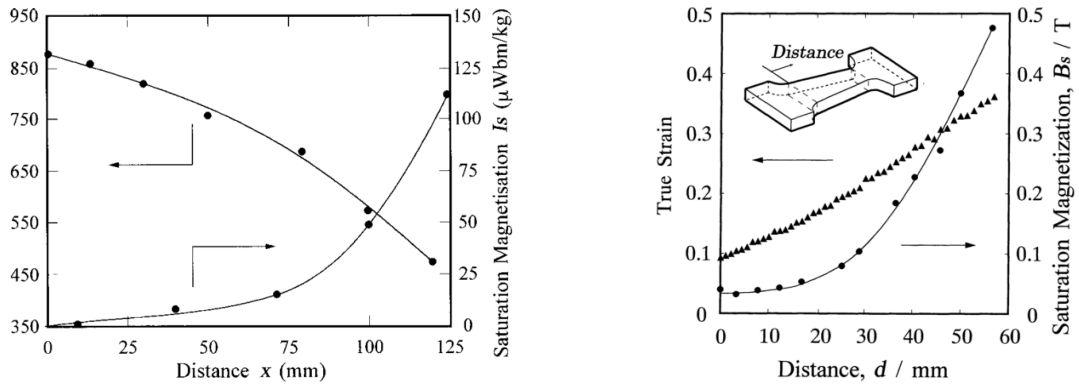

(a) **(b)**

Figure 2.16: Magnetically graded 304 steel achieved by mechanical or thermal processing. a) Change in saturation magnetisation with annealing temperature [28]. b) Change in saturation magnetisation with strain [29].

2.2 Issues with Additive Manufacture

2.2.1 Keyhole Melting & Absorptivity

Most SLM-built materials exhibit melt pools with a semicircular cross-section, where the size of the melt pool is limited by conduction into the substrate. However, at high energy density the melt pool depth increases dramatically compared to the width, becoming keyhole shaped [9] (Figure 2.17). This is observed in both additive manufacturing processes and conventional welding [30].

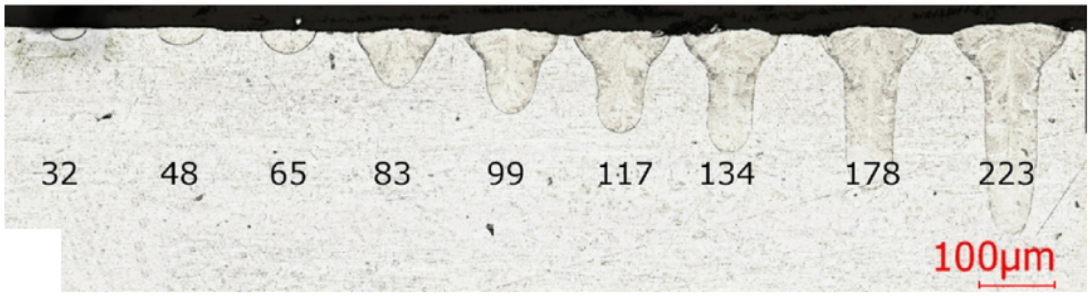

Figure 2.17: Cross-section of melt tracks in 316L showing onset of keyhole-mode melting with increasing laser power [31].

Keyhole melting can start once the the melt pool reaches boiling point. If a vapour bubble forms it can trap laser energy, the bubble is then dragged to the bottom of the melt pool by convection currents, and the additional energy is absorbed there increasing the melt pool depth. Various models have tried to identify the onset of keyhole melting and predict the depth of keyhole melt pools [9, 32, 33]. In general, they have normalised melt pool depth using the beam radius and identified the onset of keyhole melting on a scale of normalised enthalpy, which is comparable with energy density (Figure 2.18).

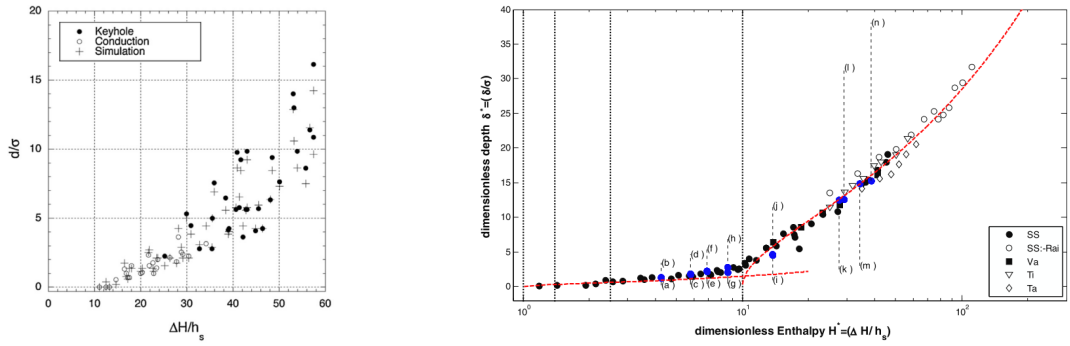

(a) **(b)**

Figure 2.18: a) Predicted and experimental melt pool depths for 316L [9]. b) Predicted and experimental melt pool depths for a range of compositions [32].

The melt pool characterstics are determined by the laser parameters (power, scan speed, beam radius), the material parameters (thermal diffusivity, density) and by the absorptivity, the efficiency with which the material absorbs the laser energy. This has often been measured by calorimetry, melting single tracks on to a flat sample of known thickness, normally around 100 µm, and measuring the temperature change at different positions [31, 34].

Further, absorptivity has been shown to be dependent on laser parameters [31]. Measurements on a flat stainless steel disc showed low absorptivity (25 %) at low power, then a sharp increase followed by saturation at around 75 % to 80 % (Figure 2.19). The sharp increase coincided with the onset of keyhole melting (Figure 2.17).

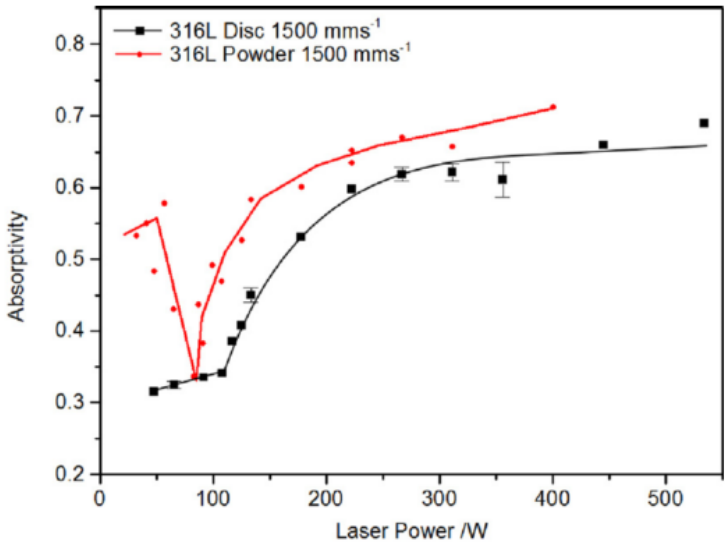

Figure 2.19: Change in absorptivity with laser power for 316L stainless steel disc and powder at a) 100 mm s^{-1} and b) 1500 mm s^{-1} [31].

Stainless steel powder showed similar behaviour but with higher absorptivity at low power (Figure 2.19), which was attributed to multiple reflections between particles trapping the laser energy. There was also a sharp drop at the onset of keyhole melting, which was explained by the powder melting, making the absorptivity comparable with that of the flat disc. This demonstrates that it may not be appropriate to use a single fixed value of absorptivity across a wide range of energy density.

While this type of measurement is useful, these experiments were all carried out under very controlled conditions (smooth powder, single track) which are not necessarily representative of a full build environment.

High-speed imaging and complementary Schlieren imaging have been used to investigate the movement of the laser plume and ejected particles above the melt pool [35]. At low power and low speed (50 W 0.1 m s^{-1}) the laser plume and particles were ejected forward from the melt pool (Figure 2.20a). At higher power and higher speed (200 W 1 m s^{-1}) the plume and particles were ejected backwards (Figure 2.20b).

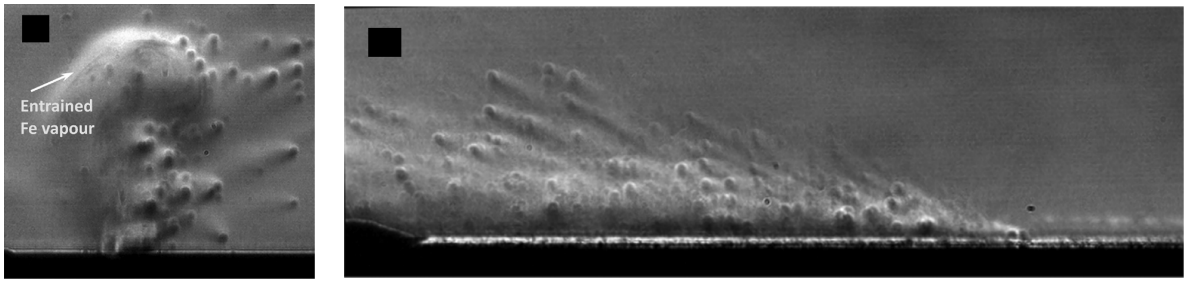

(a) 50 W 0.1 m s^{-1} **(b)** 200 W 1 m s^{-1}

Figure 2.20: Schlieren imaging of laser plume above melt pool. Laser moving from left to right of image. [35].

If the plume is forward of the melt pool, the laser must travel through a combination of plasma, heated gas and metal vapour to reach the build surface. Conversely, if the plume is behind the melt pool the laser has a clear path to the melt pool with limited interaction with the plume. A long interaction time could allow some of the laser energy to be absorbed by the plume before reaching the build surface, influencing the effective absorptivity at the build surface. This may be a partial explanation of the change in absorptivity with laser parameters shown above (Figure 2.19).

The imaging was extended to consider changes in behaviour for the multiple hatches and layers required for a full build, rather than just a single track. For multiple hatches the plume and ejected particles were angled away from the previously melted hatch. The initial layers showed denudation of powder around the molten region, but this was corrected during the subsequent layers, and had disappeared by layer 6 (Figure 2.21).

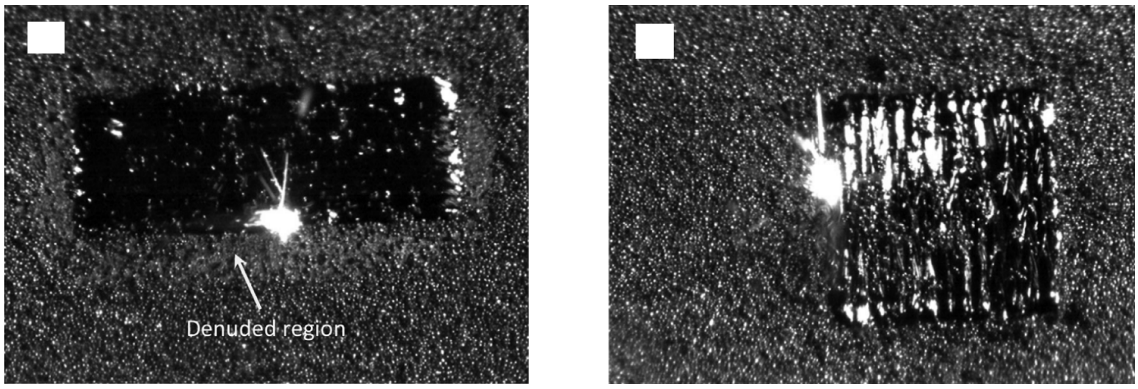

(a) Layer 1 **(b)** Layer 6

Figure 2.21: High-speed imaging of denudation around the molten material [35].

The change in plume angle will further change the laser interaction time, and the denudation of powder will influence how the laser beam is focussed on the build surface. The overall conclusion is that it may not be appropriate to consider absorptivity as a fixed value, measured from single track, single layer experiments; it can be affected by laser parameters, changes at the onset of keyhole melting and may also change through the early layers of a build.

2.2.2 Porosity

Porosity is a major concern with AM, as it can impact mechanical behaviour. It can be classified into *lack of fusion* and *keyhole pores*. Lack of fusion occurs when the energy density is insufficient to achieve full melting of the powder, leaving irregularly shaped cavities. These are often of a similar size to the melt pool, and may follow the melt pool boundary or appear in the junction between melt pools [36, 37] (Figure 2.23).

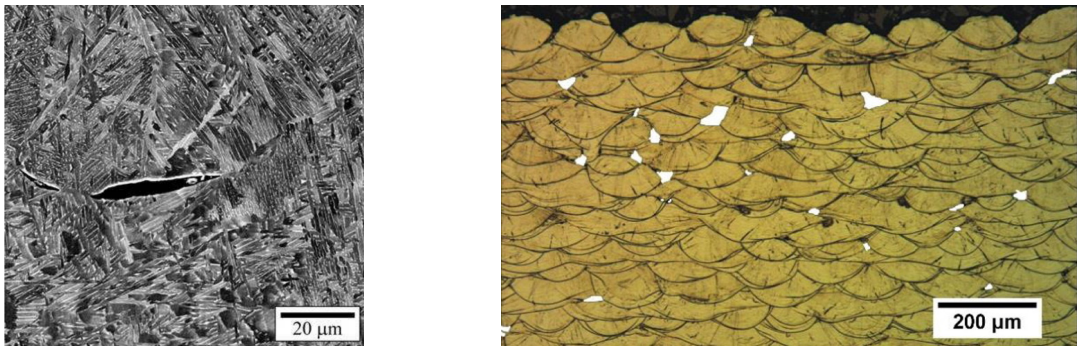

(a) **(b)**

Figure 2.22: Examples of lack-of fusion porosity. a) EBM-built Ti-6Al-4V [36]. b) SLM-built CoCrMo [37]

Keyhole porosity is caused by the vapour bubble getting trapped within the melt pool. This is dependent on a variety of factors including the geometry of the vapour bubble, the aspect ratio of the melt pool, outgassing from the melt, convection currents and unstable collapse of the vapour bubble [38, 39]. Keyhole pores are generally spherical in shape and can often be found near the bottom of a melt pool.

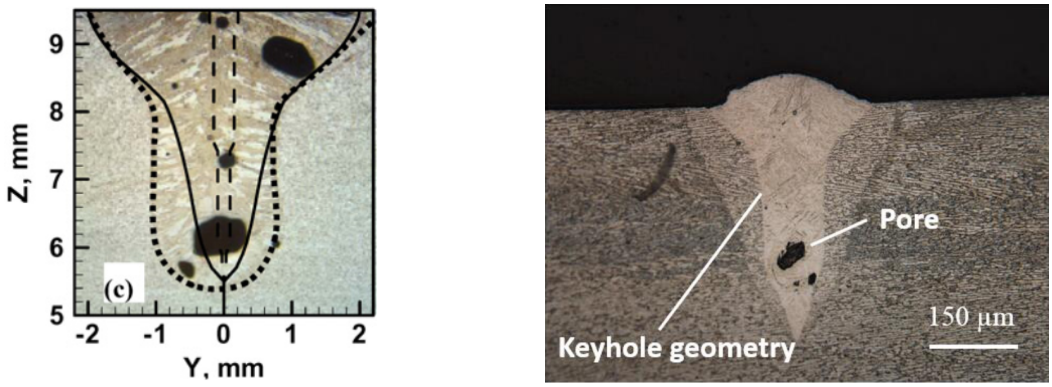

(a) **(b)**

Figure 2.23: Examples of keyhole porosity. a) Powder-bed laser-built 304L steel [33]. b) SLM-built Ti-6Al-4V [40].

The ideal for a good quality AM product is to achieve the 'Goldilocks' region: enough energy density for full densification but not enough to cause keyhole melting.

2.2.3 Segregation

Equilibrium solidification assumes that the front moves sufficiently slowly for full diffusion in both solid and liquid. The solid composition will be uniform and will match that of the initial liquid [41, 42]. However, this is very unlikely in SLM as the solidification rates are too fast.

The Scheil-Gulliver approach assumes no diffusion in the solid, but complete mixing in the liquid from a combination of diffusion and convection [41, 42]. The resulting microstructure would exhibit coring, where the solute concentration would be lowest at the middle of the dendrites and gradually rise towards the outer edge, finishing with interdendritic eutectic.

Another approach is to assume no diffusion in the solid and limited mixing in the liquid, caused by diffusion without convection, which then creates a boundary layer ahead of the solid-liquid interface [41, 42]. This will also exhibit coring, although the concentration profile across the dendrite will be slightly different from the Scheil-Guliver solidification.

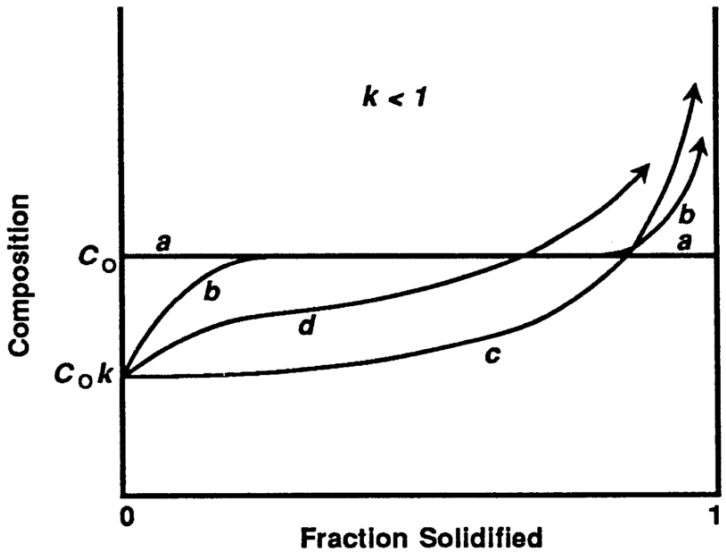

Figure 2.24: Concentration profiles for various solidification models: a) Equilibrium; b) No mixing in solid, diffusion in liquid; c) No mixing in solid, complete mixing in liquid; d) No mixing in solid, partial mixing in liquid [43].

These models are all based on assumptions about the amount of mixing that may take place in each phase, and the reality may move between them at different stages of solidification. There may be additional mixing in the liquid from turbulence or convection currents, there may also be diffusion in the solid, particularly of interstitial alloying elements such as carbon and nitrogen. Overall, rapid solidification processes would be expected to show some segregation of solute across the dendrites and interdendritic material.

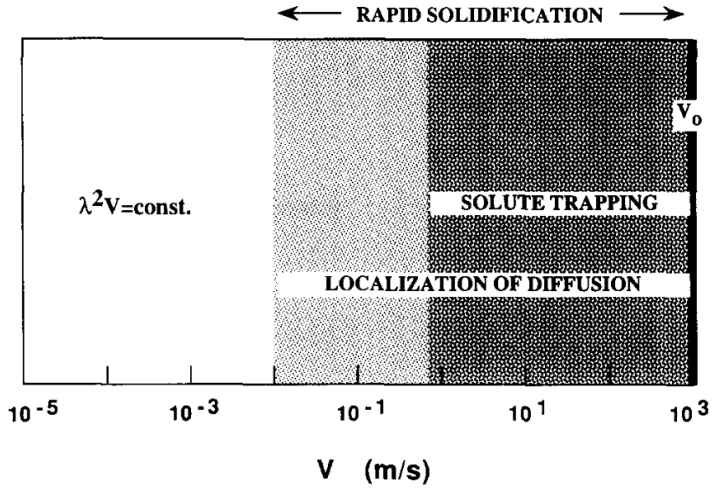

Figure 2.25: Characteristic phenomena appearing in metals under rapid solidification processing [44].

At extremely high front velocities it is also possible to get solute trapping where the front moves too fast for solute to be rejected and transported away from the interface (Figure 2.25), although this is faster than most SLM processes [41, 44].

In steels, segregation can affect the phase solidifying. The first solidification product may be δ-ferrite, but the liquid composition may then change sufficiently that γ-austenite starts to solidify instead. The resulting structure would have ferrite at the dendrite core, surrounded by austenite (Figure 2.26). Different compositions could show the converse behaviour with an austenite core and interdendritic ferrite.

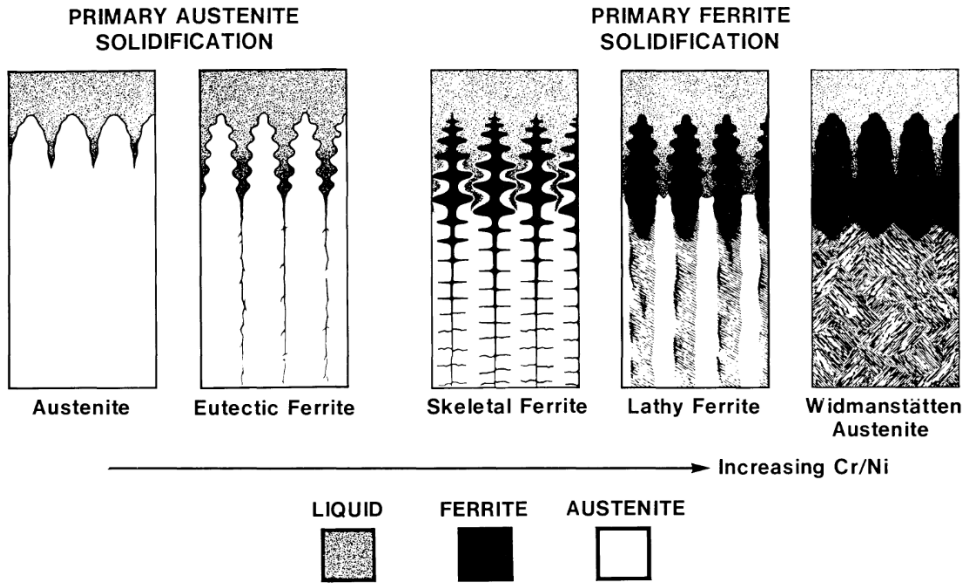

Figure 2.26: Solidification and transformation behaviour for steels with increasing Cr/Ni ratios [43].

The microstructure of AM steels will be discussed in more detail later (Section 2.4), but normally consists of cells approximately 1 µm in diameter, where segregation would be likely to occur between the cell body and the boundaries. This is at the resolution limit for EDS (Figure 2.27), so segregation is either only just measurable, or often only apparent when studied by atom probe tomography.

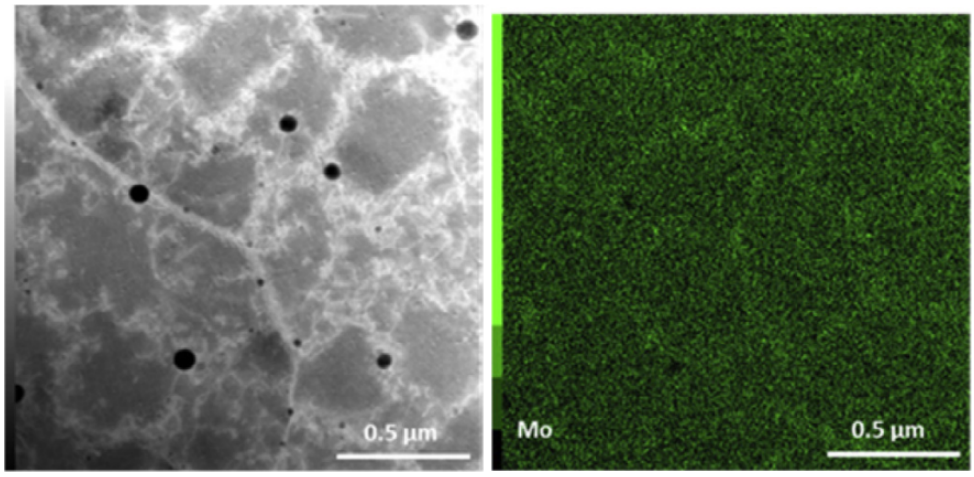

Figure 2.27: STEM showing segregation of heavier elements and EDS showing enrichment of molybdenum to cell boundaries in 316L steel [45].

The Scheil-Guliver approach was used on SLM-built 17-4PH [46], predicting initial BCC δ-ferrite, followed by FCC γ-austenite with niobium-rich FCC carbide near the end of solidification. The model also predicted partitioning of chromium, copper, niobium and carbon into the liquid. EDS confirmed the NbC carbides, although it showed chromium enrichment at the centres of the cells rather than the boundaries, possibly in the BCC cell cores (Figure 2.28).

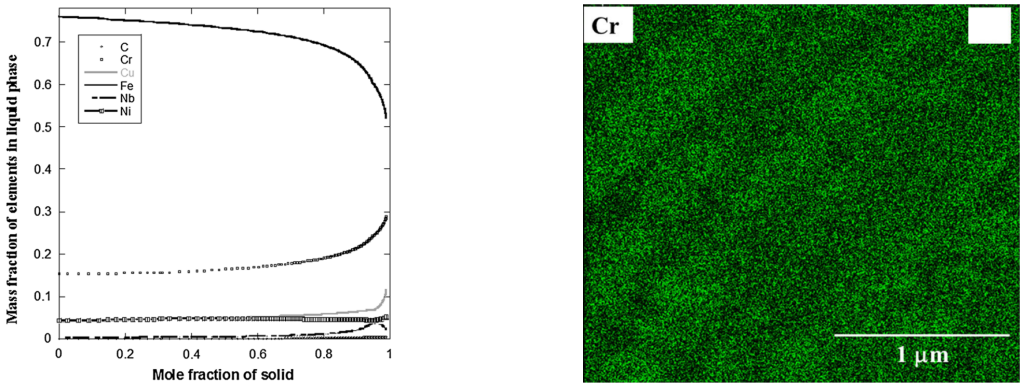

(a) **(b)**

Figure 2.28: a) Scheil-Gulliver composition profile predicted for 17-4PH showing enrichment of Cr, Cu and C in final liquid. b) EDS map of SLM-built 17-4PH showing Cr concentration. [46]

2.2.4 Residual Stress

A further complication with additively manufactured components is the development of residual stress [8, 47], which can cause distortion of the finished component [7, 48].

At the scale of the melt pool, stress has been described using a thermal gradient mechanism (Figure 2.29) [8]. Initially, the hot melt pool expands, but it is constrained by the cooler bulk which is then under compression. Next, the melt pool shrinks as it solidifies and cools, again constrained by the bulk which is now under tension.

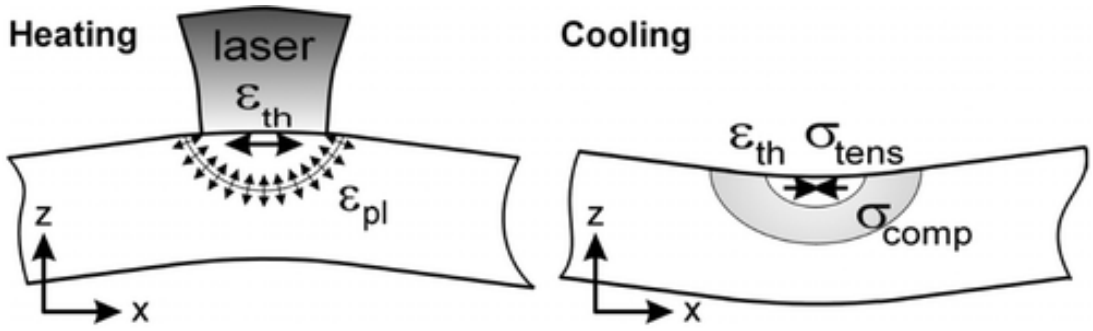

Figure 2.29: Schematic of thermal gradient mechanism of residual stress in SLM [8].

Similarly, but at the scale of the component, is the cool-down mechanism (Figure 2.30) [8]. The topmost layer is at a higher average temperature than the lower layers, and shrinks as it cools down. This is resisted by the cooler layers below, putting the topmost layer into tension and the bulk into compression.

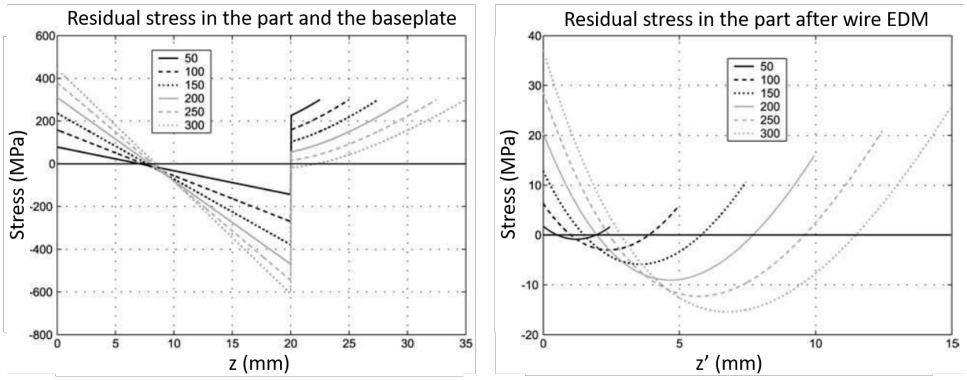

Figure 2.30: Modelling prediction of residual stress due to cool-down mechanism and effect of number of layers [8].

Neutron diffraction has been widely used to map residual stress across AM components

from a range of alloys [49, 50]. A different approach is the contour method [51], where the surface is very gently cut using EDM, to minimise deformation from the cutting process, then the surface topology is mapped using a profilometer and related back to the residual stress. Another technique uses a rosette of strain gauges attached to the sample surface, a hole is drilled at the centre of the rosette, and the resulting relieved strains are measured [52, 53].

The experimental results show complex behaviours, with different studies measuring strain in different locations and directions. A contour method study on CrCoMo reported stresses increasing with build height, being tensile at the edges of the component and compressive in the centre [54], which would correlate with the cool-down mechanism described above.

2.2.5 In-Situ Heat Treatment

As with conventional welding, the melt pool created by the laser is surrounded by a heat affected zone (HAZ). A single point on the sample surface is initially melted when the laser passes directly overhead, but will then be reheated when the laser passes nearby due to the extent of the HAZ.

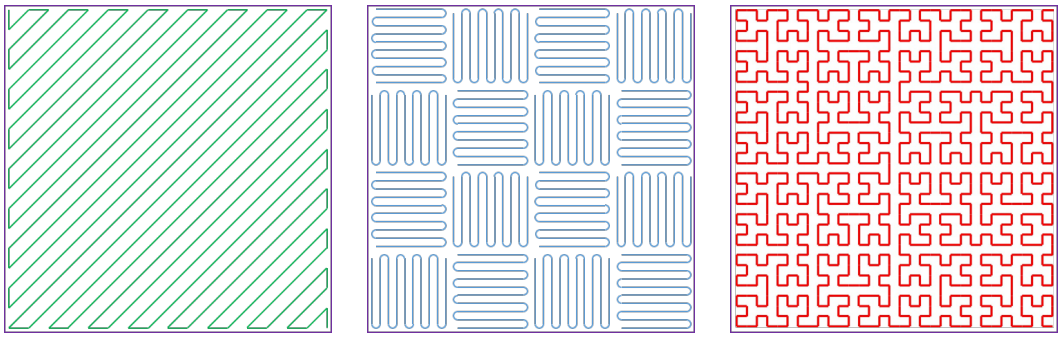

(a) Meander **(b)** Chessboard **(c)** Fractal [55]

Figure 2.31: Schematic scan strategies with different time delays. The meander strategy (a) has long hatches in the middle and short hatches near the ends leading to varying delay times across the surface. The chessboard (b) has more consistent but much shorter hatches. The fractal (c) has very short hatches but would give a more uniform heat per unit area than the meander strategy [55].

The temperature profile of the reheating will depend on the laser parameters, the hatch spacing and layer thickness and the scan strategy. These determine the size of the HAZ,

how close the laser passes and the amount of cooling between passes (Figure 2.31). The result is a series of very short duration heat treatments of varying peak temperature, which could have the ability to modify the microstructure by driving recovery, recrystallisation and precipitation.

This type of in-situ heat treatment was demonstrated by thermocouple data extracted during a LENS build of a single-walled box from H13 tool steel (Figure 2.32a) [56]. There was a peak each time the laser passed above the fixed thermocouple (in the build plane), but the peaks gradually reduced in temperature as layers were added. Similar patterns have been predicted for EBW-built Inconel 718, where the temperature and cooling rate at a fixed point were modelled during the addition of multiple layers (Figure 2.32b) [10].

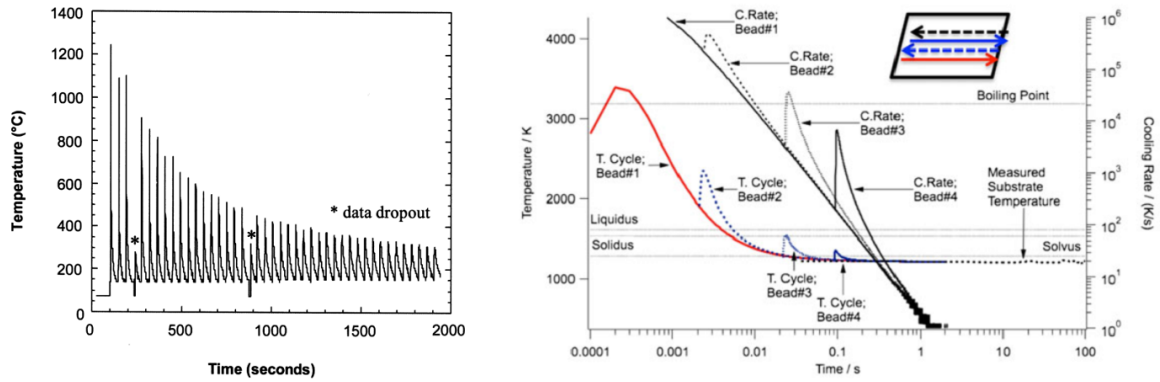

(a) **(b)**

Figure 2.32: a) Thermocouple data captured during build of a single-walled box in H13 tool steel [56]. b) Predicted temperature and cooling rate at a fixed point resulting from subsequent layer addition in Inconel 718 [10].

In-situ heat treatment has been seen to affect AM microstructures. Inconel 718 built by EBW showed a microstructure gradient with three distinct regions [57] (Figure 2.33). The top 750 µm layer had a cored dendritic structure, further down was a more diffuse dendritic structure, then the bulk of the material had columnar grains with no dendrites remaining. Similar behaviour has been reported for SLM-built Ti-6Al-4V, where increasing energy input was shown to cause sufficient in-situ heat treatment to drive the decomposition of α'-martensite into $\alpha + \beta$ during the build [58].

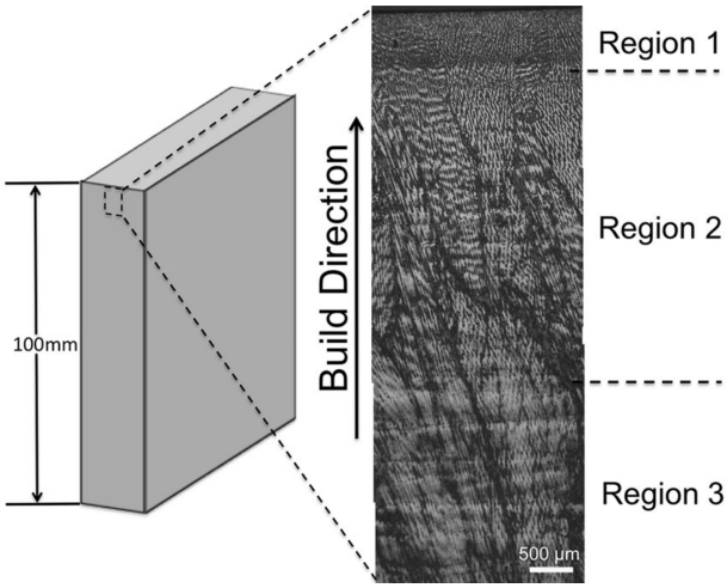

Figure 2.33: Development of microstructure through top section of Inconel 718 EBW build [57]. Region 1 was 750 µm thick and characterised by a cored dendritic structure. Region 2 was 3.5 mm thick and had a more diffuse dendritic structure with coarsening of the primary dendrites and dissolution of the secondary arms. Region 3 was the main bulk of the material, which had a columnar grains with no dendritic structure remaining.

2.3 Stainless Steels

Steels are one of the most widely used manufacturing materials, with applications in every industry, in our workplaces and in our homes. The term includes a huge range of different alloys, tailored to thousands of different applications, from the common 18-8 (304) stainless steel [59] through to high entropy steels developed to achieve high strength combined with high ductility [60].

Stainless steels are a specific group of steels which are corrosion resistant as a result of containing at least 10 wt% chromium [61] in addition to other alloying elements. Chromium oxidises rapidly when exposed to air, creating a protective layer of chromium oxide on the surface. Once formed, this layer is robust and protects the material underneath from further oxidation. Other elements can then be added to modify material properties further, e.g. for heat-resistance or weldability.

The precipitation hardened steels are a subset of stainless steels, which contain alloying elements designed to nucleate and grow precipitates during heat treatment. These pre-

cipitates harden the material by impeding the movement of dislocations. The hardness achieved depends on the size, quantity and distribution of the precipitate phase within the matrix, which itself depends on the time and temperature of the ageing stage of heat treatment.

2.3.1 Phases of Stainless Steel

Steels are able to form a wide range of different phases depending on their composition, thermal history and mechanical processing. The initial solidification phases are primary ferrite and primary austenite; primary denoting the product of solidification rather than solid-state transformation. Solid-state transformation can then result in other phases including martensite, bainite and pearlite, some of which can also exist in a number of different forms. Thermally controlled transformations can be represented on a time-temperature-transformation diagram, showing the different microstructures achieved by different cooling rates, although it is also possible to drive the martensitic transformation by deformation.

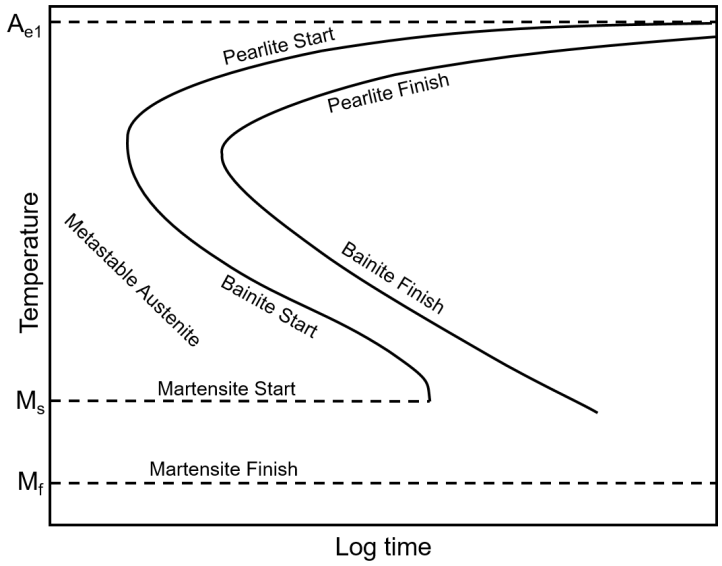

Figure 2.34: Schematic Time-Temperature Transformation diagram.

This work will focus on the phases most commonly observed in 17-4PH: γ-austenite, α-ferrite and δ-ferrite, α'-martensite and ϵ-martensite.

2.3.1.1 Austenite

Austenite is a face-centred cubic (FCC) phase, which can form either on solidification from the melt (primary γ-austenite) or as the result of solid-state transformation from martensite during austenitisation heat treatment (reverted austenite).

Pure iron only takes on the austenite structure at elevated temperature (912 °C to 1394 °C), but a number of alloying elements (e.g. Ni, Mn, N) can extend the region of austenite stability to allow austenite to be stable at room temperature (Figure 2.35). Common austenitic alloys include 304, 301, and 316, which are used for surgical instruments, food preparation equipment and in the chemical industry.

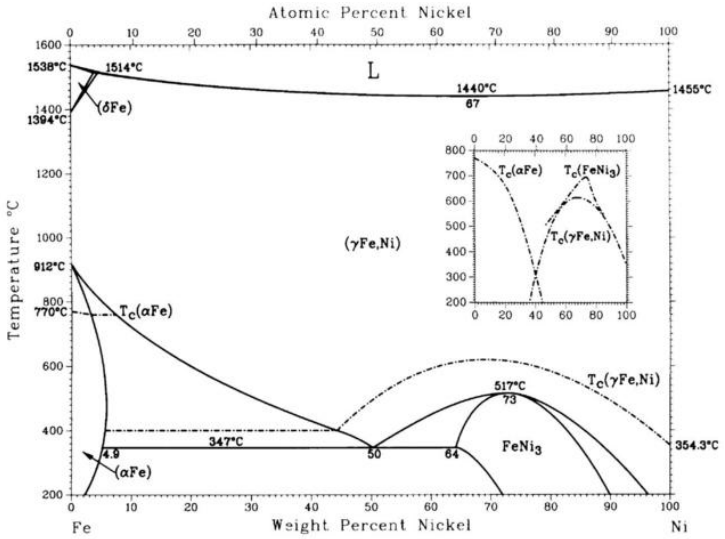

Figure 2.35: Iron-Nickel phase diagram [62].

The lattice parameter for austenite depends on the concentration of alloying elements. It can be calculated (in nm) from the following expression (Equation 2.1), where w_i is the weight fraction of each alloying element [63–65]. This shows that interstitial carbon has a stronger influence on lattice dimension than the main substitutional elements (Cr, Ni).

$$\begin{aligned} a_\gamma = {} & 0.3578 + 0.33w_C + 0.0095w_{Mn} - 0.002w_{Ni} \\ & + 0.006w_{Cr} + 0.056w_{Al} + 0.031w_{Mo} + 0.018w_V \end{aligned} \tag{2.1}$$

2.3.1.2 Ferrite

Ferrite is a body-centred cubic phase, which can form either on solidification from the melt (primary δ-ferrite) or as the result of solid-state transformation from austenite (α-ferrite). The transformation from austenite to α-ferrite is diffusive and is therefore very slow at lower temperatures. This diffusive nature means that α-ferrite may have a different composition from the primary austenite.

Pure iron has the ferrite BCC crystal structure at room temperature. Alloying elements such as chromium, molybdenum and silicon will increase ferrite stability (Figure 2.36). However, as the primary austenite to α-ferrite transformation is diffusive, it can be suppressed by high cooling rates, leading to martensitic transformation (Figure 2.34). Ferritic grades of stainless steel include 430L, which has applications in the petrochemical and automotive industries.

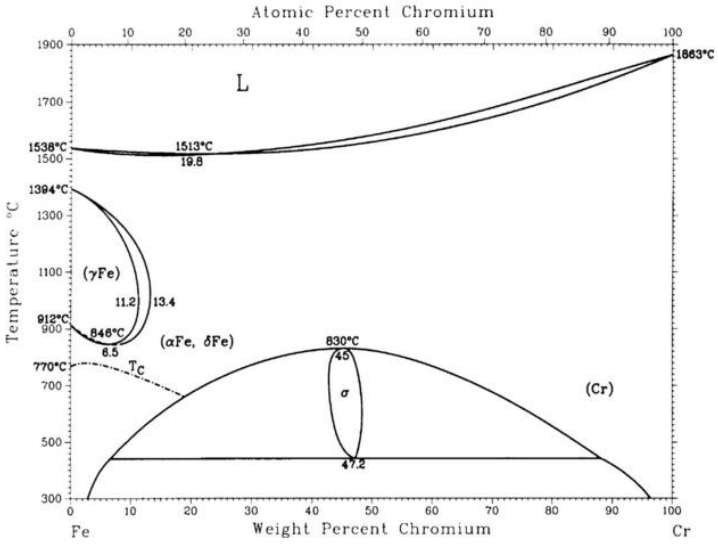

Figure 2.36: Iron-Chromium phase diagram [62].

As with austenite, the lattice parameter of ferrite depends on the concentration of alloying elements. In this case, a_α (in nm) is given by Equation 2.2, where x_i is the mole fraction of each alloying element, and $a_{Fe} = 0.286\,64\,\text{nm}$ [63].

$$\begin{aligned} a_\alpha = 0.28664 + \left\{(3a_{Fe}^2)^{-1}\left[(a_{Fe} - 0.0279x_C)^2(a_{Fe} + 0.2496x_C) - a_{Fe}^3\right]\right\} \\ - 0.003x_{Si} + 0.006x_{Mn} + 0.007x_{Ni} + 0.031x_{Mo} + 0.005x_{Cr} + 0.0096x_V \end{aligned} \tag{2.2}$$

2.3.1.3 α'-Martensite

α'-martensite is a metastable body-centred-cubic/body-centred-tetragonal phase. It can be caused by cooling from primary (prior) austenite at a rate too fast to allow diffusive transformation to ferrite (see Section 2.3.2) or by deformation of primary austenite (see Section 2.3.3). The transformation is displacive (shear), occurring through the coordinated rearrangement of atoms at a local scale.

The displacive nature of the martensitic transformation mean it is forced to take on the composition of the prior austenite, there is no opportunity for carbon to diffuse away. The carbon will be accommodated on the interstitial sites in the BCC lattice, although it is preferentially located on one set of these, causing the to lattice stretch from BCC to BCT with increasing carbon content. For low-carbon martensite, the BCC lattice parameter can be calculated using the same equation as for ferrite (Equation 2.2), and the two structures are sufficiently similar that it is not possible to distinguish ferrite and martensite by XRD.

Because the transformation involves local rearrangement, the austenite and martensite lattices are geometrically related. This relationship often can be observed as close-packed planes in the two crystal structures being near-parallel, and corresponding directions also being near-parallel.

The simplest description of this is the Bain relationship (Figure 2.37), where the austenite unit cell is compressed along the z axis and stretched along the x and y axes, such that a body-centred-tetragonal cell can be defined within the new shape [66]. This has the advantage of being easy to visualise, but this relationship is unfortunately not observed experimentally.

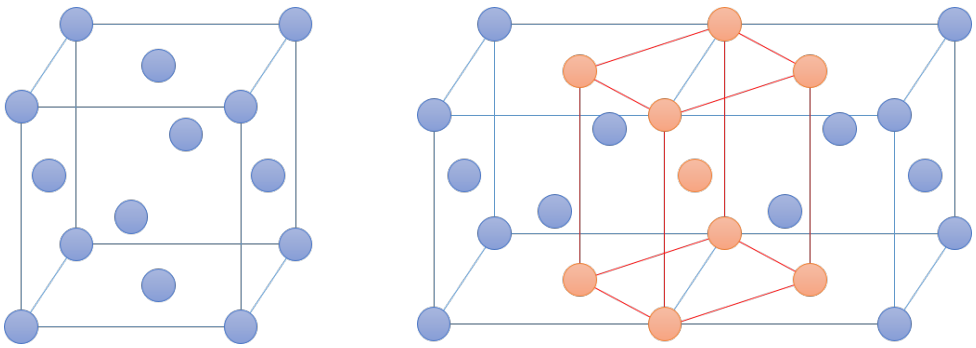

Figure 2.37: Bain orientation relationship.

More complex alternatives have been published, the most common include the Kurdjumov-Sachs and Nishiyama-Wassermann relationships, found in mild steel and Fe-30wt%Ni alloys respectively [67–69].

Kurdjumov-Sachs

$$\{111\}_\gamma \,||\{011\}_\alpha$$
$$< 10\bar{1} >_\gamma \,||< 11\bar{1} >_\alpha$$

Nishiyama-Wassermann

$$\{111\}_\gamma \,||\{011\}_\alpha$$
$$< 10\bar{1} >_\gamma \text{ about } 5.3^\circ \text{ from } < 11\bar{1} >_\alpha \text{ towards } < \bar{1}1\bar{1} >_\alpha$$

Martensite formed within a large austenite grain is often described in terms of packets, blocks and laths (Figure 2.38). A packet is a group of laths with the same habit plane, consisting of blocks of laths which have the same orientation (variant). The sizes of these packets and blocks, which determine the mechanical properties, have been shown to be dependent on composition, particularly carbon content [70].

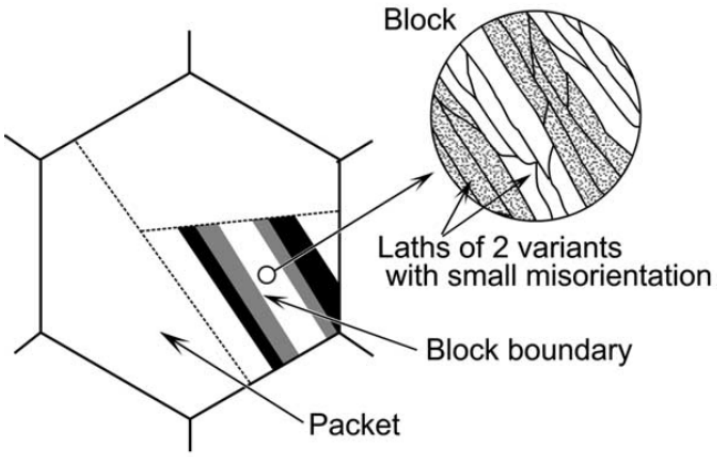

Figure 2.38: Schematic of packet, block and lath structure of martensite [70].

2.3.1.4 Other Phases

ϵ-martensite is a hexagonal-close-packed phase, normally observed at high temperature but it can be also be seen as a side-product or intermediate during deformation-driven martensitic transformation [71].

Other phases that can be seen include bainite, cementite and pearlite. Transformation to these from primary austenite depends on composition and the thermal history during

the cooling phase. These phases are not commonly observed in processing of 17-4PH, so are outside the scope of this work, but further information can be found in the literature [72].

2.3.2 Thermally-Induced Martensitic Transformation

Thermally induced α'-martensite is the product of solid-state transformation from primary austenite under cooling conditions that are too rapid to allow the diffusive transformation to α-ferrite. The transformation occurs over a temperature range, bounded by the martensite start M_s and martensite finish M_f temperatures, and which depends on a number of factors including alloy chemistry and prior austenite grain size.

The martensite start temperature M_s can be defined as the point when the free energy change from austenite to martensite, $\Delta G^{\gamma-\alpha'}$, is sufficient to provide the driving force for nucleation $\Delta G^{\gamma-\alpha'}_{Ms}$ (Figure 2.39) [73]. The magnitude of this driving force is observed to vary with composition, but is in the region of $-700\,\mathrm{J\,mol^{-1}}$ to $-1400\,\mathrm{J\,mol^{-1}}$ [74, 75].

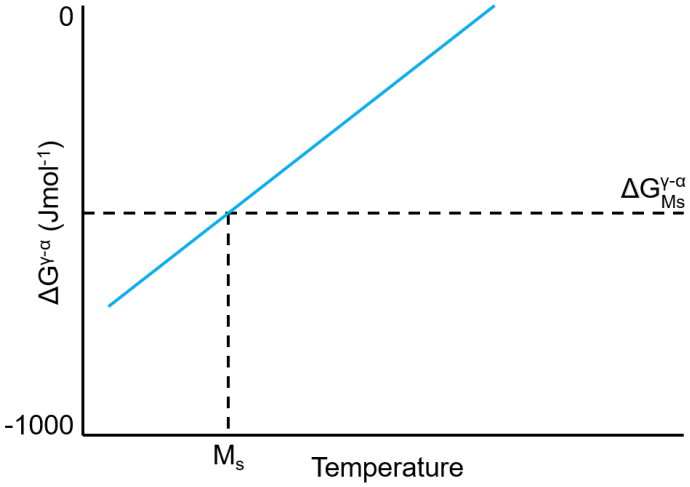

Figure 2.39: Schematic definition of martensite start temperature.

2.3.2.1 Constitution Diagrams

For a fixed composition, the probability of transformation to thermally-induced martensite rather than ferrite is dependent on cooling rate but, because martensite is a metastable phase, it cannot be predicted by equilibrium thermodynamics. Instead, constitution dia-

grams were developed to predict the room temperature structure expected for a range of compositions under welding conditions. Welding has sufficiently fast cooling rates that it forces non-equilibrium cooling, although not as fast as the cooling rates associated with additive manufacture.

The constitution diagrams all use the same basic layout with the concentration of ferrite-stabilising elements on the x-axis and the concentration of austenite-stabilising elements on the y-axis [76–78]. These are represented as Cr_{eq} (chromium equivalent) for ferrite stabilisers and Ni_{eq} (nickel equivalent) for austenite stabilisers. The exact equation that goes into each of these varies between the diagrams, with differences in both the elements selected and the weightings of those elements. There is also variation in the extent over which the diagram is validated.

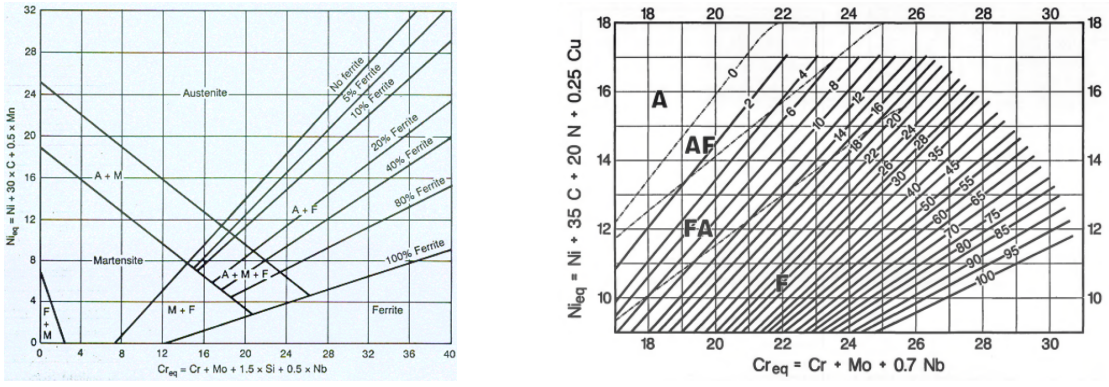

(a) **(b)**

Figure 2.40: a) Schaeffler constitution diagram [76]. b) WRC1992 constitution diagram [77].

One of the most commonly used, and earliest, constitution diagrams is the Schaeffler diagram (Figure 2.40a) [76]. This is relatively simple, predicting single, dual-phase or triple-phase regions, however it fails to consider the austenite-stabilising effect of nitrogen and incorrectly predicts the effect of manganese [77]. Later versions, such as the WRC1992 diagram (Figure 2.40b), include nitrogen and exclude manganese; they also express ferrite content in terms of Ferrite Number (FN) rather than wt% Ferrite [77].

While the WRC1992 diagram is more accurate, the range of validity is smaller, and it does not cover the martensitic region at lower Cr_{eq} and Ni_{eq}. The alloy used in this work, 17-4PH, is a martensitic steel, whose composition using the WRC1992 calculations would have $Cr_{eq} = 15 - 18$ and $Ni_{eq} = 3 - 9$; outside the validity range. Using the Schaeffler diagram, the same composition would give $Cr_{eq} = 15 - 20$ and $Ni_{eq} = 3 - 8$, well within

the validity range. For this reason, the Schaeffler diagram will be used in this work to give guidance on expected microstructures from rapid solidification.

2.3.2.2 Effect of Prior Austenite Grain Size

It has been widely demonstrated that martensite start temperature M_s is dependent on the prior austenite grain size [74, 79–81], with sub-micron grain sizes able to suppress thermally-driven martensitic transformation well below room temperature.

In [74], data from a range of steel compositions was collated and used to develop a relationship between the change in martensite start temperature ΔM_s and austenite grain volume V_γ (Figure 2.41). This relationship is described by Equation 2.3, where a and b are constants, f is the first detectable fraction of martensite and m is the aspect ratio of the martensite plate (assumed to be 0.05).

$$\Delta M_s = \frac{1}{b}\, ln \left[\frac{1}{a\, V_\gamma} \left\{ exp\left(-\frac{ln(1-f)}{m} \right) - 1 \right\} + 1 \right] \tag{2.3}$$

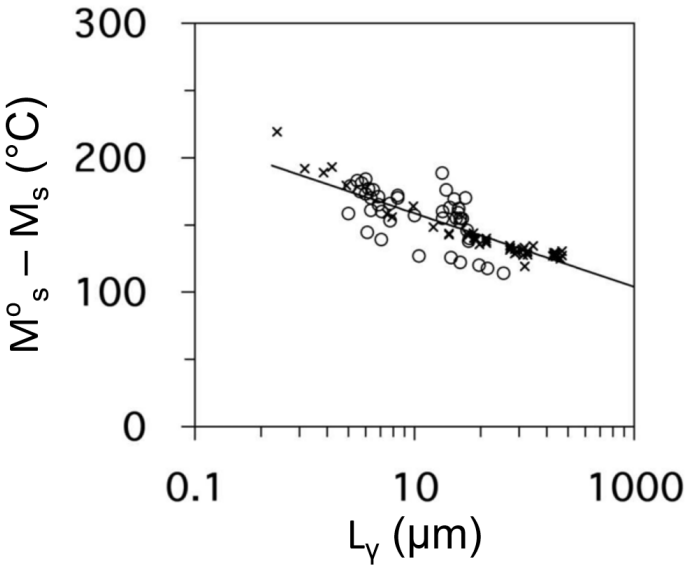

Figure 2.41: Relationship between prior austenite grain size L_γ and suppression of martensite start temperature [74].

A common approach used when studying this effect has been to force martensitic transformation through deformation (e.g. cold rolling, drawing), followed by heat treatment

to drive austenite reversion. The duration of the heat treatment is used to control the grain size of the reverted austenite, after which the sample is cooled and monitored for martensitic transformation. However, similar behaviour has been seen from fine austenite grain sizes achieved through rapid solidification [79, 82].

In [81] it was shown that as austenite grain size reduced, the morphology of the martensite also changed. Large grained austenite transformed into multi-variant lath martensite, arranged into blocks and packets within the original austenite grain boundary; whereas very fine grained austenite (<1 µm) transformed into martensite of a single variant (Figure 2.42).

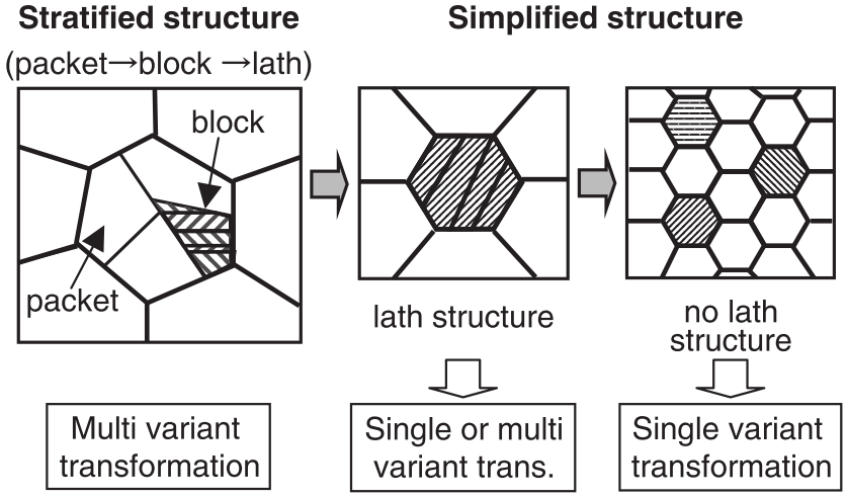

Figure 2.42: Schematic of observed change in martensite morphology with austenite grain size [81].

The study considered first the elastic strain energy associated with the lattice displacement of the martensitic shear transformation, for both single and multi-variant transformations. It found the strain energy for single-variant transformation to be given by Equation 2.4, where E_i and ϵ_i were the Young's modulus and elastic strain in each lattice plane individually. This gave the strain energy associated with single-variant transformation to be $1839\,\mathrm{MJ\,m^{-3}}$.

$$\Delta E_v = \tfrac{1}{2}E_1\epsilon_1^2 + \tfrac{1}{2}E_1\epsilon_1^2 + \tfrac{1}{2}E_1\epsilon_1^2 \tag{2.4}$$

In contrast, the elastic strain energy for multi-variant transformation was given by Equation 2.5, where E^* was the Young's modulus for polycrystalline iron and ϵ^* was the mean

strain. This gave a strain energy of only $68\,\mathrm{MJ\,m^{-3}}$, considerably lower than that for single-variant.

$$\Delta E_v = \tfrac{3}{2} E^* \epsilon^{*2} \tag{2.5}$$

In addition, there was the shear deformation necessary to accommodate this lattice displacement, estimated at $36\,\mathrm{MJ\,m^{-3}}$, and the additional boundary energy estimated at $2\,\mathrm{MJ\,m^{-3}}$. These were the same for both single and multi-variant transformation conditions, bringing the total transformation energy to $1877\,\mathrm{MJ\,m^{-3}}$ for single-variant and $106\,\mathrm{MJ\,m^{-3}}$ for multi-variant.

This transformation energy is offset by the chemical driving force ΔE for transformation, obtained by undercooling ΔT below the martensite start temperature. For multi-variant transformation, only 130 K of undercooling would be necessary to provide sufficient driving force to complete the martensitic transformation (Figure 2.43). However, for single-variant transformation, 2300 K of undercooling would be required for transformation to reach completion, which is clearly impossible.

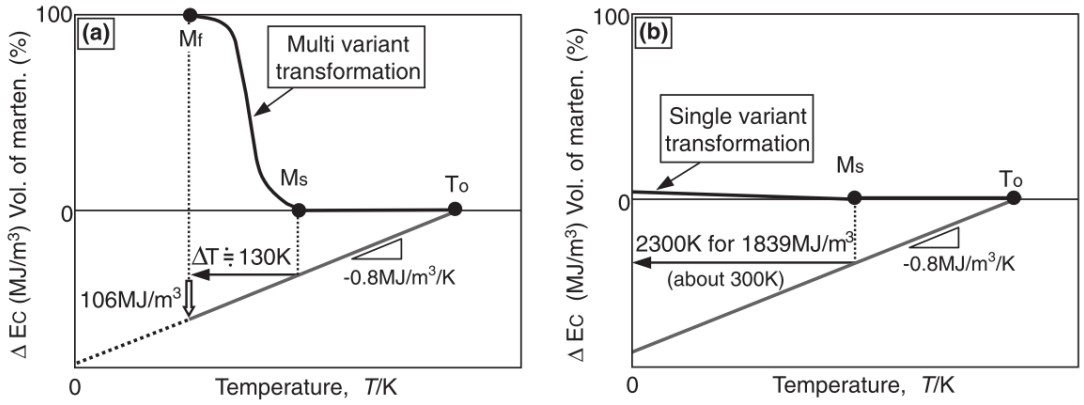

Figure 2.43: Schematic showing change in fraction of martensite and chemical driving force ΔE_c with temperature for a) Multi variant b) Single variant [81].

This showed that if multi-variant transformation could be suppressed, and the transformation was forced to be single-variant, then the transformation would be unable to go to completion and a high proportion of austenite would be retained.

The final consideration was the elastic strain energy associated with nucleation of a new martensite lath of thickness x, which was assumed to be accommodated over the size of the austenite grain d, given in Equation 2.6.

$$\Delta E_v = \tfrac{1}{2}E_1\epsilon_1^2\left(\frac{x}{d}\right)^2 + \left\{\tfrac{1}{2}E_1\epsilon_1^2 + \tfrac{1}{2}E_1\epsilon_1^2\right\}\left(\frac{x}{d}\right) \tag{2.6}$$

By plotting the strain ΔE_v against grain size d (Figure 2.44), it was shown that the energy required for nucleation increases dramatically for grain sizes below 1 µm.

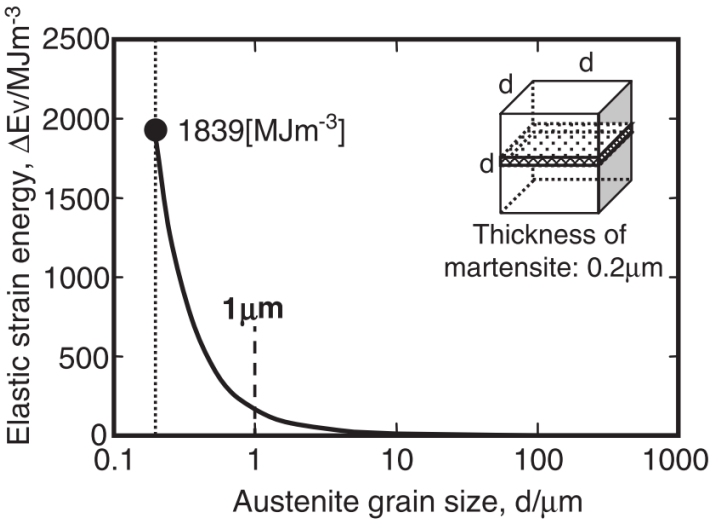

Figure 2.44: Change in elastic strain energy of nucleation with austenite grain size [81].

In summary, the strain energy associated with nucleation rises significantly for grain sizes below 1 µm, making multi-variant martensite nucleation very difficult. However, single-variant transformation requires an extremely high level of undercooling to provide sufficient driving force for transformation to go to completion, so only partial transformation is achieved, resulting in an increased amount of retained metastable austenite.

One of the earlier examples of micro-scale functional grading used different lasers to achieve grain structure variation in 316 stainless steel (Figure 2.12), where the 400 W laser produced a fine grain size while the 1000 W laser produced a coarser grain size. If a similar approach could be achieved with 17-4PH within the confines of the available equipment, the variation in grain size could be sufficient to either suppress or allow martensitic transformation, giving an alternative route to achieving an AM-built, magnetically graded material.

2.3.3 Deformation-Induced Martensitic Transformation

It is also possible to cause martensitic transformation from prior austenite through deformation. This has interesting effect on mechanical behaviour, where increasing strain drives an increasing phase fraction of martensite, increasing the work hardening rate and thereby producing an extended plastic region (Figure 2.45). The process is called TRansformation Induced Plasticity (TRIP). There are two types of TRIP steels: those which are fully austenitic before deformation, and those which have a small quantity of retained austenite within a ferritic-bainitic matrix, often called TRIP-assisted steels [83, 84].

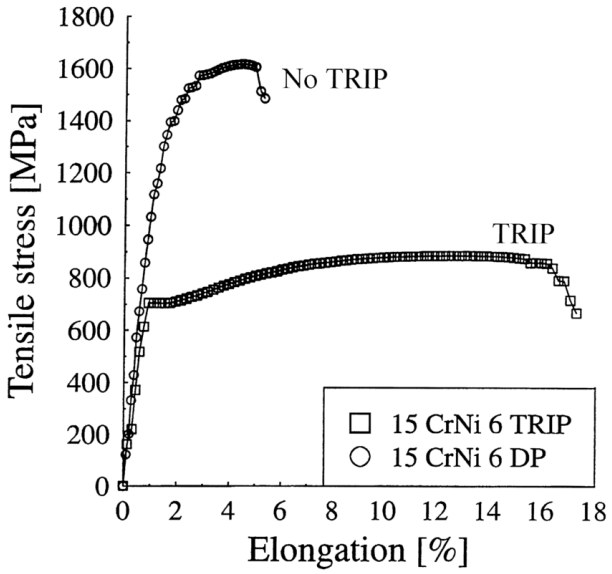

Figure 2.45: Stress-strain curves for a low-alloy ferritic-bainitic steel, with and without retained austenite, showing the effect of transformation induced plasticity (TRIP) [83].

Martensite formed through deformation is differentiated into stress-assisted and strain-induced. The Olson-Cohen model [71] defined these in distinct zones, with stress-assisted below the yield point and strain-induced above (Figure 2.46), however recent work has shown that the stress-assisted transformation can happen above the yield point and may even dominate [85, 86].

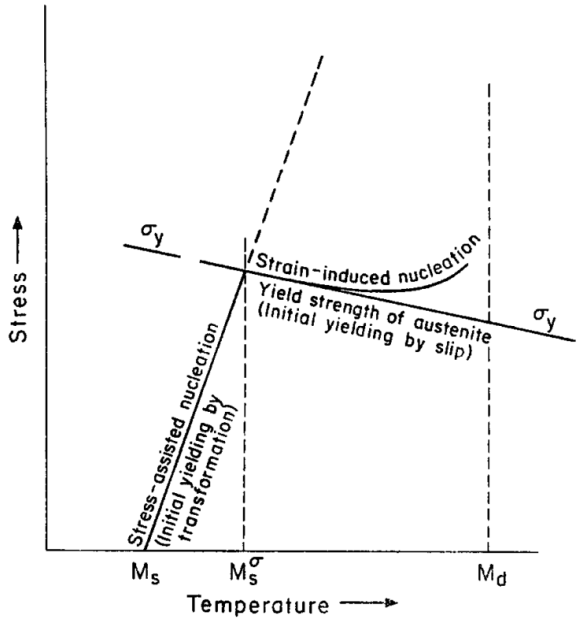

Figure 2.46: Olson & Cohen model of deformation martensite mechanisms [71]. Below M_s there is a chemical driving force for transformation and no additional stress is required. Between M_s and M_s^σ the transformation is stress-assisted. Above M_s^σ the material yields and transformation is strain-induced. Above M_d there can be no transformation.

2.3.3.1 Stress-Assisted Transformation

Martensitic transformation starts when the free energy change from austenite to martensite $\Delta G^{\gamma-\alpha'}$ reaches a critical value, $\Delta G_{Ms}^{\gamma-\alpha'}$ (Figure 2.47) [72]. In the case of thermally-activated martensite with no applied stress, this is reached by undercooling to the martensite start temperature, M_s.

An applied stress will interact with the shape change associated with martensitic transformation, with an interaction energy U, the magnitude and direction of which depends on the orientation relationship between the applied stress and each of the 24 potential martensite variants. If the orientation is such that transformation to one of these variants would relieve the stress, U will contribute to the free energy change, raising M_s and allowing stress-assisted transformation.

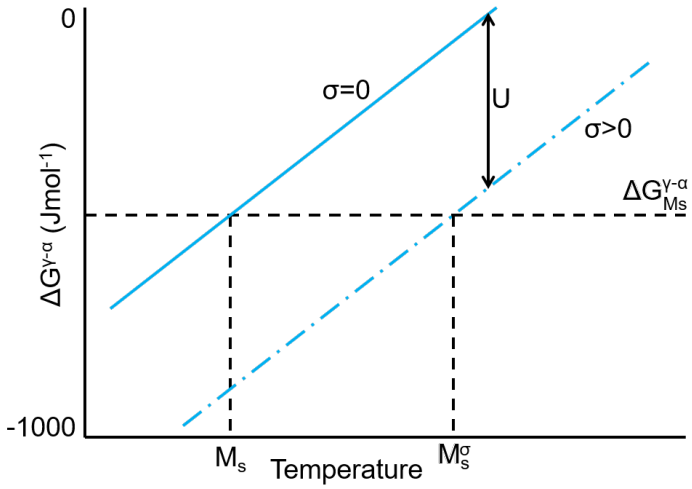

Figure 2.47: Action of an applied stress to raise M_s [72].

The geometric relationship between austenite and martensite allows 24 possible variants of martensite for a single austenite grain (see Section 2.3.1.3). Thermal martensite will display an equal distribution of all 24 possible variants, but deformation martensite will have a biased distribution with more of the variants that are preferentially orientated with the applied stress direction [72].

There is also a grain-size dependence on morphology, similar to that observed for thermally-induced martensite in [81]. In 301LN, coarse-grained (28 µm) prior austenite was observed to transform to martensite with several variants per austenite grain, whereas fine-grained (0.5 µm) prior austenite transformed to martensite with only one or two variants per austenite grain (Figure 2.48).

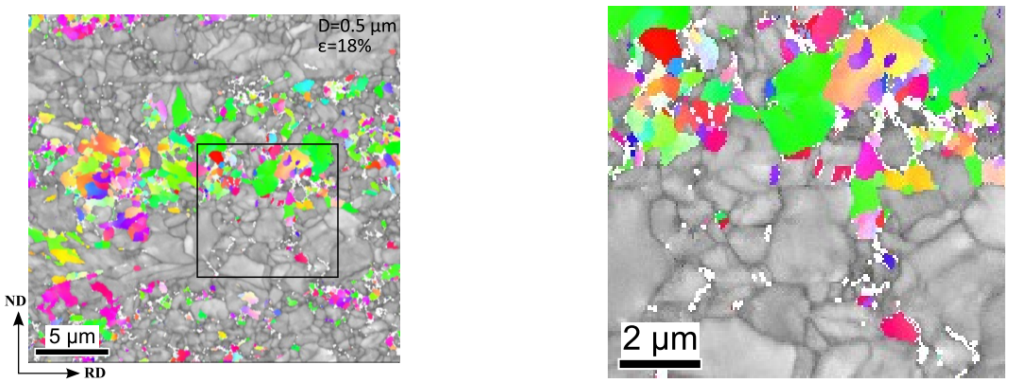

(a) **(b)**

Figure 2.48: a) EBSD of 301LN steel with 0.5 µm prior austenite grain size subjected to 18 % strain in tension. b) Detail from a). [87]

2.3.3.2 Strain-Induced Transformation

In contrast, strain-induced transformation requires the formation of new nucleation sites. There is much discussion in the literature about the exact mechanism, with different behaviour observed for different materials and under different experimental conditions (strain rate, temperature, pre-processing). α'-martensite has been seen to nucleate from intersections between, and from within, a number of structures including ϵ-martensite laths, strain bands, γ twin boundaries and γ grain boundaries (Figure 2.49).

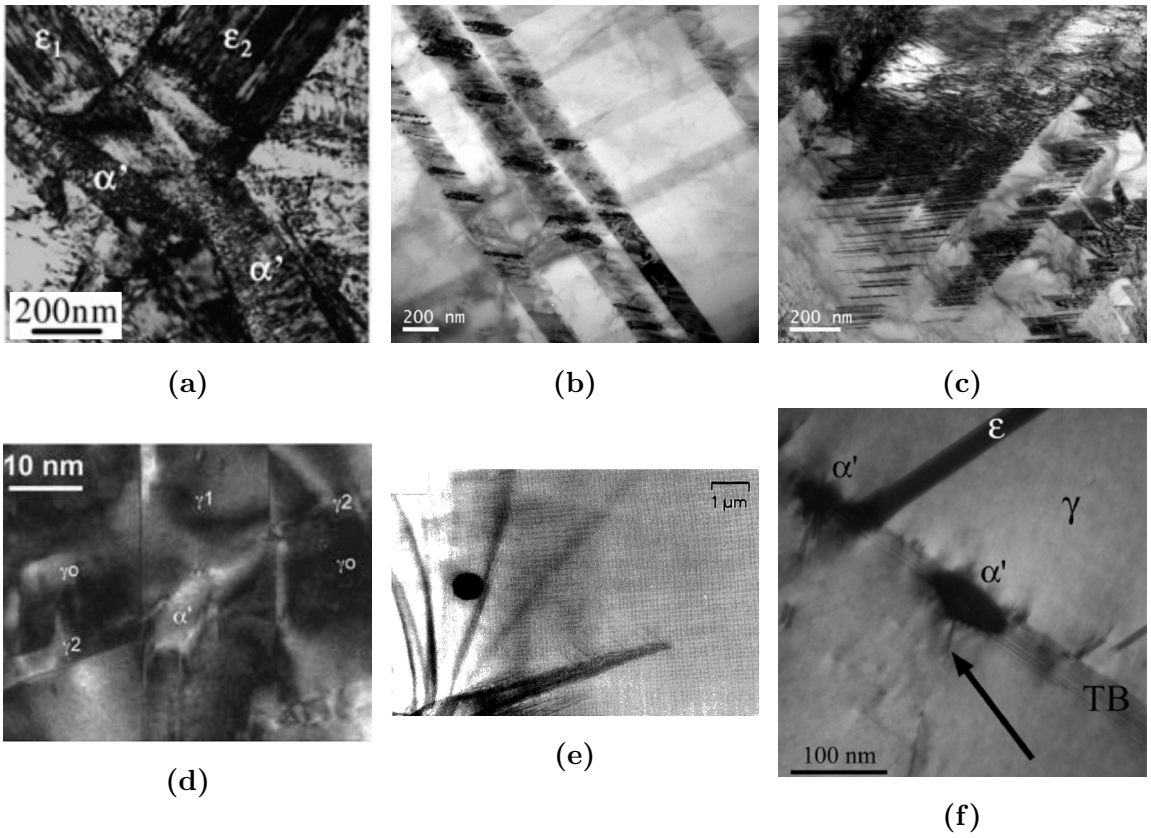

Figure 2.49: a) BF TEM showing α' nucleation on intersection of ϵ laths in Fe-Mn-C-N [88]. b) BF TEM showing α' nucleation from intersecting strain bands in 310LN steel [89]. c) BF TEM showing α' nucleation within a strain band in 310LN steel [89]. d) BF HRTEM showing α' from mechanical γ twins in 316 steel [90]. e) HVEM showing α' nucleation from γ grain boundary (bottom left) with no ϵ in Fe-Ni-Mn-C [91]. f) BF TEM showing α' nucleation at intersection of annealing twin boundary (TB), ϵ and slip band (arrow) in 304L steel [92].

The absence of ϵ-martensite does not necessarily mean strain-induced transformation has not occurred. Firstly, some studies have shown ϵ-martensite to be an intermediate stage which then transforms to α'-martensite, so the phase fraction may be very low [71].

Secondly, in 301LN, the transformation process has been shown to be dependent on prior austenite grain size, with coarse material following $\gamma - \epsilon - \alpha'$, while fine material showed no intermediate ϵ-martensite and a direct $\gamma - \alpha'$ transformation occurred instead, with α' nucleation on grain boundaries (Figure 2.50) [87].

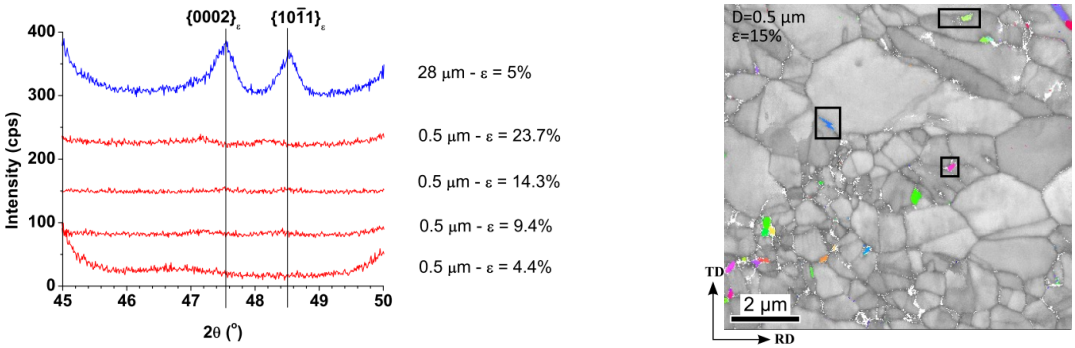

(a) **(b)**

Figure 2.50: a) Effect of prior austenite grain size and strain on XRD peak intensity of ϵ-martensite in 301LN steel. b) EBSD image of 0.5 µm grain size austenite, under 15% strain, with α'-martensite nucleation on grain boundaries. α'-martensite (coloured by inverse pole figure) superimposed on austenite (shaded by band contrast) in 301LN. [87]

It was initially accepted that the stress-assisted and strain-induced mechanisms dominated at different levels of applied stress, following the Olson-Cohen approach (Figure 2.46), however this has recently been shown to be incorrect, with stress-assisted transformation observed above the yield point [85, 86, 93]. Data from older studies has been reviewed, and it has been demonstrated that the behaviour can be explained with stress-assisted transformation as the dominant mechanism [94].

This situation arose because many studies on *apparently* strain-induced transformation had been carried out by tensile testing with large plastic strains, where it was not possible to isolate the effect of applied stress on the chemical driving force and the effect of strain to introduce lattice defects as new nucleation sites. More recent studies on strain-induced transformation have involved deformation at elevated temperature, where transformation cannot occur, followed by stress-free cooling [95].

Given that, stress-assisted transformation was judged to be the dominant mechanism [94], and that this does not require stacking faults with transformation of ϵ-martensite as an intermediary or alternative, it is possible that there could be a linkage with the grain-size dependence reported in 301LN in [87]. Larger grains, able to accommodate the elastic

strain associated with stacking faults would follow a strain-induced $\gamma - \epsilon - \alpha'$ sequence, while smaller grains, unable to accommodate the stacking faults required to nucleate ϵ-martensite would wait until the applied stress was high enough to provide sufficient driving force for direct $\gamma - \alpha'$ stress-assisted transformation.

2.3.3.3 Tension and Compression

As described in Figure 2.47, an applied stress acts to provide an additional driving force for martensitic transformation, effectively increasing the M_s. It was demonstrated that in Fe-Ni and Fe-Ni-C alloys, tensile stress raises M_s most strongly, compressive stress raises it but to a lesser extent, while hydrostatic pressure lowers M_s (Figure 2.51a) [96].

However, further work on 304 austenitic stainless steel showed that the relationship was more complex (Figure 2.51b). In the early stages of deformation, compression resulted in a higher volume fraction of martensite than tension. Then in the later stages, at high strain, the situation reversed and tension resulted in more martensite than compression [97].

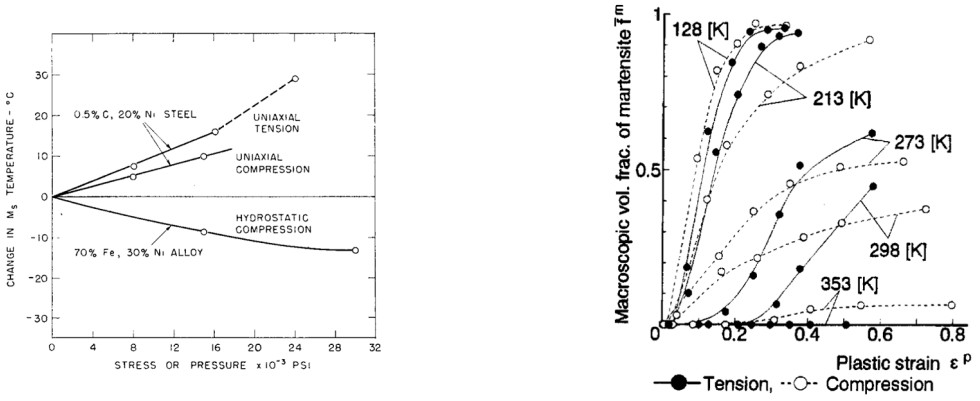

(a) **(b)**

Figure 2.51: a) Effect of applied stress on M_s in Fe–20Ni–0.5C [96]. b) Martensite volume fraction under plastic strain in 304SS [97].

Overall, it can be expected that tension and compression will both drive martensitic transformation, although their relative weightings may depend on alloy chemistry, and how far the deformation and associated transformation have progressed.

2.3.3.4 TRIP Probability

As discussed earlier, the likelihood and extent of thermally-induced martensitic transformation at room temperature depends on the cooling rate, alloy chemistry and prior austenite grain size. Similar considerations apply for deformation-induced martensitic transformation, which can itself be influenced by alloy chemistry, prior austenite grain size and the deformation conditions (e.g. strain rate).

Analogous to M_s, the M_{d30} temperature is defined as the temperature at which 50 vol% of austenite transforms to deformation-martensite due to a true strain of 30 % [98, 99]. This definition arises due to the difficulty in measuring the deformation-induced start M_s^σ and finish M_d temperatures directly. In 1954, an empirical expression for M_{d30} was developed by Angel based on alloy composition in wt% [98]:

$$\begin{aligned} M_{d30}(^\circ\mathrm{C}) = 413 - 463(\mathrm{C} + \mathrm{N}) - 9.2\mathrm{Si} - 8.1\mathrm{Mn} \\ - 13.7\mathrm{Cr} - 9.5\mathrm{Ni} - 18.5\mathrm{Mo} \end{aligned} \tag{2.7}$$

Assuming mechanical testing is carried out at room temperature, if the M_{d30} for a particular alloy is below room temperature then strain-induced transformation is unlikely, while if M_{d30} is above room temperature then transformation is possible [99]. The M_{d30} calculated using Equation 2.7 for the allowed composition range of 17-4PH is 67 °C to 179 °C, well above room temperature and indicating it is susceptible to martensitic transformation under deformation.

A later study on 301 and 304 stainless steels reviewed this and a modified version was developed, shown in Equation 2.8 [100]. This has a much stronger weighting for nickel and includes copper and niobium, both of which are present in 17-4PH and both of which are given strong weightings. For the composition range of 17-4PH this modified expression gives an M_{d30} of −68 °C to 161 °C. This is a much wider range than that predicted by Equation 2.7, and suggests that some compositions of 17-4PH have M_{d30} below room temperature and could therefore be stable against deformation-induced martensitic transformation.

$$M_{d30}(^{\circ}\mathrm{C}) = 551 - 462(\mathrm{C}+\mathrm{N}) - 9.2\mathrm{Si} - 8.1\mathrm{Mn} \\ - 13.7\mathrm{Cr} - 29(\mathrm{Ni}+\mathrm{Cu}) - 18.5\mathrm{Mo} - 68\mathrm{Nb} \tag{2.8}$$

In [100], the effect of prior austenite grain size on M_{d30} was also considered (Figure 2.52). A further refinement was developed relating M_{d30}^{gs}, the M_{d30} modified by grain size, to η, the ASTM grain size number, which was validated for grain sizes of 6 µm to 124 µm and for alloys with $M_{d30} \approx 35\,^{\circ}\mathrm{C}$.

$$M_{d30}^{gs} = M_{d30} - 1.42(\eta - 8) \tag{2.9}$$

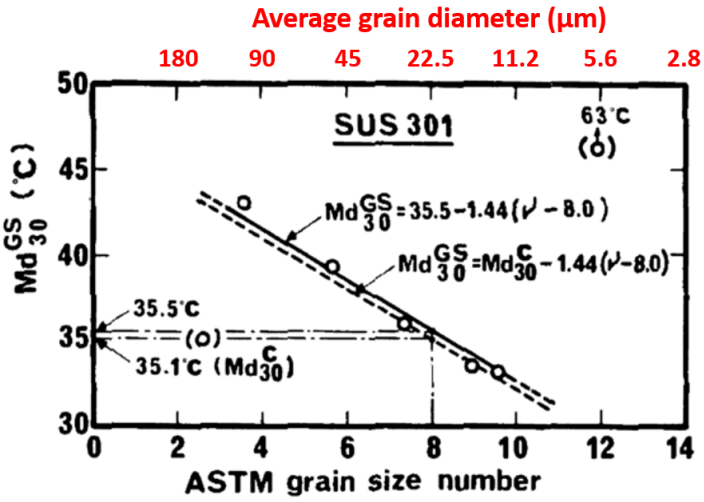

Figure 2.52: Relationship between M_{d30}^{gs} and prior austenite grain size [100]. Annotated with average grain size in microns [101].

Similar behaviour was observed in [87], where samples of different grain sizes were subjected to tensile strain at constant 25 °C and monitored for the volume fraction of α'-martensite transformed (Figure 2.53a). This showed that to achieve 50 vol% transformed, the true strain required was approximately 0.3 for a sample with 0.9 µm grain size, but only 0.25 for the sample with 25 µm grain size. Taking the alternative view, for a true strain of 0.3, equivalent to an engineering strain of 35 %, the sample with 0.9 µm grain size showed 50 vol% transformation, while the sample with 28 µm grain size showed 65 vol% transformation.

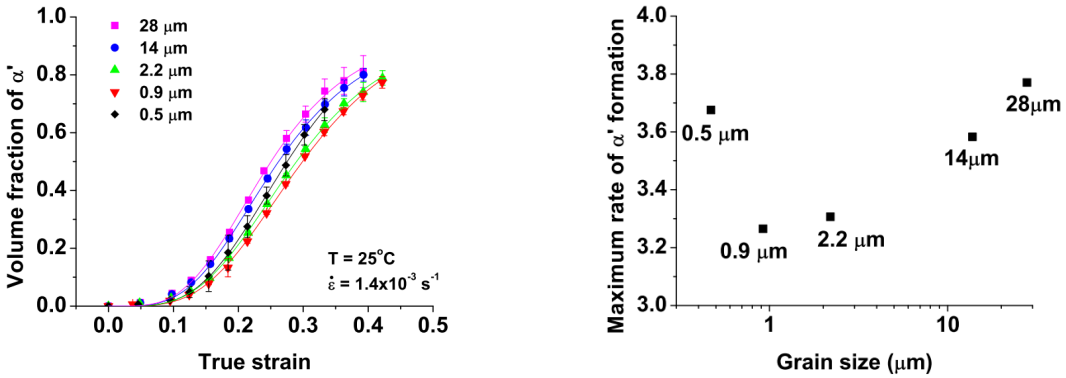

(a) (b)

Figure 2.53: a) Volume fraction α'-martensite transformed in 301LN as a result of strain in samples with varying prior austenite grain size. b) Maximum rate of α'-martensite transformation in (a) [assumed with respect to strain rather than time]. [87]

The analysis in [87] also considered the rate of martensitic transformation (Figure 2.53b). It is assumed that, as the martensitic transformation is shear and not dependent on time, this is rate with respect to strain although it was not explicitly defined in the literature.

This showed a possible further complexity, that the 0.9 µm grain size sample showed the slowest maximum transformation rate (Figure 2.53b). It was suggested that this indicated suppression of M_{d30} by prior austenite grain size reached a minimum around 1 µm. However, the gradients in the centre section of the curves where most transformation occurs were very similar, and the more significant difference was possibly in the threshold strain required to start transformation.

A qualitative explanation was proposed in [87] to explain the possible change in transformation rate with grain size. For large grain sizes, α' transformation was observed primarily nucleating from ϵ plates rather than γ grain boundaries. As grain size reduced, the fraction of ϵ reduced (Figure 2.50a), limiting the nucleation rate of α'. For very fine grain sizes, α' nucleation from grain boundaries becomes dominant (Figure 2.50b), allowing the transformation rate to increase.

2.3.3.5 Stacking Fault Energy

The TRIP probability can alternatively be considered in terms of the Stacking Fault Energy (SFE), which determines how easily a perfect dislocation can dissociate into partial

dislocations and stacking faults. In materials with low SFE, deformation results in dissociation which hinders dislocation motion, while the associated stacking faults nucleate ϵ and/or α' martensite. In contrast, in materials with high SFE dissociation does not occur as easily, so deformation is likely to result in dislocation glide.

SFE is dependent on temperature for a given composition, so investigations on Fe-22Mn-0.6C steel across a range of temperatures allowed SFE regions to be identified for each of these mechanisms [102]. While the exact values cannot be read across to other compositions, the pattern of behaviour will still apply.

$T = 673\,\mathrm{K}$	$\mathrm{SFE} = 80\,\mathrm{mJ\,m^{-2}}$	Dislocation glide
$T = 293\,\mathrm{K}$	$\mathrm{SFE} = 19\,\mathrm{mJ\,m^{-2}}$	Mechanical Twinning + Dislocation Glide
$T = 77\,\mathrm{K}$	$\mathrm{SFE} = 10\,\mathrm{mJ\,m^{-2}}$	ϵ-martensite + Dislocation Glide

In [5], the SFE of 17-4PH was calculated to be $15\,\mathrm{mJ\,m^{-2}}$ to $20\,\mathrm{mJ\,m^{-2}}$. This was determined from the average electron vacancy number, $< NLE >$, which is estimated to be 2.9 to 3.0 for the composition range allowable for 17-4PH (Equation 2.10) [103]. The $< NLE >$ is then related to the SFE according to the relationship shown in Figure 2.54, where the range for 17-4PH is highlighted. An SFE of $15\,\mathrm{mJ\,m^{-2}}$ to $20\,\mathrm{mJ\,m^{-2}}$ is at the lower end of the range described above, indicating that deformation would be likely to cause dissociation and stacking faults in 17-4PH.

$$< NLE >= [0.61\,\mathrm{Ni} + 4.66\,\mathrm{Cr} + 4.66\,\mathrm{Mo} + 2.66\,\mathrm{Fe} + 3.66\,\mathrm{Mn} + 6.66\,\mathrm{Si}]/100 \qquad (2.10)$$

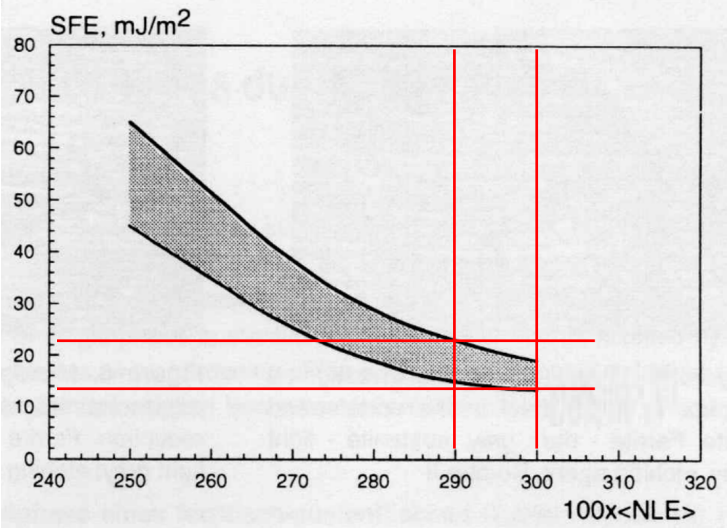

Figure 2.54: Relationship between average electron vacancy number and stacking fault energy, annotated with location of 17-4PH composition range [103].

Subsequent tensile testing carried out on SLM-built material showed TRIP behaviour (Figure 2.55), confirming that 17-4PH is capable of deformation-induced martensitic transformation, in line with the calculated M_{d30} and SFE.

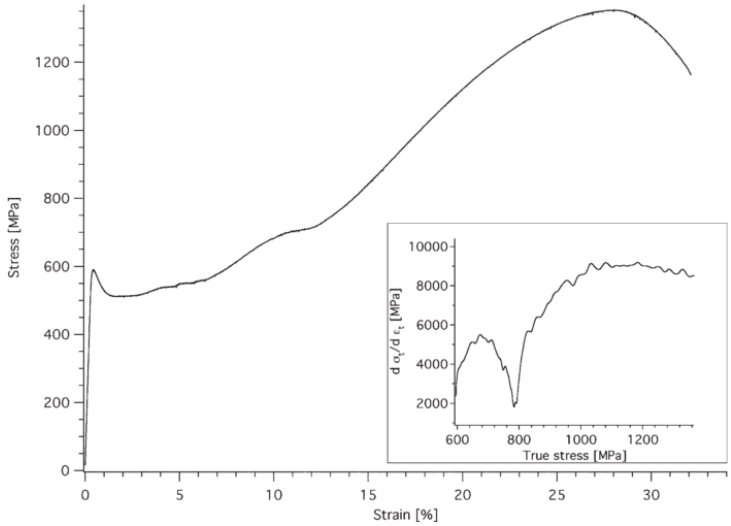

Figure 2.55: Stress-strain curve for SLM-built 17-4PH showing extended plastic region. Inset Kocks-Mecking analysis. [5]

2.3.4 Martensite Growth

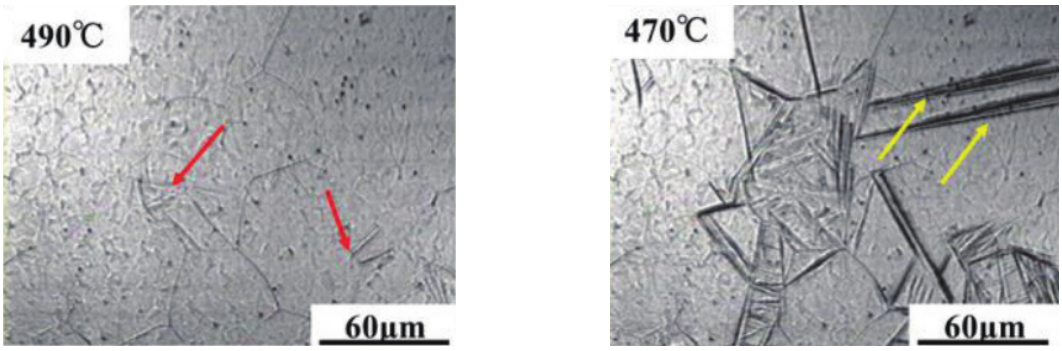

(a) (b)

Figure 2.56: In-situ observation of martensite growth in undeformed material. a) Block nucleation on grain boundaries (red arrows). b) Multiple blocks of same orientation, crossing grains and terminating at grain boundaries (yellow arrows). [104]

Martensite is often observed to nucleate from one grain boundary, grow across the grain and then stop at the opposite boundary, where the lattice disruption at the boundary is not able to support a continuation of the displacive transformation [105]. This was demonstrated in Fe-0.14C-2.14Cr-0.86Mo steel, while investigating the effect of ausforming through in-situ observation of martensite transformation [104]

Other lattice disruptions can also stop martensite growth, such as the dense dislocation walls associated with sub-grain boundaries. There is evidence of this from Fe-0.14C-2.14Cr-0.86Mo steel which had been ausformed to 20% strain at 850 °C, and contained slip bands and sub-grain boundaries resulting from the deformation. In these samples, martensite was observed to nucleate and terminate at both grain boundaries and sub-grain boundaries (Figure 2.57). This resulted in a reduction in the average size of both blocks and packets in the ausformed material.

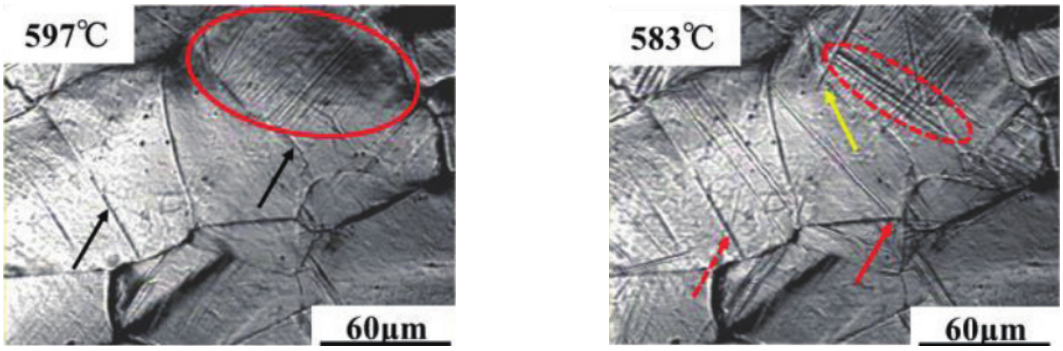

(a) **(b)**

Figure 2.57: In-situ observation of martensite growth in ausformed material. a) Slip bands (red circle) and sub-grain boundaries (black arrows). b) Block growing from grain boundary (solid red arrow), block growing from sub-grain boundary (dashed red arrow), block stopped by sub-grain boundary (yellow arrow). [104]

The sub-grain boundaries have high dislocation density, but the material either side of the boundary will have very similar grain orientation because it came from the same original grain prior to deformation. As the martensite stops growing at these sub-grain boundaries, it must be the high dislocation density which prevents further growth, rather than lattice mismatch.

Austenite can become mechanically stabilised against martensitic transformation, when the dislocation debris resulting from plastic deformation resists the motion of glissile interfaces [105]. Experimental work combined with neural network modelling has shown that martensitic transformation is accelerated by deformation at low strains, but reaches a maximum for true strain > 2 when the austenite becomes mechanically stabilised (Figure 2.58) [106].

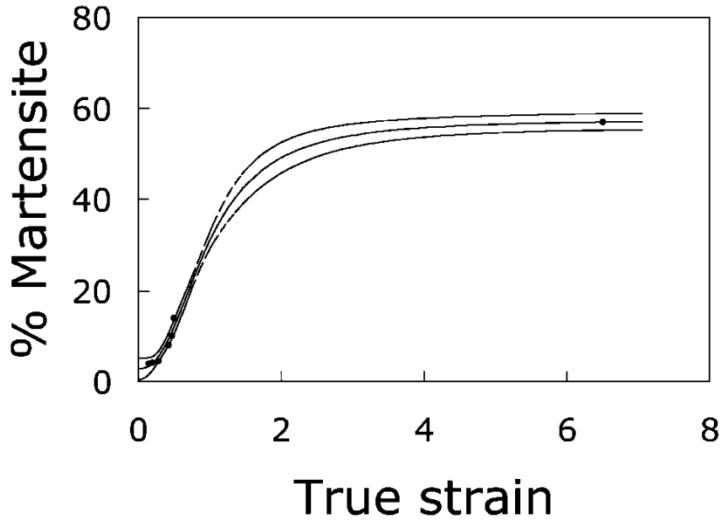

Figure 2.58: Experimental and modelling data for mechanically stabilised 316L wires [106].

2.3.5 Austenite Reversion

Austenite reversion is the reverse of the martensitic transformation. It normally involves heating the material into a region above the austenite start temperature A_{c1} to allow a time-dependent diffusive transformation to take place. However, many studies have shown that while this diffusion-controlled mechanism dominates at low heating rates, at high heating rates transformation can occur by a shear mechanism [107–111]. This shear mechanism has a very high activation energy ($900\,\mathrm{kJ\,mol^{-1}}$ [108]), but the extent of reaction is independent of time.

The diffusion and shear austenite reversion mechanisms can be illustrated by a Reversion-Temperature-Time diagrams (Figure 2.59). A_s and A_f are the diffusive start and finish transformation temperatures with the curves indicating their time dependency. $A_s^{'}$ and $A_f^{'}$ are the shear start and finish temperatures, which have no time dependency. R_s is the expected start of recrystallisation and T_0 is the temperature where the Gibbs free energy of austenite and ferrite are equal.

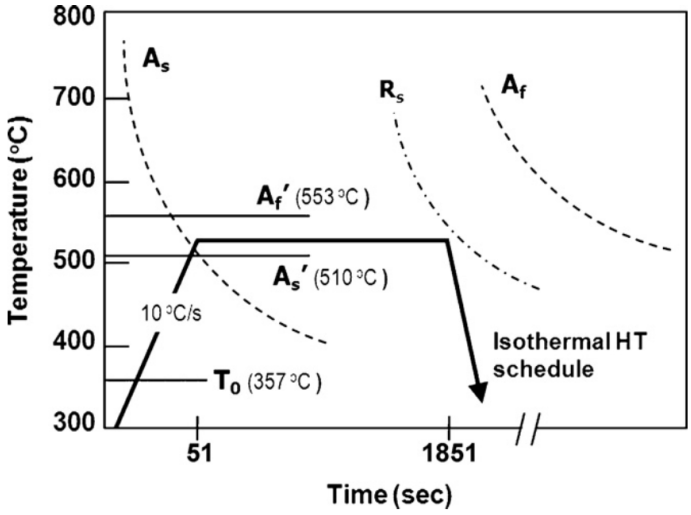

Figure 2.59: Reversion-Temperature-Time diagram for Fe-0.023C-10.91Cr-9.23Ni-6.97Mn [109].

A heat treatment which follows the indicated line would initially see some shear transformation as it moves through $A_s^{'}$, but this would be incomplete because it does not reach $A_f^{'}$. As it passes A_s, the diffusion-driven transformation would start, and would continue during the isothermal hold. The cooling stage occurs before the reverted austenite has time to start recrystallisation and before all martensite has reverted.

The temperatures on these diagrams are strongly dependent on alloy chemistry, particularly the Ni/Cr ratio. A high Ni/Cr ratio increases the Gibbs free energy change between the FCC and BCC structures, bringing down the $A_s^{'}$ temperature and making shear transformation easier, whereas a low Ni/Cr ratio will cause $A_s^{'}$ to increase. This can be seen from the literature on Fe-Cr-Ni alloys (Table 2.1).

Table 2.1: Alloy Chemistry and $A_s^{'}$ Temperature

Reference	Cr wt%	Ni wt%	Ni/Cr	$A_s^{'}$ K	$A_f^{'}$ K	Range
[110]	17.62	8.78	0.50	*	1023	*
[110]	15.62	9.83	0.63	803	903	100
[109]	10.91	9.23	0.84	783	833	50

*Not provided

Compared with these alloys, the Ni/Cr ratio of 17-4PH is low (0.23) so the $A_f^{'}$ would be expected to be high, around 1110 K by extrapolation. This is in reasonable correlation with the $A_s^{'}$ (1123 K) and $A_f^{'}$ (1243 K) temperatures under rapid heating (200 K s^{-1}) observed by dilatometry on 17-4PH [108].

The diffusionless shear transformation is effectively a direct reversal of the previous martensitic transformation, so is independent of time provided there are sufficient defect sites available for nucleation. In the case of the SLM-built material, it is expected that the martensite will be highly dislocated (1×10^{16} m^{-2} [5]), providing many suitable nucleation sites. The extent of transformation will then depend purely on the temperature reached.

Austenite reversion can be accompanied by compositional changes which may affect austenite stability, and therefore influence the proportion of retained austenite on subsequent cooling [111]. A Fe-13Cr-7Ni-3Si steel was analysed by diffusive austenitisation over a range temperatures using XRD to measure the proportion of retained austenite after cooling to room temperature. The results showed the fraction of retained austenite increasing with heat treatment temperature, reaching a peak at 650 °C and then reducing (Figure 2.60a).

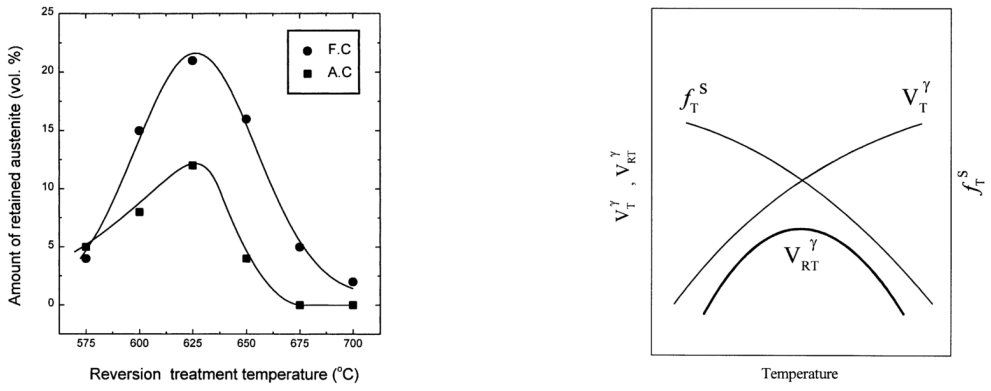

Figure 2.60: a) Influence of austenitisation heat treatment temperature and air or furnace cooling on volume fraction retained austenite. b) Competing effects of volume fraction reverted austenite V_T^{γ} and austenite stability f_T^s on volume fraction retained austenite V_{RT}^{γ}. [111]

The initial increase in retained austenite was attributed to a larger volume fraction of reverted austenite as the heat treatment temperature was increased. But with increasing heat treatment temperature, EDS showed that the nickel content of the retained austenite

decreased, increasing the M_s, and making austenite less stable, leading to a reduction in fraction of retained austenite (Figure 2.60b).

While this type of compositional variation is not unexpected from diffusional austenitisation, which must involve time at temperature, it may not necessarily occur in a shear austenitisation. If the material is heated fast enough to drive the shear transformation, but then cooled equally rapidly, the amount of compositional change that can take place will be comparatively limited, although it may still be possible if there are extreme composition gradients left after solidification.

Austenite reversion can be used to achieve grain refinement in austenitic stainless steels [112–114]. The material is manufactured by conventional methods and mechanically processed to achieve deformation-driven martensitic transformation. It is then heated into the austenite reversion zone, with the temperature kept as low as possible to minimise grain growth, and once fully reverted is quenched back to room temperature. The result is a nano-grained austenite which has significantly improved yield strength compared to the initial condition.

This suggests that for a material with a 'large-grain' martensite start temperature above room temperature, the grain refinement from austenite reversion could reduce the grain size sufficiently to stabilise austenite and increase the proportion of retained austenite.

2.4 Selective Laser Melting of Steels

SLM is widely used for a range of stainless steel compositions, both for research and commercial manufacturing applications. Many of the common stainless steel grades are now available as powder designed for SLM processing, including 316, 17-4PH, 430L and 18Ni300 [115]. Much work has been carried out optimising SLM processing parameters for build quality, and quantifying differences in material properties between SLM and conventionally manufactured material.

One key difference between conventionally manufactured and SLM-built stainless steels is the microstructure. In their as-built state SLM steels are characterised by rounded melt pools, with radially oriented large 10 µm to 100 µm grains, each containing a forest of 0.5 µm to 2 µm solidification cells. This general morphology persists across a range of steel compositions and processing parameters, suggesting it is typical of the as-built

condition. Section 2.4.1 will discuss the solidification conditions associated with SLM that result in this type of microstructure.

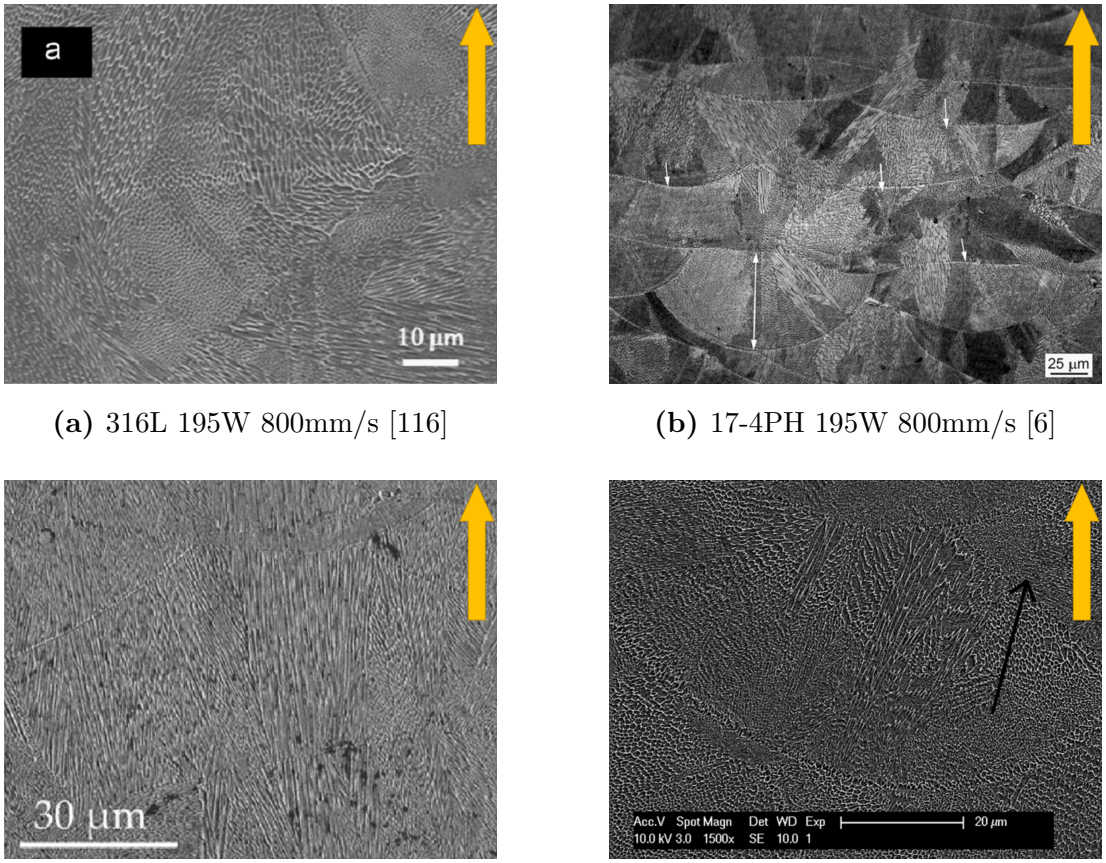

(a) 316L 195W 800mm/s [116]

(b) 17-4PH 195W 800mm/s [6]

(c) 18Ni300 100W 150mm/s [117]

(d) H13 170W 800mm/s [118]

Figure 2.61: Examples of grain structures from additively manufactured steels. Yellow arrows indicate build direction.

EBSD of AM-built 316L showed significant misorientation between grains, but also some misorientation within grains shown by mottled colouration in Figure 2.62a [116]. TEM showed the solidification cells to be separated by dense dislocation walls, 0.1 µm thick (Figure 2.61). These dislocation walls are geometrically necessary to accomodate the orientation mismatch between adjacent cells.

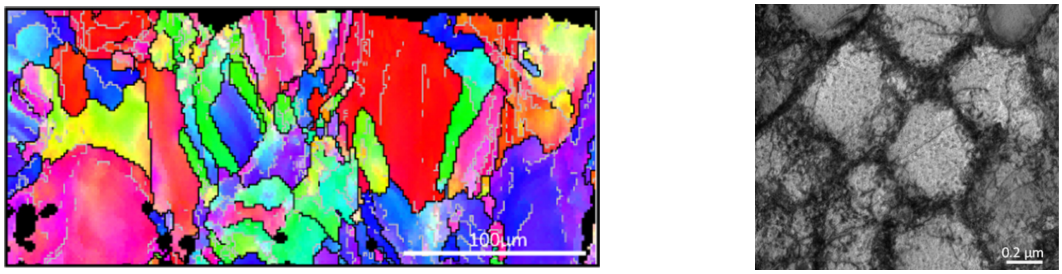

(a) **(b)**

Figure 2.62: a) EBSD of AM-built 316L with grain orientation mapping. b) TEM image of dense dislocation walls around solidification cells in 316L. [116].

Similar structures have been investigated in SLM-built CM247LC [119]. EBSD grain orientation mapping was carried out across a single grain using a 0.05 µm step size and plotted as misorientation from the grain average (Figure 2.63). This found low misorientation between adjacent cells, although more significant mismatch was accrued over the size of the grain.

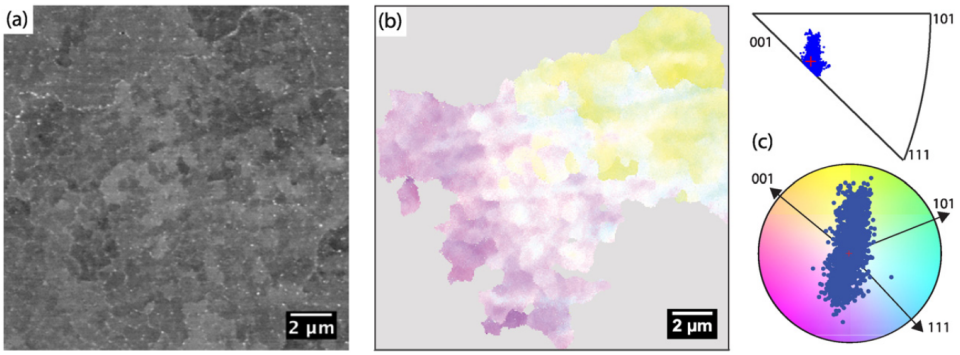

Figure 2.63: a) SEM image of SLM-built CM247LC showing solidification cells. b) EBSD map inside a single grain showing misorientation of each individual point from the average orientation of the grain. c) IPF-Z and colour map showing orientations of the individual data points sampled at 5%, red cross indicates grain average. [119]

Selected area diffraction patterns of a region containing approximately 10 of these solidification cells showed multiple spots for each reflection, with a maximum of 7° misorientation around the [110] axis (Figure 2.64) [119].

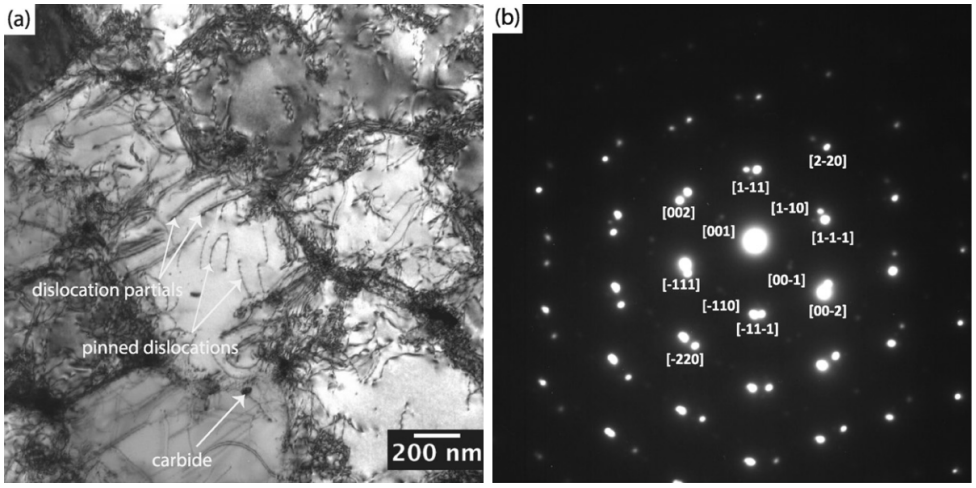

Figure 2.64: a) Selected area bright field TEM of SLM-built CM247LC showing dislocation structure. b) [110] selected area diffraction pattern from region shown in a). [119]

2.4.1 Solidification Microstructure Selection in AM

The SLM process has a comparatively small melt pool at high temperature, surrounded by a bulk substrate at ambient temperature. The melt pool has a tear-drop shape, similar to that observed in conventional welding [120].

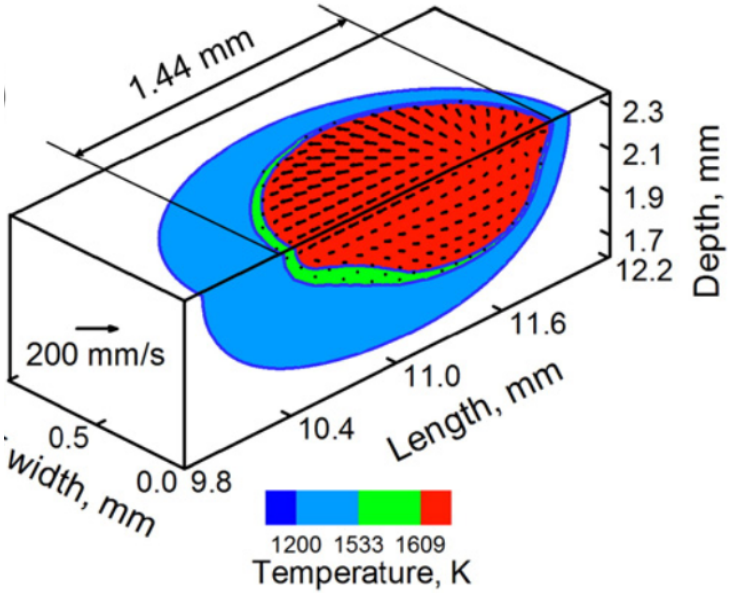

Figure 2.65: Predicted melt pool geometry in AM [47].

At steady state, the solidification front velocity V at the tail of the beam will be equal to

the average scanning speed v. This is normally $0.1\,\mathrm{m\,s^{-1}}$ to $1\,\mathrm{m\,s^{-1}}$, which is within the range of rapid solidification [44]. Solidification rates for SLM are quoted to be $\dot{T}$ =$10^5\,\mathrm{K\,s^{-1}}$–$10^6\,\mathrm{K\,s^{-1}}$, although some authors put them as high as $10^7\,\mathrm{K\,s^{-1}}$ [44, 121].

The relationship between $\dot{T}$, V and thermal gradient G is given by Equation 2.11 [122], indicating that G for SLM processes will also be approximately $10^5\,\mathrm{K\,m^{-1}}$–$10^6\,\mathrm{K\,m^{-1}}$ [44]. The local thermal gradient will change around the melt pool, from a maximum at the base of the melt pool to a minimum at the tail. Solidification front velocity will change in the opposite manner, from a maximum at the tail of the melt pool to a minimum at the base.

$$\dot{T} = G\,V \tag{2.11}$$

Planar growth is stable for either very low front velocities ($< v_{cs}$) or very high front velocities ($> v_a$) [123]. These limiting conditions depend on the liquidus-solidus temperature interval ΔT_0, the Gibbs-Thomson coefficient Γ, the partition coefficient κ, the solute diffusion coefficient in liquid D_t and the weighted thermal gradient G^*.

$$v_{cs} = \frac{G^* D_t}{\Delta T_0} \tag{2.12}$$

$$v_a = \frac{\Delta T_0 D_t}{\Gamma \kappa} \tag{2.13}$$

Assuming $G^* = G$, for 17-4PH steel this gives $v_{cs} \approx 6{\times}10^{-6}\,\mathrm{m\,s^{-1}}$ and $v_a \approx 2.2\,\mathrm{m\,s^{-1}}$. The front velocities achieved in SLM are between these bounds, so a cellular/dendritic structure will prevail, corresponding to those shown in Figure 2.61.

Further, there is an established empirical relationship (Equation 2.14) between $\dot{T}$ and primary dendrite arm spacing λ_1. The constants a and n are material dependent, but for stainless steel these have been found experimentally to be $a = 60 - 100\,\mathrm{m\,s\,K^{-1}}$ and $n = 0.2 - 0.5$ [124–126].

$$\lambda_1 = a\dot{T}^{-n} \tag{2.14}$$

Equation 2.14 was developed for processes with cooling rates of $10^{-2}\,\mathrm{K\,s^{-1}}$–$10^2\,\mathrm{K\,s^{-1}}$, and

becomes increasingly sensitive to experimental error when applied to processes outside this range, such as SLM [54].

Given that $\dot{T}$ is the product of G and V, Equation 2.14 implies that these are equally important in determining λ_1. Kurz & Fisher however, derived a theoretical relationship for the tip radius (assumed equal to primary dendrite arm spacing) where they predicted temperature gradient to have a stronger effect than front velocity (Equation 2.15) [122].

$$\lambda_1 = 4.3\, G^{-1/2} \left\{ \frac{\Delta T_0\, D\, \Gamma}{\kappa\, V} \right\}^{1/4} \tag{2.15}$$

For the average SLM conditions described above, the Equation 2.14 predicts λ_1 in the range 1 µm to 5 µm. In comparison, Equation 2.15 would predict λ_1 of 2 µm to 9 µm. These predictions are close given the approximation in the input values, while the observed microstructures (Figure 2.61) are at the lower end of the range in both cases. This may indicate that the thermal gradient driving tip radius in an AM build is higher than that quoted, possibly because the critical gradient is partway round the melt pool. There will also be an influence from the selection of material parameters.

2.5 Magnetic Behaviour

This project is primarily concerned with the development of a magnetically graded material; exploiting the magnetic properties of different phases of stainless steel to drive a change in magnetic behaviour through a change in phase composition.

2.5.1 Types of Magnetic Behaviour

When a magnetic field H is applied to a material, the response is called the magnetic induction B. The relationship between B and H is called the magnetisation M, given by Equation 2.16 [127, 128]. In the cgs units system, H is expressed in Oersteds (Oe), B in gauss (G), and M in either magnetic moment per unit volume (emu cm^{-3}) or per unit mass (emu g^{-1}).

$$B = H + 4\pi M \tag{2.16}$$

Magnetic behaviour is characterised by plotting M (or B) against H, to observe magnetic response over a range of applied field strengths (Figure 2.68). Paramagnetic, diamagnetic and antiferromagnetic materials need very high applied field strengths to observe any significant magnetisation. Ferro- and ferri-magnetic materials show magnetisation at much lower applied field strengths and exhibit hysteresis. Diamagnetic materials tend to exclude the magnetic field from their interior; the magnetic flux through the material is lower than that outside the material. All other types of magnetic materials have higher flux inside the material than outside, although to varying degrees.

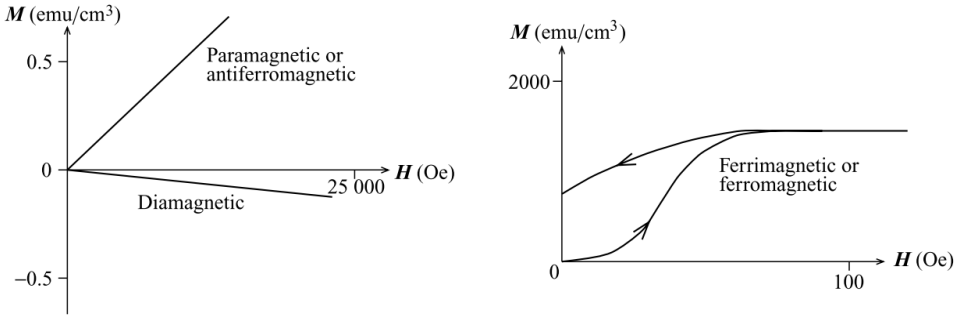

Figure 2.66: Schematic M against H for magnetic materials [127].

The hysteresis loops for ferromagnetic materials can provide additional information about their magnetic behaviour (Figure 2.67) [128]. Starting from zero, the magnetisation increases with applied field until it reaches m_s where it flattens off. When the field is removed, the magnetisation falls but does not come fully back to zero, instead it reaches m_r, the *residual magnetisation* or *remanence*. Applying the field in the opposite direction will reduce the magnetisation, with the field strength necessary to bring the magnetisation back to zero, H_c, defined as the *coercivity*. At sufficiently high applied field strength the material will again saturate.

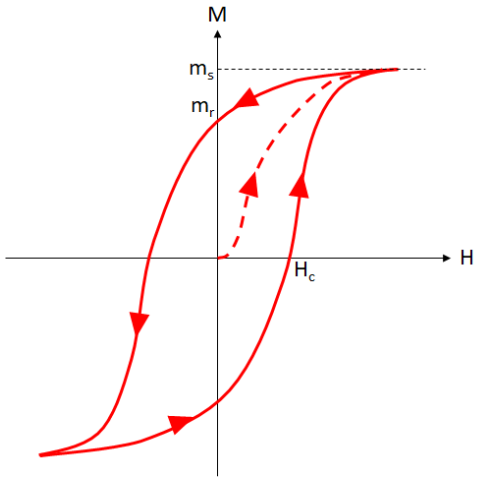

Figure 2.67: Schematic hysteresis loop for ferromagnetic material.

In the literature, the saturation magnetisation and residual magnetisation are normally defined using capital letter notation (M_s and M_r). However, in this work the decision has been made to use lower case notation (m_s and m_r) to avoid confusion with the martensite start and finish temperatures (M_s and M_f).

Materials which have a large coercivity (i.e. a high applied field is necessary to reduce their magnetisation to zero) are known as *hard* magnetic materials. These are suitable for use as permanent magnets and include materials such as NdFeB (H_c = 10 000 Oe to 30 000 Oe) [129]. Materials with a low coercivity are known as soft magnetic materials, retaining little magnetisation when the applied field is removed. Howver, to be useful for temporary and easily reversible storage, a soft magnetic material must also have a high permability μ so that it can achieve a high level of magnetisation for a relatively small applied field. Examples include materials like Permalloy (H_c = 0.2 Oe–2 Oe, μ=100000 [128, 130]), which is used in write heads for magnetic recording media.

The materials commonly used for rotos in synchronous motors are soft magnetic alloys called 'electrical steels'. These are iron-silicon alloys, normally containing up to 3.2 wt% silicon, and may also have small additions of other elements including manganese and aluminium. One example is CarTech® Silicon Core Iron B-FM, which has a coercivity of 0.7 Oe and a maximum permability of 5000 [131].

2.5.2 Susceptibility and Permeability

Magnetic behaviour can be described in terms of the *susceptibility* χ, defined as the way in which the magnetisation M varies with the applied field H, the gradient of the M-H curve. Paramagnetic, diamagnetic and antiferromagnetic materials all have constant χ, a linear relationship between M and H, and retain no magnetisation when the applied field is removed. In contrast, ferromagnetic and ferrimagnetic materials have variable χ, a non-linear relationship between M and H, with χ reaching a maximum at the *saturation magnetisation* m_s.

$$\chi = \frac{M}{H} \tag{2.17}$$

In practice, the susceptibility is generally used for paramagnetic and diamagnetic materials, whereas the *permeability* μ is used for ferro- and ferri-magnetic materials. This is comparable with the susceptibility, but is defined as the ratio of B to H.

$$\mu = \frac{B}{H} \tag{2.18}$$

$$\mu = 1 + 4\pi\chi \tag{2.19}$$

These terms can be used to characterise different types of magnetic behaviour, referring back to Figure 2.68. Diamagnetic materials have a small, negative χ and a slightly negative μ. Paramagnetic and antiferromagnetic materials have a small positive χ with small positive μ. Ferro- and ferri-magnetic materials have variable χ and μ where both are functions of H.

2.5.3 Origin of Magnetic Behaviour

While the M-H curves illustrate the behaviour of the different types of magnetic material, the origin of this behaviour is in the electrons, through contributions from their orbital motion and spin. Paired electrons (same shell, opposite spin) cancel out, but unpaired electrons have a net magnetic moment. Magnetic behaviour is driven by the ordering arrangements of these dipoles (Figure 2.68).

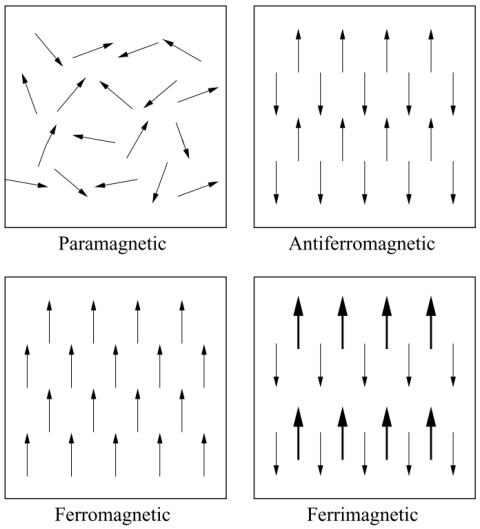

Figure 2.68: Schematic ordering of dipoles in magetic materials [127].

In a paramagnetic material the dipole moments are arranged randomly with no ordering, while antiferromagnetic materials have ordered dipole moments but they are arranged anti-parallel, so both materials have an overall magnetisation of zero. Ferromagnetic materials have ordered dipoles all facing the same direction giving an overall magnetisation. Ferri-magnets, while showing anti-parallel ordering, have one set of dipole moments that are larger, also resulting in a net magnetisation. On heating a ferro- or ferri-magnetic material, the thermal agitation of the atoms increases, opposing their ability to respond to an applied magnetic field. At the Curie temperature T_c the material will become paramagnetic, when the thermal agitation is too strong and the dipoles remain randomly oriented.

For pure iron, $T_c = 1043\,\mathrm{K}$, below the ferrite-austenite transformation temperature of $1185\,\mathrm{K}$ [128]. This means that, on heating, pure iron reaches the Curie temperature and becomes paramagnetic while still in the BCC ferrite crystal structure, and then transforms to FCC austenite at a higher temperature.

Diamagnetic behaviour is slightly different. When a magnetic field is applied, currents are generated inside the atoms by induction. These are induced in the direction opposing the applied field, so their magnetic moments must also oppose the applied field. In this manner, all materials actually exhibit diamagnetic behaviour, it is just that it is only observed when there is no dipole-driven magnetic behaviour to mask it.

2.5.4 Magnetic Behaviour of Stainless Steel

A range of models have been developed to describe the electron interaction that gives rise to magnetic behaviour, of which the *Itinterant Electron Model* is the most suitable to describe the 3d transition metals including iron, nickel and cobalt [132]. At a simple level, the interaction can be regarded as dependent on the strength of coupling between the the wavefunctions of adjacent atoms.

This is described by the Bethe-Slater curve, which shows the exchange integral, J_{ex} for transition metals as a function of the ratio between interatomic distance r_a and the radius of the 3d electron shell r_{3d}. Elements above the horizontal axis display ferromagnetic behaviour, where the exchange energy reaches a minimum with the spins parallel, while those below are anti-ferromagnetic, where the exchange energy reaches a minimum with the spins antiparallel. The interatomic distance is determined by crystal structure and lattice parameter [133, 134].

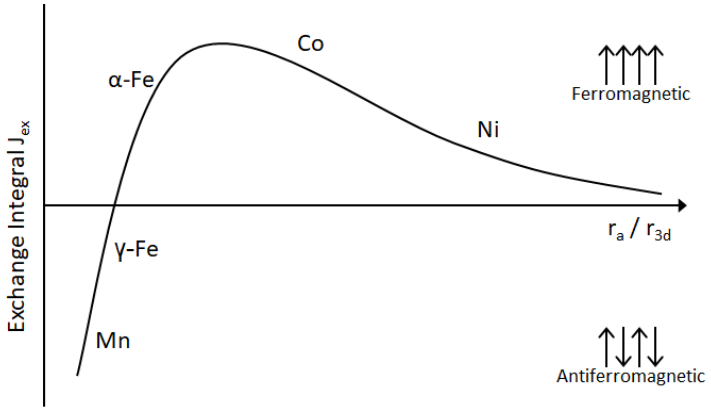

Figure 2.69: Schematic Bethe-Slater curve [128]

α-ferrite and α'-martensite phases of stainless steel are ferromagnetic [27, 128, 135], in common with the low-temperature ferritic form of pure iron. The crystal is body-centred cubic, with the body-diagonal as the close packed direction. At room temperature, taking the lattice dimension to be $a_\alpha = 2.866\,\text{Å}$ and with two atoms per unit cell, the atomic volume is $1.18\times10^{-2}\,\text{nm}^3$, while the distance between atoms in the close-packed direction is $a_\alpha = 2.482\,\text{Å}$ [63].

The γ-austenitic phase of stainless steel is paramagnetic [27, 128, 135]. The austenite crystal is face-centered cubic, with the face-diagonal as the close-packed direction. Taking the room temperature lattice parameter to be $a_\gamma = 3.573\,\text{Å}$ [63], the distance between

atoms in the close-packed direction is $a_\gamma = 2.526\,\text{Å}$, larger than that of ferrite. However, with four atoms per unit cell, the atomic volume is smaller at only $1.14\times10^{-2}\,\text{nm}^3$. This reduced atomic volume moves austenite lower on the Bethe-Slater curve, out of the ferromagnetic region [136].

2.5.5 Coercivity

Dipoles in a a ferromagnetic material are grouped into domains. As the applied field strength increases, preferentially orientated domains will grow at the expense of less well-orientated domains, until there is a single domain through the material (Figure 4.7). This will then rotate as a whole until it is aligned with the applied field direction.

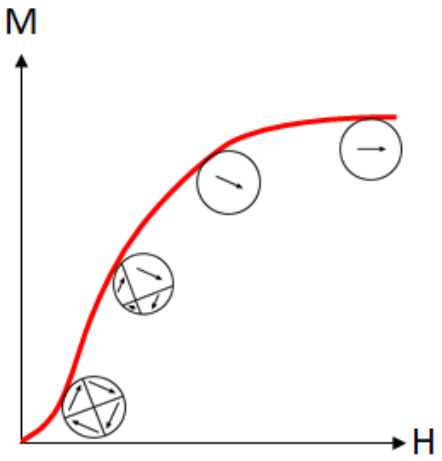

Figure 2.70: Schematic domain growth and rotation for ferromagnetic material.

This growth is achieved through domain wall motion; the domain wall being a region which separates domains with either a 90° or 180° rotation between them [127]. Domain walls can range from a few nanometers thick in NdFeB, to around 40 µm in iron [128], and even up to 10 µm thick in other materials [127]. The early stages of domain-wall motion are normally reversible if the applied field is removed. However, once the wall encounters defects (e.g. dislocations) it becomes pinned by them in a manner similar to dislocation motion being pinned by precipitates. This can be overcome by increasing the applied field and pushing the wall past the defect, but this will leave 'spike domains' attached to the defect as it moves past (Figure 2.71). This is not perfectly reversible; if the applied field is removed the domains are unable to return to their original positions so some net

magnetisation remains (remanence). An applied field in the opposite direction is required to push the domain walls back past the crystal defects (coercivity).

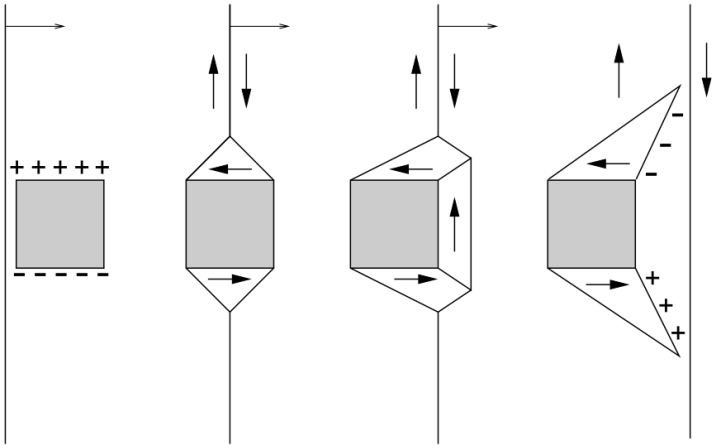

Figure 2.71: Schematic formation of spike domains as a domain wall passes a crystal defect [127].

2.5.6 Magnetic Characterisation

The coercivity and remanence determine the magnetic hardness of a material but they can be affected by crystal imperfections, particularly the dislocation density. In contrast, the saturation magnetisation m_s is independent of crystal structure, although it may take a higher applied field to reach saturation in a more highly dislocated material.

In a multi-phase material, the bulk saturation magnetisation m_{sbulk} is the rule-of-mixtures weighted average of the the saturation magnetisations for the individual phases m_{sx}, and can be used to determine the weight fraction f_x of each phase [128].

$$m_{sbulk} = \sum_x f_x m_{sx} \tag{2.20}$$

This approach is commonly used for determining the relative phase fraction of ferromagnetic α'-martensite and paramagnetic γ-austenite (Equations 2.21 and 2.22).

$$f_{\alpha'} = \frac{m_s}{m_{s\alpha'}} \tag{2.21}$$

$$f_\gamma = 1 - f_{\alpha'} \tag{2.22}$$

The m_s for an individual phase can be determined experimentally, by driving a sample of single-phase material to saturation, or it can be approximated by:

$$m_{s\alpha'} = x_{Fe} m_{Fe} \tag{2.23}$$

where x_{Fe} is the wt% of iron in the alloy and m_{Fe} is the saturation magnetisation of pure iron [137].

For fully martensitic low sulphur 17-4PH stainless steel, $m_{s\alpha'}$ was observed experimentally to be 162.4 emu g^{-1} [138]. Taking m_{Fe} to be 217.6 emu g^{-1} [139] and x_{Fe} to be 76 wt% from the chemical analysis in [138], Equation 2.23 would give $m_{s\alpha'}$ of 165.3 emu g^{-1}. These values are in very good agreement, but 162.4 emu g^{-1} will be used for quantitative phase analysis in this work because it includes the contribution from all alloying elements.

The mass magnetisation emu g^{-1} will be used throughout this study because it avoids the requirement to measure and correct for porosity, which would be needed for conversion to the more commonly used volume magnetisation emu cm^{-3}. It also allows more straightforward calculation of phase fraction in wt%, rather than vol%.

Chapter 3

Scope & Objectives

Reviewing the phases that can be achieved in stainless steel, the scope of this project has been defined to focus on the solid-state transformation between paramagnetic austenite and ferromagnetic martensite. This is preferred over the equilibrium transformation between austenite and ferrite because it can be controlled both thermally and mechanically.

The scope of the project has then been defined as a set of questions:

- Can thermally-driven martensitic transformation be suppressed in SLM-built 17-4PH to yield a fully austenitic material?
- Can martensitic transformation be triggered and controlled (thermally or mechanically) in-situ to give variation in phase fraction in the as-built material?
- Do these materials show different magnetic properties?
- Can these materials be combined to produce a microstructurally and magnetically graded material?
- Can this approach be used to fabricate a magnetically graded rotor for a synchronous motor?
- Can a model be created to predict the melt pool geometry, cooling rate and other associated parameters?

The scope has been further defined to concentrate on 17-4PH stainless steel, also known as UNS17400 or Alloy 630. This is a common precipitation hardened stainless steel, which

nominally contains 17 wt% chromium, 4 wt% nickel and 4 wt% copper in addition to a number of other elements (Table 3.1).

Table 3.1: 17-4PH Alloy Specification (wt%) [140, 141]

	Fe	Cr	Ni	Cu	Mn	Si	Nb+Ta	P	S	C
max	balance	17.50	5.00	5.00	1.00	1.00	0.45	0.04	0.03	0.07
min	balance	15.00	3.00	3.00	-	-	0.15	-	-	-

17-4PH is a martensitic steel, conventionally hardened by the growth of Cu-rich precipitates after ageing in the range 450 °C to 600 °C for 4 h [140, 141]. It is generally used for applications requiring high strength, hardness and moderate corrosion resistance, including structural aircraft components and chemical processing equipment.

The specification limits for sulphur and phosporous reflect the degree of grain boundary embrittlement that these elements can cause. Modern manufacturing methods normally achieve these limits by at least an order of magnitude however the specification limits cannot be updated because this would risk making components manufactured using older batches of this alloy non-conforming.

This alloy has been selected because the literature suggests that, under SLM cooling rates, it is able to form a dual-phase microstructure consisting of paramagnetic γ-austenite and ferromagnetic α'-martensite [5, 6, 142, 143]. Further, different studies have reported different ratios of these two phases, suggesting the proportion may be influenced by the choice of build parameters. These are summarised in Table 3.2, where the hatch spacing is the distance between adjacent passes of the laser beam.

Table 3.2: Microstructures of SM-built 17-4PH Samples

	α' wt%	γ wt%	Build	Power W	Speed $mm\,s^{-1}$	Layer µm	Hatch µm
[6]	25 - 50	50 - 75	Nitrogen	195	800	40	100
[142]	70 - 75	25 - 30	Nitrogen	195	600 - 1200	40	100
[142]	68 - 76	24 - 32	Nitrogen	70 - 195	287 - 800	40	100
[143]	15	85	Nitrogen*	200	1000	20	100
[6]	92	8	Argon	195	800	40	100
[5]	28	72	Argon	200	†	†	†
[143]	≈ 100	≈ 0	Argon*	200	1000	20	100

Within this summary there is a study showing a near uniform $\gamma : \alpha'$ ratio for different build parameters, but the parameter range explored was fairly small [142]. A couple of studies used the build environment to change the phase ratio [6, 143], but there was still variation even within the samples just built under argon.

All of these phase fractions were measured from XRD traces, either by Rietveld refinement or using intensity factors. One of the studies reported differences in phase fraction depending on the plane chosen for sectioning [6], which would be consistent with the crystallographic texture suggested by the observation of columnar grain growth aligned to the build direction reported in [143]. Further, given that austenite can undergo deformation driven transformation to martensite, there may have been some level of transformation during sample preparation (cutting & polishing), potentially increasing the α'-martensite wt% reported by XRD.

*Nitrogen atomisation

†Not provided

Chapter 4

Experimental

This chapter deals with the various experimental processes used in the building, analysis and characterisation of the additively manufactured samples used in this study. It also covers discussion of the metallic powders and other consumables. The health and safety issues with the experimental methods used are detailed in Appendix B.

4.1 17-4PH Stainless Steel Metallic Powder

The 17-4PH powder used in this study was sourced from Carpenter Powder Products. The powder chemistry was analysed by AMG Analytical and found to be conforming to the commercial specification for 17-4PH (Table 4.1). The nitrogen level was sufficiently high to suggest that the powder may have been atomised in a nitrogen atmosphere.

Table 4.1: 17-4PH Powder Composition (wt%)

Fe	Cr	Ni	Cu	Mn	Si	Nb	N	Mo	C
balance	15.51	4.56	4.31	0.79	0.71	0.26	0.129	0.09	0.05
Co	V	W	P	S	Al	Ti	B	Sn	Ta
0.05	0.03	0.02	0.014	0.007	< 0.05	< 0.02	< 0.02	< 0.02	< 0.02

The particle size was measured using a Malvern Mastersizer 3000, and 95 vol% was found to be in the range 15 µm to 45 µm, which is suitable for use in Selective Laser Melting (Figure 4.1). This was confirmed by SEM imaging (Figure 4.2).

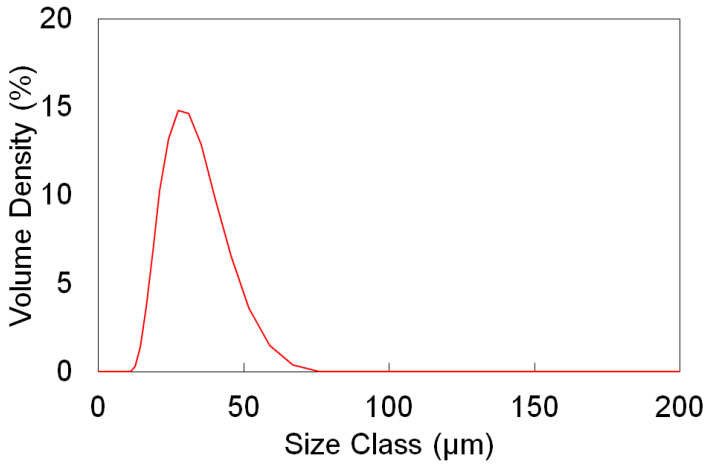

Figure 4.1: 17-4PH powder particle size distribution

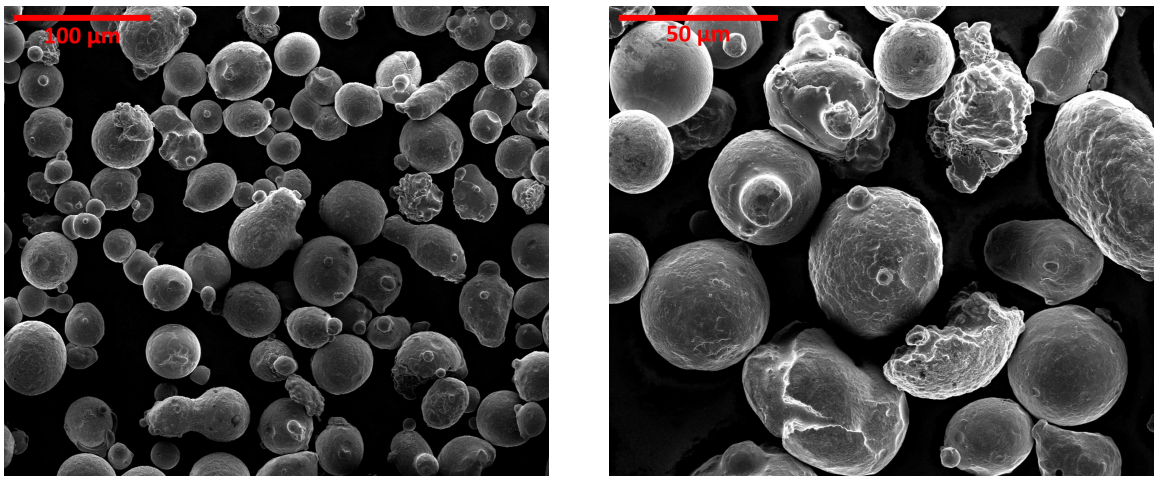

(a) **(b)**

Figure 4.2: SEM images of 17-4PH powder: a) Scale bar 100 µm b) Scale bar 50 µm.

4.2 Renishaw SLM125

4.2.1 Machine Hardware

The SLM125 was originally designed for the manufacture of small, high precision components (e.g. dental implants) from stainless steel [144].

Figure 4.3: Renishaw SLM125. 1) Access door. 2) PC cabinet. 3) E-stop. 4) Touch-screen control panel. 5) Reset button. 6) Electrical cabinet. 7) Gloves. 8) Isolator. 9) Viewing window. 10) Wheels. [144]

The key components of the machine are: laser, baseplate, powder delivery hopper, wiper blade, powder collection system. There are also ancillary items including a vacuum cleaner, powder sieves, powder filter and argon supply.

The laser is a 200 W, 1070 nm continuous wave fibre laser manufactured by SPI. This is modulated and positionally controlled to create a pulsed effect: the laser is switched on and stationary for a specified exposure time, then off while the laser moves by a specified point spacing, and then switched on for the next exposure. The result is a series of individual pulses with overlapping melt pools.

The powder delivery system is a hopper at the back of the upper chamber which can hold up to 20 kg of metal powder (Figure 4.4a). There are a series of powder delivery holes at the base of the hopper which are kept covered, but can be opened by pushing back the cover plate to release powder.

The baseplate is a stainless steel plate 125 mm × 125 mm square and approximately 10 mm thickness. It is located in the centre of the upper chamber, screwed down in the corners (Figure 4.4b). It is initially set level with the floor of the chamber, and then incrementally moved down by the layer thickness during the build.

The wiper blade is fitted across the width of the upper chamber, and consists of a support

cartridge holding a silicon rubber bead (Figure 4.4c). When the wiper blade moves to the back of the chamber it pushes open the cover plate on the hopper, releasing a dose of powder. The wiper blade then moves forward, pushing the powder forwards in an even layer (Figure 4.4e).

The excess powder falls through holes in front of the baseplate into a powder collection system located in the lower build chamber. At the end of the build the collected powder must be sieved before being reused.

Detailed operating instructions are included in Appendix C.

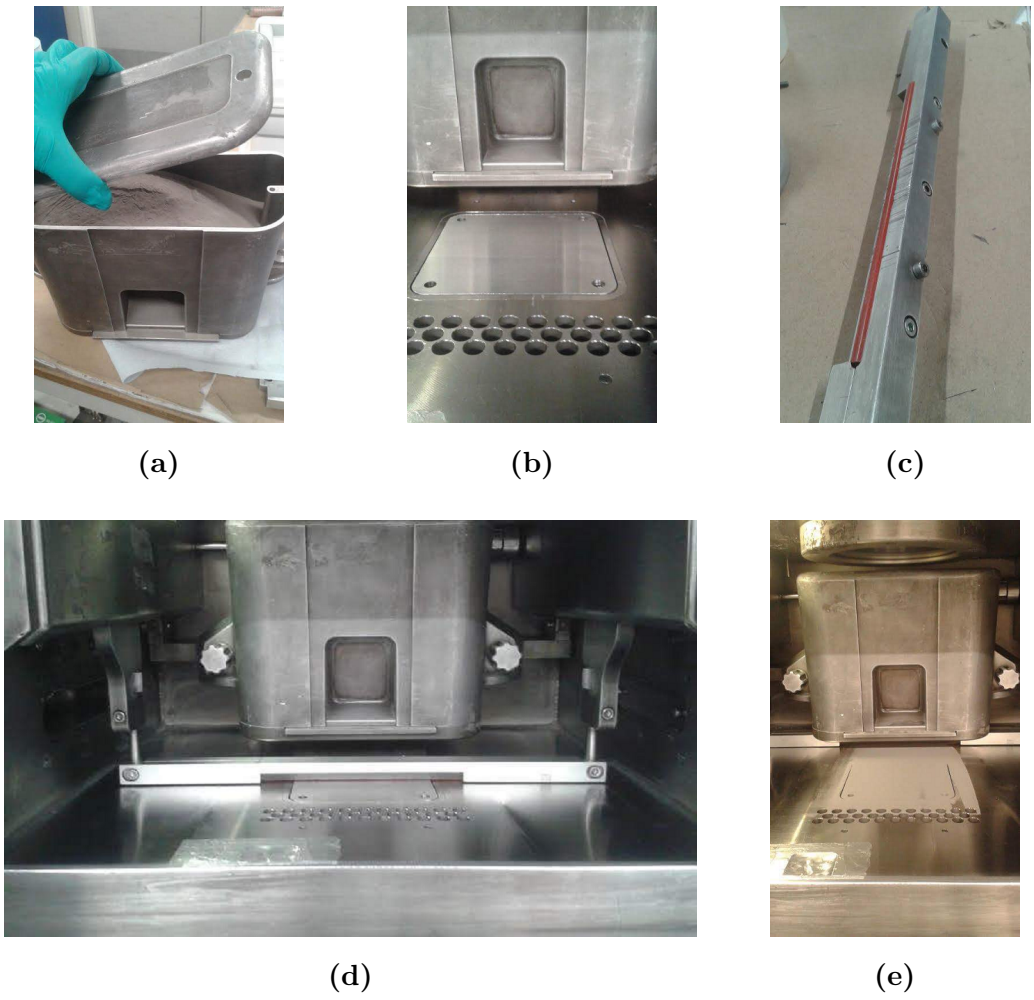

(a) **(b)** **(c)**

(d) **(e)**

Figure 4.4: Key components of Renishaw SLM125. a) Hopper filled with powder. b) Hopper and baseplate located inside upper chamber, holes at front lead to overflow powder collection. c) Wiper blade showing silicon bead. d) Wiper blade installed in upper chamber. e) Powder layer.

The SLM125 has the option for using a heated baseplate, but this was not used for any of the trials discussed in this study.

4.2.2 Build File Creation

Powder-bed additive manufacturing processes work on a build file defined in a series of layers. The initial geometry is defined as a .stl (stereolithography) file, originally created in the CAD system designed by 3D Systems, but now used as the industry standard. The .stl file can be converted into layers by a number of proprietary software packages, the one used in this work was the Marcam Engineering MTT AutoFab package, Version 1.6.

In addition to the layer geometry, the software also incorporates the parameters for the laser into the build file. The parameters include the power, exposure time, point spacing, hatch spacing, scanning style and focus offset for the body of the sample, the outer edge (border) and the final layer (skin). All samples in this study used a focus offset of 4 mm. The same build parameters were used for the body, border and skin of the samples.

Where graduated samples were required, these were created as a stepped series of individual STL files, one for each condition. To achieve good bonding between conditions the individual STL files were overlapped by 0.1 mm within AutoFab.

4.3 Aconity Mini

The Aconity Mini was not used for any sample manufacture, but was used to gather pyrometer data from the in-process monitoring systems. The Mini is designed for lab-scale investigative work rather than production builds. It therefore has considerably more flexibility than the SLM125 for user control of parameters, but is also much more complex. As the Mini was only used for a pyrometer trial, its full capabilities were not required for this work.

Figure 4.5: Aconity Mini

The basic design of the Aconity Mini is very similar to the Renishaw SLM125, being a powder bed system with a similarly sized baseplate, and it works within the same laser parameter window. The only significant difference is that it uses a continuous-mode laser, rather than the pulsed laser used in the SLM125.

4.4 Characterisation

4.4.1 Vibrating Sample Magnetometer

The vibrating sample magnetometer (VSM) used in this study was a Microsense Model 10 based at the University of Manchester (Figure 4.6).

Figure 4.6: Microsense Model 10 VSM

The sample (maximum 1 mm thickness, 8 mm diameter) is attached to a quartz rod, positioned in the centre of the machine and an external magnetic field is applied. If the sample is magnetic then it will be magnetised through domain growth and rotation (Figure 4.7). The dipole moment of the aligned domains within the sample in turn create their own magnetic field.

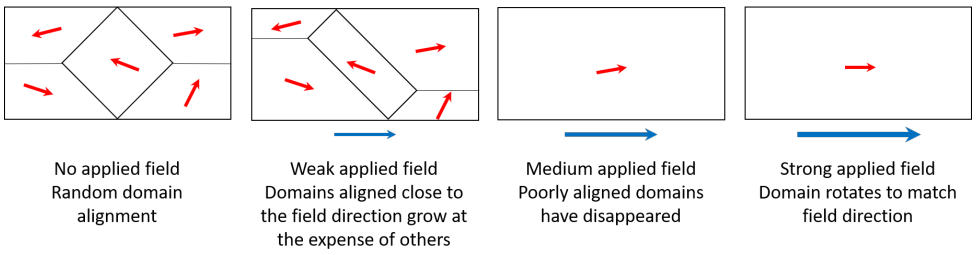

Figure 4.7: Domain growth and rotation

The sample is then vibrated up and down, causing the domain alignment to adjust and changing the magnetic field caused by the dipole moment. This alternating magnetic field is detected by pick-up coils, where it induces a measurable current (Figure 4.8). The current is proportional to the magnetisation of the vibrating sample.

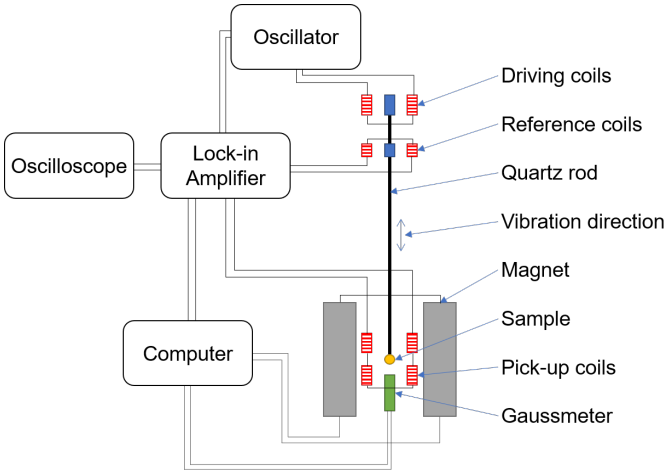

Figure 4.8: Schematic of vibrating sample magnetometer

Hysteresis loops (Figure 4.9) are generated by first determining the applied field necessary to cause saturation in the sample, then the applied field is reduced until the sample is saturated in the reverse direction, and then increased back to the start. Data is collected for magnetisation parallel with the sample (blue in Figure 4.9) and perpendicular to the sample (red in Figure 4.9).

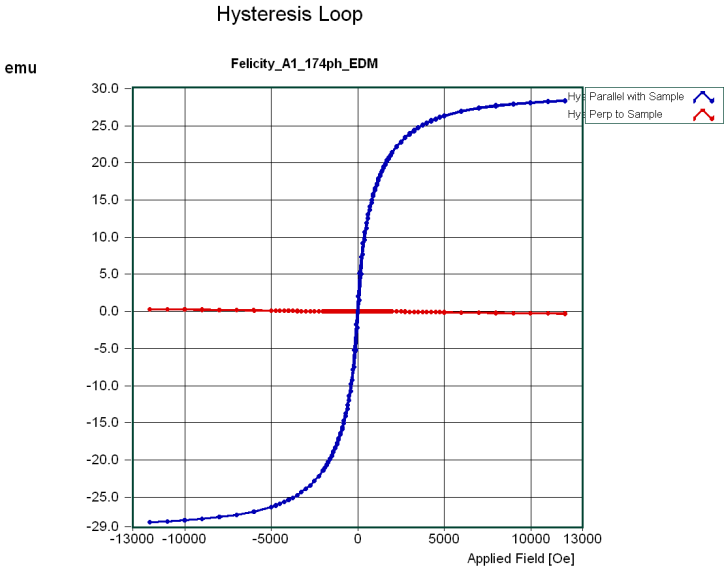

Figure 4.9: Example hysteresis loop generated by Microsense Model 10

VSM is a bulk characterisation technique, although it can only accommodate small samples. The output is for the sample as a whole, it cannot distinguish between different magnetic behaviours in different regions. To assess spatial variation in magnetic be-

haviour it would be necessary to take small samples from specific regions around a larger sample, and assess them individually.

The VSM generated hysteresis loops from the following program:

Table 4.2: VSM Program

Applied Field From Oe	Applied Field To Oe	Step Size Oe
12000	5000	1000
5000	2000	250
2000	-2000	100
-2000	-5000	250
-5000	-12000	1000
-12000	-5000	1000
-5000	-2000	250
-2000	2000	100
2000	5000	250
5000	12000	1000

4.4.2 Feritscope

A Fischer Feritscope FMP30 (Figure 4.10) was used for quantitative analysis of the proportion of magnetic phase within the samples. It is normally used to report the phase fraction of ferrite, but can be used equally well to measure the phase fraction of martensite.

Figure 4.10: Fischer Feritscope FMP30

The Feritscope measures by magnetic induction in accordance with ISO 2178:2016 [145],

using the magnetic permeability of the material to determine the proportion of magnetic phase present [146]. A primary coil generates a magnetic field which interacts with the magnetic phases in the material. Changes in this magnetic field cause a change in magnetic flux in the material, which induces a voltage in a secondary coil. The magnitude of the voltage is proportional to the amount of magnetic phase present. All magnetic phases (e.g. α-ferrite, δ-ferrite, α'martensite) are included in the analysis. Correction factors can be applied for standard errors including if the sample is very small, if the surface is curved, if the material has residual magnetisation or if the surface is rough.

Permeability is the ratio of the flux density B produced within the material to H the strength of the applied field. Plastic deformation reduces permeability because dislocations interact with magnetic flux, pinning it in a similar manner to precipitation hardening pinning dislocations. The result is a cold worked material achieves a lower flux density B for the same applied field H than the same material after annealing [128].

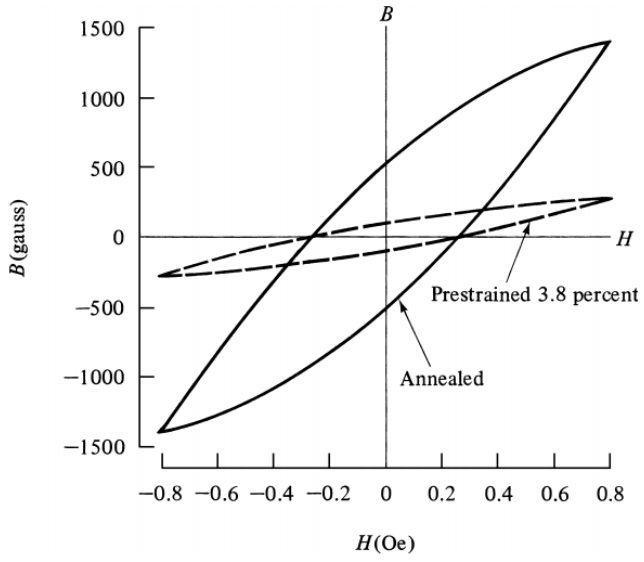

Figure 4.11: Effect of cold work on magnetisation curves [128].

Other imperfections (inclusions, lattice defects, porosity) will have a similar effect, although the mechanism and strength of interaction will depend on the size of the imperfection. Generally the effect is strongest when the imperfection is of a similar scale to the domain wall thickness ($\approx 400\,\text{Å}$). While additively manufactured samples are often porous, the pores are generally much larger than this, so are not expected to have a significant impact on the permeability.

The measurement is very quick, taking only a couple of seconds per point, so it is easy to take multiple measurements to reduce the effect of measurement variation. The interaction volume is sufficiently small to allow multiple measurements to be taken across a surface to assess spatial variation (e.g. with build height). The output is a single value (wt% or ferrite number), rather than the detailed hysteresis information generated by VSM, so it cannot distinguish hard and soft magnetic materials.

Two Feritscopes were used during this study. The first was located at PTS (TQM) Ltd in Stafford, and the second was on loan to from Rolls-Royce plc. Both were calibrated in wt% ferrite using calibration standards provided by Fischer.

4.4.3 X-Ray Diffraction

X-ray diffraction (XRD) was used for phase identification, using a PANalytical X'Pert^3 Powder machine (Figure 4.12) located in the University of Sheffield XRD Research Facility.

Figure 4.12: PANalytical X'Pert^3 Powder XRD

XRD works on interaction between the incident beam and the crystallographic planes within the sample to produce a diffracted beam which is recorded by a detector. The

technique analyses the sample surface, and for a steel sample examined with Cu $K\alpha$ radiation, 95 % of the data can come from an interaction depth as small as 2 µm [147].

The incident beam interacts with the electrons in the material. Interaction with bound electrons results in coherent scattering and generates diffracted beams that have a defined relationship to the incident beam. Diffracted beams from adjacent lattice planes can interfere destructively (out-of-phase) in which case they will cancel out, or constructively (in-phase) in which case they can be detected.

Bragg's Law (Equation 4.1) defines the relationship between the incident beam wavelength λ, the angle of the incident beam to the sample surface θ and the interplanar spacing between the crystallographic planes d_{hlk}, where n is an integer number of wavelengths (Figure 4.13).

$$n\lambda = 2d_{hlk}sin\theta \tag{4.1}$$

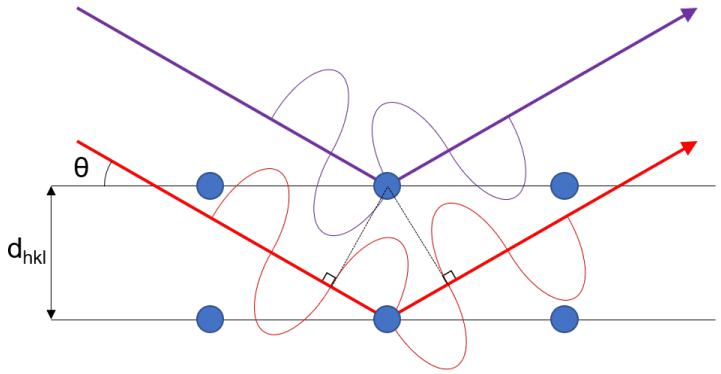

Figure 4.13: Schematic of Bragg's Law for XRD

The positions of peaks in data from the diffracted beam can be converted to interplanar spacings and used to identify phases within the material or calculate lattice dimensions. The relative intensity of the peaks within a phase is also dependent on the lattice, with some planes reflecting more strongly than others. In a multi-phase material, the intensity of peaks from different phases is also dependent on their phase fraction. This can be used for quantitative phase analysis, most commonly following a Rietveld refinement approach.

The quality of XRD data is sensitive to the position of the sample within the machine. If the surface is not exactly in line with the machine axis it can cause the position of the peaks to shift and lead to incorrect lattice calculations. It is also sensitive to sample

surface preparation, with rough surfaces or small surface areas leading to increased background noise making it difficult to correctly identify peak positions or calculate peak areas. This can be addressed by increasing the data collection time at each angular position to maximise the signal to noise ratio.

XRD works best with a finely-ground powder sample, where the top layer contains randomly distributed powder grains that have no preferred crystallographic orientation. This will result in scan data where peaks are narrow and their relative intensity can be directly related to the 'ideal' pattern for that phase. This is not possible with solid samples, where the inspected surface may exhibit crystallographic texture, meaning that some planes are over-represented and others are absent. While the peak positions will be correct, this will skew their relative intensity, making it difficult to do accurate quantitative phase analysis.

4.4.4 Microscopy

A number of samples were prepared for examination under optical microscopy, to assess for both microstructure and porosity. The samples were cut on a Struers Secotom-50, hot-mounted in Bakelite using a Buehler Simplimet mounting press, ground and then polished with diamond suspension to 0.25 µm.

Samples were also examined by Scanning Electron Microscopy (SEM) at 20 kV on a FEI Nova FEGSEM, located within the Sorby Centre at the University of Sheffield. The samples were identically prepared to those for optical microscopy, with the addition of silver paint connecting the sample to the machine stage to avoid charging.

Two etchant approaches were used. The main etchant was Kallings #2 reagent, which was mixed as required from 5 g copper II chloride, 100 ml ethanol and 100 ml hydrochloric acid.

Samples were also electroetched using 20 g oxalic acid in 200 ml distilled water. The solution was maintained at 25 °C with magnetic stirring. Etching was carried out at 6 V for 30 s, with a current density of 2 mA mm^{-2}.

4.4.5 Relative Density - Archimedes

The first approach for measuring relative density was an Archimedes (buoyancy) method using a Mettler Toledo density determination kit (Figure 4.14).

Figure 4.14: Mettler Toledo density determination kit

Firstly, the sample is weighed in air m_{air}, such that its weight is given by $W_{air} = g\, m_{air}$, where g is acceleration due to gravity. Then, the sample is weighed when submerged in water, m_{sub}, where its weight is reduced by the buoyancy force of the water, $W_{sub} = g\, m_{sub}$. The buoyancy force is equal to the weight of water displaced by the sample:

$$F_b = v\, g\, \rho_{water} \tag{4.2}$$

$$F_b = W_{air} - W_{sub} \tag{4.3}$$

where ρ_{water} is the density of the water, and v is the volume of water displaced.

By measuring the temperature of the water, ρ_{water} can be determined. Then from $W_{air} - W_{sub}$ it is possible to calculate the volume of water displaced, which is equal to the volume

of the sample. From this, and the original mass of the sample in air m_{air}, the density of the sample can be calculated.

The advantage of this method is that it is relatively quick to perform, and can be used on a bulk sample without any preparation. However, it can give variable results if the surface does not have good wettability in water, as small air bubbles can adhere to the surface affecting the buoyancy. Additionally, it is important to ensure the sample is fully dried between repeats, otherwise retained water will also cause variation.

4.4.6 Relative Density - Image Analysis

In addition to the Archimedes method, porosity measurements were also taken using ImageJ for image analysis. The raw images were taken from mounted, polished samples prior to etching, using a Nikon microscope. They were loaded into ImageJ and converted to black and white. The image was cropped to remove any of the mounting material, and then the pixels were counted: white pixels were metal, black pixels were pores. The porosity was determined as the ratio of black pixels to total pixels. To ensure a standard approach between samples, all images were taken at the same magnification and cropped to the same size.

Chapter 5

Validation Melt Tracks

This chapter covers the creation of an experimental data set from melt tracks to be used for validating the melt pool model.

5.1 Method

Discs of 3 mm to 4 mm thickness were cut from a 16 mm diameter solid bar of 17-4PH stainless steel, which had been sourced from Sigma-Aldrich. These were used as the substrates for the melt tracks.

The substrate discs were mounted on a normal 125 mm square baseplate using Blu-Tak and loaded into the Renishaw SLM125. The ram was lowered until the disc was just proud of the base of the build chamber. A flat bar was pressed down across the disc to compress the Blu-Tak and level the disc with the base of the build chamber. The ram was then lowered a further 40 µm and the disc was manually coated in powder, before bringing a wiper blade across the surface to leave a 40 µm thick layer of powder.

The builds consisted of various settings of laser power, exposure and point spacing. Each build was stopped after the first layer to give a single series of melt tracks (Figure 5.1). The substrate discs were sectioned perpendicular to the track direction, mounted, polished and etched with Kallings #2 reagent.

Figure 5.1: Example melt tracks

The measurements of melt pool depth and width have been plotted against normalised energy density, E_0^* (Equation 5.1) [148]. This dimensionless parameter depends on laser power Q, average travel speed v, layer thickness l and hatch spacing $hatch$, normalised by a range of material parameters (density ρ, specific heat capacity of the solid C_p, solidus temperature T_{sol}) and build parameters (absorption efficiency n, beam radius σ, ambient temperature T_0). See Appendix A for more detail.

$$E_0^* = \frac{1}{h^*} \frac{q^*}{v^* l^*} \tag{5.1}$$

$$\frac{1}{h^*} = \frac{\sigma}{hatch} \tag{5.2}$$

$$\frac{q^*}{v^* l^*} = \frac{n\,Q}{2\,v\,\sigma\,layer} \frac{1}{\rho\,C_{psol}\,(T_{sol} - T_0)} \tag{5.3}$$

5.1.1 Time Dependency of Laser Pulse

The SLM125 actually uses a pulsed, rather than continuous laser beam (Figure 5.2). To incorporate this in the model it has been necessary to look at the construction of the laser pulse and how a pulsed laser affects the calculation of normalised enthalpy.

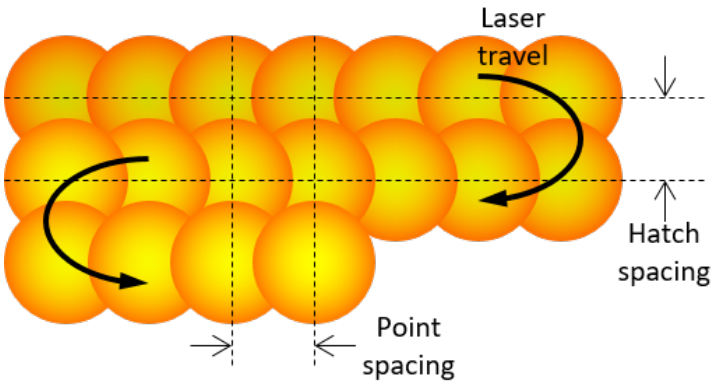

Figure 5.2: Schematic of pulsed laser showing hatch and point spacing

Ideally, the time-profile of the pulse would be a pure top-hat shape, but in reality it has a ramp-up phase at the start of the pulse which reduces the effective exposure time. This has been studied more extensively by a colleague, whose results suggest that the duration of the ramp-up is around 13 µs for 200 W power (Figure 5.3) [149].

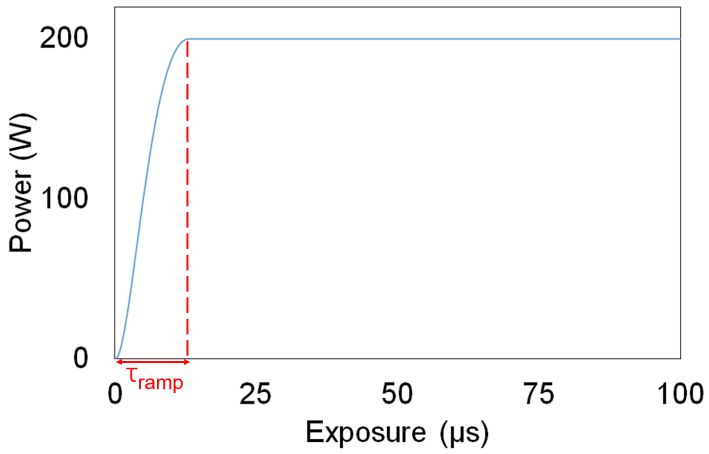

Figure 5.3: Power ramp up at start of pulsed laser exposure time [149]

This efficiency loss, n_τ, must be included in the calculation of the normalised energy density for each of the build conditions. The loss has been defined as the energy of the actual power profile, divided by the energy of the ideal top-hat profile (Equation 5.4). When this efficiency loss is factored in it has the effect of moving the experimental melt pool depths to slightly lower energy density for all build conditions.

$$n_\tau = \frac{\int_{t=0}^{t=\tau} Q(t)\ dt}{Q_{max}\ \tau} \tag{5.4}$$

The duration of the ramp up is believed to be roughly constant, independent of exposure time, so the efficiency loss is much more significant for shorter exposures (Figure 5.4).

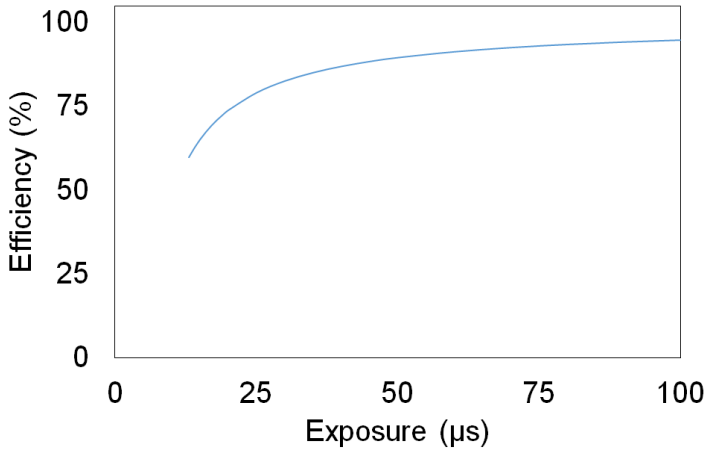

Figure 5.4: Effect of power ramp up on n_τ [149]

For the calculation of temperature field within the model it is not appropriate to just reduce the overall exposure time by this efficiency factor, because this would influence the average travel speed. When modelling the melt pool using an equation for a continuous beam, this exposure efficiency can be applied to the power in the same way as the absorption efficiency. This is not appropriate when modelling the full pulsed behaviour because reducing the maximum power could influence the overall temperature profile. Instead, the model must be adjusted to make the power time dependent (Equation 5.6), where τ_{ramp} is the duration of ramp up to maximum power Q_{max}, τ is the total exposure time and ∇_{ramp} is the gradient of the ramp up, taken from experimental data [149].

This approach assumes that the ramp-up is a straight line with constant gradient, such that lower powers would have a shorter ramp-up duration.

$$\tau_{ramp} = \frac{Q_{max}}{\nabla_{ramp}} \tag{5.5}$$

$$Q(t) = \begin{cases} \frac{\nabla_{ramp}}{t} & \text{if } t < \tau_{ramp} \\ Q_{max} & \text{if } \tau_{ramp} < t < \tau \\ 0 & \text{if } \tau < t \end{cases} \tag{5.6}$$

A further aspect of using a pulsed laser is the effect of the duty cycle on the effective

power output. A continuous 200 W laser travelling at $1\,\mathrm{m\,s^{-1}}$ over a distance of 1 m will produce 200 J of energy. However, a pulsed laser only produces energy when it is switched on, so even if it is 200 W when switched on and is also travelling at an average speed of $1\,\mathrm{m\,s^{-1}}$, if it is only on for half of the time, it will only output half the energy.

To compare a pulsed laser with a continuous laser, or use an equation derived for a continuous laser to predict behaviour of a pulsed laser, it is necessary to correct for this duty cycle. The result is that the effective power Q_{eff} is reduced compared to the actual power Q (produced during the exposure) by a factor dependent on the exposure time τ, point spacing *point* and laser travel velocity c.

$$Q_{eff} = Q \left\{ \frac{\tau}{\tau + (point/c)} \right\} \tag{5.7}$$

The average travel speed v depends on these parameters in a similar way:

$$v = \frac{point}{\tau + (point/c)} \tag{5.8}$$

5.2 Power Series

The first melt tracks were created just changing power (60 W to 200 W in 10 W steps) at constant exposure of 100 µs and constant point spacing of 30 µm. The hatch spacing was set to 200 µm to allow the individual melt tracks to be clearly distinguishable. The tracks were built as 3 mm squares, with 4 to 6 squares on each baseplate disc, giving a total of 15 melt tracks at each condition. The squares were bounded by a contour line, which overlapped with the first and last melt track of each square. There were two repeats of each condition to allow for variation in experimental set-up (e.g. reflectivity of the substrate disc, powder layer thickness and packing density).

5.2.1 Observations

All of the higher power melt tracks showed strong keyhole melting, with the depth significantly greater than the width (Figure 5.5). This is a common issue with additive manufacturing, due to the comparatively high power and small laser spot size.

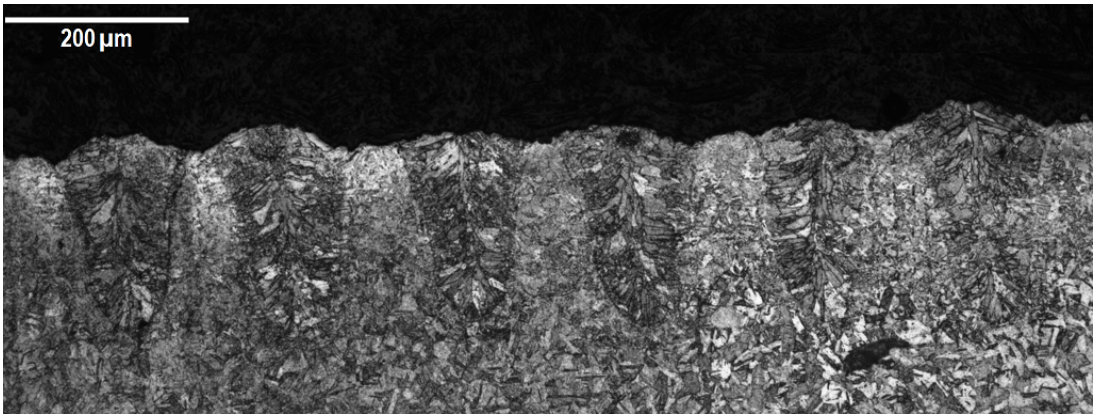

Figure 5.5: Power Series - Example melt pool cross-section at 180 W

The first and last melt pools from each section were generally shallower, potentially due to the influence of the contour premelting the powder and changing the absorption efficiency in this region. These melt pools were therefore regarded as not representative of the general build condition and were excluded from the analysis.

The data for Repeat 1 showed slightly shallower melt pools than for Repeat 2; and the difference was more pronounced for the mid-range energy densities, corresponding to 110 W to 140 W (Figure 5.10). The data for Repeat 2 followed a more uniform trend through this region, consistent with the data at both lower and higher energy density, so the Repeat 1 data in the range 110 W to 140 W was removed from the overall dataset used for validation. This difference could have been due to variation in the applied powder layer thickness.

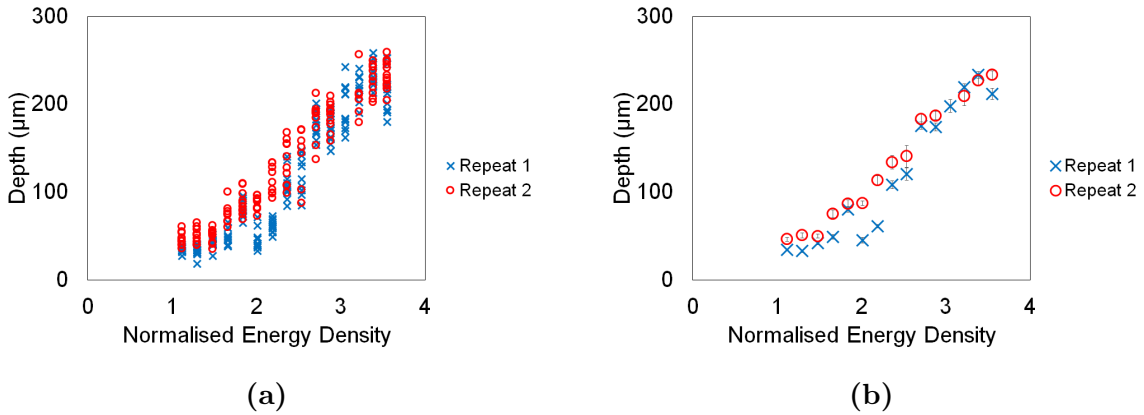

Figure 5.6: Power Series - Experimental melt pool depth. a) Raw Data b) Mean of measurements for each repeat. Error bars show standard error within each repeat.

There were some instances of alternating deep and shallow melt pools, resulting in a bimodal distribution of depth, particularly evident at 170 W (energy density of 3.05) in Repeat 1 (Figure 5.7).

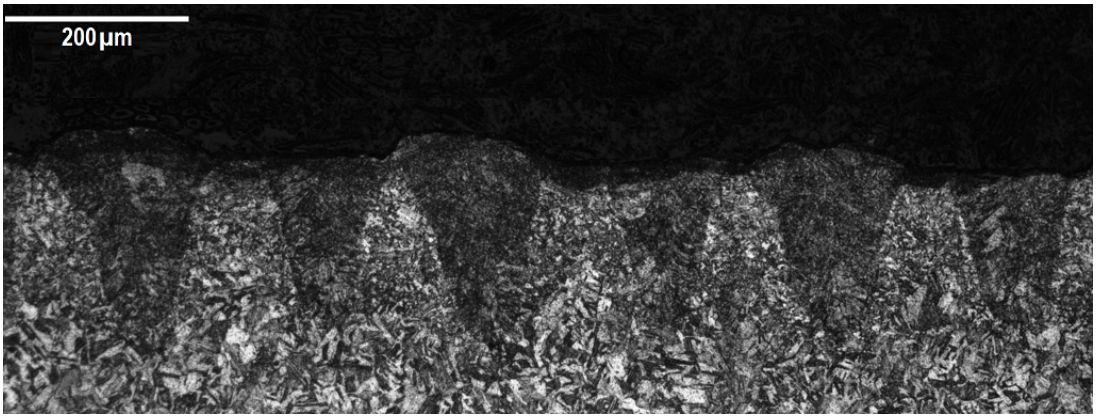

Figure 5.7: Power Series - Alternating deep and shallow melt pools at 170 W

The laser follows a raster pattern, alternating direction between subsequent hatches, so the deeper pools correspond to one direction of travel while the shallower pools correspond to the opposite direction of travel. If the section were taken near to the edge of the build space, then it is possible that the approach hatch is shallower as it is moving through new material at ambient temperature, while the return hatch is deeper as it is moving through pre-heated material. While neither of these are representative of the conditions in the middle of the build space, they do cover the two extremes that can be achieved during a build, and the mean value including both halves of the bimodal distribution was consistent with the other data.

There were also a number of misshapen melt pools which could not be measured (Figure 5.8), and some where the edge of the melt pool could not be clearly distinguished from the substrate. These were not included in the dataset because they could not be measured, but are indicative of the general process variation.

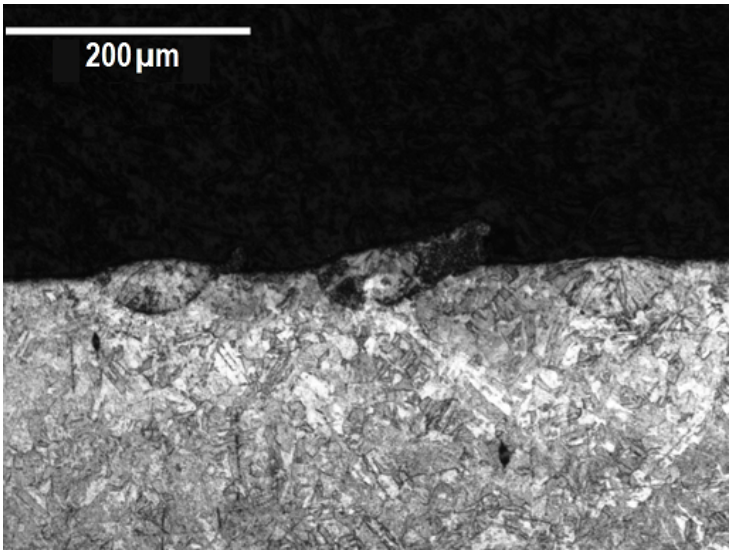

Figure 5.8: Power Series - Poorly formed melt pool at 110 W

At higher power conditions there were also melt pools with entrapped gas bubbles, which is expected given that these were in the keyhole melting regime.

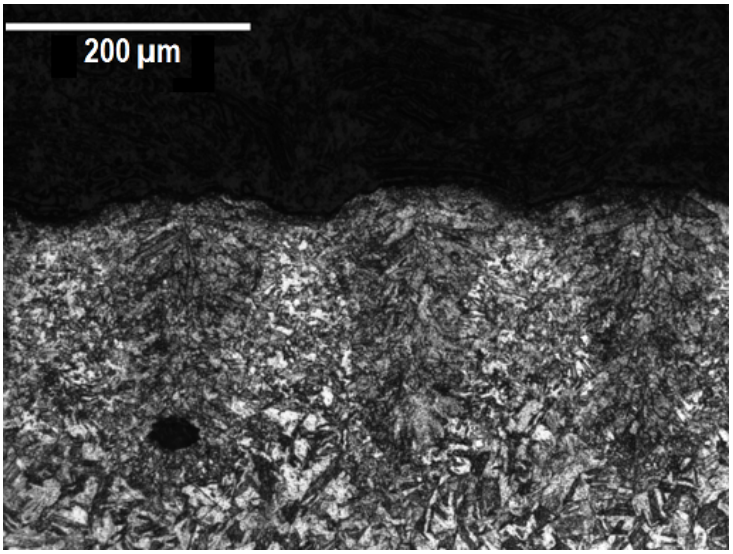

Figure 5.9: Power Series - Gas bubble trapped in keyhole melt pool at 190 W

5.2.2 Melt Track Results

In summary, the data for the two repeats was combined to generate a single dataset of melt pool depth, except for the range 110 W to 140 W which used data from Repeat 1 only. Similar data was also generated for melt pool width, although using all data from

both Repeat 1 and Repeat 2.

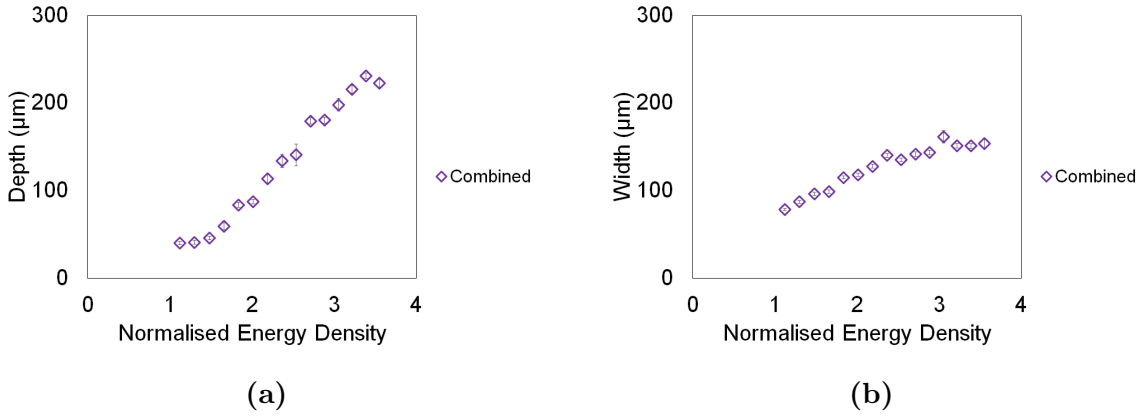

Figure 5.10: Power Series - Final dataset for a) Depth b) Width

Using the aspect ratio (depth / half width), the results were then classified as either conduction mode (<= 1) or keyhole mode (> 1).

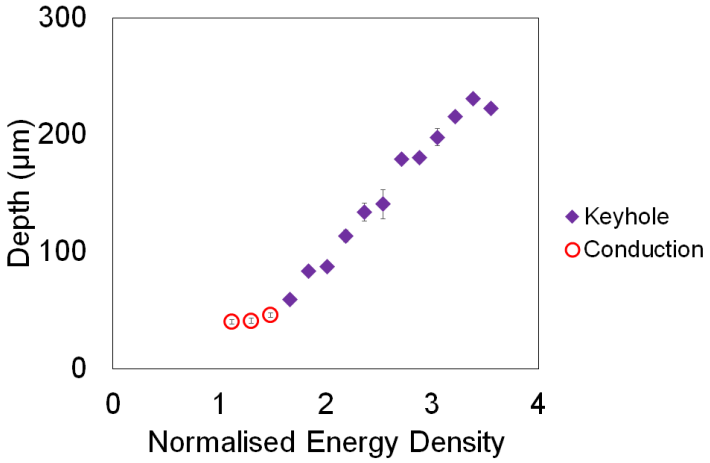

Figure 5.11: Power Series - Mean depths classified by type. Error bars show standard error.

5.3 Design of Experiment Series

The Renishaw SLM125 uses a pulsed laser, which is assumed to be stationary during the exposure time, then moves by a defined point spacing to the position for the next exposure. The melt pool geometry is then a function of the laser power, exposure time and point spacing, as well as a number of other variables (e.g. absorptivity, material properties etc). While the Power Series of melt tracks described above is valuable, it does

not explore the sensitivity of melt pool geometry to variation in either exposure time or point spacing.

To investigate this further, an additional DoE Series was carried out using a Box-Behnken design and following the same method as that described above (Table 5.1). A measured depth of zero indicates that there were no measurable melt pools, either because they were too poorly formed or because they were not present in the mounted and polished condition, suggesting that the melt pool depth was less than the layer thickness.

Table 5.1: DoE melt track experimental results

Power Q W	Exposure τ µs	Point Spacing *point* µm	E_0^*	Mean Depth µm
80	40	60	0.28	0
140	40	90	0.31	0
80	70	90	0.34	0
200	40	60	0.64	0
80	100	60	0.74	68
200	70	90	0.80	58
140	100	90	0.85	61
140	70	60	0.87	56
140	40	30	0.94	55
80	70	30	1.02	51
200	100	60	1.78	119
200	70	30	2.41	150
140	100	30	2.54	128

The data was plotted in Minitab, to investigate the relative effect of power, exposure time and point spacing on melt pool depth. The initial analysis included two-way and square interactions, but these were found not to have a significant effect ($p >> 0.05$) so they were excluded and the analysis was repeated just with linear interactions. This showed that power, exposure time and point spacing were all significant ($p < 0.05$) (Figure 5.12).

Response Surface Regression: Depth versus Power, Exposure, Point

Analysis of Variance

Source	DF	Adj SS	Adj MS	F-Value	P-Value
Model	3	27066.3	9022.1	27.23	0.000
Linear	3	27066.3	9022.1	27.23	0.000
Power	1	5408.0	5408.0	16.32	0.002
Exposure	1	12880.1	12880.1	38.88	0.000
Point	1	8778.1	8778.1	26.50	0.000
Error	11	3644.2	331.3		
Lack-of-Fit	9	3644.2	404.9	*	*
Pure Error	2	0.0	0.0		
Total	14	30710.4			

Model Summary

S	R-sq	R-sq(adj)	R-sq(pred)
18.2013	88.13%	84.90%	74.60%

Figure 5.12: Minitab analysis of Box-Behnken DoE

The analysis was then repeated excluding the data points where the depth had been recorded as zero (Figure 5.13). These values were not true measurements of zero depth, rather situations where the melt pool depth was less than the powder layer thickness so no melt pool had been recorded. The effect was to increase the significance of the power, exposure and point spacing, reduce the value of S (the distance that data points sit from the regression line), and increase the R^2 parameters which describe the amount of variation in the response that can be explained by the predictor.

Response Surface Regression: Depth versus Power, Exposure, Point

Analysis of Variance

Source	DF	Adj SS	Adj MS	F-Value	P-Value
Model	3	12178.0	4059.34	41.42	0.000
Linear	3	12178.0	4059.34	41.42	0.000
Power	1	6434.6	6434.56	65.66	0.000
Exposure	1	5057.6	5057.62	51.61	0.000
Point	1	6604.7	6604.74	67.40	0.000
Error	7	686.0	98.00		
Lack-of-Fit	5	686.0	137.20	*	*
Pure Error	2	0.0	0.00		
Total	10	12864.0			

Model Summary

S	R-sq	R-sq(adj)	R-sq(pred)
9.89939	94.67%	92.38%	82.66%

Figure 5.13: Minitab analysis of Box-Behnken DoE excluding zero depth data points

The R^2(adj) includes an adjustment for the number of terms in the model, while the R^2(pred) is a measure of how well the model will predict for new observations. The low value of R^2(pred) compared with R^2 and R^2(adj) suggests that the model may be overfitted, and not predict new observations as as well as it fits the existing data.

The analysis also generated an expression for the response surface (Equation 5.9).

$$Depth = -30.8 + (0.433\,Q) + (1.338\,\tau) - (1.104\,point) \tag{5.9}$$

5.4 Melt Tracks and Actual Builds

A comparison was made between these melt tracks, created for validation of the melt pool model, and some of the full experimental builds which will be presented in Chapter 7.

At one extreme was a build created with 200 W power, 100 µs exposure, 30 µm point spacing and 30 µm hatch spacing, which had wide keyhole melt pools, approximately 200 µm to 250 µm in depth (Figure 5.14a). These were compared with melt tracks from the Power Series which were created with the same power, exposure and point spacing, but with a 200 µm hatch spacing. The general shape and depth of the melt pools were comparable (Figure 5.14b), suggesting that hatch spacing does not strongly affect melt pool geometry under these conditions and indicating that the melt tracks were representative of the actual build.

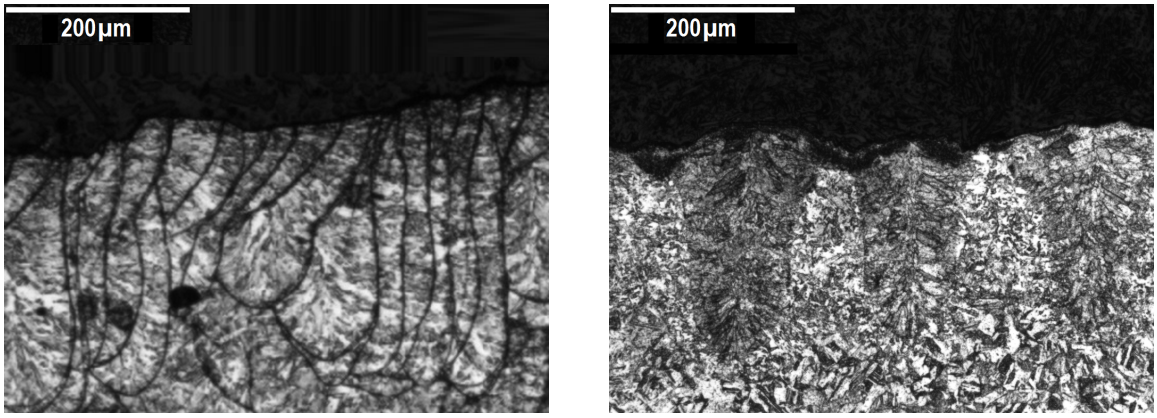

(a) Build: 200 W, 280 mm s^{-1} **(b)** Melt Track: 200 W, 280 mm s^{-1}

Figure 5.14: Comparison between a) actual build and b) validation melt track at high energy density.

The extent of the melt tracks shown in Figure 5.14b is not as obvious as those in Figure 5.14a, but was determined by a combination of the change in contrast, and a change

from equiaxed to columnar structure. The base of the melt pools showed a strong columnar structure, radially oriented from the edge of the melt pool towards the centreline.

At the other extreme was a build created with 200 W power, 100 µs exposure, 90 µm point spacing and 90 µm hatch spacing. This had much narrower weld pools, but they were still strongly keyhole in shape and around 200 µm to 250 µm in depth (Figure 5.15a).

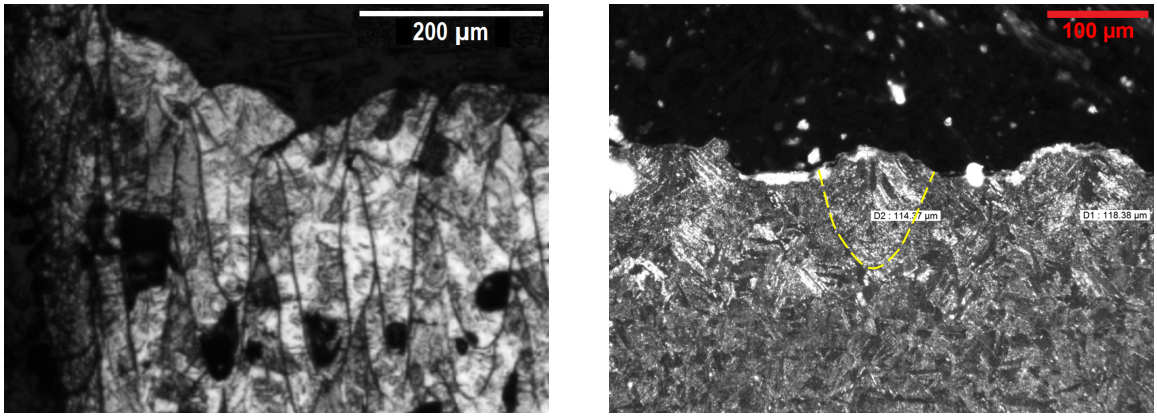

(a) Build: 200 W, 738 mm s^{-1} **(b)** Melt Track: 200 W, 523 mm s^{-1}

Figure 5.15: Comparison between a) actual build and b) validation melt track at low energy density. Edge of one melt track highlighted (yellow dashed line) for clarity.

The Power Series and Box-Behnken series did not include melt tracks at this exact condition, but the closest comparable was the Box-Behnken melt track at 200 W power, 100 µs exposure and 60 µm point spacing. This had much smaller melt pools, only around 100 µm to 120 µm in depth, which had a much smaller aspect ratio (Figure 5.15b). This was a significant difference in melt pool shape, and the difference would be expected to be even greater for a melt track with a 90 µm point spacing.

5.4.1 Substrate Density

One proposed explanation was that the melt tracks had been built on baseplate discs cut from fully dense bar, whereas the actual build was only around 92 % dense. This reduced density could have caused a higher temperature melt pool for the same energy input, and therefore more extreme keyhole melting. Another possibility was the effect of hatch spacing, given that the melt tracks were created with 200 µm hatch and the actual build had 90 µm hatch.

To quantify the effect of these, a further set of melt tracks was created using a piece of previously built material as the substrate, rotated through 90° to allow the new melt pools to be distinguishable. The substrate was built using 200 W power, 100 µs exposure, 90 µm point spacing and 90 µm hatch spacing with 40 µm layer thickness. The melt tracks were created with the same parameters, to make the conditions more representative of an actual build (Figure 5.16).

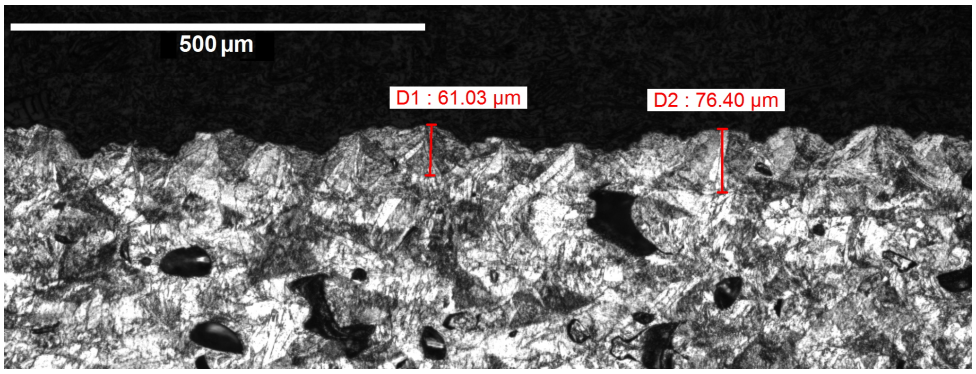

Figure 5.16: Melt tracks created on SLM-built material

The melt pool depths were comparable with those created on solid plate, around 60 µm to 90 µm in depth and semi-circular in shape. Even the deepest ones were not the high aspect ratio keyhole melt pools shown in Figure 5.15a. While the change in substrate material may have been more representative of the actual build conditions, it was not the driver for the observed difference in melt pool shape.

5.4.2 Absorptivity

In addition to the two actual builds shown above, three further samples were built with intermediate point and hatch spacings which also all showed melt pool depths of 200 µm to 250 µm. This consistency of melt pool depth with scanning speed (fixed laser power) indicated that, in this instance, the melt pool depth was effectively independent of point and hatch spacing, which conflicts with the Box-Behnken DoE analysis above.

As discussed earlier (Section 2.2.1), measurements of absorptivity are often taken from single tracks on a single layer. High-speed and Schlieren imaging showed that the plume above the melt pool can be affected by the presence of previous hatches, tilting away from them and changing the interaction between the plume and the laser [35]. The imaging also showed that the early layers of a build can suffer from denudation around the molten

region, which is then corrected during subsequent layers before reaching a steady-state. This demonstrated that while single track, single layer data is useful, it may not be fully representative of steady-state build conditions.

All of the substrates used for the melt tracks were ground to a '600-grit' standard before being used to improve uniformity of the powder layer thickness. However, visual inspection of the as-built samples showed significant differences in surface roughness and reflectivity between the high and low energy density conditions (Figure 5.17); see Chapter 7 for more detail. The high energy density material, where the melt pools from the build were comparable to those from the melt tracks, had a smooth and reflective surface, similar to that of the substrate discs. In constrast, the low energy density material, where there was a difference in melt track geometry between actual build and melt track, had a much rougher and less reflective surface.

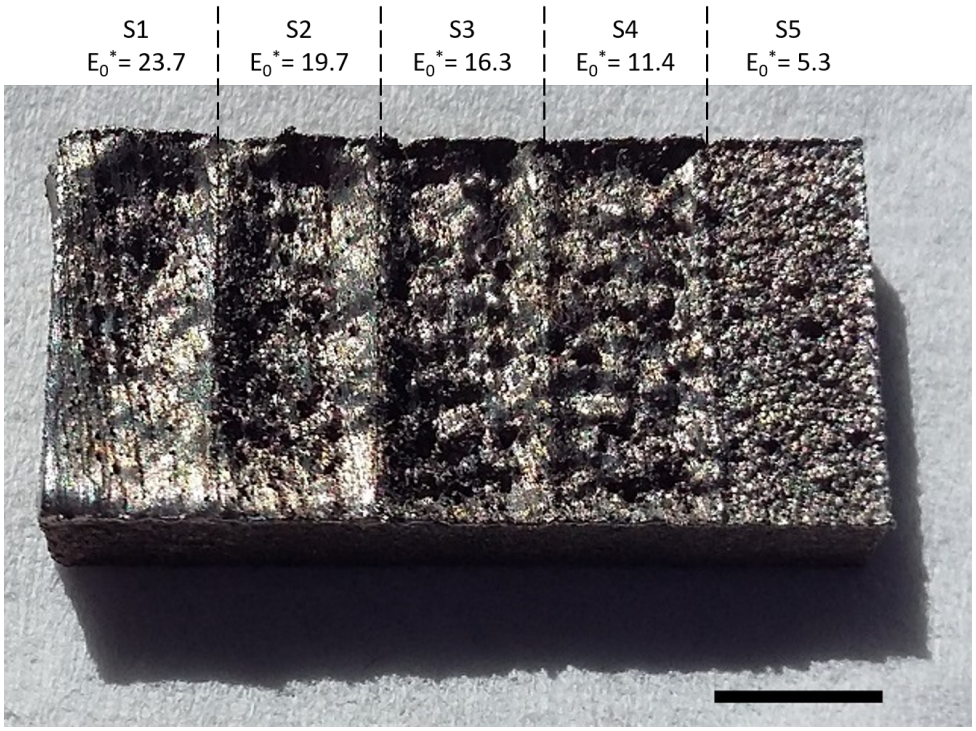

Figure 5.17: Actual build graded from high to low energy density showing variation in surface roughness and reflectivity. Scale bar is 4 mm.

It is proposed that the differences in melt pool geometry between the melt track and the full build can be explained by changes in absorption efficiency driven by the effect of multiple layers/hatches and combined with changes in surface roughness and reflectivity.

5.5 Summary

The Power Series generated trends for melt pool depth and width with increasing energy density driven by a change in laser power. With increasing energy density the melt pool shape changed from conduction mode to keyhole mode, characterised by a significant increase in melt pool depth and aspect ratio.

Due to the pulsed nature of the SLM125, the melt pool geometry is also dependent on a combination of exposure time and point spacing, rather than simply average travel speed. A further set of melt tracks were created following a Box-Behnken design of experiments approach. This showed depth to be very dependent on exposure time, although less dependent on point spacing. The analysis did generate an equation for the response surface, but the goodness of fit indicated this would not be sufficient for high quality predictions of melt pool depth.

Comparisons between the melt tracks and actual builds showed that at high energy density there was good correlation between the melt tracks and actual builds, but at low energy density the melt tracks were much shallower and less distinctly keyhole in shape than the melt pools measured in the actual builds. Further, the actual builds showed consistent melt pool depths across a range of point spacings, which was not in line with Box-Behnken response surface prediction.

The literature has shown that absorption efficiency can be influenced by laser parameters, and that it can take a number of layers before the build surface reaches a smooth steady-state. It is therefore suggested that the difference in melt pool geometry between (single-track, single-layer) melt tracks and actual builds could be explained by changes in absorption efficiency caused by multiple hatches and layers, combined with the variation in surface roughness and reflectivity observed from the built samples.

This analysis has been mostly concerned with the measurement of melt pool depth, to be used for comparing experimental data with the predictions from a Matlab model. Accepting the issues around differences between melt tracks and actual builds, the data can still be used to develop the model through the following stages:

- Predicting melt pool geometry in conduction mode
- Identifying the onset of keyhole melting

- Predicting melt pool geometry during keyhole melting with uniform absorptivity

It will then be possible to use empirical evidence from actual builds to modify the absorptivity and achieve the correct melt pool depth, so that the model can be used to predict cooling rates and other associated outputs for the actual build conditions.

Chapter 6

Melt Pool Modelling

It is possible to consider AM modelling at a variety of length scales: i) the micro-scale of the powder particles, ii) the meso-scale of the melt pool, segregation and the grain structure, iii) the macro-scale of the component, residual stress and porosity [150] (Figure 6.1).

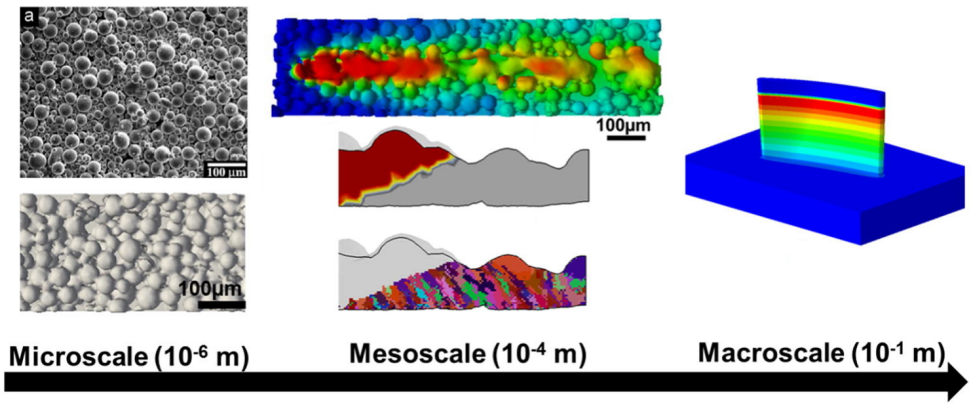

Figure 6.1: Length scales for melt pool modelling. Modified from [150].

This chapter covers the development of a Matlab model to predict melt pool geometry, cooling rate and other associated characteristics (e.g. duration of in-situ heat treatment). The model has been validated against the melt track data described in Chapter 5.

6.1 Model Inputs & Assumptions

6.1.1 Beam Velocity

The beam velocity c, (velocity at which the laser travels between points) used in the calculation of average travel velocity v, has been taken to be $4.1\,\mathrm{m\,s^{-1}}$. This is a fixed parameter within the Renishaw SLM125 machine set-up, and has been confirmed by video evidence captured using a high speed camera [151]. For the range of point spacing and exposure times used in this study, a 10 % variation in travel velocity c would give less than 3.5 % variation in average velocity v.

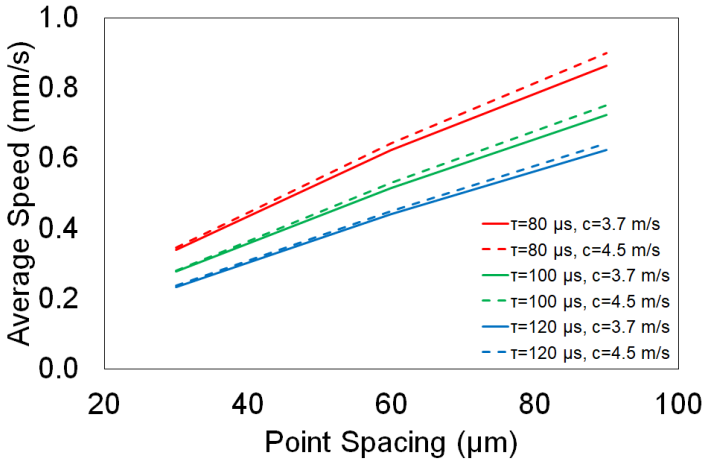

Figure 6.2: Sensitivity of average speed v to variation in travel speed c.

This can be further demonstrated by examination of Equation 6.1, used to calculate v, where the point spacing is divided by the sum of the exposure time and the travel time. The average speed is only sensitive to travel speed c for very short exposures or very large point spacings, when the travel time is a significant proportion of the exposure time.

$$v = \frac{point}{\tau + (point/c)} \tag{6.1}$$

The builds presented in later chapters have used an exposure time of 100 µs, with point spacings of 30 µm to 90 µm; under these conditions the travel time is less than 25 % of the exposure time. It was judged that this was not a sufficiently high proportion to justify developing a more accurate method of confirming travel speed.

6.1.2 Beam Radius

The beam radius σ of the SLM125 was quoted by Renishaw to be 35 µm [152]. This is reasonable given that the width of the Power Series melt pool tracks reported in the previous chapter reached a minimum of 70 µm to 80 µm at the lowest energy density (Figure 6.3).

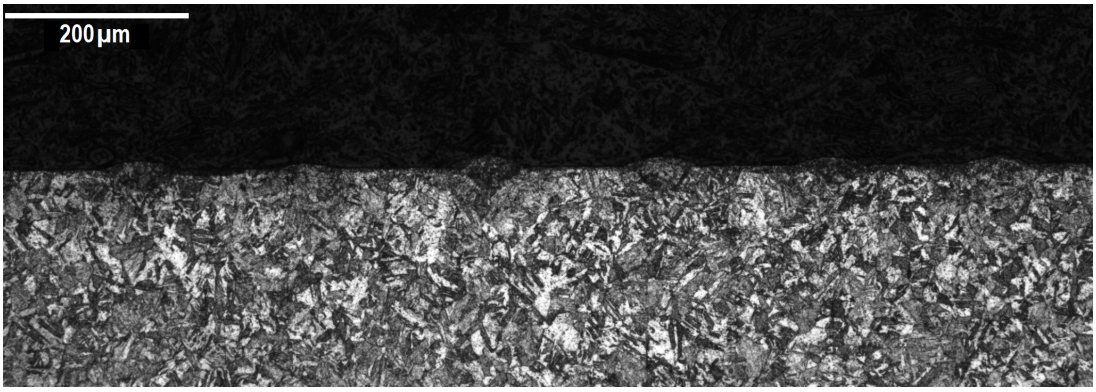

Figure 6.3: Melt tracks at 60 W power showing melt pool widths of 70 µm to 80 µm.

Much of this chapter will use melt pool predictions based around the Eagar equation for the temperature distribution of a continuously moving Gaussian beam, assuming no change in phase (Equation 6.13) [153]. This will be more fully explained later (Section 6.3), however the key part at this stage is the term governing the distance over which heat is transferred into the material: $2a_s t + \sigma^2$, which is a function of the thermal diffusivity in the solid a_s, the time t and the beam radius σ.

$$T - T_0 = \int_{t=0}^{t=t_{max}} \frac{nQ}{\pi\rho C_{psol}(4\pi a_s)^{1/2}} \frac{t^{-1/2}}{2a_s t + \sigma^2} \exp\left\{\frac{X^2 + Y^2 + 2Xvt + v^2t^2}{4a_s t + 2\sigma^2} - \frac{Z^2}{4a_s t}\right\} dt \tag{6.2}$$

For the build conditions used in this work, the exposure time is constant at 100 µs. 17-4PH stainless steel has a thermal diffusivity of $a_s = 6.32\times10^{-6}\,\mathrm{m^2\,s^{-1}}$ (see Appendix A), so the $4a_s t$ term is around $2.5\times10^{-9}\,\mathrm{m^2}$ and the σ^2 term around $1.2\times10^{-9}\,\mathrm{m^2}$. A basic sensitivity analysis showed that 10 % variation in σ around a central value of 35 µm would cause less than 10 % variation in the value of $[4a_s t + \sigma^2]$ (Figure 6.4).

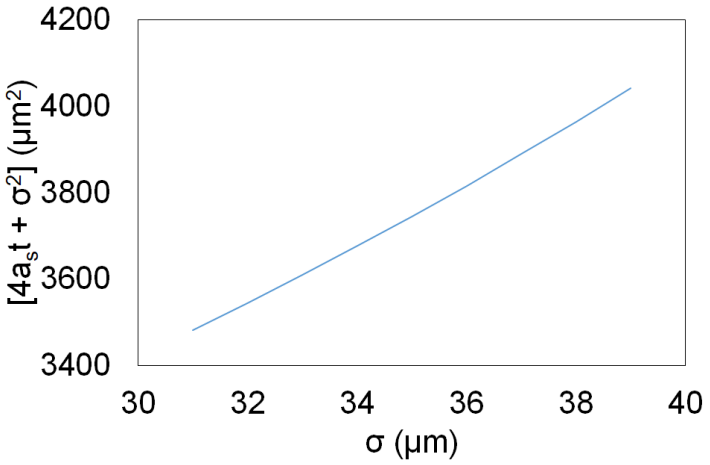

Figure 6.4: Sensitivity of $[4a_s t + \sigma^2]$ to variation in beam radius σ.

6.1.3 Powder Packing Density

The model is designed to predict the melt pool geometry for a hatch in the centre of the sample volume, where there are a number of solid layers already built below the melt pool and a number of hatches already built in the current layer. The melt pool therefore has solid material below and behind it, and must extend into this solid to achieve sufficient overlap for good densification. While the material immediately ahead of the beam is randomly packed powder, with an approximate 64 % packing density [154], the material properties have been taken to be that of the fully dense material due to the relative proportions of powder and solid within the melt pool.

6.1.4 Absorption Efficiency & Energy Density

Measurements with varying laser power and/or scanning speed on 316L stainless steel have shown that absorption efficiency n_{abs} in laser powder additive manufacturing is dependent on energy density [31]. At low energy density n_{abs} is around 50 %, and is governed by reflection between the powder particles. As energy density increases, the powder starts to melt and n_{abs} drops to 35 %, comparable with absorption for a flat plate of the same material.

Then at even higher energy density, the melt pool moves from 'conduction' mode, where size is limited by thermal conduction through the bulk, to 'keyhole' mode, where the melt

pool temperature exceeds boiling point and vapour bubbles start to form. These bubbles trap the laser energy, but get forced down to the bottom of the melt pool by convection currents. Their energy is dispersed at the base of the melt pool, making it deeper and forming a characteristic keyhole shape. In this mode, absorption efficiency increases due to the laser being trapped inside the bubble, until at very high energy density it saturates around $n_{abs} = 70\,\%$.

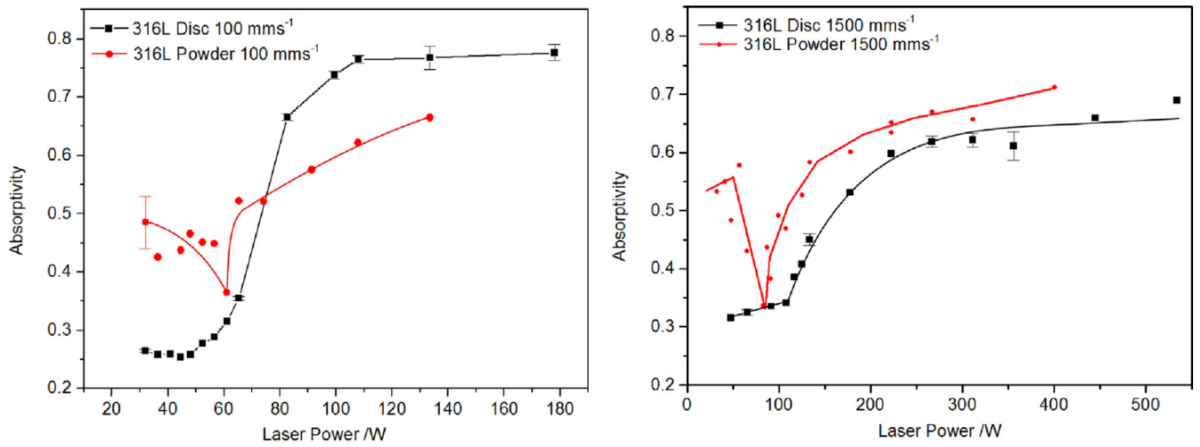

(a) v=100 mm s^{-1} **(b)** v=1500 mm s^{-1}

Figure 6.5: Absorptivity of 316L steel with a 100 µm powder layer compared to the absorptivity of a bare disc [31]

A number of researchers have related the normalised melt pool depth to the normalised enthalpy, and shown that the onset of keyhole melting can be predicted from a threshold value of enthalpy that is valid across a range of different material types and build conditions [9, 32]. The calculations used have some slight differences in the prefactors applied, but are of the same general form using the absoprtion efficiency n, power Q, enthalpy at melting h_s, thermal diffusivity a, average scanning speed v and beam radius σ.

$$\frac{\Delta H}{h_s} = \frac{n\,Q}{h_s\sqrt{a\,v\,\sigma^3}} \tag{6.3}$$

where h_s is the enthalpy at melting; itself dependent on the density ρ, specific heat capacity C_p and solidus temperature T_{sol}:

$$h_s = \rho\,C_p\,T_{sol} \tag{6.4}$$

From the previous chapter, the validation melt tracks at low power (60 W to 80 W) were classified as conduction mode, while those at higher powers were classified as keyhole mode, all at constant average travel velocity of $280\,\mathrm{mm\,s^{-1}}$. This is a faster scanning speed than the closest comparable measurements reported on 316L stainless steel, which were at $100\,\mathrm{mm\,s^{-1}}$.

Using Equation 6.3, it was determined that the conduction mode melt tracks at 60 W and $280\,\mathrm{mm\,s^{-1}}$ had the same normalised enthaply as 36 W at $100\,\mathrm{mm\,s^{-1}}$. In this region, Figure 6.5a shows the absorption efficiency of 316L stainless steel to be 45 %, so this value was used as the nominal fixed n_{abs}, although later discussions will cover the development of a variable absorption efficiency.

There are some discrepancies in the material parameters used between the different forms of Equation 6.3 found in the literature. King specifies the diffusivity as that of the liquid phase, a_l, but does not state whether the density or specific heat capacity are for liquid or solid [9]. Given that they are used to calculate the enthalpy at melting it would be implied that these are for the solid. Hann specifies 'density at melting' which again implies density of solid, but makes no explicit statement for specific heat capacity or diffusivity [32]. Using a_l gives a normalised enthalpy roughly 10 % higher than that when using a_s for the same build parameters [33].

While the normalised enthalpy approach is useful, it does not include the effect of hatch spacing, which can be significant when the return time between adjacent hatches is very short (i.e. for small feature sizes). An alternative parameter is the normalised energy density, E_0^*, which has a slightly different relationship between power and scanning speed, but also includes the effect of hatch spacing [148]. This was defined in the previous chapter, but is repeated here for clarity (Equation 6.5).

$$E_0^* = \frac{1}{h^*}\,\frac{q^*}{v^* l^*} \tag{6.5}$$

$$\frac{1}{h^*} = \frac{\sigma}{hatch} \tag{6.6}$$

$$\frac{q^*}{v^* l^*} = \frac{n\,Q}{2\,v\,\sigma\,layer}\,\frac{1}{\rho\,C_{psol}\,(T_{sol} - T_0)} \tag{6.7}$$

To maintain commonality with the previous chapter, and recognising the effect of hatch

spacing, assessment of the quality of model prediction will be carried out using experimental data plotted against the normalised energy density.

6.1.5 Time Dependency of Laser Pulse

Following on from the previous chapter, the same definitions have been used for the adjustments made to reflect the time dependency of the power during the laser pulse. These are reproduced here for clarity as the ramp up behaviour (Equation 6.8 & Equation 6.9), the duty cycle (Equation 6.10) and the average travel speed (Equation 6.11).

$$\tau_{ramp} = \frac{Q_{max}}{\nabla_{ramp}} \tag{6.8}$$

$$Q(t) = \begin{cases} \frac{\nabla_{ramp}}{t} & \text{if } t < \tau_{ramp} \\ Q_{max} & \text{if } \tau_{ramp} < t < \tau \\ 0 & \text{if } \tau < t \end{cases} \tag{6.9}$$

$$Q_{eff} = Q \left\{ \frac{\tau}{\tau + (point/c)} \right\} \tag{6.10}$$

$$v = \frac{point}{\tau + (point/c)} \tag{6.11}$$

6.2 Version 1: Rosenthal

The Rosenthal equation (Equation 6.12) is a common starting point for steady state temperature field calculations for a continuous laser moving at uniform velocity [155]. The form of the equation used here is for a 3D temperature field generated by a point source in a semi-infinite solid.

The parameters used are the absorption efficiency n, effective power Q_{eff}, thermal conductivity k, average travel speed v and the thermal diffusivity of the solid a_s (Appendix A). The solution is defined in a moving frame of reference, where X is the direction of laser travel, Y is the transverse direction and Z is the vertical (build) direction .

$$T - T_0 = \frac{n\, Q_{eff}}{2\pi k} \exp\left\{\frac{-v\,(X + (X^2 + Y^2 + Z^2)^{1/2})}{2a_s\,(X^2 + Y^2 + Z^2)^{1/2}}\right\} \tag{6.12}$$

Equation 6.12 generates an infinite temperature at the origin due to the point source, but this has been corrected for within the Matlab model by replacing the infinite temperature with the average of the immediately adjacent cells. This correction has no effect on the calculated size of the melt pool or the cooling rate.

The Rosenthal equation assumes no change of phase, so for regions above T_{sol} the temperature will actually be lower than predicted by Equation 6.12 due to the latent heat of melting, LH_m. To account for this the model identified all cells above T_{sol} and calculated the heat input to each cell caused by the laser (Figure 6.6). Where the heat input was sufficient to reach T_{sol} but not to exceed $T_{sol} + LH_m$, the temperature was set to T_{sol}. Where the heat input exceeded $T_{sol} + LH_m$, the overall heat input was reduced by LH_m and then the residual was converted back to temperature. This was only an approximation because it did not account for the partial development of liquid through the mushy zone.

```
%adjust temperatures within melt pool for latent heat of melting
Qmelt=(rho.*(step.^3)).*LHm;                %Latent heat of melting for a cell
Tl=T;
Tl(Tl<Tsol)=0;                              %Identify cells above the solidus
Tl(Tl>=Tsol)=(Tl(Tl>=Tsol)-T0);             %Delta T for cells above solidus
Q2=(rho.*cp_sol.*Tl).*(step.^3);            %Heat input from laser to each cell
QSol=(rho.*cp_sol.*(Tsol-T0).*(step.^3));   %Heat required for a cell to reach solidus
Q2(Q2>0)=(Q2(Q2>0))-(QSol);                 %Excess heat after reaching solidus
Q2(Q2<Qmelt)=0;                             %If excess heat less than latent heat of melting set to zero
Q2(Q2>=Qmelt)=(Q2(Q2>=Qmelt))-Qmelt;        %Excess heat after reaching solidus
Tl=(Q2)./(rho.*cp_liq.*(step.^3));          %Recalculate delta T from adjusted heat using liquid specific heat capacity
T(T>=Tsol)=(Tsol);                          %Clear additional temperature from cells above solidus in main temperature matrix
T=(T+Tl);                                   %Add back in to main temperature matrix
```

Figure 6.6: Code for latent heat of melting correction

The melt pool dimensions were extracted from isothermal contours at T_{sol} using the following definitions (Figure 6.7):

- Depth - the maximum depth achieved, normally found slightly behind the beam
- Width - the maximum width achieved, again normally found slightly behind the beam
- Length - the maximum length on the surface from just ahead of the beam to the furthest extent behind it

- Volume - the volume contained within a 3D solidus isotherm

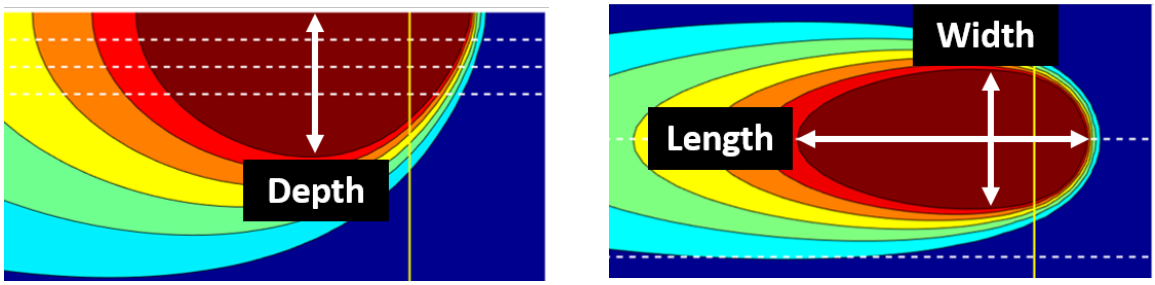

(a) Melt Pool Depth

(b) Melt Pool Length & Width

Figure 6.7: Melt Pool Dimension Definitions

The solidification cell diameter is determined by the tip radius, which is fixed at the liquidus surface, so contours 5 °C either side of liquidus have been used for the calculation of thermal gradient and cooling rate. The thermal gradient, solidification front velocity and cooling rate vary with position around the melt pool. The standard output from the model was defined at the tail of the melt pool, on the surface and directly behind the beam where the solidification front velocity is horizontal and equal to the beam velocity (Figure 6.8). However, alternative code was also written to calculate at the base of the melt pool, where the solidification front velocity is vertical.

```
%Cooling rate calculations
[C6,~]=contour(x,z,T_side,[(Tliq-5),(Tliq-5)]);     %generate a contour at 5C below liquidus
[C7,~]=contour(x,z,T_side,[(Tliq+5),(Tliq+5)]);     %generate a contour at 5C above liquidus

%At the back (tail) of the melt pool
C6Back=C6(1,(find(~(C6(2,:)),1,'first')));          %identify the x position where the 'below' contour reaches the surface
C7Back=C7(1,(find(~(C7(2,:)),1,'first')));          %identify the x position where the 'above' contour reaches the surface

A4_G_back(aa)=(10)./(C7Back-C6Back);                %calculate thermal gradient from the difference in x positions
A4_V_back(aa)=v;                                    %solidification front velocity is equal to beam velocity
A4_Tdot_back(aa)=A4_G_back(aa)*A4_V_back(aa);       %Tdot = G * V

%At the base of the melt pool
[C6Base,C6ID]=min(C6(2,:));                         %identify the z position of maximum depth for the 'below' contour
C7Base=min(C7(2,2:end));                            %identify the z position of maximum depth for the 'above' contour

Vvert_dt=(abs((C6(1,C6ID))-(C6(1,(C6ID-1))))./v;    %calculate the delta time for one meshgrid step
Vvert_dz=(abs((C6(2,C6ID))-(C6(2,(C6ID-1)))));      %calculate the delta depth for one meshgrid step

A4_G_base(aa)=(10)./(C7Base-C6Base);                %calculate thermal gradient from the difference in z positions
A4_V_base(aa)=Vvert_dz./Vvert_dt;                   %calculate the vertical isotherm velocity at the base of the melt pool
A4_Tdot_base(aa)=A4_G_base(aa)*A4_V_base(aa);       %Tdot = G * V
```

Figure 6.8: Code for calculation of thermal gradient and cooling rate

The analysis was carried out over a meshgrid with a step size of 5 µm with no adjustment for keyhole melting at higher energy densities and no calculation of residual heat from previous hatches. The Matlab code is included in Appendix D.

The model was used to predict melt pool geometry for the Power Series validation conditions (Figure 6.9). For the lower energy density, conduction mode melt pools the model predicted a similar order of magnitude for both melt pool depth and width, although the model prediction was generally larger than the experimental observation. However, the model was unable to predict the transition to keyhole mode melting, and therefore significantly under-predicted melt pool depth at higher energy densities.

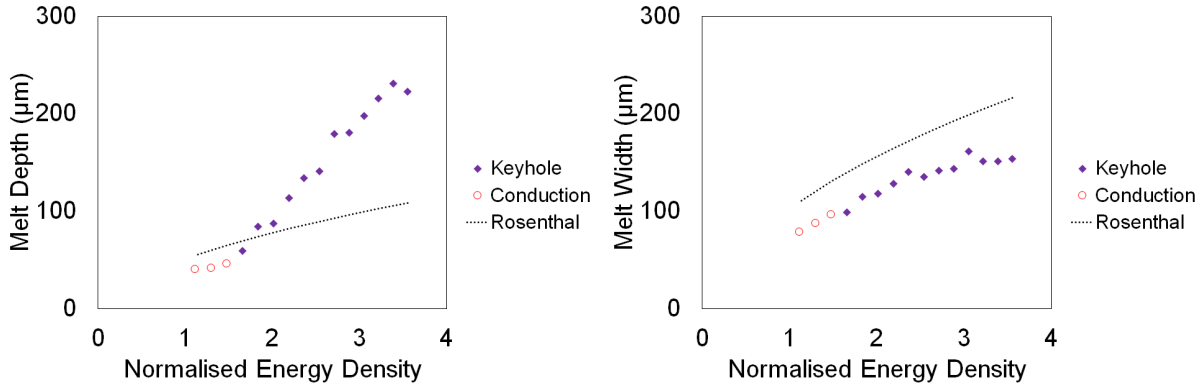

(a) Melt Depth **(b)** Melt Width

Figure 6.9: Rosenthal Model Prediction

The code included the generation of top view and side section view images for visualisation of the melt pool geometry (Figures 6.10 & 6.11). The side view included white dotted lines for the layer thickness to indicate the amount of remelting predicted. The top view included white dotted lines for the centreline and middle of first and second hatches to indicate the extent of hatch overlap. Both images included a yellow solid line showing the position of the laser beam. The melt pool was defined by the hottest isotherm at T_{sol}, while the coldest isotherm was at 50 % of T_{sol}, defining the extent of the heat affected zone (HAZ).

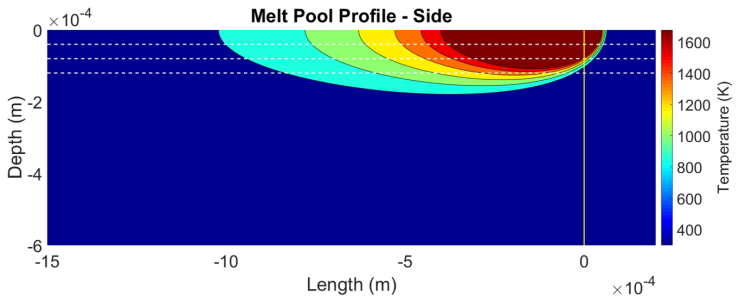

Figure 6.10: Side view of Rosenthal melt pool at 200 W power, 30 µm point spacing, 100 µs exposure.

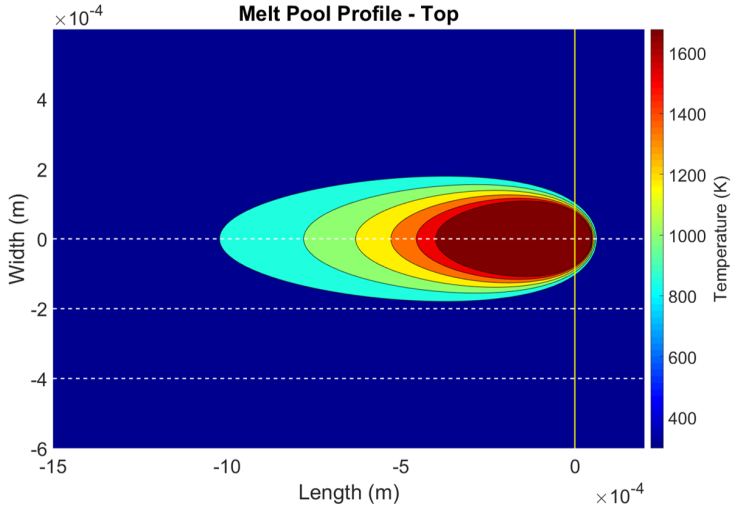

Figure 6.11: Top view of Rosenthal melt pool at 200 W power, 30 µm point spacing, 100 µs exposure.

The predicted melt pool had a classic teardrop shape, with the maximum depth slightly behind the beam.

6.3 Version 2: Continuous Eagar

The next version of the model used the Eagar equation for the temperature distribution of a continuously moving Gaussian beam, assuming no change in phase [153].

$$T - T_0 = \int_{t=0}^{t=t_{max}} \frac{n\,Q_{eff}}{\pi\rho C_{psol}(4\pi a_s)^{1/2}} \frac{t^{-1/2}}{2a_s t + \sigma^2} \exp\left\{\frac{X^2 + Y^2 + 2Xvt + v^2t^2}{4a_s t + 2\sigma^2} - \frac{Z^2}{4a_s t}\right\} dt \tag{6.13}$$

Whereas the Rosenthal equation is a steady state solution, the Eagar equation is for the temperature distribution at a chosen time t. To achieve steady state, Equation 6.13 was recalculated at progressively longer durations until the melt pool volume remained constant. For the conditions used to generate the melt pool tracks, this gave around 0.008 s to reach steady state, equivalent to 70 to 80 exposures. Again the analysis was carried out over a meshgrid with a step size of 5 µm with no adjustment for keyhole melting

at higher energy densities and no calculation of residual heat from previous hatches. The Matlab code is included in Appendix D.

The Eagar model prediction was generally similar to the Rosenthal across the range of energy density (Figure 6.12) although slightly shallower and wider than the Rosenthal which is expected from a Gaussian rather than point source. Again, being a conduction model, the Eagar was unable to predict the transition to keyhole melting.

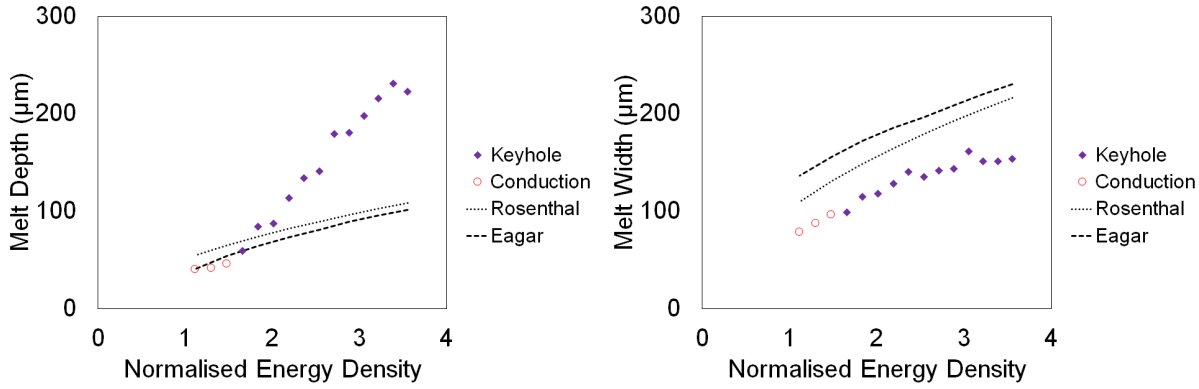

(a) Melt Depth **(b)** Melt Width

Figure 6.12: Eagar Model Prediction

6.4 Version 3: Pulsed

The Eagar (continuous Gaussian) model was then modified to calculate a series of overlapping individual melt pools, rather than a continuous beam.

Recalling the discussion from Section 6.1.5, the power ramp-up at the start of the exposure was incorporated as a time-dependent power (Equation 6.9), rather than using the exposure efficiency factor n_τ. Further, there was no requirement to factor the power output down by the duty cycle (Equation 5.7) because the pulsed model included the effect of the power being switched off between pulses.

Additionally, rather than reaching a true steady state, the melt pool will expand and contract depending on how far through the most recent pulse it is calculated. However, consideration of the melt pools generated in the previous model iterations shows that the widest and deepest point is 100 µm–150 µm behind the beam. This suggests that the width and depth are driven more by the accumulation of residual heat from previous

pulses than the most recent pulse. To maximise the effect of the heat input from the most recent pulse, the decision was made to evaluate the melt pool geometry at the very end of the most recent pulse.

Assuming that the beam is stationary during the exposure time, the average travel velocity v was set to zero, removing a number of terms in the original Eagar equation. This, when integrated over the full exposure time, generated an expression for the temperature field resulting from the most recent pulse, which only requires a heating phase.

$$T - T_0 = \int_{t=0}^{t=\tau} \frac{nQ}{\pi\rho c(4\pi a_s)^{1/2}} \frac{t^{-1/2}}{2a_s t + \sigma^2} \exp\left\{\frac{X^2 + Y^2}{4a_s t + 2\sigma^2} - \frac{Z^2}{4a_s}\right\} dt \tag{6.14}$$

Figure 6.13 shows how the temperature profile for the most recent pulse develops as a percentage of the exposure time (heating phase). This data was generated before the correction to account for the latent heat of melting, so the peak temperature is higher than would actually be observed.

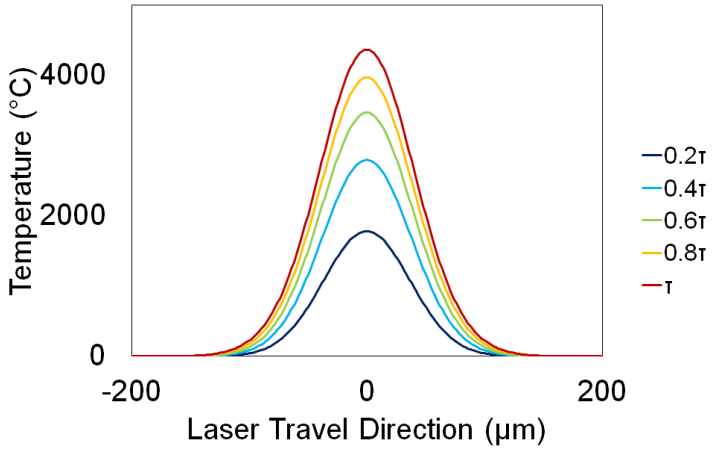

Figure 6.13: Build up of temperature profile during exposure time

For previous pulses, it is necessary to also include a decay (cooling) term. Taking a similar approach to that used by Moat et al [156], Equation 6.14 was adjusted to include the cooling effect and calculate the temperature field for the previous i pulses, including an offset in the laser travel direction by the point spacing.

$$T - T_0 = \sum_i \int_{t=0}^{t=\tau} \frac{nQ}{\pi\rho c(4\pi a_s)^{1/2}} \frac{(t_{max} + (t-\tau))^{-1/2}}{2a_s(t_{max} + (t-\tau)) + \sigma^2}$$

$$\exp\left\{\frac{(X + (i\ point))^2 + Y^2}{4a_s(t_{max} + (t-\tau)) + 2\sigma^2} - \frac{Z^2}{4a_s(t_{max} + (t-\tau))}\right\} dt \tag{6.15}$$

where

$$t_{max} = \tau + \left[i\left(\tau + \frac{point}{c}\right)\right] \tag{6.16}$$

Figure 6.14 shows the cooling phase superimposed on the heating phase for a single pulse, again expressed as a percentage of the exposure time. The profile on cooling is much wider, as energy is no longer being supplied to the centre of the melt pool and the heat gradually dissipates through the material. Similarly to Figure 6.13, the data shown in this graph has not been corrected for the latent heat of melting.

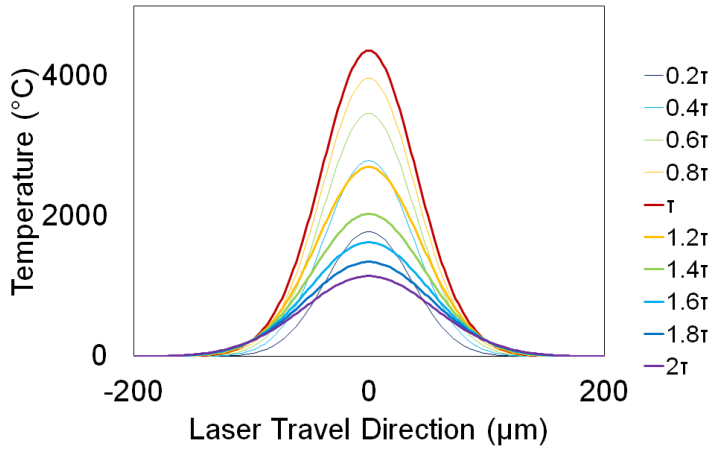

Figure 6.14: Decay of temperature profile after exposure time

The Pulsed model was a summation of Equations 6.14 and 6.15, which started from a first pulse exactly in the centre of the sample and terminated when the i-th pulse reached the extent of the sample size (50 pulses for a 3 mm sample size at a point spacing of 30 µm). The Matlab code is included in Appendix D.

The following image sequence (Figure 6.15) shows how the melt pool geometry developed and reached steady state as more points were included in the summation.

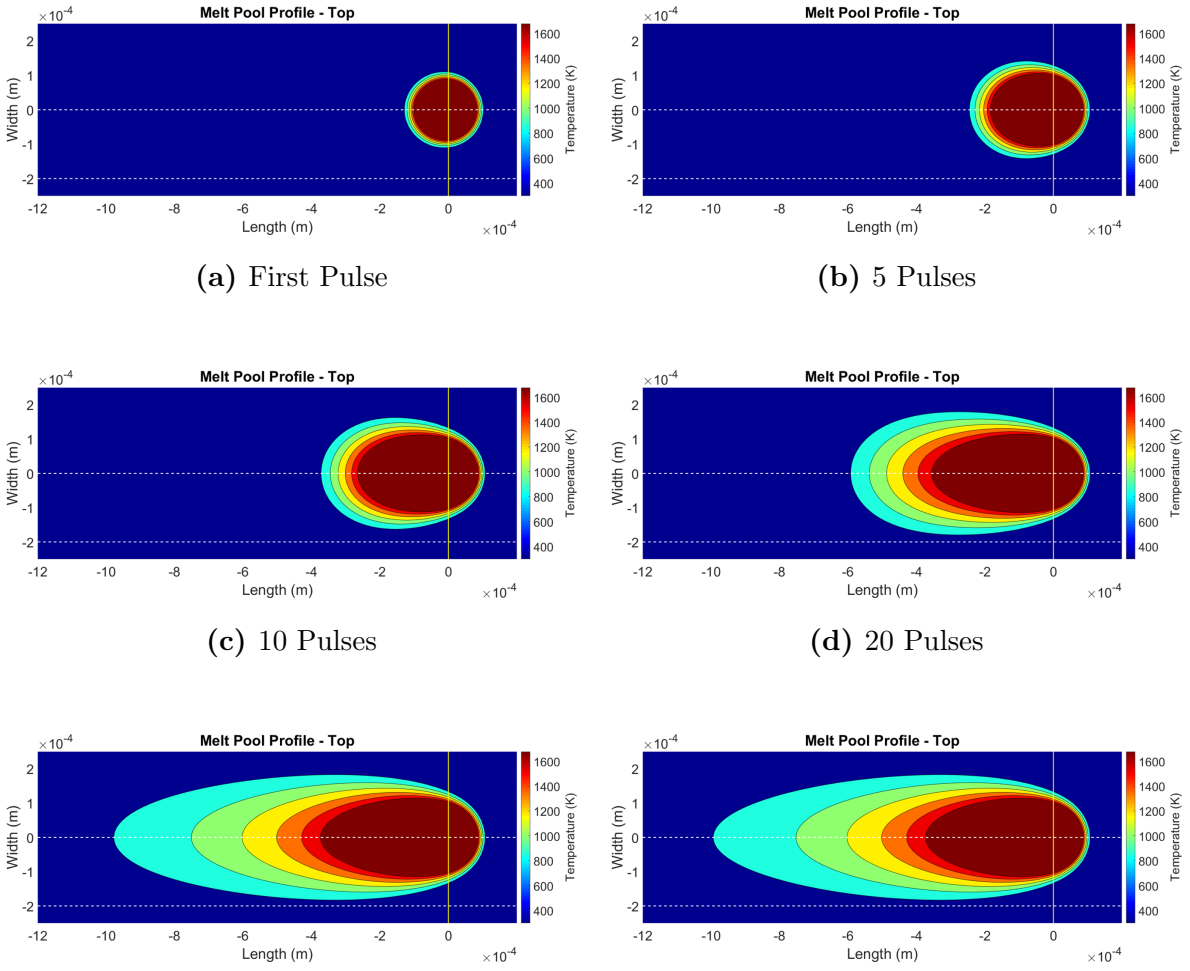

(a) First Pulse

(b) 5 Pulses

(c) 10 Pulses

(d) 20 Pulses

(e) 50 Pulses

(f) 100 Pulses

Figure 6.15: Pulsed Model Summation at 200 W power, 30 µm point spacing, 100 µs exposure.

The Pulsed model gave only marginally different predictions from the continuous Eagar model (Figure 6.16). These conditions have very long exposures with a short point spacing, so the pulsed nature is not expected to give a significantly different melt pool shape. The similarity in prediction supports the use of the duty cycle (Equation 5.7) as a factor when comparing a continuous and pulsed laser output.

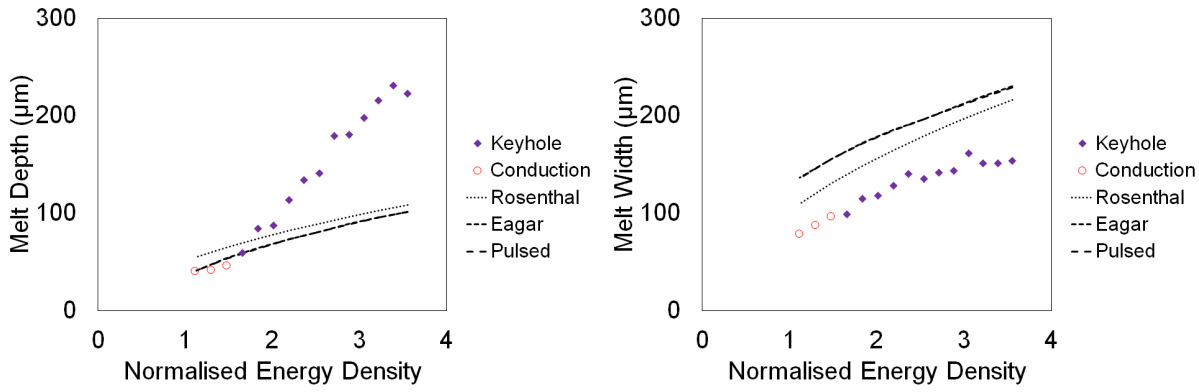

(a) Melt Depth **(b)** Melt Width

Figure 6.16: Pulsed Model Prediction

To review the assumption made at the start of this section, that the melt pool depth and width were more dependent on residual heat accumulated from previous pulses than that from the current pulse, the model was also run with fixed build parameters but evaluated once at the start of the most recent pulse and again at the end of the most recent pulse. The outcome was a less than 0.1 % change in depth and width.

6.5 Version 4: Hatches

The next iteration included the effect of residual heat from previous j hatches (Figure 6.17). This was achieved by extending the summation term across decaying points in the laser travel direction X to include those offset in the transverse direction Y.

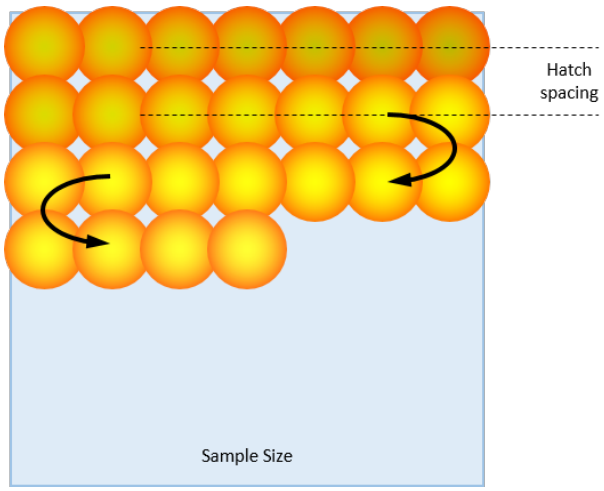

Figure 6.17: Schematic showing previous hatches relative to sample size

Rather than going to the extent of the sample size, which would have caused a 100× increase in processing time, the decision was made to terminate the summation when the temperature change from the central point of the hatch dropped below 1 °C. The analysis was still carried out using the time-dependent power term defined in the previous model to account for the ramp-up at the start of the pulse. As with the Pulsed model, the analysis was carried out assuming the laser was exactly in the middle of the sample, so it does not account for fluctuations in energy density when the hatch reaches the edge of the sample and reverses direction.

The equation for the temperature field due to previous hatches is shown below (Equation 6.17), which was added to the terms for the most recent pulse (Equation 6.14) and the previous pulses on the first hatch (Equation 6.15). The Matlab code is included in Appendix D.

$$
\begin{aligned}
T - T_0 = & \int_{t=0}^{t=\tau} \frac{nQ}{\pi\rho c(4\pi a_s)^{1/2}} \frac{t^{-1/2}}{2a_s t + \sigma^2} \\
& \exp\left\{\frac{X^2+Y^2}{4a_s t + 2\sigma^2} - \frac{Z^2}{4a_s t}\right\} dt \\
& + \sum_j \sum_i \int_{t=0}^{t=\tau} \frac{nQ}{\pi\rho c(4\pi a_s)^{1/2}} \frac{(t_{max} + (t-\tau))^{-1/2}}{2a_s(t_{max} + (t-\tau)) + \sigma^2} \\
& \exp\left\{\frac{(X + (i\,point))^2 + (Y + (j\,hatch))^2}{4a_s(t_{max} + (t-\tau)) + 2\sigma^2} - \frac{Z^2}{4a_s(t_{max} + (t-\tau))}\right\} dt
\end{aligned}
\tag{6.17}
$$

where

$$
t_{max} = \tau + \left[(i+j)\left(\tau + \frac{x}{c}\right)\right] + \left[\frac{Sj}{v}\right] \tag{6.18}
$$

The effect is to extend the melt pool sideways in the direction of the previous hatches (Figure 6.18). The effect is strongest at the tail end of the melt pool, where the previous pulses are closest, and diminishes rapidly as more hatches are added.

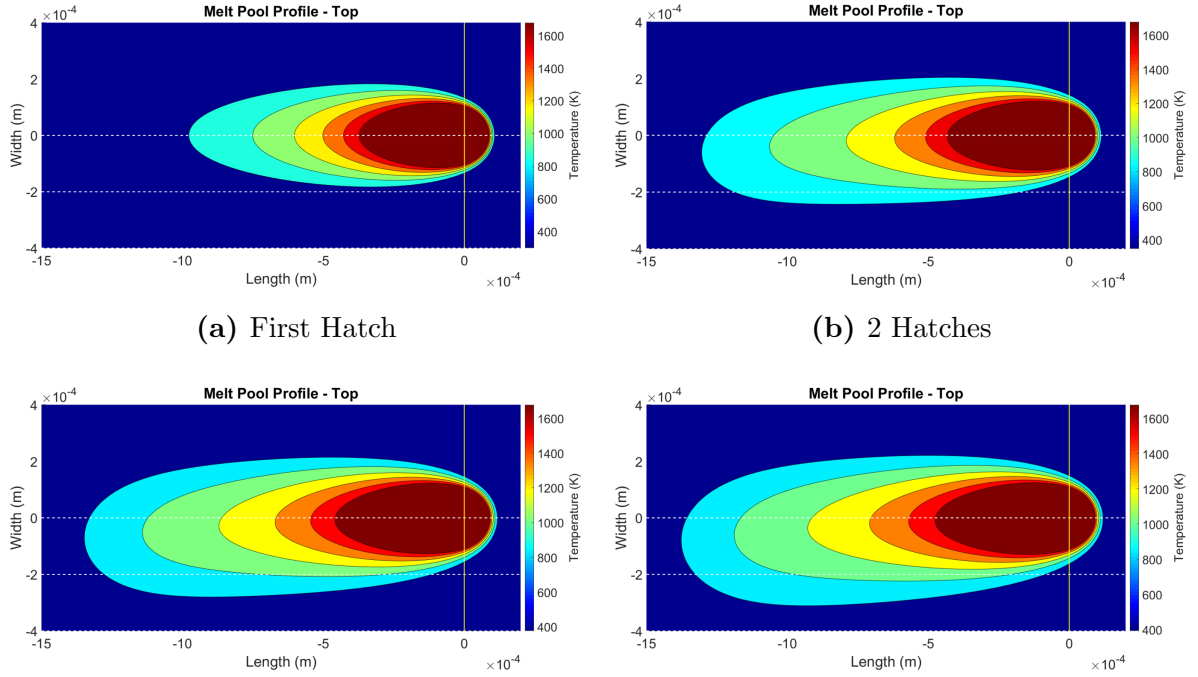

(a) First Hatch

(b) 2 Hatches

(c) 3 Hatches

(d) 4 Hatches

Figure 6.18: Hatches Model Summation

The Hatches model predicted similar depths to the Pulsed model at lower energy density, although at higher energy density the prediction was marginally deeper than that from previous model iterations. The width was predicted to be larger across the whole range of energy density, as expected from the effect shown in Figure 6.18.

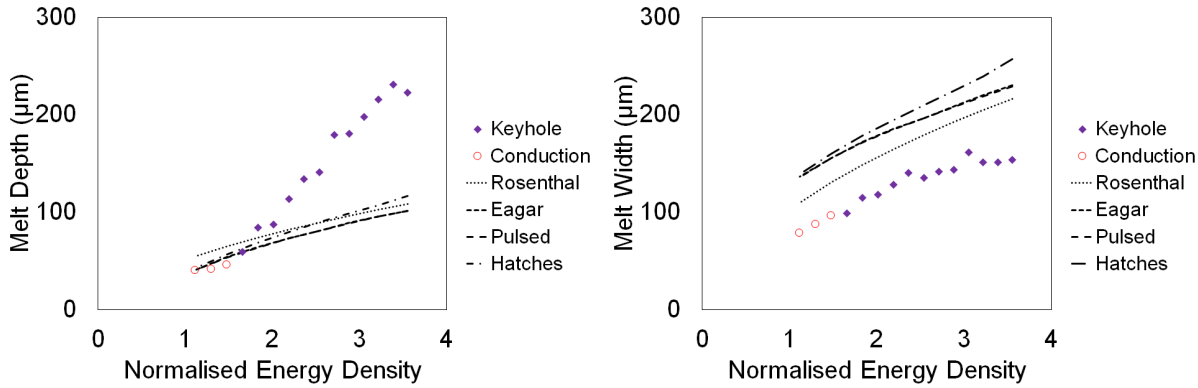

(a) Melt Depth

(b) Melt Width

Figure 6.19: Hatches Model Prediction

As with previous iterations the conduction-mode model did not predict the onset of keyhole melting, or the increased depth resulting from keyhole melting. While the accuracy

of prediction has not improved through the Pulsed and Hatches iterations, they were necessary to achieve a model which replicated the pulsed beam of the SLM125 and the effect of hatch spacing.

6.6 Onset of Keyhole Melting

Comparison of predicted and experimental melt pool depths showed that the previous models, using conduction-mode equations, were able to predict conduction-mode behaviour reasonably well but significantly under-predicted the depths of keyhole mode melt pools.

The approach taken in other studies has been to identify an onset threshold from the aspect ratio of the melt pool, or from the change in gradient on a plot of normalised energy density (or enthalpy) against melt pool depth [9, 32]. For this data, this would suggest a threshold value at an energy density of around $E_0^* \approx 1.56$ (Figure 6.21).

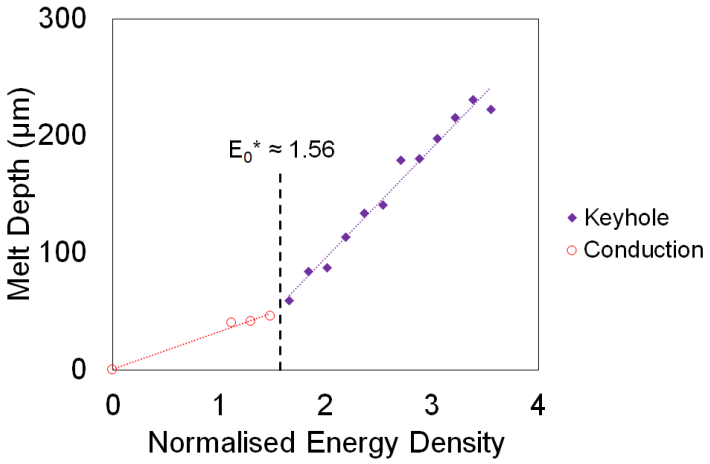

Figure 6.20: Experimental data with conduction and keyhole trendlines

While this is useful, it is limited by the variables included in the calculation. For example, two builds could have the same scanning speed, but one have small point spacing with short exposures and the other have a large point spacing with long exposures. Reviewing the duty cycle and average speed equations derived in Section 6.1.5, it can be seen that the effective power and average speed would be unaffected, provided the ratio of on-time (exposure) to off-time (travel) was maintained (Table 6.1). However, the risk of keyholing would be higher in the build with long exposures, given that the laser is stationary over

a fixed location for longer.

Table 6.1: Effect of varying point spacing and exposure on effective power and average speed

Power	Exposure	Point Spacing	Travel Speed	Effective Power	Average Speed
Q	τ	*point*	c	Q_{eff} (Equation 5.7)	v
W	µs	µm	$\mathrm{m\,s^{-1}}$	W	$\mathrm{m\,s^{-1}}$
200	100	100	4.1	160	0.5
200	10	10	4.1	160	0.5
200	1	1	4.1	160	0.5

Another difficulty is the influence of sample size (return distance) combined with hatch spacing. A large sample will have a long time between the laser passing on adjacent hatches, equal to the sample width divided by the travel speed. However a much smaller sample, built with the same parameters, will have a shorter time between the laser passing the same point so the residual heat from the previous hatch will have a greater impact. Both samples have the same amount of heat input per unit volume, but the smaller sample has a higher risk of keyhole melting.

The model does not suffer from these limitations; the temperature field it predicts includes the effect of point spacing, exposure time and sample size. If possible, it would therefore be preferable to predict the onset of keyhole melting from the temperature field directly, rather than rely on the energy density or other alternative metric derived from build parameters.

From the predicted temperature field it was possible to calculate the volume of melt pool that has sufficient heat to reach boiling point, a necessary condition for keyhole melting [9]. Plotting this against the experimental data showed that keyhole melting started when the volume at or above boiling point V_{boil} exceeded $5{\times}10^{-14}\,\mathrm{m^3}$.

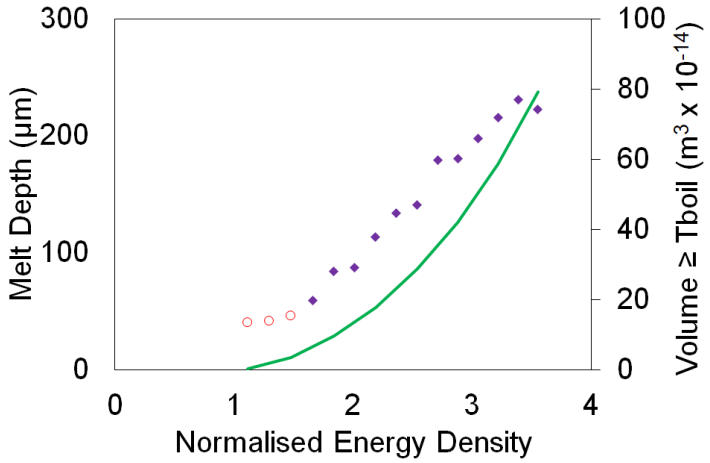

Figure 6.21: Experimental data with predicted volume above boiling point

Reviewing the ratio between measured and predicted depth against the volume at or above boiling point shows an interesting pattern: the ratio is 1 for conduction mode where V_{boil} is less than the threshold, increases for V_{boil} in the range $5\times10^{-14}\,\mathrm{m}^3$ to $45\times10^{-14}\,\mathrm{m}^3$, and then flattens out (Figure 6.22a). This is a similar pattern to that reported for the effect on absorptivity with increasing laser power in the keyhole melting regime (Figure 6.22b) [31].

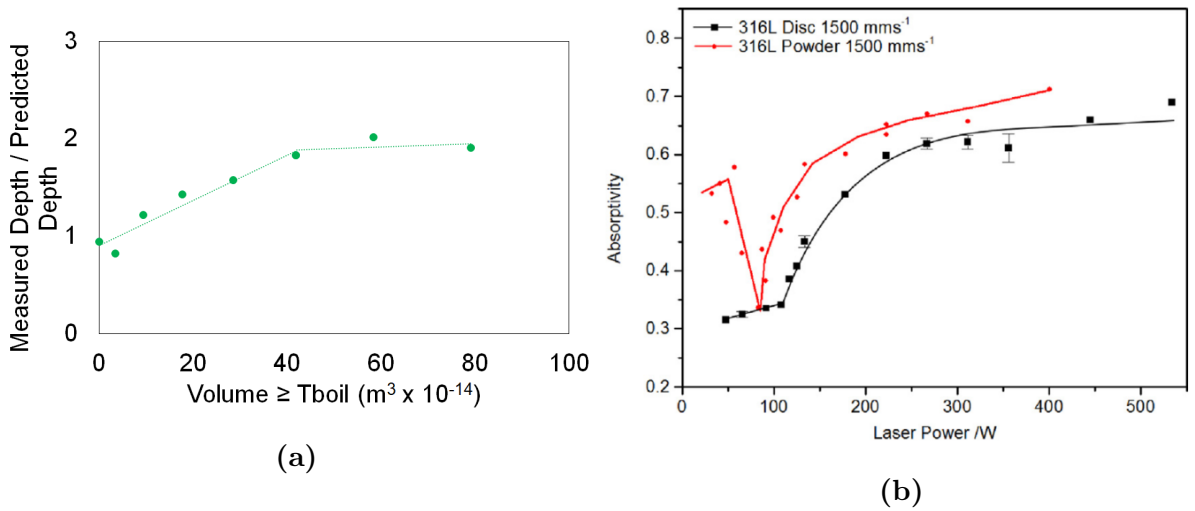

Figure 6.22: a) Ratio of predicted to measured melt pool depth against predicted volume above T_{boil}. b) Absorptivity of 316L steel [31]

Simplifying this to straight lines gives three scaling regimes:

$$Scaling = \begin{cases} 1 & \text{if } V_{boil} < 5{\times}10^{-14}\,\mathrm{m}^3 \\ 1 + 2{\times}10^{12}\,V_{boil} & \text{if } 5{\times}10^{-14}\,\mathrm{m}^3 < V_{boil} < 45{\times}10^{-14}\,\mathrm{m}^3 \\ 2 & \text{if } 45{\times}10^{-14}\,\mathrm{m}^3 < V_{boil} \end{cases} \tag{6.19}$$

6.7 Version 5: Scaled

6.7.1 Power Series

The Hatches model was updated to include these three scaling regimes, to improve depth prediction for keyhole melting. The model ran initially with scaling switched off to calculate V_{boil}, then, if V_{boil} was above the threshold and scaling was required, and the simulation automatically re-ran with the adjusted scaling. The Matlab code is included in Appendix D.

The result is a depth prediction that is much closer to the experimental Power Series data than any of the pure conduction-mode models. The width prediction is unaffected by the depth scaling and still overpredicts for all conditions.

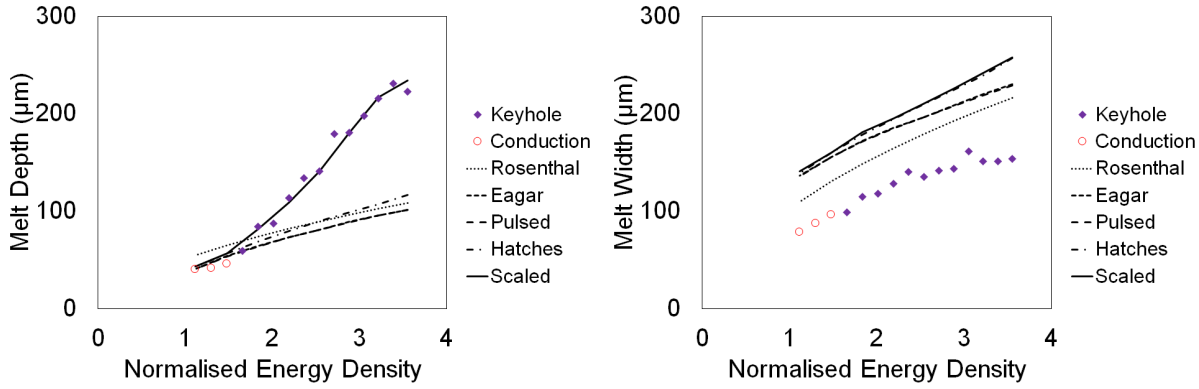

(a) Melt Depth **(b)** Melt Width

Figure 6.23: Scaled Model Prediction

For high energy density the predicted melt pool shape is now much deeper and more hemispherical than that predicted by the earlier iterations. The top view also shows the effect of previous hatches, making the temperature field less symmetrical.

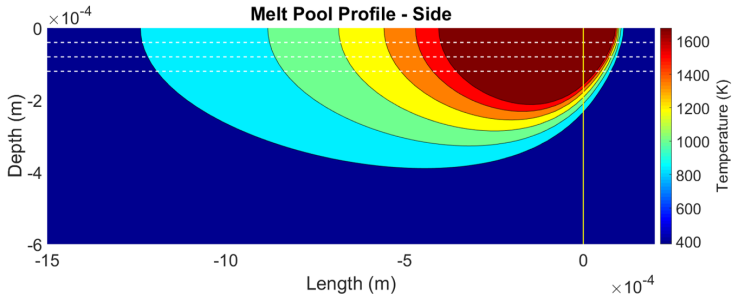

Figure 6.24: Side view of Scaled melt pool at 200 W

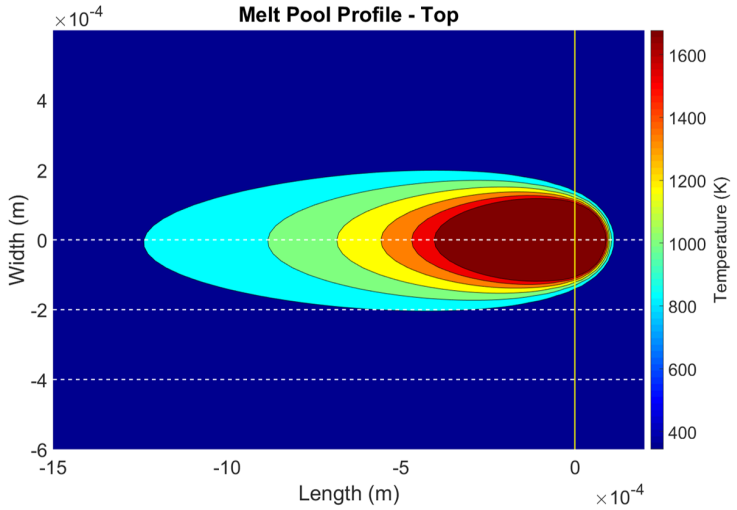

Figure 6.25: Top view of Scaled melt pool at 200 W

6.7.2 Box-Behnken DoE Series

Up to this stage, the development has been based on comparison against the Power Series of melt tracks only. To test the capability of the model further, the Scaled model was used to predict the melt pool depths for the Box-Behnken Design of Experiments conditions.

The results showed generally good correlation, particularly at the higher energy densities where there was more significant keyhole melting (Figure 6.26a). Analysis of the error (measured - predicted) supports this, with no trend in the magnitude or direction of the error with increasing energy density (Figure 6.26b). The error at low energy density was due to melt pools less than 40 µm in depth not adhering to the substrate and therefore being recorded as zero depth.

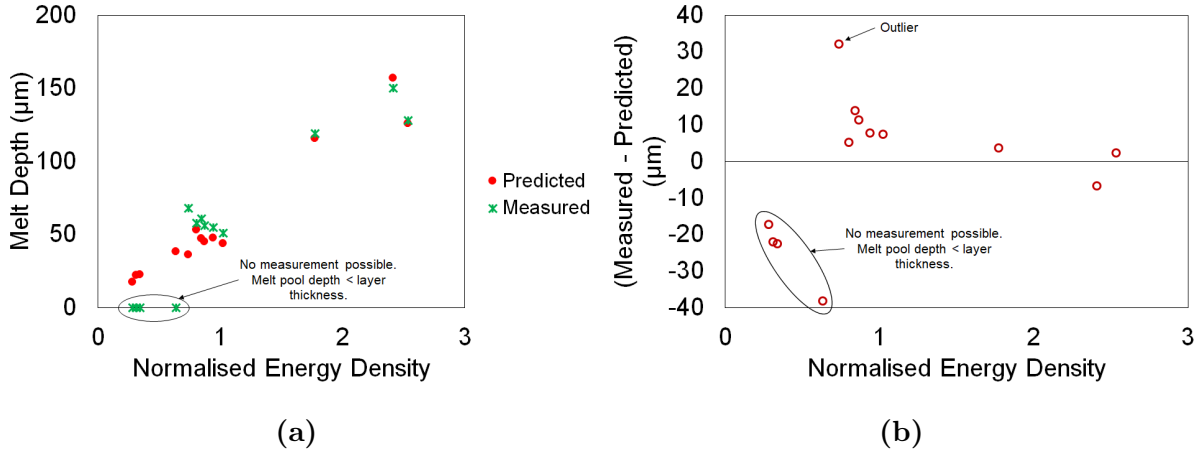

Figure 6.26: Scaled model prediction capability for Box-Behnken DoE conditions a) Measured and Predicted b) Error

There was one outlier, where the measured depth was 68 µm and the predicted depth only 36 µm, giving an error of 32 µm.

6.8 Version 6: Scaled with Varying Absorptivity

This level of correlation between the Scaled model and experimental data from melt tracks indicates that, using a fixed absorption efficiency of 45 %, the model is capable of predicting melt pool geometry with low error, giving a level of confidence in the additional outputs (cooling rate, in-situ heat treatment etc.). However, the melt tracks were created under highly controlled conditions as single-track, single-layer builds on identical substrates, which may not be fully representative of actual builds.

In Chapter 5 it was identified that the melt pool geometry was different between melt tracks and actual builds, even when using the same laser parameters. It was proposed that this was due to a change in absorption efficiency caused by a combination of the effect of multiple hatches on the laser plume, the effect of multiple layers on powder denudation around the melt pool, and the roughness and reflectivity of the build surface.

The absorption efficiency, n_{abs}, incorporates many factors including radiative losses, absorption by the powder, absorption by the constituents of the laser plume, absorption by any uncoated substrate and heat transfer between powder and substrate. It may also be affected by powder characteristics such as the particle size distribution, surface roughness

and packing density. Given this complexity, rather than attempting to measure the actual n_{abs} experienced for each set of laser parameters individually, the model has been validated against melt tracks using a fixed $n_{abs} = 45\,\%$ and then used to determine a variable and build-appropriate n_{abs} by matching the predicted and experimental melt pool depths for each build condition.

The actual builds were carried out at 200 W power and 100 µs exposure, with point and hatch spacing varying between 30 µm to 90 µm. At 30 µm spacing the actual build showed melt pools around 200 µm to 250 µm in depth, in line with the melt tracks at that condition. Using $n_{abs} = 45\,\%$, the Scaled model predicts a melt pool depth of 213 µm, which correlates well with the experimental data.

At 90 µm spacing the actual build still showed melt pools around 200 µm in depth, much deeper than the 80 µm to 120 µm observed from the melt tracks. The Scaled model at $n_{abs} = 45\,\%$ predicted melt pools of only 77 µm for this condition, at the lower end of measurements from the melt tracks and much lower than the data from actual builds. To achieve a similar outcome to the actual builds it was necessary to allow the absorptivity to increase to 90 %, where the predicted melt pool depth then increased to 194 µm.

There were three intermediate conditions at 34 µm, 40 µm and 52 µm spacing, all of which also had 200 µm deep melt pools. Taking the same approach, these required absorption efficiencies of 48 %, 55 % and 65 % respectively (Figure 6.27a). Plotting this against the normalised energy density (also calculated using the variable absorption efficiency), gave an approximately logarithmic relationship (Figure 6.27b).

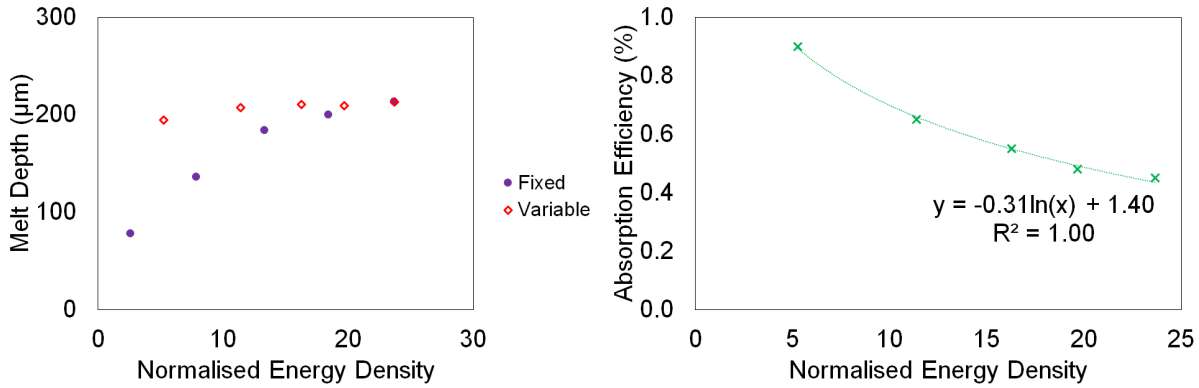

Figure 6.27: a) Model prediction with fixed and variable absorption efficiency. b) Variation in absorption efficiency required to match model prediction to actual builds.

In these builds, the power and exposure time were both fixed, but the point spacing and therefore average travel speed were allowed to vary. Reviewing the calculated values of n_{abs}, they would indicate higher absorption at higher travel speed (large point spacing), when the laser plume would be expected to be behind the beam and there would be less interaction between the laser and the constituents of the plume [35]; this was also the condition with a rougher and less reflective as-built surface. Conversely, the lower absorption was at lower travel speed (small point spacing), when the laser plume would be more in line with the laser and there would be more interaction; this also had a smoother and more reflective as-built surface.

This additional scaling was based purely on the empirical evidence from these specific build conditions, and cannot necessarily be read across to other parameter sets.

6.9 Heat Treatment

In-situ heat treatment is an unavoidable characteristic of additive manufacture. Using the temperature field predicted by the model it has been possible to calculate a predicted extent of time at temperature, based on a a series of lines along the length of the calculation space in X. The first line is immediately below the laser beam at a depth of 0.5 layer thickness from the base of the melt pool, starting from hatch at the furthest $-Y$ extent of the calculation space. Additional lines are then extracted at the same depth but offset in Y by the hatch spacing to the edge of the calculation space. This is repeated for the subsequent layers, terminating at the end of the calculation space or when the peak temperature drops below 50 % of T_{sol}. All lines are concatenated into a single output. This temperature profile is shown by the blue line in Figure 8.10.

This approach does ignore the time between heating phases, but can be used to give a cumulative picture of the time at temperature for a specific build condition (Figure 8.10).

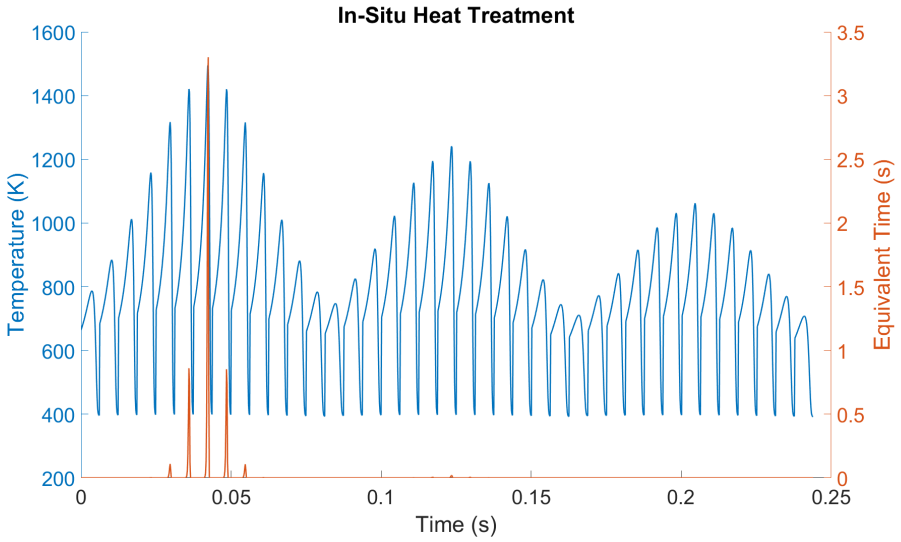

Figure 6.28: Predicted time at temperature (blue - LH axis) and predicted equivalent duration of heat treatment at 800 °C (red - RH axis)

The final stage is calculation of a single effective time at temperature (Equation 6.20) which converts an increment of time Δt_1 at temperature T_1 to the equivalent time Δt_2 at temperature T_2 for a process with activation energy Q^*, where R is the gas constant [157]. The analysis used here normalises the heat treatment to an equivalent duration at 800 °C. The equivalent time is shown by the red solid line in Figure 8.10.

$$\Delta t_1 = \Delta t_2 \, exp \, \frac{Q^*}{R} \left(\frac{1}{T_1} - \frac{1}{T_2} \right) \tag{6.20}$$

The Matlab code for this calculation is shown in Appendix D.

Chapter 7

Austenite Grain Size

Additively manufactured stainless steels have been observed to have higher levels of retained austenite than conventionally manufactured material of the same composition. It has been suggested that this could be due to the effect of rapid solidification driving a fine austenite grain size, which in turn suppresses the martensite start temperature M_s [6, 74].

This chapter explores this concept, using a combination of melt pool modelling and experimental observation to assess the range of grain sizes that can be achieved in additively manufactured 17-4PH stainless steel. It then considers whether grain size can be exploited to control the extent of martensitic transformation, with the aim of creating a microstructurally and magnetically graded material.

7.1 Background

7.1.1 Austenite Grain Size & M_s

Prior austenite grain size is known to influence the martensite start temperature M_s for thermally-driven martensitic transformation, according to Equation 7.1 [74], where $f_{\alpha'} = 0.01$ for the first detectable fraction of martensite.

$$\Delta M_s = \frac{1}{0.253} \ln \left[\frac{1}{1.57{\times}10^{-21}\, V_\gamma} \left\{ \exp\left(-\frac{\ln(1 - f_{\alpha'})}{r_{\alpha'}} \right) - 1 \right\} + 1 \right] \tag{7.1}$$

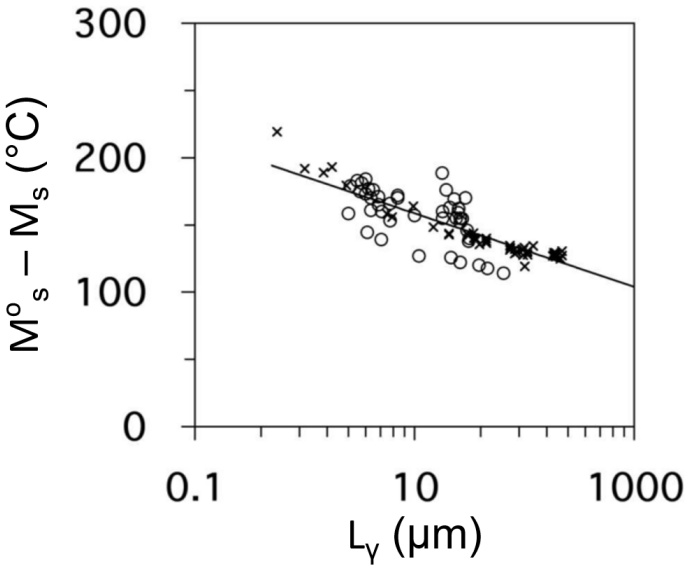

Figure 7.1: Relationship between prior austenite grain size L_γ and suppression of martensite start temperature [74].

Equation 7.1 is not simply a trend line fitted to the data shown in Figure 7.1. Instead it was derived from geometric partitioning analysis describing the relationship between the number of martensite plates per unit volume, the fraction of martensite, the aspect ratio of the martensite plates and the size of austenite compartments after being split by a martensite plate. This was combined with empirical fitting to experimental data for the number of martensite plates per unit volume as a function of temperature, and with data on the martensite start temperature as a function of austenite grain size for a range of alloys. More detail on the geometric partitioning analysis and empirical fitting can be found in [74].

This predicts the suppression against a theoretical 'large-grain' martensite start temperature M_s^0. This was defined as the point when the Gibbs free energy change $\Delta G^{\gamma\alpha}$ from austenite to ferrite of the same composition can provide the driving force for martensite nucleation. This critical value $\Delta G_C^{\gamma\alpha}$ is composition dependent, and is quoted to be 700 J mol^{-1}–1400 J mol^{-1} [74, 75, 158].

Alternatively, the martensite start temperature can be determined experimentally [135, 159], in which case the result is constrained to the exact composition used in the analysis and can be affected by both the measurement technique and the austenite grain size of the sample.

M_s was measured experimentally for a specific composition of 17-4PH, designated 'Alloy X' (Table 7.1) through a combination of dilatometry, magnetisation and high resolution neutron diffraction [135]. The dilatometry and magnetic results showed $M_s = 120\,°C$, while neutron diffraction data indicated $M_s = 130\,°C$.

Table 7.1: 17-4PH 'Alloy X' Composition [135] (wt%)

Fe	Cr	Ni	Cu	Mn	Si	Nb	C	Mo	Co	S	P
balance	15.61	4.82	3.12	0.81	0.31	0.21	0.031	0.03	0.03	0.02	0.016

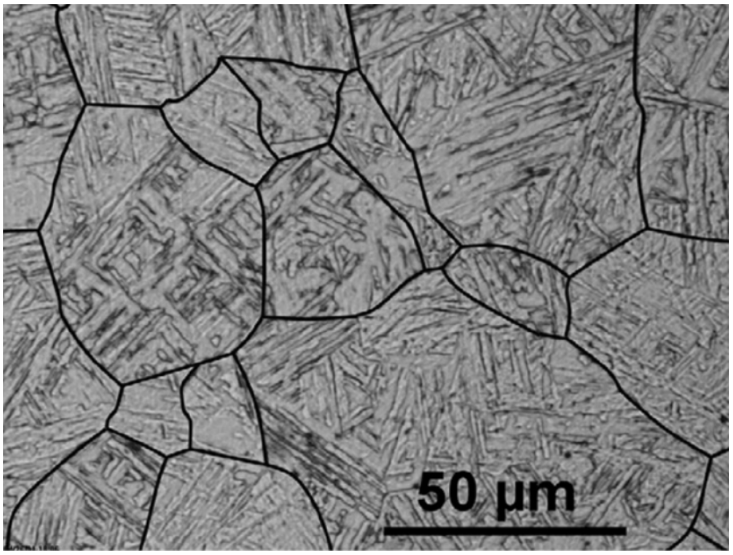

Figure 7.2: Microstructure of sample used for experimental determination of M_s in 17-4PH 'Alloy X' [135].

The grain size of the 'Alloy X' samples was quoted to be $L_\gamma = 16\,\mu m$, although the micrograph showed closer to $L_\gamma = 30\,\mu m$ (Figure 7.2). From Equation 7.1 it can be determined that this would have suppressed M_s by 145 °C–153 °C, giving $M_s^0 = (274 \pm 9)\,°C$ for the 'Alloy X' composition.

Combining the theoretical and experimental approaches, the Gibbs free energy change for 'Alloy X' on transformation from austenite to ferrite has been calculated over 100 °C–500 °C [160, 161]. From this, it was determined that the critical Gibbs free energy change corresponding to M_s^0 was $\Delta G_C^{\gamma\alpha} = (1458 \pm 52)\,J\,mol^{-1}$.

'Alloy X' meets the 17-4PH specification, but has some slight differences compared with the composition used in this work, designated 'Alloy Y' (Table 7.2) [162]. This shift

in chemistry may affect the Gibbs free energy of austenite and ferrite with respect to temperature, and the value of $\Delta G_C^{\gamma\alpha}$.

Table 7.2: 17-4PH 'Alloy Y' Powder Composition [162] (wt%)

Fe	Cr	Ni	Cu	Mn	Si	Nb	C	Mo	Co	S	P
balance	15.51	4.56	4.31	0.79	0.71	0.26	0.05	0.09	0.05	0.007	0.014

An expression exists for calculating the critical Gibbs free energy change $\Delta G_C^{\gamma\alpha}$, based on the concentration of element i expressed in atomic fraction X_i [158, 163]. This determines the Gibbs free energy change at the experimentally determined M_s rather than at the 'large-grain' M_s^0, but can be used to quantify the impact of a change in composition on $\Delta G_C^{\gamma\alpha}$.

$$\begin{aligned}\Delta G_C^{\gamma\alpha} = {} & 1010 + 4009\, X_C^{0.5} + 1879\, X_{Si}^{0.5} + 1980\, X_{Mn}^{0.5} + 172\, X_{Ni}^{0.5} \\ & + 1418\, X_{Mo}^{0.5} + 1868\, X_{Cr}^{0.5} + 1618\, X_V^{0.5} + 752\, X_{Cu}^{0.5} \\ & + 714\, X_W^{0.5} + 1653\, X_{Nb}^{0.5} + 3097\, X_N^{0.5} - 352\, X_{Co}^{0.5}\end{aligned} \tag{7.2}$$

Using Equation 7.2, the change in $\Delta G_C^{\gamma\alpha}$ due to the difference between 'Alloy X' and 'Alloy Y', was determined to be 401 J mol^{-1}, bringing $\Delta G_C^{\gamma\alpha}$ for 'Alloy Y' up to (1859±52) J mol^{-1}. Using Thermocalc to calculate $\Delta G^{\gamma\alpha}$ for 'Alloy Y', it was determined that $\Delta G_C^{\gamma\alpha}$ was reached at $M_s^0 = (188\pm8)\,^{\circ}\mathrm{C}$ (Figure 7.3).

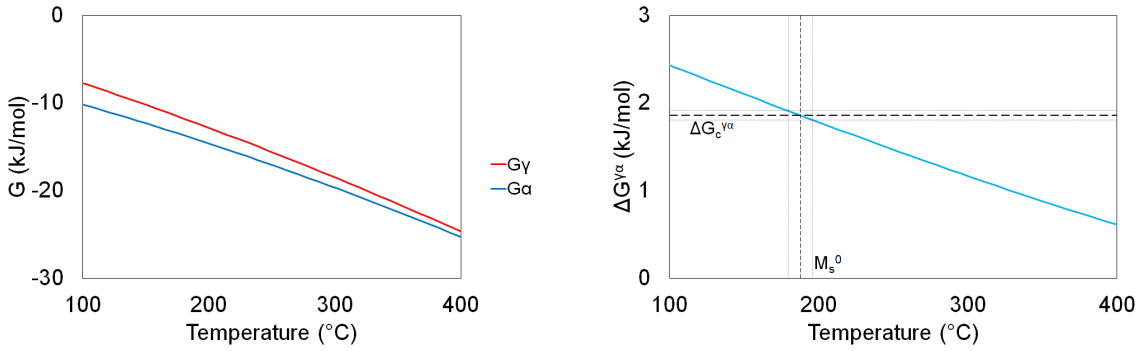

(a) **(b)**

Figure 7.3: a) Thermocalc prediction of Gibbs free energy of austenite and ferrite for 'Alloy Y' composition [160, 161]. b) Gibbs free energy change associated with transformation, and determination of M_s^0 from $\Delta G_C^{\gamma\alpha} = (1859\pm52)\,\mathrm{J\,mol^{-1}}$.

Using this value of M_s^0, Equation 7.1 was then used to predict the variation in effective M_s with grain size expected from 'Alloy Y' (Figure 7.4a). This was combined with the Koistinen-Marburger relationship (Equation 7.3) [164] to predict the volume fraction of retained austenite at room temperature, T_0 (Figure 7.4b).

$$f_\gamma = \exp[-1.1\times10^{-2}\,(M_s - T_0)] \tag{7.3}$$

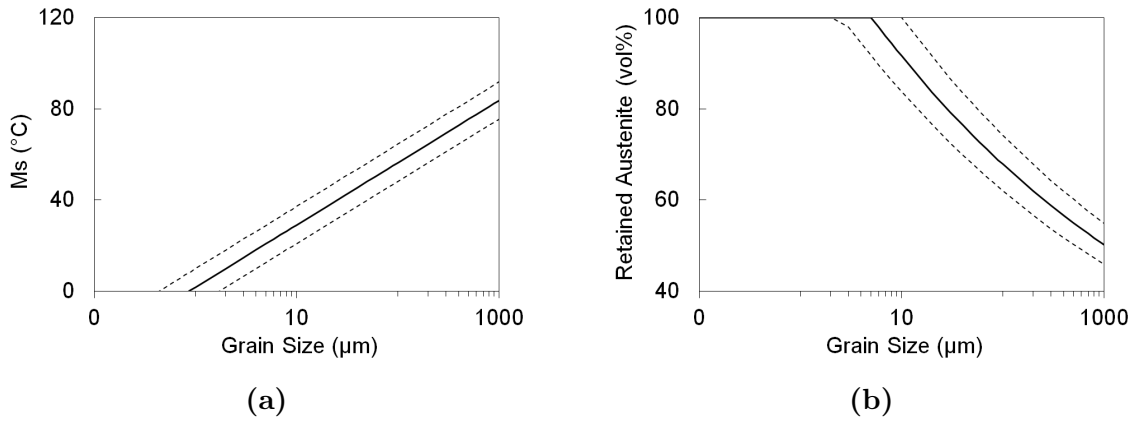

Figure 7.4: Prediction of a) effective M_s and b) volume fraction of retained austenite at room temperature as a function of austenite grain size for 'Alloy Y' composition. Dotted lines indicate error in calculation of M_s^0.

7.1.2 Relevance to SLM-built material

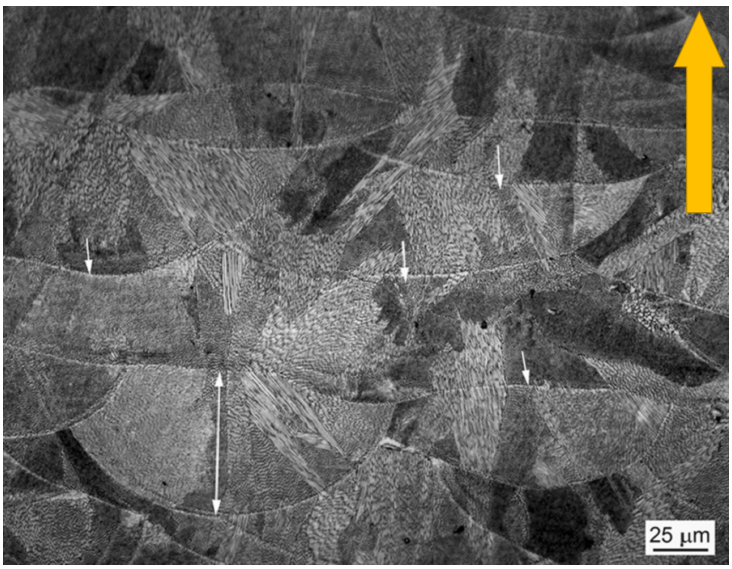

Figure 7.5: Example microstructure of SLM built 17-4PH 195W 800mm/s. Arrow indicates build direction. [6]

Selective laser melting is a rapid solidification process, with high thermal gradients driven by a very small, high temperature, melt pool surrounded by a large substrate which acts as a heat sink. At steady state, the solidification front velocity V at the back of the melt pool matches the laser travel speed ($\approx 1\,\mathrm{m\,s^{-1}}$) with thermal gradient $G \approx 10^5\,\mathrm{K\,m^{-1}}$–$10^6\,\mathrm{K\,m^{-1}}$ and cooling rate $\dot{T} \approx 10^5\,\mathrm{K\,s^{-1}}$–$10^6\,\mathrm{K\,s^{-1}}$ [44, 121, 122]. The solidification front velocity is in the range for cellular solidification [123], and cellular microstructures have been reported for SLM-built steels under a range of different building parameters (Figure 7.5) [6, 116–118].

Expressions have been developed which relate the solidification conditions to the primary dendrite arm spacing λ_1. There is an empirical relationship, reproduced here as Equation 7.4, where a and n are material dependent constants, reported to be $a = 60 - 100\,\mathrm{m\,s\,K^{-1}}$ and $n = 0.2 - 0.5$ [124–126].

$$\lambda_1 = a\,\dot{T}^{-n} \tag{7.4}$$

Alternatively, there is a theoretical relationship, reproduced here as Equation 7.5 which reflects a stronger dependency on thermal gradient than front velocity [122]. The values for the material parameters in Equation 7.5 are included in Appendix A.

$$\lambda_1 = 4.3\, G^{-1/2} \left\{ \frac{\Delta T_0\, D\, \Gamma}{\kappa\, V} \right\}^{1/4} \tag{7.5}$$

For the solidification conditions described above, the empirical approach gives λ_1 in the range 1 µm–5 µm, while the theoretical approach predicts λ_1 of 2 µm–9 µm. These are both slightly larger than the reported cell diameters from literature, so the thermal gradient may actually be higher than $10^5\,\mathrm{K\,s^{-1}}$, however these expressions can be used as an upper limit for the predicted cell diameter. The thermal gradient and front velocity will also vary in magnitude and direction around the melt pool, so the critical values may not be at the surface, but lower down where thermal gradient is larger and front velocity smaller.

The microstructures reported in the literature have austenite grains of 10 µm–100 µm containing solidification cells around 1 µm diameter (Figure 7.5). Depending on composition, Figure 7.4b predicts that the main grains alone could be sufficient to suppress much of the martensitic transformation, giving between 65 vol% and 90 vol% retained austenite. However, there is evidence that the cell boundaries may also play a role.

Firstly, martensite growth has been observed to stop at sub-grain boundaries in ausformed material [104]. These sub-grain boundaries have high dislocation density with minimal lattice mismatch because both sides were originally from the same grain. This is a similar structure to the solidification cells in SLM-built material, where each cell has a similar orientation to the adjacent cells but they are separated by dense dislocation walls [116, 119].

More specifically, mechanical test results for SLM-built 316L showed yield strength correlating better with cell size rather than grain size (Figure 7.6a) [165]. TEM of a deformed sample showed minimal misorientation between adjacent cells ($< 1.5°$), so it was suggested that the cell boundaries were constructed from geometrically necessary dislocations (Figure 7.6b). These are associated with a strong dislocation trapping and retention mechanism, consistent with dislocation trapping observed by in-situ XRD.

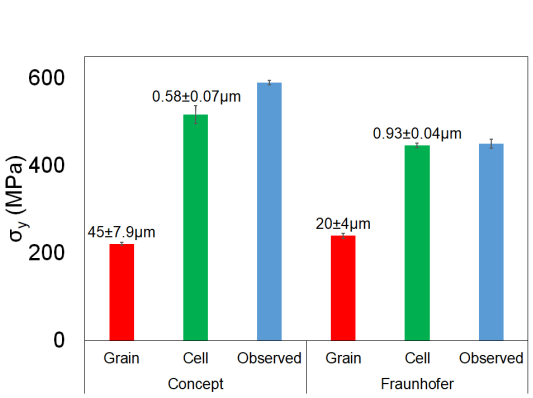

(a)

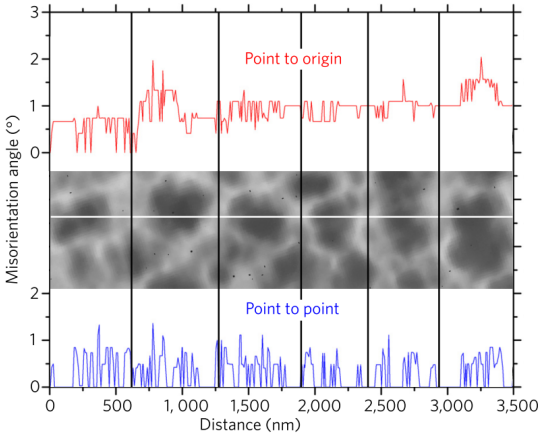

(b)

Figure 7.6: a) Hall-Petch prediction of yield stress using grain size and cell size respectively, compared with experimental observation for 316L samples manufactured by either Concept or Fraunhofer SLM machines; annotation shows measured grain and cell sizes. b) Misorientation angle variation across multiple cells after 3 % deformation. [165]

This indicates that the cell boundaries may be capable of preventing movement of the glissile $\gamma - \alpha'$ interface in a similar manner to grain boundaries [105]. If is the case, given their size, they would drive more significant suppression of M_s than the grain boundaries, causing a higher proportion of austenite to be retained to room temperature.

The aim of this work is to achieve a magnetically and microstructurally graded material, where the paramagnetic areas must be fully austenitic and ferromagnetic areas must be at least partially martensitic. For the current composition 'Alloy Y', a fully austenitic structure is predicted to correspond to sizes below 5 µm (Figure 7.4b). Assuming cell boundaries are capable of suppressing martensite, then the 1 µm cell sizes from normal SLM cooling rates would be expected to give fully austenitic material suitable for the paramagnetic regions, but it would be necessary to drive much slower cooling rates to allow the cells to coarsen and enable some martensitic transformation in the ferromagnetic regions.

It is noted that the literature reports 17-4PH built by SLM under argon to have between 28 wt% and 90 wt% martensite [5, 6]. This suggests that either the cell boundaries are not capable of suppressing martensite, there is a secondary mechanism driving transformation, or the results were affected by unintended transformation post-build which has influenced the XRD analysis. This apparent discrepancy will be reviewed later in this chapter.

7.2 Melt Pool Modelling

The melt pool model developed in Chapter 6 has been used to predict the variation in cooling rate, and therefore solidification cell diameter, that can be achieved within the capabilities of the Renishaw SLM125. The specific version used was the 'Hatches' model, with fixed 45 % absorption efficiency.

7.2.1 Thermal Gradient & Front Velocity

The model has been used to calculate the thermal gradient G and cooling rate $\dot{T}$ from the temperature field behind the beam using isotherms 5 °C either side of the liquidus temperature. This was calculated at the back of the melt pool, on the surface, directly behind the beam where the solidification front velocity V is equal to beam velocity. It was also calculated at the base of the melt pool where the solidification front velocity is vertical, and much slower, but the thermal gradient is higher.

The laser on the Renishaw SLM125 laser can deliver between 30 W and 200 W power, however it is a pulsed laser so this is factored down by the duty cycle (Equation 7.6), where τ is the exposure time, *point* is the point spacing and c is the travel speed between points.

$$Q_{eff} = Q \left\{ \frac{\tau}{\tau + (point/c)} \right\} \tag{7.6}$$

The power ramp-up at the start of each exposure has a duration of approximately 13 µs, so it is undesirable to use exposures significantly shorter than this as they will not reach maximum power during the exposure time [149].

The model was used to investigate sensitivity to build parameters from 200 W power at 200 µs exposure and 10 µm point spacing, down to 100 W power at at 20 µs exposure and 50 µm point spacing (Figure 7.7).

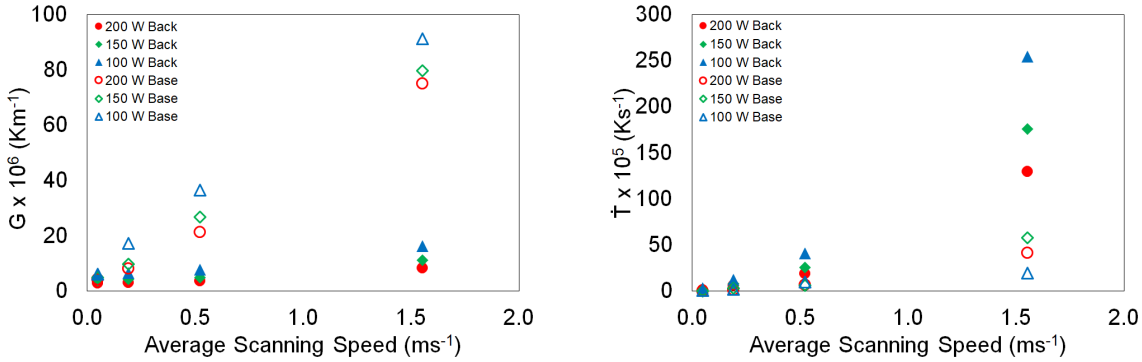

(a) Thermal Gradient **(b)** Cooling Rate

Figure 7.7: Predicted sensitivity of cooling rate and thermal gradient to build parameters. Closed symbols indicate values at the back of the melt pool. Open symbols indicate values at the base of the melt pool.

As expected, the thermal gradient at the back of the melt pool was lower than that at the base of the melt pool, with a corresponding effect on cooling rate. Increased power caused the melt pool volume to increase, reducing the thermal gradient and cooling rate, while increased scanning speed (shorter exposure, larger point spacing) caused the melt pool volume to reduce, increasing thermal gradient and cooling rate.

At the back of the melt pool, the solidification front velocity varied between $0.05\,\mathrm{m\,s^{-1}}$ to $1.5\,\mathrm{m\,s^{-1}}$; this is wider than the range normally quoted for SLM because the process has been pushed to extremes [44, 122]. The predicted thermal gradient at this position varied between $3.0{\times}10^{6}\,\mathrm{K\,m^{-1}}$ to $1.6{\times}10^{7}\,\mathrm{K\,m^{-1}}$, with solidification rates of $1.5{\times}10^{5}\,\mathrm{K\,s^{-1}}$ to $2.5{\times}10^{7}\,\mathrm{K\,s^{-1}}$, which are at the upper end of the range quoted earlier.

7.2.2 Primary Dendrite Arm Spacing

Equation 7.4 (empirical) and Equation 7.5 (theoretical) were used to calculate the primary dendrite arm spacing λ_1 for each condition (Figure 7.8). For the highest energy density they predicted λ_1 up to $3\,\mu\mathrm{m}$ at the back of the melt pool, and up to $4\,\mu\mathrm{m}$ at the base. At lower energy density the predicted λ_1 was smaller, driven by the change in thermal gradient. The theoretical expression generally predicted a slightly coarser microstructure than the empirical relationship ($\approx 50\,\%$ increase), although the empirical has a wide margin of error due to uncertainty in the values of a and n.

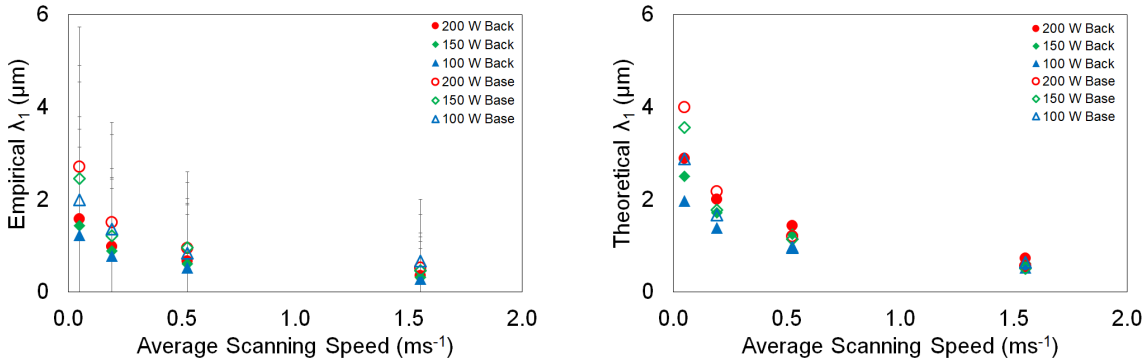

(a) λ_1 Empirical **(b)** λ_1 Theoretical

Figure 7.8: Predicted primary dendrite arm spacing. a) Empirical, error bars show uncertainty in a and n. b) Theoretical. Closed symbols indicate values at the back of the melt pool. Open symbols indicate values at the base of the melt pool.

7.2.3 Modelling Summary

The results from the melt pool model support the observations from the literature, that the solidification conditions associated with SLM are all consistent with cellular growth, and with cell sizes of less than 5 µm.

Assuming the cell boundaries are capable of suppressing thermally-activated martensite, even material built with a 5 µm cell diameter would have > 98 vol% retained austenite. This might show slight ferromagnetic behaviour, but the energy density required to achieve this cooling rate would be expected to give very poor build quality due to porosity from keyhole melting and high levels of melt pool turbulence.

Material built at lower energy density would have correspondingly higher solidification rates, smaller cell sizes and higher levels of retained austenite.

7.3 Experimental

7.3.1 Method

To test the model prediction, a series of experiments were conducted on the Renishaw SLM125 using 17-4PH powder. These builds were tailored to have high energy density,

producing larger melt pools with slower solidification rates, with the aim of achieving coarser solidification cells. The power, exposure time and layer thickness were kept constant, while the point spacing and hatch spacing were varied (Figure 7.9a). These 'Square Series' builds had equal point and hatch spacing, maintaining a square array of melt pools (Figure 7.9b).

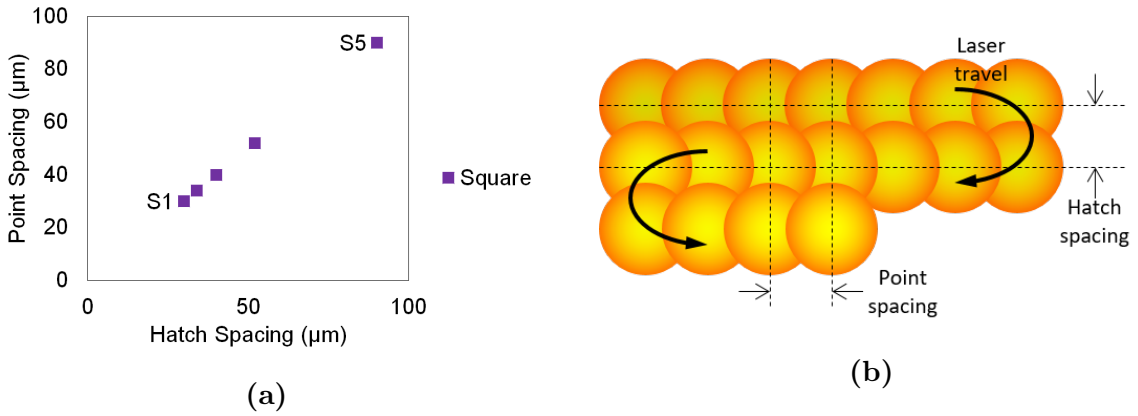

Figure 7.9: a) Point and hatch spacings used for Square Series. b) Schematic showing point and hatch spacing definitions.

Predictions of cooling rate were initially made using a fixed absorptivity of 45 %. This showed a trend for cooling rate to reduce with increasing energy density, while thermal gradient increased (Figure 7.10).

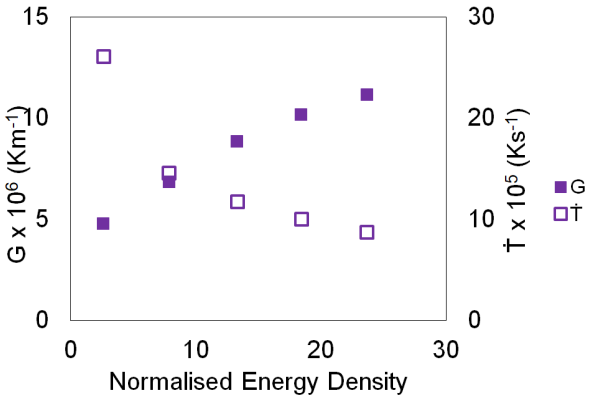

Figure 7.10: Predicted cooling rate and thermal gradient for Square Series using fixed 45 % absorptivity

In the earlier chapters on development of the model, it was identified that melt pool depth from the Square Series builds was constant across the range of energy density,

rather than shallower melt pools at lower energy density (full microstructural data will be shown later in this chapter). This was accompanied by a change in surface roughness and reflectivity. It was found that a variable absorptivity was necessary to replicate the experimentally observed melt pool depths. This variable absorptivity was used to recalculate the predicted cooling rate, thermal gradient and the normalised energy density (Table 7.3 and Figure 7.11).

Table 7.3: 17-4PH Square Series Build Parameters

SampleID	Power W	Exposure µs	Point Spacing µm	V $mm\,s^{-1}$	Hatch µm	Absorptivity	E_0^*
S1	200	100	30	280	30	0.45	23.7
S2	200	100	34	314	34	0.48	19.7
S3	200	100	40	364	40	0.55	16.3
S4	200	100	52	461	52	0.65	11.4
S5	200	100	90	738	90	0.90	5.3

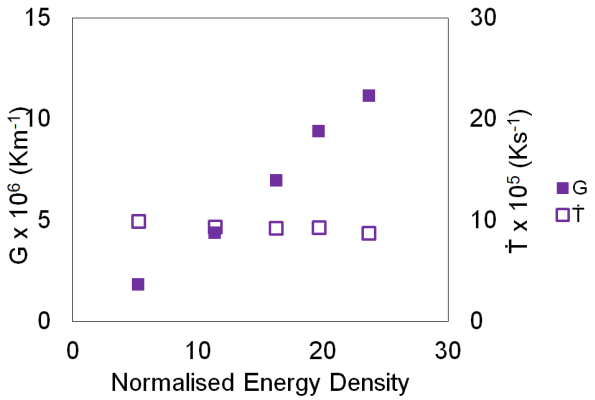

Figure 7.11: Predicted cooling rate and thermal gradient for Square Series using variable absorptivity as per Table 7.3

.

The effect of the variable absorptivity was to make the cooling rate nearly constant across all conditions, while the thermal gradient actually reduced with reducing energy density due to the increase in solidification front velocity V. Putting these solidification conditions into Equation 7.5, gives a predicted range of solidification cell size of 1.8 µm to 2.2 µm.

These parameters were used to build a range of samples, all utilising the meander scan strategy with 67° rotation between layers, a 40 µm layer thickness and under a protective argon atmosphere.

- Cylinders, 8 mm in diameter and 10 mm height, built for each condition individually. The rough top surface (∼1 mm) of the cylinders was removed and discarded, then 2 mm thick discs were cut for magnetic characterisation by VSM, and the remaining material was used for XRD.
- Fully graded cuboids made from 4 mm thicknesses of each of the Square series conditions, built simultaneously and graded perpendicular to the build direction. These were sectioned vertically (build direction), and used for porosity and microstructural assessment.
- Cuboids, 10 mm square x 14 mm height, of each of the S1 and S5 conditions individually which were sectioned vertically (build direction) to expose the internal surface.

Immediately after the build was removed from the machine, the samples were checked for magnetic response using a small hand-held magnet. This qualitatively identified that the higher energy density (S1 & S2) material showed a definite magnetic response, and the lower energy density material (S3-S5) showed no magnetic response. This was done to record the magnetic behaviour before the samples were removed from the baseplate, in case the act of removal was sufficient to cause deformation-induced martensite.

Samples were then removed from the baseplate and sectioned by electro-discharge machining (EDM). This is a low-deformation technique, chosen to minimise the risk of unintended martensitic transformation.

7.3.2 Surface Roughness

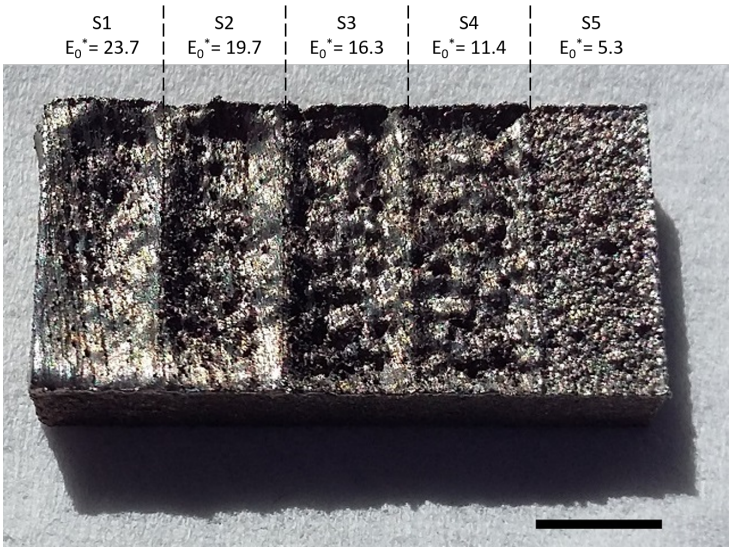

Figure 7.12: Fully graded cuboid before sectioning. High E_0^* (S1) at left hand end, low E_0^* (S5) at right hand end. Scale bar is 4 mm.

Figure 7.12 shows the top surface (build plane) of one of the fully graded cuboids, which were made from 4 mm thicknesses of each of the Square series conditions. The top surface of the high energy density (S1) end was smoother and more reflective, with more significant swelling at the corners. The top surface of the low energy density (S5) end was rougher, although with less swelling. The intermediate conditions followed a transition between these two extremes.

7.3.3 Vibrating Sample Magnetometer (VSM)

The primary method of magnetic characterisation used was VSM, which is a bulk technique, although the maximum sample size is very small. The samples did not require any surface preparation, giving confidence that the reported fraction martensite was representative of the as-built condition.

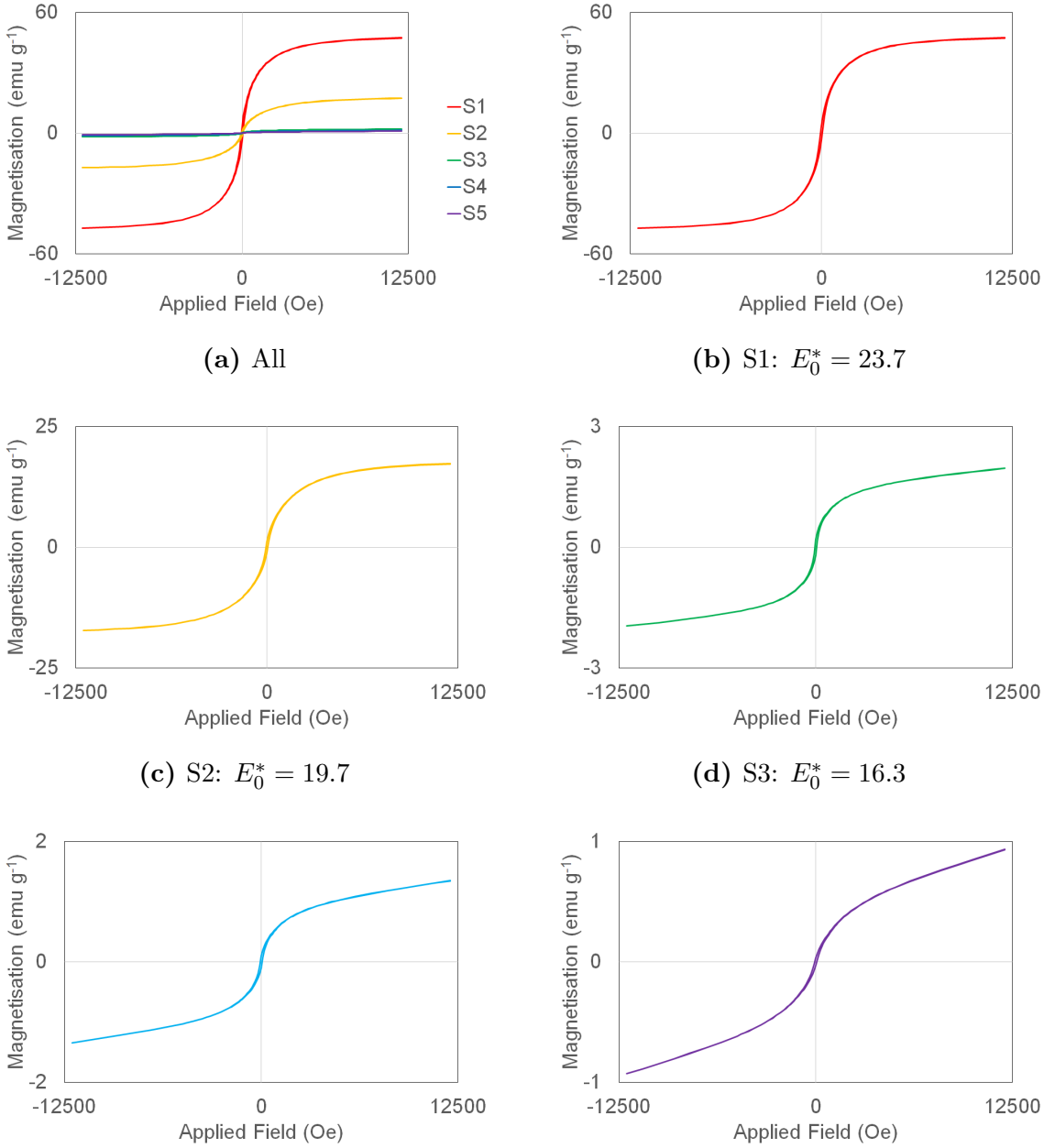

(a) All

(b) S1: $E_0^* = 23.7$

(c) S2: $E_0^* = 19.7$

(d) S3: $E_0^* = 16.3$

(e) S4: $E_0^* = 11.4$

(f) S5: $E_0^* = 5.3$

Figure 7.13: Hysteresis loops generated by VSM for 17-4PH Square Series. The y-axis scale has been adjusted to give maximum clarity for each condition.

The results showed a clear change in magnetic properties across the range of energy density (Figure 7.13), corresponding to the qualitative assessment carried out while the samples were still attached to the baseplate.

The highest E_0^* sample (S1) showed a strongly ferromagnetic response, reaching saturation ($47\,\mathrm{emu\,g^{-1}}$) at 10 000 Oe applied field.

In contrast, the lowest E_0^* (S5) sample showed a primarily paramagnetic response, with magnetisation rising proportional to the applied field but at a much slower rate than for the ferromagnetic material. Paramagnetic materials will eventually saturate, but this was not achieved within the measurement range. The S5 sample did show a small ferromagnetic response at very low applied field, shown by the slight 's-bend' between $-1000\,\text{Oe}$ and $1000\,\text{Oe}$, indicating a very small quantity of ferromagnetic material was present.

Intermediate conditions showed a trend of behaviour between these two extremes.

The hysteresis loops were used to calculate the bulk saturation magnetisation, m_s, which is a structure independent characteristic unaffected by porosity or dislocations [128].

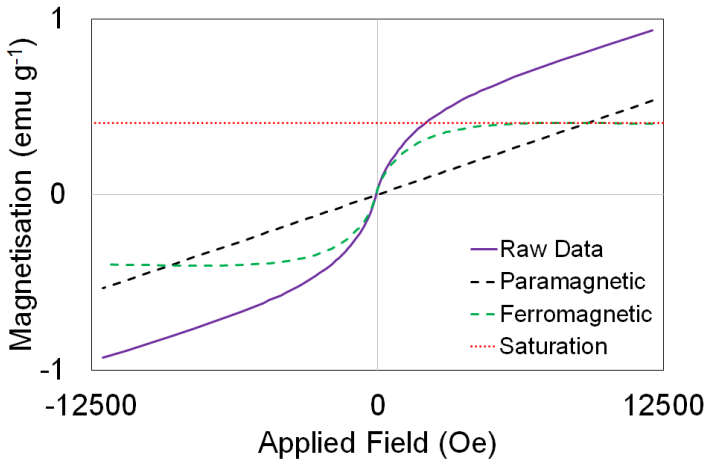

Figure 7.14: Separating paramagnetic and ferromagnetic contributions to hysteresis for low E_0^* (S5) data. The raw data (purple solid line) includes both paramagnetic (black dashed line) and ferromagnetic (green dashed line) contributions. With the paramagnetic contribution removed, the saturation magnetisation (red dotted line) of the ferromagnetic contribution can be determined.

Assuming that all samples contain some paramagnetic austenite, it was necessary to remove the paramagnetic contribution before reading off the saturation magnetisation (Figure 7.14). The paramagnetic response is a straight line until very high applied fields where it will eventually saturate. The S5 data was used to calculate the straight line paramagnetic response across the range of applied field used for this analysis. This was then subtracted from the raw data to leave the ferromagnetic response, from which the maximum magnetisation achieved was taken as the saturation magnetisation.

Taking the saturation magnetisation of fully martensitic 17-4PH to be $m_{s\alpha'} = 162.4\,\text{emu}\,\text{g}^{-1}$

[138], the phase fraction of martensite in each sample was calculated from the bulk saturation magnetisation (Figure 7.15). This illustrated that the higher E_0^* samples had a higher phase fraction of martensite, although there was no clear correlation with cooling rate.

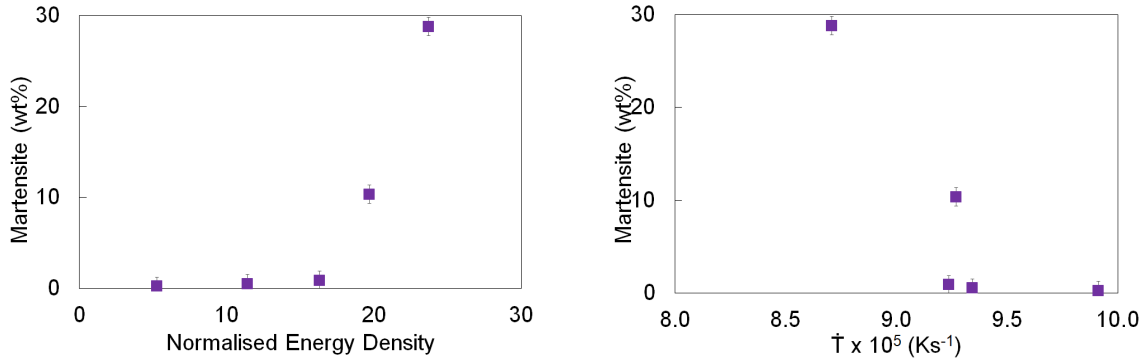

(a) **(b)**

Figure 7.15: a) Phase fraction martensite against E_0^*. b) Phase fraction martensite against $\dot{T}$.

The hysteresis loops were also used to extract information about the soft magnetic properties of the material. All samples had coercivity of < 100 Oe, although accurate values were difficult to obtain given the step size between test points through this region (Figure 7.16a).

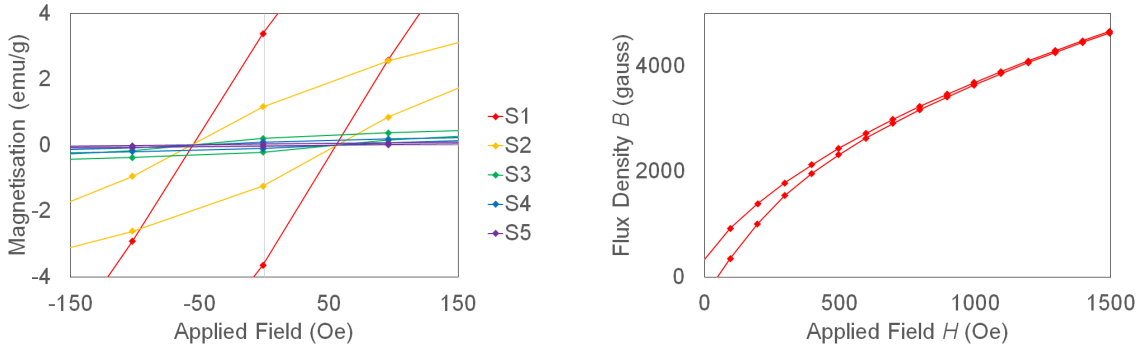

(a) **(b)**

Figure 7.16: a) Coercivity of Square Series samples. b)B-H curve of high energy density (S1) sample.

The permeability of the high energy density (S1) sample was estimated from the B-H curve for the ferromagnetic material only; after the paramagnetic contribution had been removed (Figure 7.16b), using Equations 7.7 and 7.8. This showed the permeability to

reach a maximum of around 10, although a more accurate value might be obtained with more data points at low applied field and starting measurement from an applied field of zero.

$$B = H + 4\pi M \tag{7.7}$$

$$\mu = \frac{B}{H} \tag{7.8}$$

This shows that while the material does display 'soft' magnetic behaviour, it has both higher coercivity and lower permeability than common electrical steels used for rotor applications, making it less efficient at easily magnetising and de-magnetising. This is not unexpected given that 17-4PH was selected for its solid-state transformation properties rather than its magnetic properties.

7.3.4 X-Ray Diffraction (XRD)

Samples from lower down the individual cylinders were used for XRD analysis to confirm phase identification (Figure 7.17). The scans were carried out from 40° to 100°, with a step size of 0.039° and 1120 s per step. The beam was not monochromatic, so the data includes reflections from both Cu$K\alpha_1$ and Cu$K\alpha_2$.

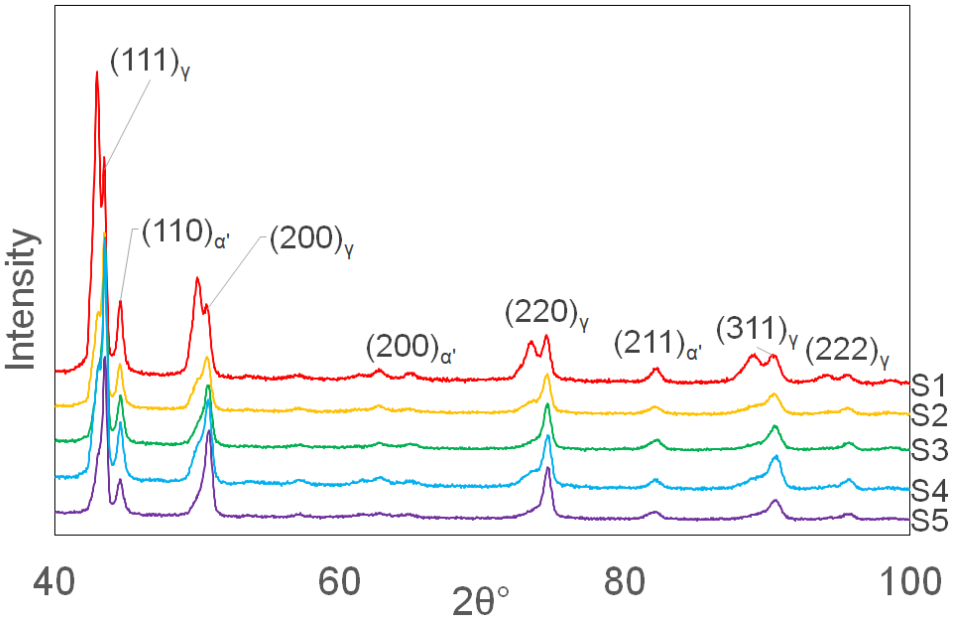

Figure 7.17: XRD for 17-4PH Square Series

The data showed clear peaks for FCC γ-austenite and BCC α'-martensite. In low-carbon alloys martensite and ferrite have very similar lattice structures, and cannot be distinguished by XRD, but α'-martensite is more likely than α-ferrite in 17-4PH. The intensity of the martensite peaks was higher for the high energy density samples, indicating an increased phase fraction α'-martensite which correlated with the VSM observations. The data showed crystallographic texture, so it was not suitable for quantitative phase analysis using Rietveld refinement.

Unexpectedly, the data showed a split in the austenite peaks, most clearly visible at higher 2θ, which was present across all five samples across all austenite peaks. The beam was not monochromated, however this split could not be explained by reflections from $K_{\alpha 1} = 1.5406\,\text{Å}$ and $K_{\alpha 2} = 1.5444\,\text{Å}$ wavelengths. Firstly, assuming an austenite lattice parameter of 3.60 Å, the (111) peak from $K_{\alpha 1}$ would be at 43.51° and the peak from $K_{\alpha 2}$ at 43.62°. This shift is only 0.11°, which is much smaller than the 0.53° shift observed in the data. Secondly, the α'-martensite only shows single peaks, yet it would have been equally affected by the use of both wavelengths.

This suggests there were two different austenite phases present with slightly different lattice parameters. Further scans were carried out across the range of each pair of austenite peaks individually, using 0.039° step size and 5000 s per step. The secondary austenite phase will be discussed in more detail in a later chapter.

In addition to the scans of EDM-cut material, shown in Figure 7.17, sample from the highest and lowest energy density conditions were scanned in the EDM-cut condition through 40° to 100°, then ground to '600-grit' finish and re-scanned. The results showed that even this level of sample preparation greatly increased the intensity of the martensite peaks at the expense of the lower-2θ austenite peaks, although there was little change in the intensity of the higher-2θ austenite peaks (Figure 7.18).

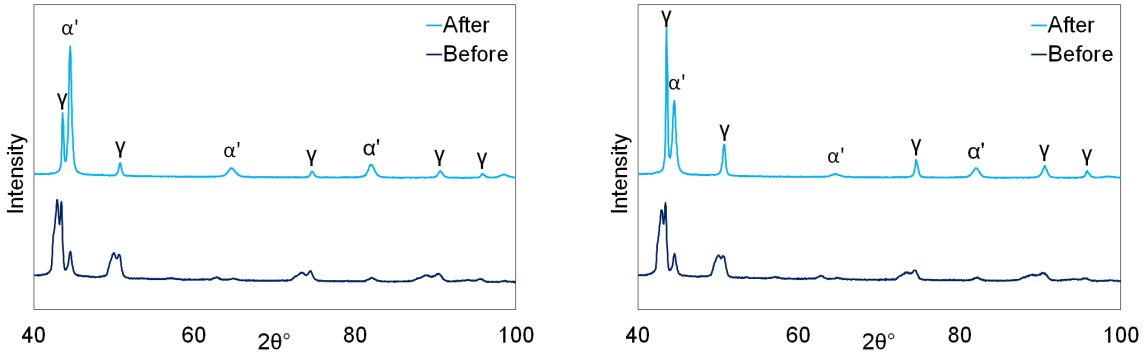

(a) S1: $E_0^* = 23.7$ **(b)** S5: $E_0^* = 5.3$

Figure 7.18: XRD for 17-4PH before and after manual polishing, showing change in phase fraction of γ_1, γ_2 and α'.

This confirms that sample preparation can increase the measured phase fraction of martensite in additively manufactured 17-4PH, meaning that quantitative phase analysis taken from a polished sample is not necessarily representative of the as-built condition. This may partially contribute to the increased phase fraction of martensite reported in the literature compared with that expected from an analysis of the grain/cell sizes.

This also shows that the austenite phase at lower 2θ has completely disappeared after sample preparation, even though it was comparable with higher 2θ austenite phase initially, which may explain why it has not been reported previously.

7.3.5 Microscopy

The samples prepared for optical microscopy were vertical sections (build direction) through a fully graded cuboid, built from 4 mm thicknesses of each of the Square series conditions in order of energy density. The samples were mounted and polished, then either electro-etched with oxalic acid or conventionally etched with Kallings #2 reagent.

7.3.5.1 Optical - Electroetched

The composite image for the whole sample is shown in Figure 7.19, with detail images for highest and lowest energy density shown in Figure 7.20.

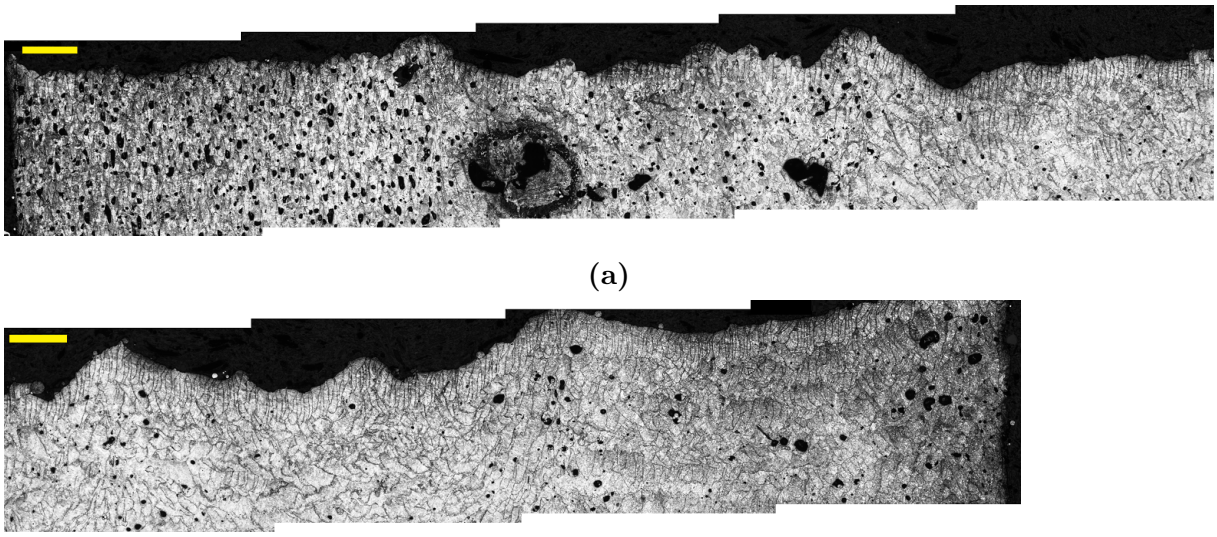

(a)

(b)

Figure 7.19: Composite image of electro-etched sample showing melt pool definition, from low E_0^* (S5) at left hand end of (a) to high E_0^* (S1) at right hand end of (b). Scale bar is 500 µm.

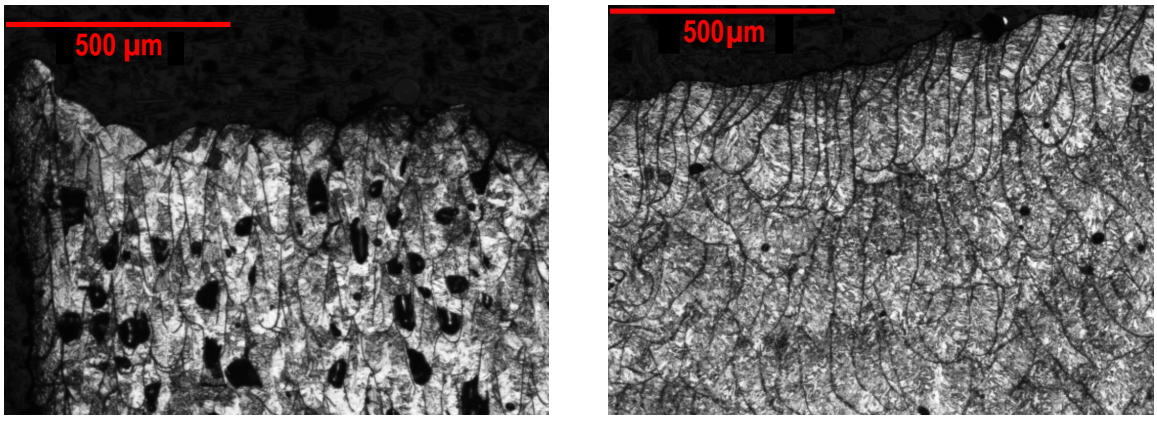

(a) **(b)**

Figure 7.20: Individual images of electro-etched structure for a) low E_0^* (S5) and b) high E_0^* (S1) conditions. Scale bar is 500 µm.

The melt pool depth was fairly consistent across the five build conditions, in the range 200 µm–250 µm. There was a change in melt pool shape from a narrow, tapering profile

at the low energy density end to a classic, wide keyhole profile at the high energy density end.

There was good bonding between the different conditions, with no apparent cracking along the interfaces. The top surface was very uneven, particularly for the higher energy density conditions in Figure 7.19b, possibly caused by the high energy input resulting in more disturbance of the powder layer and material loss to evaporation.

As predicted by the model, all conditions showed keyhole melting and there was significant keyhole porosity, particularly in the lowest energy density (S5) sample.

7.3.5.2 Scanning Electron Microscopy (SEM) - Kallings #2

Low magnification SEM was used to assess the size of the larger main grains, which were identified by regions of cells with identical growth direction. Figure 7.21 and Figure 7.22 show this for the highest (S1) and lowest (S5) energy density conditions respectively. Representative example grains have been outlined in yellow on each of the images, and melt pool boundaries outlined in red. These main grains were comparable in size with those from literature, between 10 µm to 30 µm across, with no observable difference in grain size between the two conditions.

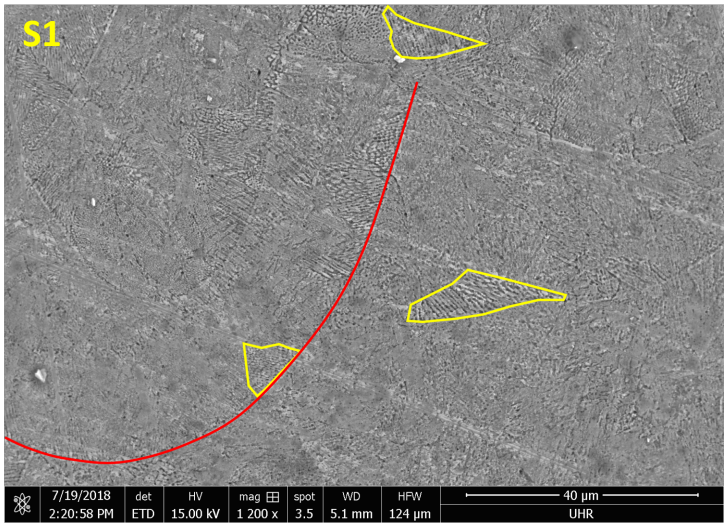

Figure 7.21: Lower magnification SEM for S1 sample $E_0^* = 23.7$, showing main grains and melt pool outlines. Scale bar 40 µm.

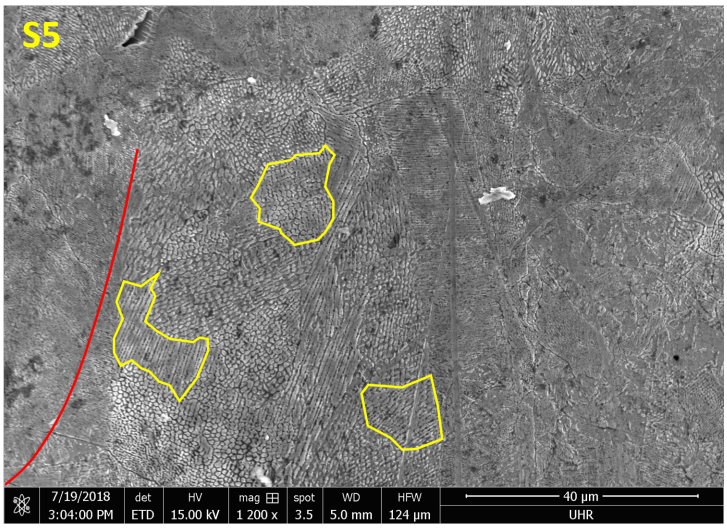

Figure 7.22: Lower magnification SEM for S5 sample $E_0^* = 5.3$, showing main grains and melt pool outlines. Scale bar 40 µm.

There was some variation between different regions within the samples, illustrated in Figure 7.23). The cell size within a grain was generally constant, but the cell size varied between grains. The grains with finer cells tended to be located near the base of the melt pools, where the cooling rate is expected to be highest.

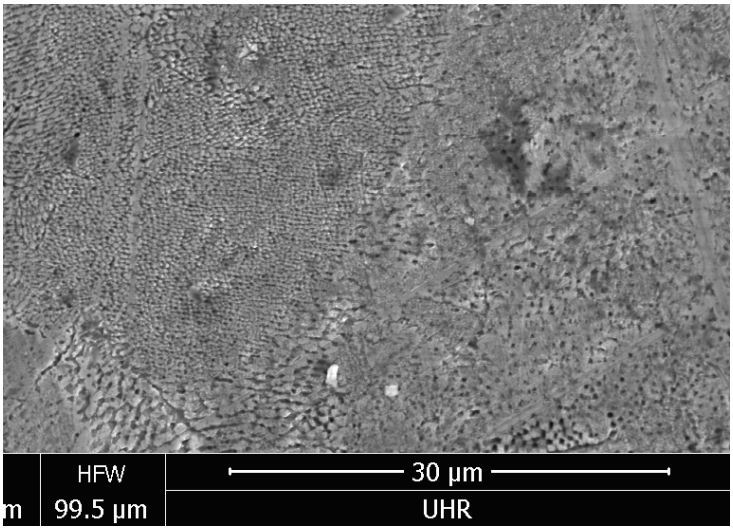

Figure 7.23: Variation in cell size within S4 sample, with finer cells inside the melt pool and coarser cells around the outside.

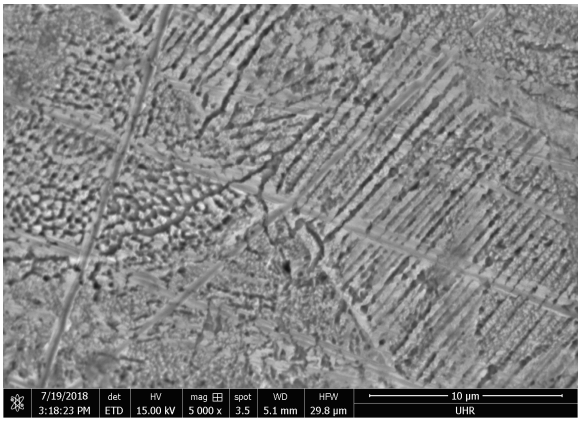

(a) S1 sample $E_0^* = 23.7$

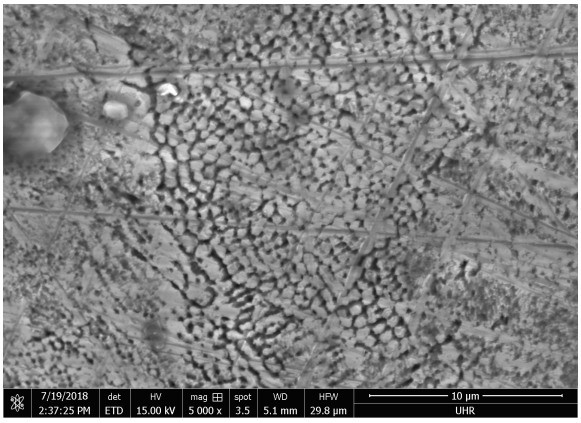

(b) S2 sample $E_0^* = 19.7$

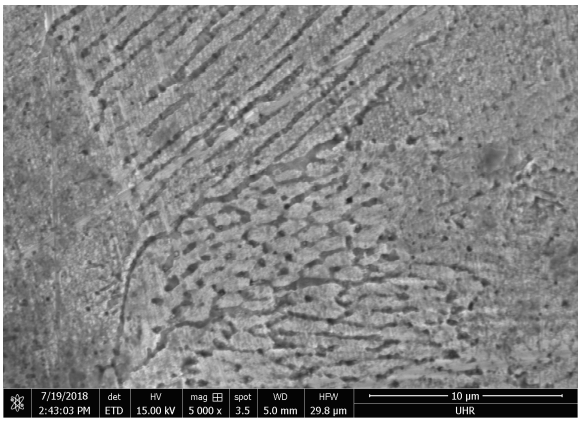

(c) S3 sample $E_0^* = 16.3$

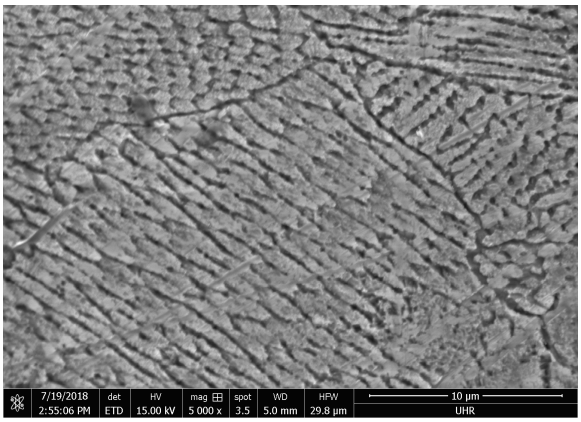

(d) S4 sample $E_0^* = 11.4$

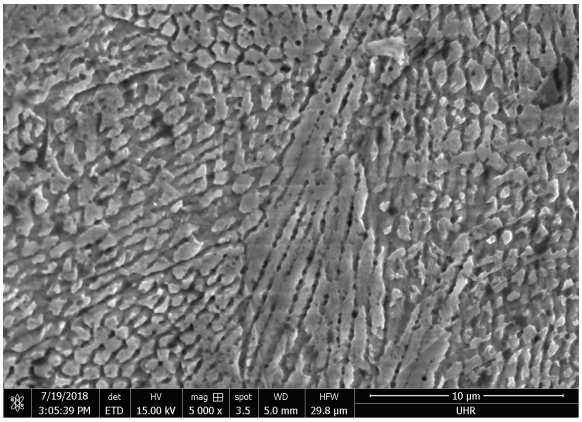

(e) S5 sample $E_0^* = 5.3$

Figure 7.24: High magnification SEM. Scale bar 10 µm

High magnification SEM confirmed that all samples retained a cellular structure after cooling to room temperature (Figure 7.24). The cell diameters were consistent across all five samples with no apparent trends in cell diameter with energy density. This is expected given that all conditions were predicted to have comparable solidification conditions.

7.3.5.3 Porosity

All samples showed significant porosity, both by image analysis and by relative density measurement (Figure 7.25). The majority of the pores were attributed to keyhole melting, being spherical and located near the base of the melt pools (Figure 7.20). However, the lowest energy density condition also showed a number of more irregularly shaped pores, potentially indicating some lack-of-fusion. While this level of porosity indicates an issue for overall build quality, it would not impact the measurement of saturation magnetisation (in emu g^{-1}) or determination of martensite phase fraction.

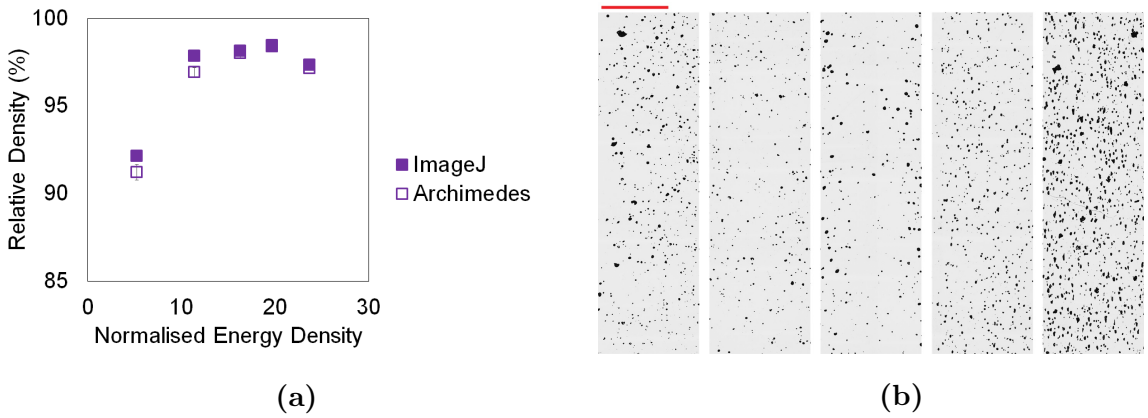

Figure 7.25: Porosity analysis of Square Series. a) Determination of relative density by Archimedes density balance and ImageJ image analysis. b) Optical microscopy showing shape, size and distribution of pores from high E_0^* (S1) at left-hand end to low E_0^* (S5) at right-hand end; scale bar is 2 mm.

7.4 Discussion

It has been observed that stainless steels built by Selective Laser Melting generally exhibit hierarchical microstructures consisting of large grains (10 µm to 100 µm) containing solidification cells around 1 µm in diameter. It has also been reported that martensitic steels such as 17-4PH have a higher level of retained austenite when built by SLM than when manufactured by conventional techniques, and that this may be due to the fine austenite grain size suppressing the martensite start temperature.

This aspect of the work investigated whether the increase in retained austenite could reasonably be explained by the high cooling rates associated with SLM. It then considered

whether it would be possible to select appropriate build parameters to modify the cooling rate and drive controlled variation in the relative proportions of austenite and martensite to achieve a microstructurally graded material.

Reviewing the literature indicated that the grains alone would be small enough to increase the proportion of retained austenite up to 90 vol%. Assuming the solidification cell boundaries were also capable of suppressing martensitic transformation, then cells $< 5\,\mu m$ would be small enough to suppress all thermally-activated martensitic transformation and give a fully paramagnetic, austenitic structure.

Melt pool modelling predicted that for the range of operating conditions available on the Renishaw SLM125 the solidification rates would be $1.4\times10^{5}\,K\,s^{-1}$ to $2.5\times10^{7}\,K\,s^{-1}$, all consistent with cellular solidification. Even at the highest energy density with the slowest solidification, the maximum predicted cell size was 4 µm, which would result in ≈ 100 vol% retained austenite.

This conflicted with literature showing as low as 8 % retained austenite for SLM-built 17-4PH with cell sizes of 0.5 µm. To investigate this discrepancy, a set of trials were conducted using the Renishaw SLM125. The trials were designed to have high energy density (E_0^*) and slow solidification rates.

SEM and optical microscopy showed all samples to have the expected hierarchical microstructure: grains of 10 µm–30 µm containing solidification cells 0.5 µm–1 µm in diameter, although some areas were identified with even finer cells. There were no apparent trends in grain or cell size with E_0^*. This is in good agreement with the model for these conditions, which predicted cell diameters of 1.8 µm–2.2 µm across the experimental range of energy density. This was based on the thermal gradient across the liquidus at the back of the melt pool, combined with the theoretical relationship between G, V and λ_1 (Equation 7.5).

The magnetic (VSM) results showed a trend from a paramagnetic response at low E_0^* (S5) to a ferromagnetic response at high E_0^* (S1), indicating that there had been a change in the magnetic behaviour resulting from the change in build parameters. XRD confirmed that the ferromagnetic phase was α'-martensite and the paramagnetic phase was γ-austenite, although the austenite actually appeared as two separate phases with slightly different lattice parameters.

Considering first the low energy density (S5) condition, its fully austenitic structure re-

quired thermally-activated martensitic transformation to have been completely suppressed during cooling to room temperature. The grains would have partially suppressed M_s, but not necessarily below room temperature, depending on error in the calculation of the 'large-grain' M_s^0 and in the relationship between grain size and M_s suppression (Equation 7.1). This supports the view that solidification cell boundaries are also capable of contributing to suppressing M_s, giving the fully austenitic structure.

Looking then at the high energy density (S1) condition, this had a nearly identical microstructure but with up to 28 wt% martensite. This martensite cannot be the unintended result of sample preparation because all VSM samples were prepared using identical low-deformation techniques. The similarity in microstructure indicated that thermally-activated martensite must have been equally suppressed on cooling from solidification, so there must have been a secondary mechanism driving transformation.

In summary, it was confirmed that the high cooling rates associated with selective laser melting drive cellular solidification with grain and cell sizes that are capable of significantly suppressing the thermally activated martensite start temperature. For the specific composition of 17-4PH used ('Alloy Y') this was predicted to result in a fully austenitic material at room temperature, which was confirmed experimentally. However, at very high energy density, experimental samples showed some martensite present in spite of the grain/cell size effect, indicating a secondary mechanism was driving transformation.

This secondary mechanism may have also been a factor in samples reported in the literature, potentially explaining the variation in phase fraction reported from SLM-built 17-4PH samples with comparable cellular microstructures. Additionally, XRD was used to confirm that even minor surface preparation caused significant deformation-driven martensitic transformation, which may have also have been an issue for some of the samples reported in the literature.

Chapter 8

In-Situ Heat Treatment

The previous chapter discussed the role of fine grains and solidification cells in suppressing the thermally-activated martensitic transformation in SLM-built 17-4PH stainless steel. It was determined that the solidification rates of SLM drive austenite to solidify in a cellular manner, with grains $< 100\,\mu m$ containing solidification cells $1\,\mu m$ in diameter. It was shown that this microstructure would fully stabilise austenite down to room temperature in 17-4PH, and that it would not be possible to use cooling rate, and therefore grain/cell size, to control the extent of martensitic transformation.

However, experimental data also showed that while the lowest energy density sample was fully austenitic as expected, the higher energy density sample had up to 28 wt% martensite in spite of the fine cellular microstructure. This indicated a secondary mechanism was present, capable of overriding the stabilising effect of the microstructure and allowing transformation.

In-situ heat treatment is an unavoidable characteristic of additive manufacture, due to the heat affected zone caused by the addition of subsequent layers. This chapter considers the effect of in-situ heat treatment on the microstructure of SLM-built 17-4PH, assessing whether it could have allowed the grain/cell boundaries to recover sufficiently for partial martensitic transformation in the higher energy density builds.

8.1 Background

Selective laser melting is a layer-by-layer process. For each layer, the laser-beam heat-source passes over the surface following a pre-determined tool path and melts the required geometry. Directly under the laser beam is a small melt pool, which is surrounded by a heat affected zone (HAZ) similar to that created during conventional welding. The size and shape of the HAZ are dependent on the laser and material parameters, and it can extend through multiple previous layers. Considering a specific point within the sample, it will experience temperature transients both when the laser passes directly overhead and when it is on nearby hatches. These transients create an overall 'time at temperature' profile which constitute the in-situ heat treatment.

There is evidence that in-situ heat treatment is capable of modifying the microstructure during an AM build. Inconel 718 built by EBW showed microstructural variation with depth, from a cored dendritic structure at the surface through to a columnar structure in the bulk [57]. However the EBW process was operated at much higher energy density than the SLM builds considered here, so the extent of heat treatment will have been correspondingly greater.

For SLM-built material, a Ti-6Al-4V build showed that in-situ heat treatment was capable of driving decomposition from α-martensite to $\alpha + \beta$ during the build [58]. However, it was determined that the majority of decomposition had taken place around 400 °C. This is a much lower temperature than that required for dislocation recovery in stainless steels, so the effective duration of heat treatment would have been much greater.

8.1.1 Recovery Processes

Recovery takes place through two main processes: annihilation and rearrangement. These both require the movement of dislocations, which can happen by a combination of glide, climb and cross-slip.

Glide is the movement of a dislocation in the slip plane; it does not require diffusion and is therefore possible at low temperatures. Climb is the movement of a dislocation perpendicular to its slip-plane; this requires the diffusion of vacancies, so is easier at high temperatures. Cross-slip is a screw dislocation moving to a different slip plane of the same type; because cross-slip is just a variant of glide, it does not require diffusion and

can occur at low temperatures. Most dislocations move in sections, rather than the whole line moving simultaneously, creating *kinks*, steps within the same slip plane, and *jogs*, steps between slip planes.

Dislocations which have the same slip plane but opposite sign will attract and annihilate, while those of the same sign will repel. Where annihilation is not possible, or not complete, dislocations will accumulate in tangles which then form sub-grain boundaries. These sub-grains will eventually recrystallise; growing into fewer, larger grains with lower dislocation density.

Dislocation recovery is dependent on the stacking fault energy (SFE). A low SFE increases the probability of a perfect dislocation dissociating into partial dislocations and stacking faults [166]. In an FCC structure, an edge dislocation with two additional half planes at the dislocation core is able to maintain the FCC stacking sequence (ABAB) and therefore is a perfect dislocation (Figure 8.1a). However, if the SFE is low, the two planes at the dislocation core can become separated, forming partial dislocations and associated stacking faults (Figure 8.1b) [167]. Dissociation into partial dislocations hinders both climb and cross-slip, which are the primary mechanisms of recovery [166].

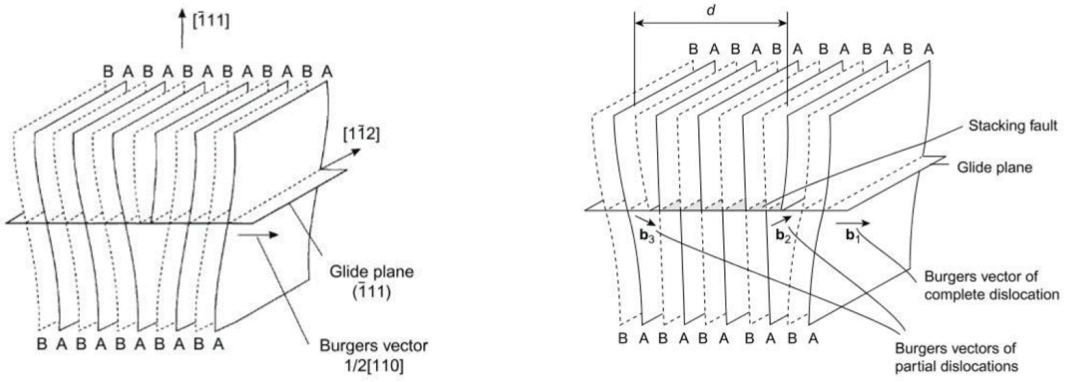

(a) **(b)**

Figure 8.1: a) Perfect edge dislocation with two adjacent half planes maintaining stacking sequence. b) Dissociated partial egde dislocations each with one half plane and associated stacking fault. [167]

Stainless steels are at the lower end of the range of SFE (Figure 8.2), making them susceptible to dislocation dissociation. As climb and cross-slip normally control the rate of recovery, this suggests that recovery may be slower in stainless steels than in other metals [166].

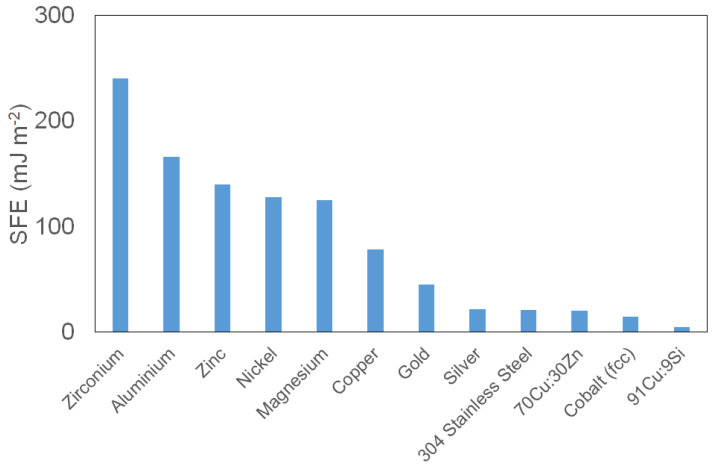

Figure 8.2: Stacking fault energies for some common metals [147].

8.1.2 Recovery Kinetics

Each of the mechanisms described above (glide, climb, cross-slip) has its own kinetics, but as they can rarely be observed independently it is difficult to quantify them individually. Instead, the kinetics of recovery are usually observed indirectly, monitoring the change in a bulk property such as yield strength or hardness.

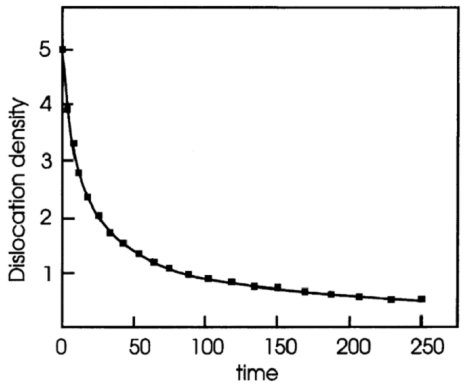

Figure 8.3: Results of computer simulation showing variation in dislocation density with heat treatment time [166]

At the start of recovery there is a high dislocation density giving many possibilities for glide, climb and cross-slip. This leads to a low activation energy which in turn drives fast recovery rates. As recovery proceeds, the opportunities for dislocation motion reduce, the activation energy increases and the rate of recovery falls (Figure 8.3) [166, 168]. The

activation energy Q_{act} is then dependent on the extent of recovery and can be measured as a function of the bulk property.

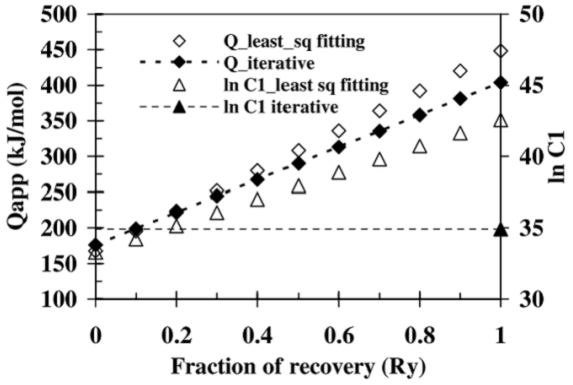

Figure 8.4: Dependence of the activation energy on the fraction of recovery [169].

The dependence of Q_{act} on the fraction of recovery for a low-carbon steel was determined experimentally (Figure 8.4) [169, 170]. Samples were annealed at a variety of times and temperatures and the extent of recovery monitored by hardness measurements and magnetic assessment of coercivity. This found the rate of recovery followed Arrhenius-type behaviour with Q_{act} (in $\mathrm{kJ\,mol^{-1}}$) given by:

$$Q_{act} = 168 - 281(1 - R_y) \tag{8.1}$$

where R_y is the fraction of recovery. An alternative approach for estimating Q_{act} is the expression for bulk diffusion proposed by Brown & Ashby [171], which relies on the solidus temperature T_{sol} and the gas constant R.

$$Q_{act} = 18.4\, T_{sol}\, R \tag{8.2}$$

For 17-4PH, Equation 8.2 would give an activation energy of $Q_{act} = 256\,\mathrm{kJ\,mol^{-1}}$. This is in the middle of the experimental range determined from Figure 8.4, although taking Q_{act} to increase with the fraction of recovery would give a more accurate picture of the kinetics. For the remainder of this chapter, a value of $Q_{act} = 309\,\mathrm{kJ\,mol^{-1}}$ will be used, which corresponds to 50 % recovery from Equation 8.1.

8.1.3 Heat Treatment of SLM-Built Steel

In the Chapter 7, it was shown that steels built by SLM exhibit very different microstructures from their conventionally manufactured counterparts, which will impact how they behave during heat treatment. Further, the literature on heat treatment of SLM-built material covers a variety of durations and temperatures, making direct comparison difficult.

Using Equation 8.3 it is possible to convert an increment of time Δt_1 at temperature T_1 to an equivalent time Δt^* at temperature T^* for a process with activation energy Q_{act} [157]. This allows different heat treatments to be normalised to a single temperature for comparison. The normalising temperature chosen for this work is $T^* = 800\,°C$.

$$\Delta t^* = \Delta t_1 \, exp \, \frac{Q_{act}}{R} \left(\frac{1}{T^*} - \frac{1}{T_1} \right) \tag{8.3}$$

In [45], SLM-built 316L was subjected to heat treatment at a range of times and temperatures to investigate the effect on microstructure. After 6 min at 800 °C the structure exhibited clumping (Figure 8.5), where groups of solidification cells of similar orientations had grouped into sub-grains 3 µm to 5 µm across, but higher magnification showed that the cell structure was still present within these sub-grains although with reduced dislocation density at the cell walls [45].

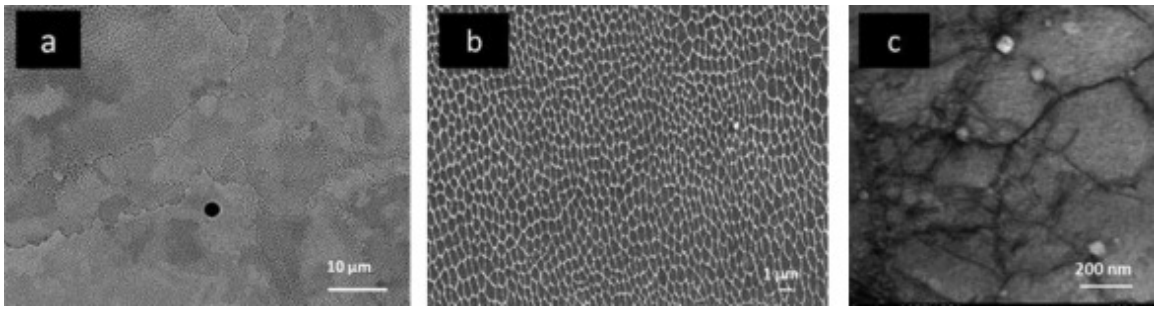

Figure 8.5: Structure of SLM-built 316L steel after heat treatment at 800 °C for 6 min: a) Low magnification; b) High magnification; c)TEM [45].

Extending the heat treatment time to 1 h had no further effect on microstructure (Figure 8.6). While this is post-build rather than in-situ processing, it shows that for structures similar to the as-built condition shown in Figure 8.6a, the cellular microstructure persists after this level of heat treatment without significant coarsening.

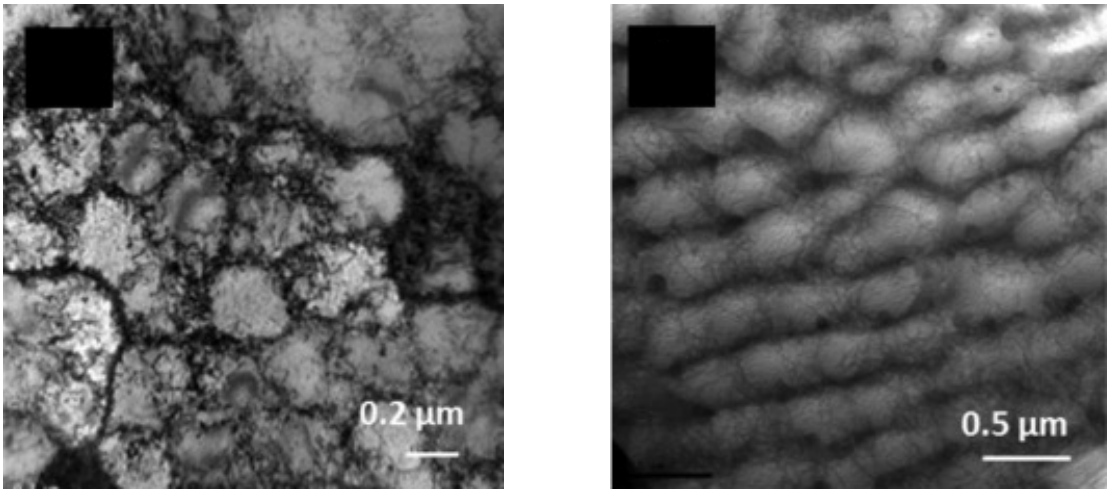

Figure 8.6: TEM of solidification cells in 316L: a) As-built; b) After heat treatment at 800 °C for 1 h [45].

Similar results have been published on post-build heat treatment of other SLM-steels and from heat treatment of similar microstructures achieved through deformation processing. These are summarised in Table 8.1, although comments about the extent of recovery are subjective and not necessarily comparable between sources.

Table 8.1: Heat Treatment Comparisons

Ref	Material	Time s	Temperature °C	Time at 800 °C s	Condition
[46]	17-4PH	3600	650	1.3×10^{1}	No change
[45]	316L	360	800	3.6×10^{2}	Reduction in dislocation density at solidification cell walls, no coarsening
[172]	Fe-30Ni-Nb	10	925	3.7×10^{2}	No reported change
[45]	316L	3600	800	3.6×10^{3}	Reduction in dislocation density at solidification cell walls, no coarsening
[172]	Fe-30Ni-Nb	300	925	1.1×10^{4}	Recovery started
[172]	Fe-30Ni-Nb	1000	925	3.7×10^{4}	Partial recovery of some dislocation walls
[46]	17-4PH	3600	1050	2.5×10^{6}	Fully recovered

The most extreme condition (1050 °C for 1 h) was reported to have achieved full recovery with no trace of the melt pools visible under optical microscopy (Figure 8.7a). XRD confirmed the proportion of retained austenite had reduced from 50 vol% in the as-built condition to less than 20 vol% after heat treatment, although there was still some evidence of microsegregation where the cell structure had been (Figure 8.7b) [46].

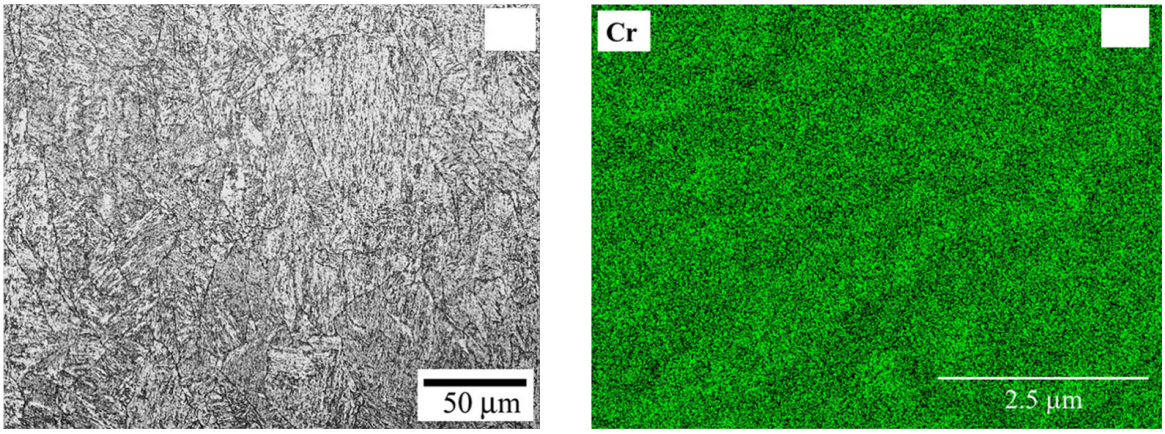

(a) **(b)**

Figure 8.7: 17-4PH after heat treatment at 1150 °C for 1 h: a) Optical micrograph showing martensitic structure with no trace of melt pools or solidification cells; b) X-ray map for chromium showing residual segregation on scale of solidification cells [46].

Using this as a maximum condition, combined with Equation 8.1, it has been possible to construct an Arrhenius relationship between the equivalent time at 800 °C, the rate of recovery (Figure 8.8a) and the fraction recovered (Figure 8.8b). These are normalised relationships as the rate constants are not known, but they support the comparisons of recovery extent for the heat treatments listed in Table 8.1.

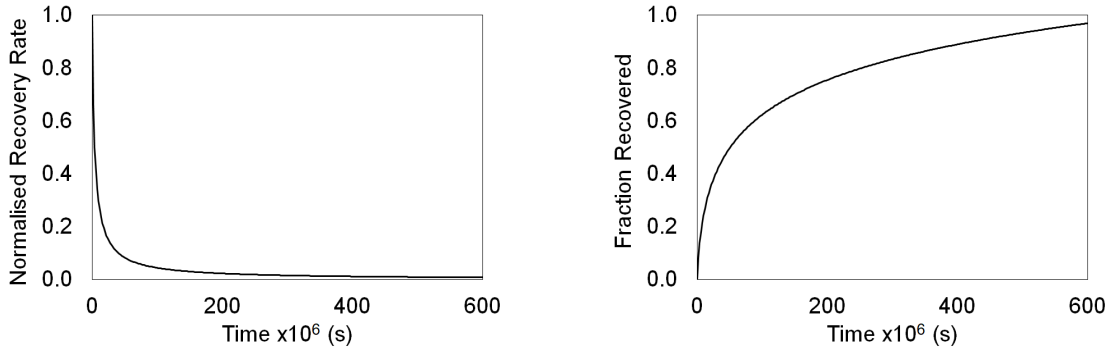

(a) **(b)**

Figure 8.8: a) Predicted normalised rate of recovery during heat treatment at 800 °C. b) Predicted fraction recovered during heat treatment at 800 °C.

It is possible to make an order-of-magnitude assessment about the amount of heat treatment experienced by an 'average' SLM process. The melt pools reported in the literature for a representative good-quality build of 17-4PH were approximately 60 µm deep and

120 µm wide [6]. From the modelling work shown in Chapter 6, the melt pool length can be estimated to be up to three times the width and the melt pool to be a semi-ellipsoid, giving a total melt pool volume of 1.4×10^6 µm^3.

Further, the model indicates the heat affected zone to be up to ten times the volume of the melt pool, making the volume of HAZ to be 1.4×10^7 µm^3. The build in [6] used a layer thickness of 40 µm, a hatch spacing of 100 µm and an average travel speed of 0.8 m s^{-1}, so a particular volume of material will be within the HAZ for approximately 5 ms duration over the total build time.

The temperature through the HAZ is not uniform, and there are steep temperature gradients. The average temperature by volume within the HAZ will be much lower than the linear average between the solidus temperature and the point at which diffusion can be regarded to have stopped. This will significantly affect the rate of recovery; for example the rate of recovery at 800 °C is 10^5 times lower than that at 1400 °C. Taking the volume average temperature to be 1000 °C, this gives an equivalent heat treatment duration of < 2 s at 800 °C.

This is very early on the recovery curves (Figure 8.8), so while the activation energy will be low, and the rate of recovery will be high, the actual fraction recovered will be very limited. Using the qualitative observations in Table 8.1 it would be expected that there would be at most a reduction in dislocation density at the solidification cell walls but with no coarsening. This is highly sensitive to the approximations made for the size of the HAZ and for the volume average temperature, however it correlates with the observations from literature which show comparably sized solidification cells in as-built steels across a range of build conditions.

8.2 Melt Pool Modelling

Recognising that there are many approximations in the assessment above, the melt pool model was used to give a more detailed prediction across the range of build parameters that can be achieved on the Renishaw SLM125.

The model was used to generate the temperature profile resulting from the HAZ of individual hatches within each layer. It then used Equation 8.3 to normalise each timestep of that profile (fixed duration, variable temperature) to an equivalent duration at 800 °C

(fixed temperature, variable duration), which were summed to give a single equivalent overall heat treatment for comparison against the data in Table 8.1.

The model did not include the time between layers for powder recoating, which would add cooling time between sections of heat treatment. The model also did not predict the general increase in ambient temperature during the build. Both of these would have negligible impact on the overall in-situ heat treatment because they happen at comparatively low temperature ($<<$ 650 °C) and the rate of recovery would therefore be extremely slow.

In addition to the melt pool geometry, which determined the size and shape of the heat affected zone, key drivers for the heat treatment profile included the hatch spacing and layer thickness. Taking the maximum condition from the previous chapter, models were run with 200 W power, 200 µs exposure and 10 µm point spacing, giving an average travel speed of 50 mm s^{-1}. The layer thickness and hatch spacing were each varied between 20 µm to 60 µm, with the absorptivity fixed at 45 %.

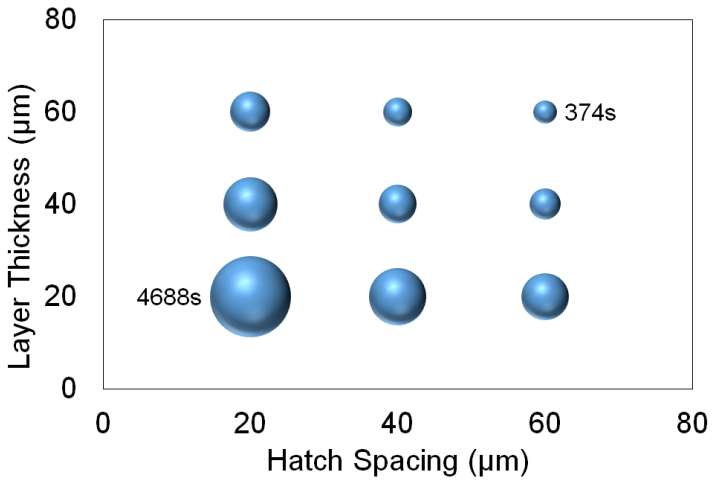

Figure 8.9: Sensitivity of equivalent heat treatment duration to variation in layer thickness and hatch spacing. Maximum and minimum durations shown in labels. Area of bubble indicates heat treatment duration.

The results confirmed that both hatch spacing and layer thickness affected the duration of in-situ heat treatment, with layer thickness having a slightly stronger effect (Figure 8.9).

Figure 8.10 shows one of the heat treatment profiles. The short-range periodicity (0.05 s) corresponds to the hatches, while the long-range periodicity (2.6 s) corresponds to the layers. The equivalent duration of heat treatment increases dramatically with temperature, driven by the exponential term in Equation 8.3.

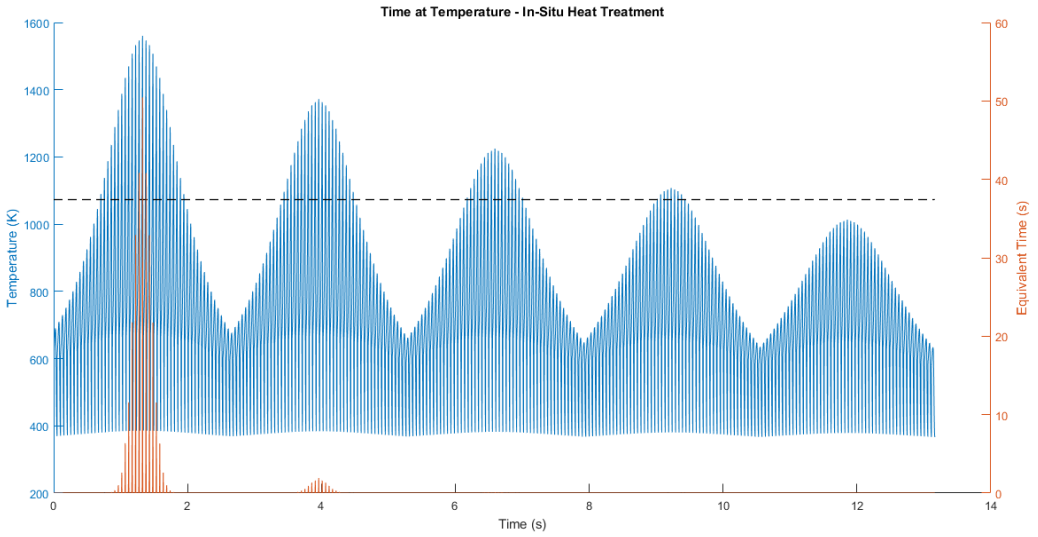

Figure 8.10: Example heat treatment prediction from model for condition with 20 µm hatch spacing and 60 µm layer thickness. Blue line (LH axis) is temperature. Red line (RH axis) is equivalent duration at 800 °C.

The highest temperature peaks correspond to the central hatches from each layer, where the laser is directly above the region being modelled. A smaller layer thickness results in a larger number of these high temperature peaks, while a smaller hatch spacing drives more peaks within each layer, but at much lower temperature.

The maximum equivalent heat treatment predicted by the model was 4688 s at 800 °C, for the condition with 20 µm hatch spacing and 20 µm layer thickness. Reviewing the data in Table 8.1 and Figure 8.8, it is unlikely that this would result in any appreciable level of recovery, $<< 1\,\%$.

An alternative approach would be to remelt each layer multiple times. This strategy has been employed for reducing the residual stress in additively manufactured samples of 18Ni300 maraging steel, and for reducing porosity and surface roughness in 316L [173, 174]. However, in 316L it was found that remelting refined the sub-grain microstructure rather than driving recovery, although the energy density very low so this would have had a very small HAZ [174].

Overall the model predicted that while in-situ heat treatment did occur, the time-at-temperature achievable with SLM was insufficient to drive any significant recovery, and was therefore unlikely to enable thermally-driven martensitic transformation. This is

consistent with the microstructures of additively manufactured steels presented in the previous chapter. If in-situ heat treatment resulting from normal processing parameters were sufficient to drive recovery and coarsening, then a greater variety of microstructures would be observed in the as-built condition.

8.3 Experimental

8.3.1 Method

To test the prediction from the model, and add to the data from the Square Series (S1-S5) samples from the previous chapter, a further two sets of build conditions were investigated experimentally (Figure 8.11). The Hatch Series (H1-H4) used the same laser parameters as the high E_0^* (S1) condition from the Square series, but varying hatch spacing to change the number of heating cycles. The Point Series (P1-P4) had a similar approach, varying point spacing to change the size of the heat affected zone. Point spacing was chosen over layer thickness as it would allow multiple samples to be built concurrently.

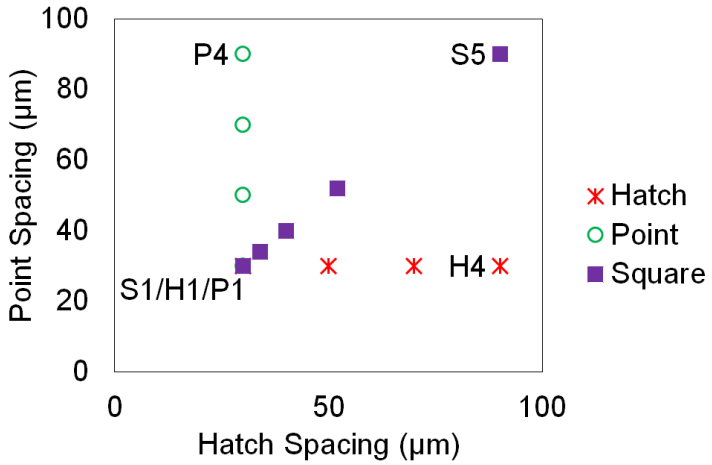

Figure 8.11: Spacings used for Square, Point & Hatch Series

The predictions of in-situ heat treatment duration were initially made using a fixed absorptivity of 45 % (Figure 8.12). For the Square Series this showed a dramatic difference between the prediction for high energy density (S1), 18 s, and that for the low energy density (S5), < 0.1 s. The Point Series showed a similar trend, indicating the strong effect of changing the size of the melt pool, while the Hatch Series showed a lesser effect.

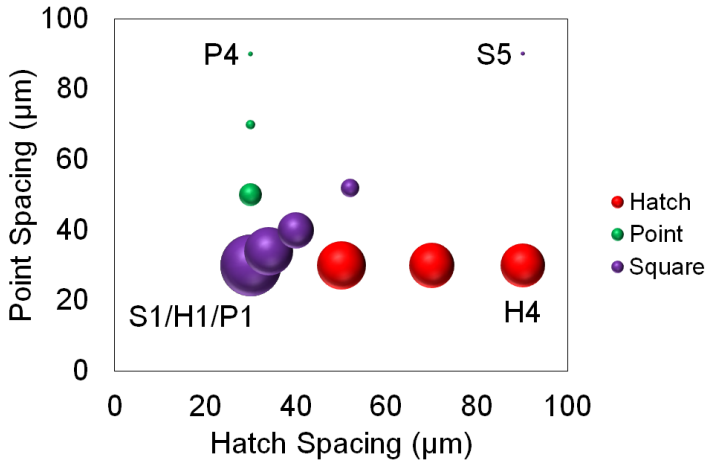

Figure 8.12: Predicted equivalent heat treatment duration for Square, Point & Hatch Series using fixed 45 % absorptivity. Area of bubble indicates heat treatment duration.

However, as presented in the previous chapter, the build data from the Square Series had actually indicated a variable absorptivity was more representative, caused by variation in surface roughness and reflectivity with energy density. This variable absorptivity was assumed to be driven by the melt pool characteristics, which were more strongly affected by point spacing than by hatch spacing. The absorptivity for the Hatch Series was therefore fixed at 45 %, while that of the Point Series was allowed to vary in a similar manner to that developed for the Square Series (Table 8.2).

Table 8.2: 17-4PH Square, Hatch & Point Series Build Parameters

SampleID	Power watt	Exposure µs	Point Spacing µm	Hatch µm	Absorptivity	E_0^*
S1	200	100	30	30	0.45	23.7
S2	200	100	34	34	0.48	19.7
S3	200	100	40	40	0.55	16.3
S4	200	100	52	52	0.65	11.4
S5	200	100	90	90	0.90	5.3
H1	200	100	30	30	0.45	23.7
H2	200	100	30	50	0.45	14.2
H3	200	100	30	70	0.45	10.1
H4	200	100	30	90	0.45	7.9
P1	200	100	30	30	0.45	23.7
P2	200	100	50	30	0.61	19.3
P3	200	100	70	30	0.70	15.8
P4	200	100	90	30	0.90	15.8

Re-running the model, the variable absorptivity significantly modified the predicted in-

situ heat treatment duration for the lower energy density conditions from the Square and Point Series (Figure 8.13). This was expected given that the melt pool was now of much greater depth for these conditions. The Hatch Series was unaffected. The overall effect was to reduce the range of predicted heat treatment durations to between 7.3 s and 18 s.

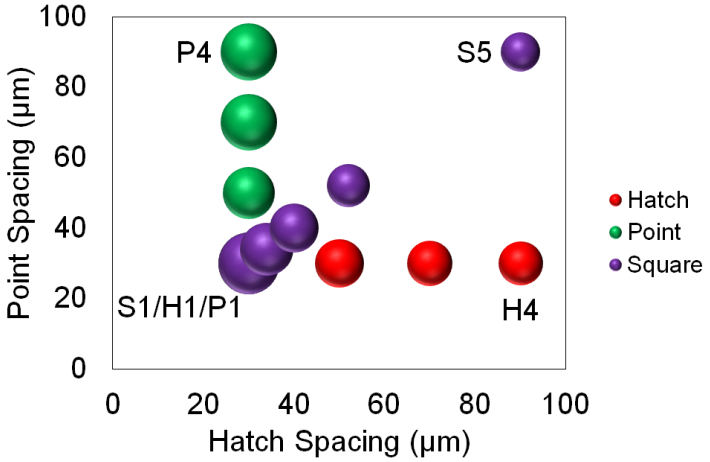

Figure 8.13: Predicted equivalent heat treatment duration for Square, Point & Hatch Series using variable absorptivity as per Table 8.2. Area of bubble indicates heat treatment duration.

The Hatch and Point series conditions were used to build a set of 8 mm diameter cylinders, 10 mm high, using the meander scan strategy. No additional samples were built for the Square Series conditions. The H1/P1 sample was a single sample shared between the Hatch and Point series, built using identical conditions to the S1 sample from the Square series.

8.3.2 VSM

Following the same method applied to the Square Series conditions in the previous chapter, VSM was carried out on discs cut from the Hatch and Point Series cylinders and the phase fraction of martensite was determined from the saturation magnetisation (Figure 8.14).

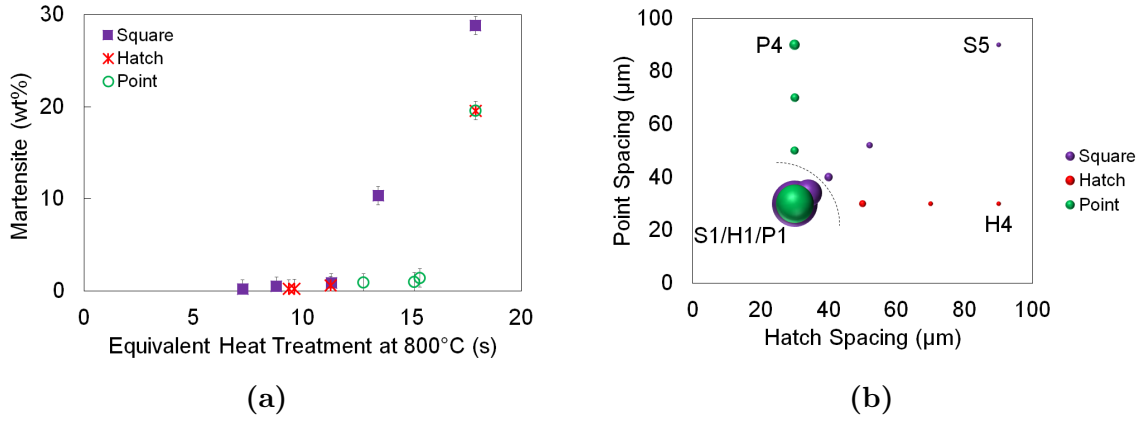

Figure 8.14: Martensite content for Square, Hatch & Point Series: a) by heat treatment duration. b) by point and/or hatch spacing, where area of bubble indicates wt% martensite.

The data did show higher martensite content for the samples with longer duration heat treatment (and higher energy density), however it did not follow a consistent trend. The only samples with any significant martensite content were those with $> 13\,\mathrm{s}$ equivalent heat treatment (S1 & S2), which is still far too short for any significant recovery according to the data from Table 8.1.

Comparing the variation in martensite content (Figure 8.14b) with that of heat treatment duration (Figure 8.13), shows this more clearly. There was a very sudden drop in martensite content between the highest energy density conditions (bottom left corner) and all other conditions yet there was minimal change in heat treatment duration.

A further observation was that the H1/P1 sample was manufactured to the same conditions as the S1 sample, but showed slightly lower martensite content even though their in-situ heat treatment should have been identical.

8.3.3 Feritscope

A Feritscope was used to give spatially resolved measurements across the internal and external surfaces of a vertically sectioned cuboid from the highest E_0^* (S1) sample. This showed a higher martensite phase fraction on the external surface, and a strong increase in martensite phase fraction with distance from the baseplate (Figure 8.15).

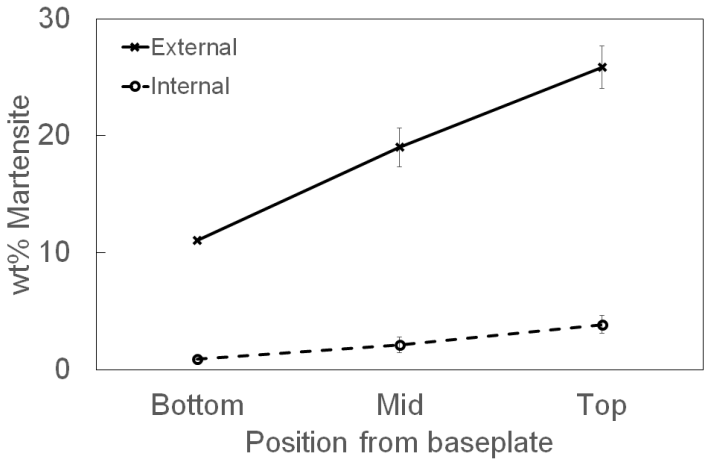

Figure 8.15: Spatial variation in martensite content for high E_0^* (S1) sample.

Feritscope measurements were also taken from the Square series cylinders, just below the discs cut for VSM, to allow comparison between measurement techniques. The results (Figure 8.16) confirmed the trend in overall martensite content although the wt% martensite was generally lower in the Feritscope data than the VSM data. This is consistent with the height effect observed in Figure 8.15, given that the Feritscope measurements were taken from lower down the cylinders than the VSM discs.

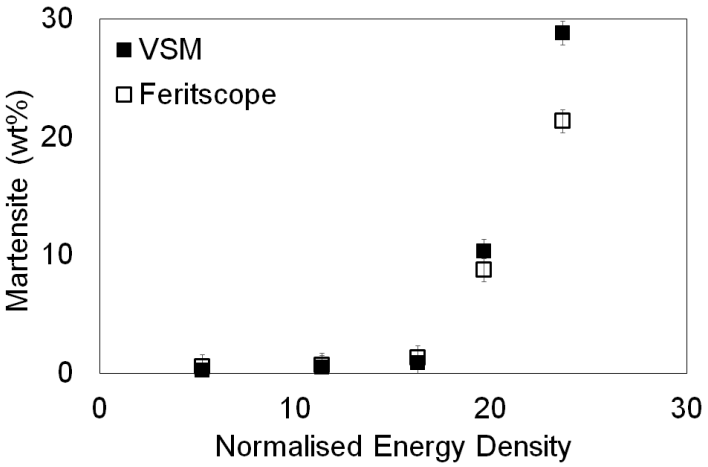

Figure 8.16: Comparison of Feritsope and VSM for Square series.

8.3.4 XRD

The XRD results presented in the previous chapter showed a split in the austenite peaks indicating the presence of two austenite phases with different lattice parameters (Fig-

ure 8.17a). The austenite peaks were deconvoluted in Origin using Lorentz curve fitting, to determine the peak centre and full-width half-maximum (FWHM) for the two austenite phases individually (Figure 8.17b).

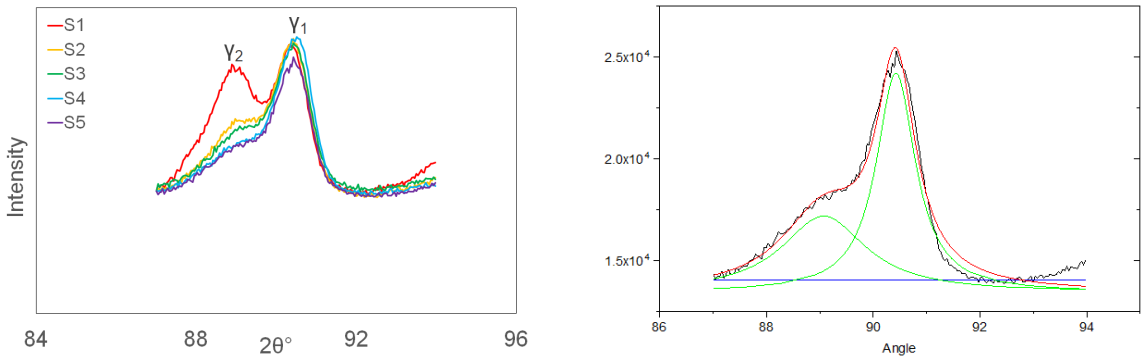

(a) All samples

(b) S5: 0.77 s at 650 °C

Figure 8.17: a) Comparison of 87° to 94° data for all samples showing split austenite peaks. b) Origin deconvolution peaks at 87° to 94° in low energy density (S5) sample. Black line is raw data, green lines are individual fitted peaks, red line is sum of fitted peaks, blue line is background.

At high energy density (S1) the two peaks have comparable intensity, giving more confidence in the deconvolution and the reported peak centres and breadths. However, at low energy density (S5) the γ_2 peak (lower 2θ) had much lower intensity, giving less confidence in the characteristics reported for this peak compared with the γ_1 peak (higher 2θ).

Assuming that recovery should affect both austenite phases equally, a Williamson-Hall plot was created for γ_1 phase, where there was better confidence in the peak characteristics [175]. This showed identical gradients for all five energy density conditions (Figure 8.18), although there was a slight offset in the y-intercept for the highest energy density condition.

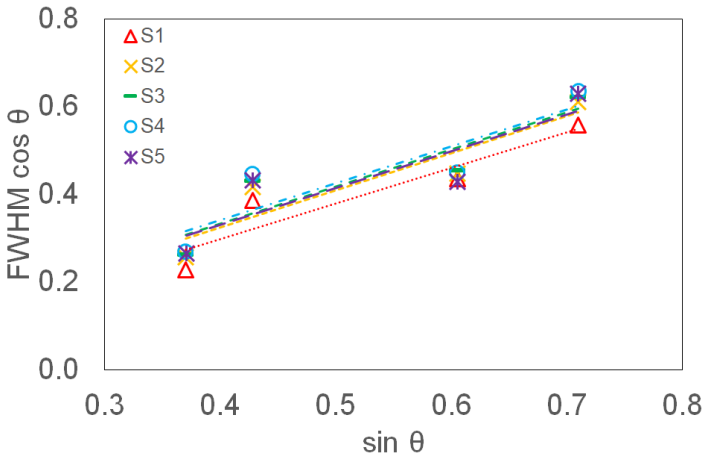

Figure 8.18: Williamson-Hall plot for γ_1 austenite phase across Square Series build conditions. $FWHM$ is the full-width-half-maximum peak breadth.

The similarity in gradient across the build conditions indicates comparable levels of strain broadening, which is supported by the shape of the original XRD peaks (Figure 8.17a). Had there been significant recovery in the higher energy density conditions, it would be expected that the reduction in dislocation density would have caused the peaks to narrow and the gradient of the line in the Williamson-Hall plot to reduce [147].

8.3.5 Microscopy

SEM was used to compare the microstructure at the very surface of the sample (assumed to have had no heat treatment) with that approximately 1 mm depth, shown for the intermediate S3 condition in Figures 8.19a and 8.19c respectively.

The cell and grain size were comparable between the surface and the bulk, indicating no apparent coarsening as a result of the in-situ heat treatment. There was more variation between the cell size within adjacent grains in the same region of the material than between the cell size in grains at the surface and in the bulk.

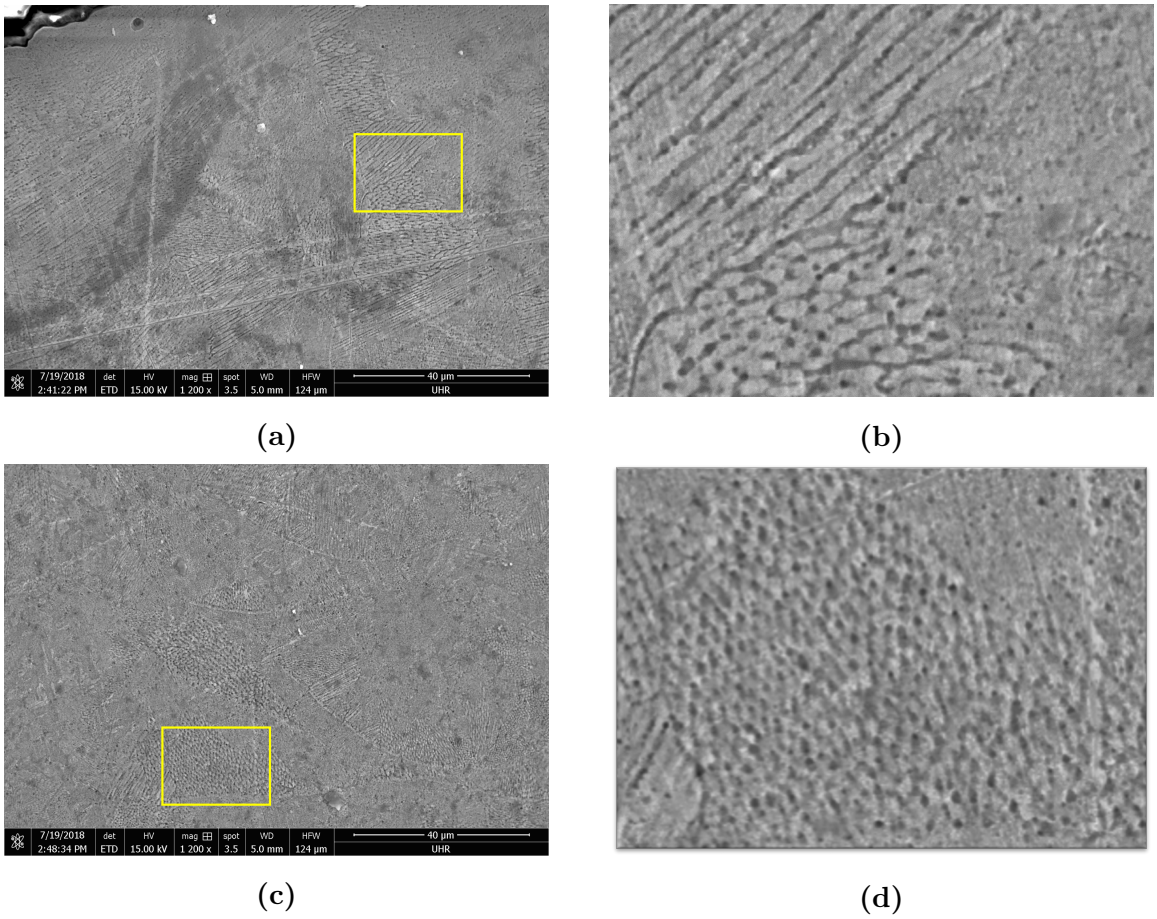

Figure 8.19: a) Microstructure of intermediate (S3) build at surface. b) Detail view identified by yellow box in (a). c) Microstructure of intermediate (S3) build at 1 mm depth. d) Detail view identified by yellow box in (c).

8.4 Discussion

The previous chapter confirmed that the microstructure of SLM-built 17-4PH consists of sufficiently fine grains and solidification cells to completely suppress the transformation from primary-austenite to thermally-activated martensite on cooling. However, the highest energy density conditions showed a proportion of martensite, indicating a secondary mechanism capable of countering the austenite-stabilising effect of the fine microstructure. This chapter investigated whether in-situ heat treatment, caused by the heat affected zone from subsequent layers and hatches, could be responsible for recovering the grain/cell boundaries sufficiently to allow partial transformation.

The literature for post-processing heat treatment of SLM-built material was combined

with kinetic information for low-carbon steel to produce an indication of the extent of recovery for a given heat treatment. Even though the activation energy at the start of recovery is low, giving a high recovery rate, approximating the size of the heat affected zone from an 'average' SLM build suggested that the duration of in-situ heat treatment would be extremely short.

Therefore the extent of recovery would be expected to be minimal, with a possible reduction in dislocation density inside the cells, but insufficient cell coarsening to allow any significant martensitic transformation. This is consistent with the observed microstructures of SLM-built steels from literature: if in-situ heat treatment were sufficient to recover the cell boundaries, then a wider range of cell sizes would be expected.

The melt pool model was used to make a more detailed analysis, including the effect of layer thickness and hatch spacing. This predicted that layer thickness was a stronger driver than hatch spacing for in-situ heat treatment, but that even with very small layer thickness and hatch spacings the durations would be too short to drive any significant recovery.

Two sets of experimental samples were built, to complement the Square Series from the previous chapter. The Hatch series had fixed point spacing and varied hatch spacing, while the Point series had fixed hatch spacing and varied point spacing. The duration of in-situ heat treatments was predicted to range from 7.3 s to 18 s at 800 °C. Phase fraction measured by VSM did show an increase in martensite content for the conditions with the longest predicted heat treatment duration, which also had the highest E_0^*, but the data did not follow a consistent trend.

If in-situ heat treatment were responsible for recovery leading to martensitic transformation, it would be expected that the very surface layers would have experienced less heat treatment and have more retained austenite, while the bulk should have experienced a uniform duration and therefore have near constant phase fraction. Instead, spatially resolved Feritscope measurements of martensite content on a high E_0^* (S1) sample showed martensite content increasing gradually with build height, to reach a maximum at the top of the sample. This was supported by microscopy which showed comparable solidification cell diameters for the surface layer and the bulk of the samples.

Williamson-Hall analysis was carried out on deconvoluted XRD peaks for one of the two austenite phases. This showed no trend in peak broadening, which would have been expected had there been a change in dislocation density with energy density.

In summary, while SLM-built material does experience in-situ heat treatment, it does not appear to be of sufficient duration (too small a HAZ at too high a travel speed) to cause any appreciable coarsening of the solidification cell structure. It is therefore unlikely that in-situ heat treatment could be responsible for the partial martensitic transformation observed in the higher E_0^* experimental samples.

Chapter 9

Thermal Strain

In the previous chapters, it was shown that SLM-built steels have such rapid solidification that they form elongated solidification cells, less than 2 µm in diameter. It has further been establised that in-situ heat treatment is of insufficient duration to drive cell coarsening. The result is that the fine microstructure suppresses thermally-driven martensite, driving the start temperature M_s below room temperature.

All of this would suggest that SLM-built 17-4PH should be fully austenitic. Experimental data confirmed this for low energy density samples, yet higher energy density samples showed up to 28 wt% martensite, in spite of a similarly fine microstructure. This could not be due to unintentional post-build deformation-induced martensitic transformation because these samples were magnetic (partially martensitic) even before being removed from the baseplate.

This chapter considers the role of thermal strain as a mechanism to drive deformation-induced martensitic transformation during the build. Thermal strain is a common issue with additively manufactured components, caused by the high thermal gradients that are set up around the melt pool and across the component as a whole.

9.1 Background

In [8], thermal strain was described in terms of two different mechanisms acting at different length scales. The *thermal gradient mechanism*, at the scale of the melt pool (Figure 9.1),

and the *cool-down mechanism* at the scale of the component (Figure 9.2). The combined result of these mechanisms is to set up a variety of stresses of different directions and magnitudes through an additively manufactured component.

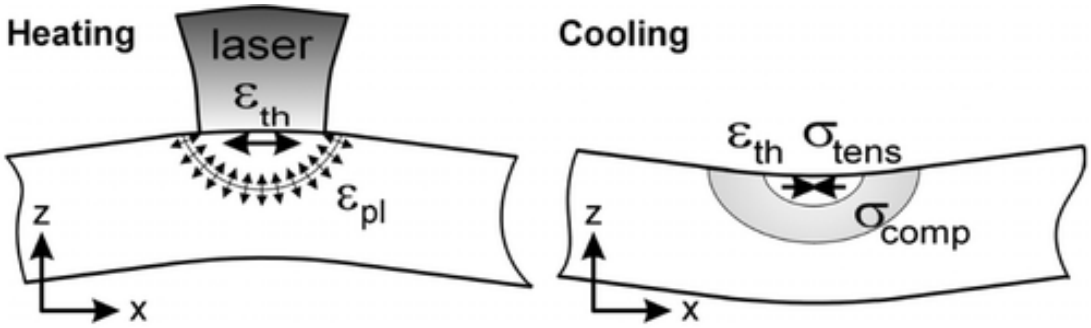

Figure 9.1: Schematic of thermal gradient mechanism of residual stress in SLM [8]

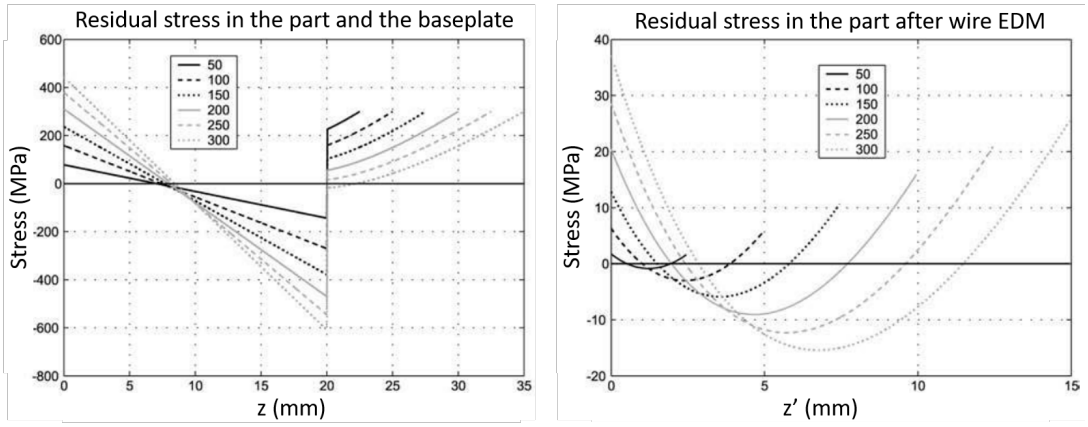

Figure 9.2: Modelling prediction of residual stress due to cool-down mechanism and effect of number of layers [8]

Different scan strategies have also been seen to generate different stress profiles, by changing the way these mechanisms interact. A fractal strategy was predicted to give less distortion in the build direction and a more uniform temperature field compared with a meander strategy [176]. Experimental evidence from CM247LC, which is known to suffer from cracking in SLM, showed a difference in cracking behaviour between chessboard and fractal scanning strategies [55].

Measurements of residual stress on AM-built components have demonstrated the complexity of these interactions. Pillars of 316L were found to have tensile vertical (build direction) stresses around the outer edge, with compressive vertical stresses in the centre; these were constant through the majority of the build height but dropped off rapidly in

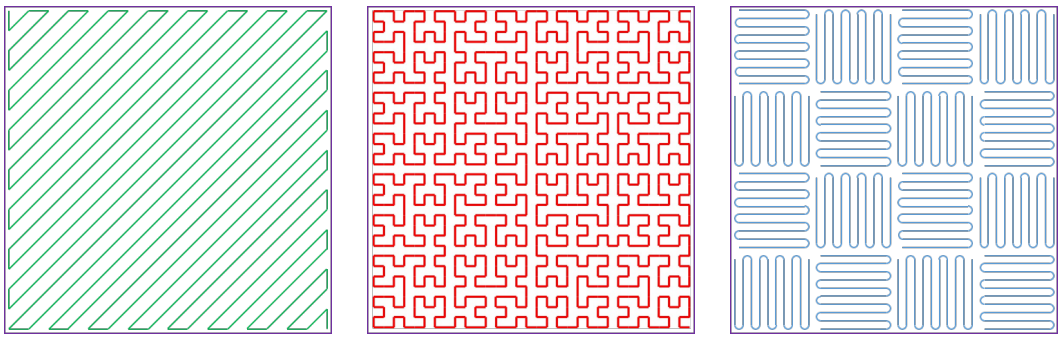

(a) **(b)** **(c)**

Figure 9.3: Scan strategies designed to modify thermal stress during AM a) Meander strategy, raster scan within each layer, direction of raster rotated between layers. b) Fractal scan, a space-filling and self-avoiding strategy [55]. c) Chessboard scan, similar to raster but with uniform vector length [55].

the top 5 mm (Figure 9.4b) [177]. Stresses in the build direction (z) were also found to be higher than those in the build plane (xy), in some cases up to 80 % of the 0.2 % yield stress [178].

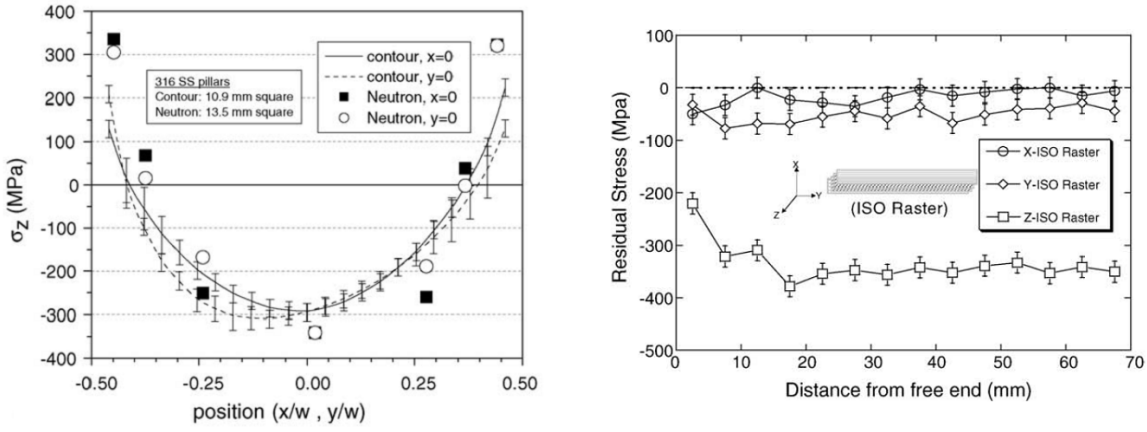

(a) **(b)**

Figure 9.4: a) Residual stress in build direction by neutron diffraction and contour method in 316L pillar. b) Residual stress in thickness direction (x), width direction (y) and build direction (z) as a function of distance from free end in a 316L rectangular sample. [177]

Similar patterns have been observed for AM-built Inconel 718 [177], and CrCoMo [54], indicating that the primary driver for residual stress is the manufacturing method rather than the material. In the case of CrCoMo, while the tensile stress was fairly consistent around 800 MPa, the compressive stress was much higher at the top of the build than at the base (Figure 9.5).

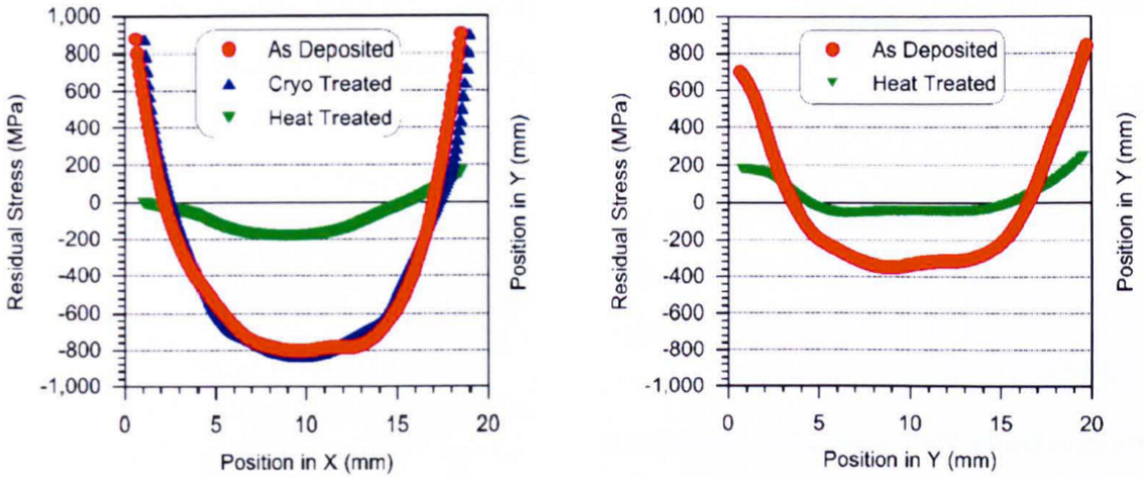

(a) 10 mm down from top surface **(b)** 10 mm up from base plate

Figure 9.5: Residual stress across the build plane in a CrCoMo sample [54]

9.2 Impact of Thermal Strain on SLM-built 17-4PH

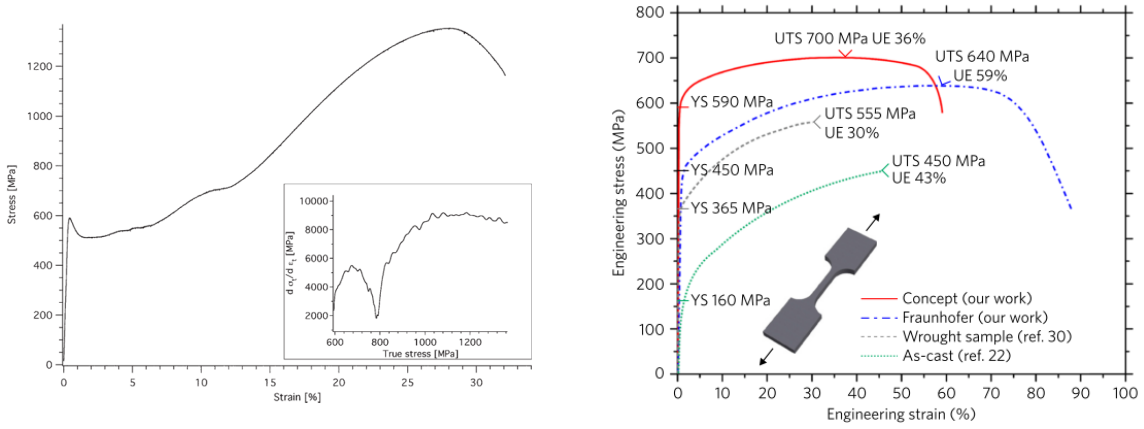

(a) **(b)**

Figure 9.6: a) Stress-strain curve for SLM-built 17-4PH [5]. b) Stress-strain curves for SLM-built 316L [165].

The yield stress for SLM-built 17-4PH was shown to be 600 MPa (Figure 9.6), although this was reported to be dual-phase material so there could have been a contribution from martensite. 316L is a fully austenitic steel, with similar composition to 17-4PH, and is quoted to have a yield stress of 590 MPa for SLM-built material with comparable grain and cell sizes [165]. This is below the maximum stress measured in the SLM-built CrCoMo

(Figure 9.5), which suggests that the residual stresses accrued during SLM could reach, or even exceed, the yield stress.

Deformation-driven martensite does not require the austenite to yield for transformation to occur. Below yield, the applied stress augments the thermal driving force from undercooling, allowing stress-assisted transformation. The applied stress has an interaction energy U, the magnitude and direction of which depend on the relationship between the stress and the 24 potential martensite variants. If the orientation of the stress is such that transformation would relieve the stress, U contributes to the free energy change, raising the martensite start temperature to M_s^σ (Figure 9.7). Above yield, this stress-assisted mechanism continues but there can also be strain-induced transformation on new nucleation sites created by dislocations dissociating into stacking faults.

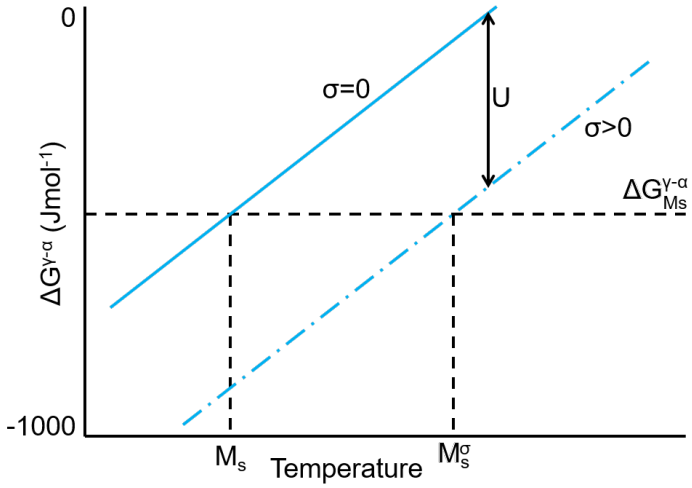

Figure 9.7: Action of an applied stress to raise M_s [72]

Retained austenite in SLM-built 17-4PH has been shown to be capable of deformation-driven transformation (TRIP), as demonstrated by the extended plastic region in Figure 9.6a. This is consistent with a low stacking fault energy of only $15\,\mathrm{mJ\,m^{-2}}$ to $20\,\mathrm{mJ\,m^{-2}}$ [5], which indicates that dislocations are readily able to dissociate into stacking faults, providing new nucleation sites for martensite [102].

Overall, analysis of the literature shows that the thermal strain accrued during an AM-built can be of a magnitude comparable with the yield stress. In the case of 17-4PH, retained metastable austenite would have a low stacking fault energy, suggesting that an applied strain could cause deformation-driven martensitic transformation in preference to slip or twinning. This indicates that thermal strain could be responsible for the martensitic

transformation observed experimentally in the high energy density samples.

9.3 Melt Pool Modelling

The thermal strain parameter ϵ^* was developed to consider strain on the scale of the melt pool (Equation 9.1), driven primarily by the build parameters [179]. It was initially developed for powder-deposition processes, but here has been applied to SLM. The parameter was designed to allow comparison between build conditions, rather than predicting an exact magnitude of strain [47].

$$\epsilon^* = \frac{\beta\,\Delta T}{E\,I}\frac{t_{dep}}{F\sqrt{\rho}}\,H^{3/2} \tag{9.1}$$

The parameter considers the effect of material parameters (coefficient of thermal expansion β, elastic modulus E, density ρ), geometry parameters (second moment of inertia I) and build process parameters (temperature different from peak to ambient ΔT, deposition time t_{dep}, heat input per unit length H) and the Fourier number F.

The deposition time t_{dep} was not explicitly defined by Mukherjee *et al* [179]. Here it has been defined as the time to process a single layer, which is then dependent on the surface area A, average travel speed v and hatch spacing $hatch$. A further refinement could be to include the effect of layer thickness and build height, but the relative weights of these are not known.

$$t_{dep} = \frac{A}{v\,hatch} \tag{9.2}$$

Equation 9.1 can then be written in the form shown in Equation 9.3, where the Fourier number F has been expanded in terms of the thermal diffusivity of the solid a_s, the melt pool length w and v. Further, the heat input per unit length H has itself been expressed as a function of laser power Q and v.

$$\epsilon^* = \frac{\beta\,\Delta T}{E\,I}\frac{A\,w}{hatch\,a_s\,\sqrt{\rho}}\left(\frac{Q}{v}\right)^{3/2} \tag{9.3}$$

Given that all the Square series samples were manufactured in 17-4PH, all the material

property terms can be set to 1 (β, E, ρ, a_s). Further, provided comparison is made between samples of the same shape, the geometry parameters can also be set to 1 (A, I). Finally, it can be assumed that for a given layer in a fixed geometry and material, the temperature difference between peak and ambient will be constant, so ΔT=1. The thermal strain parameter can now be simplified to the form shown in Equation 9.4.

$$\epsilon^* = \frac{w}{hatch} \left\{ \frac{Q}{v} \right\}^{3/2} \tag{9.4}$$

The approach taken in the previous chapters was to use the melt pool model to predict the amount of variation that could be achieved in the output parameter (e.g. solidification rate), and compare it with evidence from literature to assess whether it could drive a change in microstructure. A similar approach cannot be taken for the thermal strain parameter ϵ^*, because it is a normalised parameter. There is no value of ϵ^* which is known to be the threshold for deformation-driven martensitic transformation in 17-4PH, and it cannot be directly related to true strain.

Instead, the model has been used to quantify the sensitivity of predicted thermal strain to changes in laser power, average scan speed and hatch spacing individually (Figure 9.8a). The model has also been used to demonstrate the potential range in ϵ^* (0.005 to 2.62) that can be achieved by a combination of all build parameters (Figure 9.8b). This analysis was carried out with a fixed absorption efficiency of 45 %.

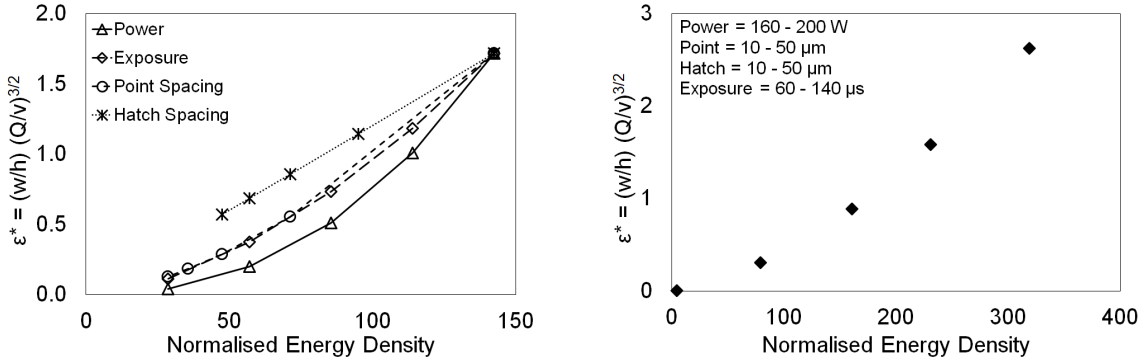

Figure 9.8: Sensitivity of normalised thermal strain parameter to build parameters a) Individually b) Combined.

Thermal strain is driven by the same factors as energy density, which can be seen from the similarity between the two expressions, recalled here as Equation 9.5 and Equation

9.6.

$$\epsilon^* = \frac{w}{hatch}\left\{\frac{Q}{v}\right\}^{3/2} \tag{9.5}$$

$$E_0^* = \frac{1}{h^*}\frac{q^*}{v^* l^*} \tag{9.6}$$

Both ϵ^* and E_0^* are proportional to $\frac{Q}{v}$, albeit to a different power, and to $\frac{1}{h}$. For a fixed geometry and material, high energy density will have large melt pools driving high strain, while low energy density builds will have smaller melt pools with less strain.

The dependency of the thermal strain parameter to laser power and average scan speed is more complex than expected from $\left\{\frac{Q}{v}\right\}^{3/2}$ because they also impact the melt pool length w. Overall the study suggests that strain is most sensitive to power, least sensitive to hatch spacing, and can be varied by more than 500× by combined changes to the build parameters.

While promising, this could be an insufficient level of variation to drive measurable change in martensite content. Alternatively all conditions could experience high enough strain to cause full transformation, or not enough strain to transform and remain fully austenitic. The strain parameter is helpful, but it does not give enough information to make predictions about microstructure without experimental data to calibrate it.

9.4 Experimental

9.4.1 Analysis of earlier data

The model was used to predict ϵ^* for the Square, Hatch and Point series conditions from the previous chapters. The prediction was made using variable absorptivity, and the values of ϵ^* were normalised against that predicted for the highest E_0^* (S1) condition. The predicted values showed nearly an order of magnitude variation in ϵ^* between the highest and lowest energy density builds.

Reviewing the VSM data, ϵ^* showed a good trend to the martensite content for both the Square and Hatch Series (Figure 9.9), although the Point Series did not match this trend.

The Point Series samples had low build quality with high levels of porosity which may have influenced the strain profile through the sample.

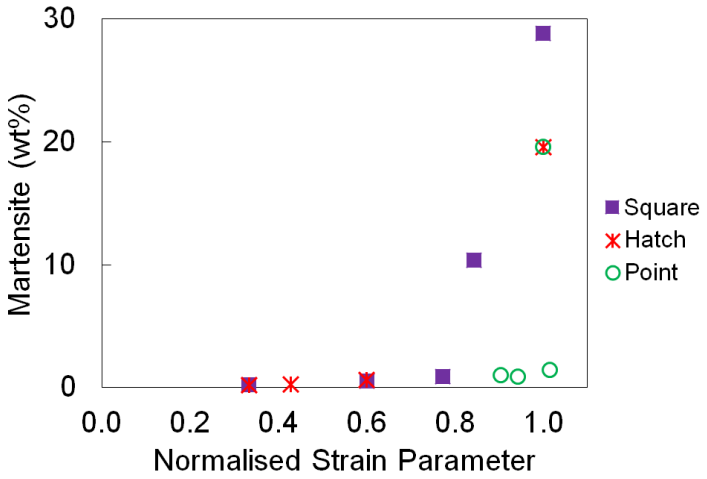

Figure 9.9: Bulk wt% martensite measured by VSM against normalised thermal strain parameter ϵ^*

The Feritscope data presented in the previous chapter (repeated as Figure 9.10) showed spatial variation in magnetic behaviour, with higher martensite content towards the top of the build, and on the outer surface compared with the middle of the build. This matches the locations of higher tensile strain found in SLM-built CrCoMo (Figure 9.5).

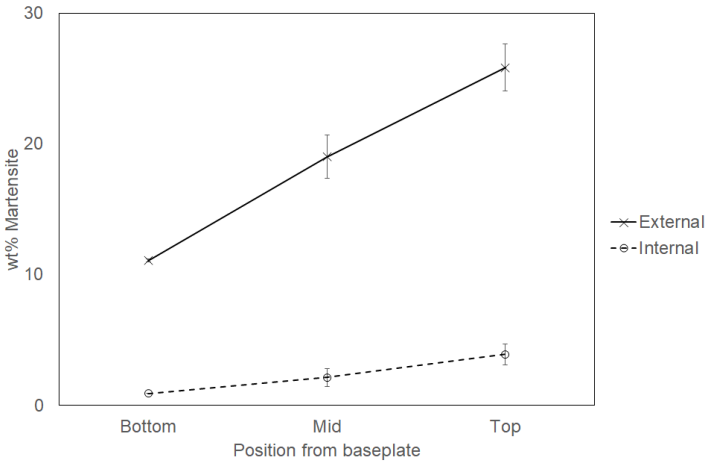

Figure 9.10: Spatial variation in martensite wt% for high E_0^* (S1) sample (repeated)

9.4.2 Method

To investigate strain independently of any other influencing factors, the next stage of experimental work focussed on changing component geometry with fixed build conditions. The component geometry is represented in Equation 9.3 through the second moment of area I and the cross-sectional area A.

The highest (S1) and lowest (S5) energy density conditions from the Square Series were used to build blocks with different cross-sections in the build plane (Figure 9.11). The blocks were all 10 mm wide and 15 mm high, and were 20 mm, 10 mm, 5 mm and 2 mm in length. All were built under argon, using a meander strategy with 67° rotation between layers. After building, the blocks were horizontally EDM wire-cut into 11 slices working from the top surface down to the baseplate, each slice approximately 1 mm thickness.

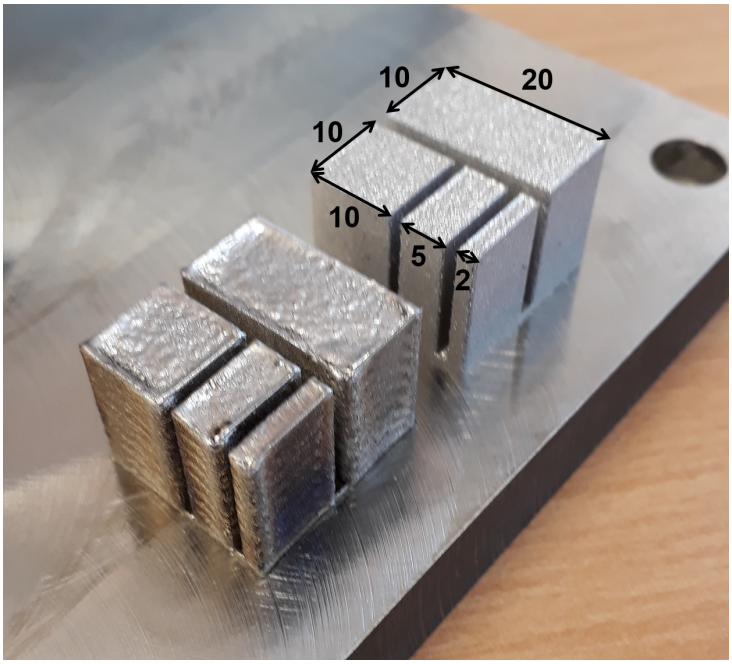

Figure 9.11: Geometry build to test for thermal strain. High energy density (S1) blocks in bottom left corner. Low energy density (S5) blocks in upper right corner. Dimensions in millimetres.

9.4.3 Feritscope

Feritscope measurements were taken in specific positions on each slice from each block, with three repeats in each position. For the high energy density (S1) blocks, the mean

readings for each slice show a trend of increasing martensite content with distance from the baseplate for all four cross-sections (Figure 9.12).

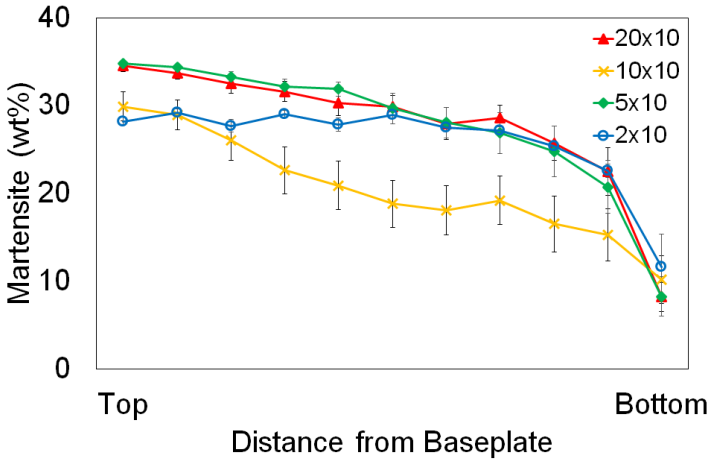

Figure 9.12: Mean martensite content of each slice by cross-section for high energy density (S1) blocks. Error bars show standard error.

The 20 mm and 5 mm blocks showed very similar trends, rising quickly through the first few millimetres up to around 25 wt% and then rising more slowly to reach 35 wt% by the top of the sample. The 2 mm block had the same initial trend but then saturated at 28 wt% after about 5 mm. The 10 mm block showed slightly different behaviour, with the martensite content rising more slowly and without reaching saturation.

The mean readings in each position on each slice also showed a secondary pattern of spatial variation across the blocks that persisted through the block height (Figure 9.13). The pattern was most distinct on the 20 mm sample, where one side of each slice showed a higher martensite content, as illustrated for a selection of slices in Figure 9.14.

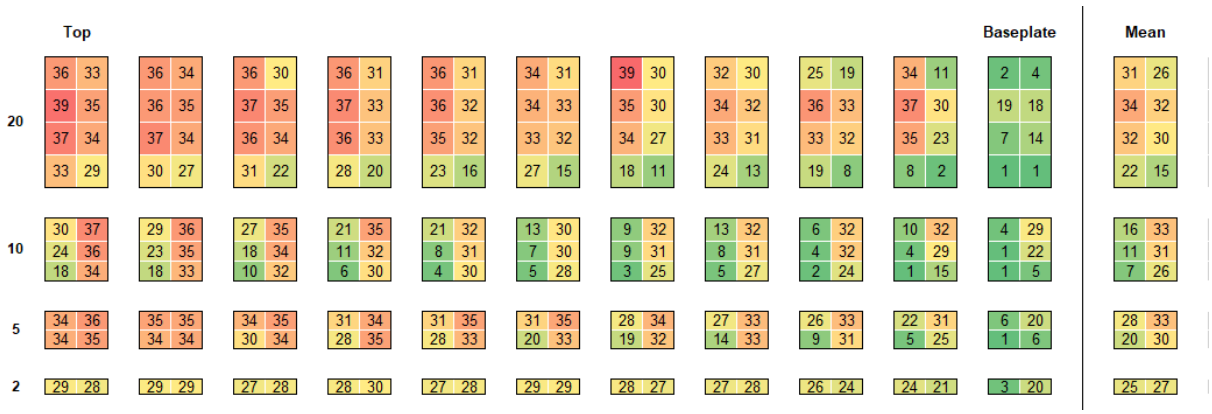

Figure 9.13: Martensite content by position for high energy density (S1) blocks

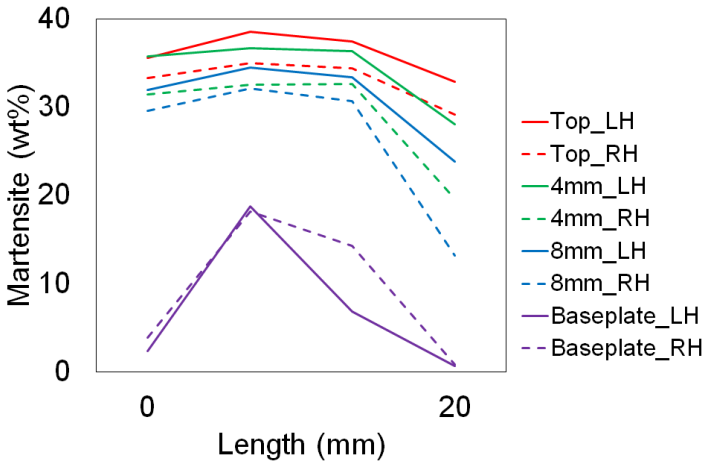

Figure 9.14: Martensite content by position for 20 mm length, high energy density (S1) block

The low energy density (S5) samples showed minimal martensite (< 0.5 wt%) for all blocks, in all positions and at all slice heights.

9.4.4 Pyrometer

A build of the same geometry was carried out on the Aconity Mini, which has a pyrometer co-located with the laser beam. The pyrometer was uncalibrated at the time of the trial, so the data was only suitable for comparative assessment rather than measurement of absolute temperatures.

The Aconity Mini uses a continuous laser beam, so the power was reduced to 186 W to bring it in line with the average power from the pulsed Renishaw SLM125, and the scanning speed was set to 280 mm s^{-1}. As with the builds on the Renishaw SLM125, there was 67° rotation between layers, a 30 µm hatch spacing and 40 µm layer thickness. The build was terminated after 30 layers.

The data was averaged across the slices, and sampled over the same area as the Feritscope data, to generate a spatially resolved representation of comparative temperature (Figure 9.15). This showed that the average temperature increased with reducing block size, and that the difference between blocks was greater than the variation within any individual block.

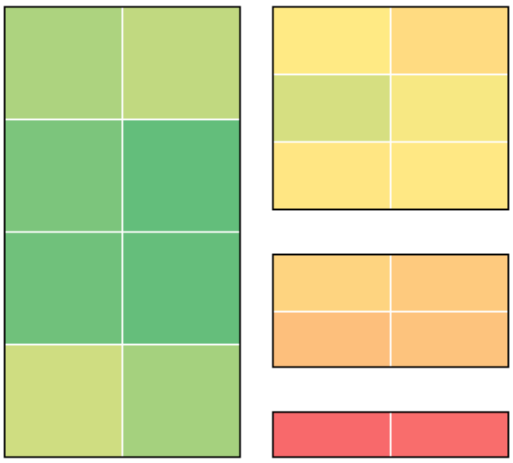

Figure 9.15: Average temperature for high energy density blocks measured by pyrometer, shown in build position on the baseplate. Red indicates high average temperature, yellow indicates intermediate temperature and green indicates low average temperature. Specific temperatures are not shown because the pyrometer was uncalibrated.

This pattern is expected because the larger samples will have a longer return time between hatches, allowing more time for the bulk to cool down and reducing the overall average temperature.

9.4.5 XRD

The XRD traces were initially examined for evidence of ϵ-martensite, which can be an intermediate/concurrent phase during transformation to deformation-martensite.

The lattice parameters for ϵ-martensite in 310LN steel are a =2.54 Å and c =4.16 Å [87]. The $\{0002\}_\epsilon$ peak would be expected near 47.6° and that of the $\{10\bar{1}1\}_\epsilon$ peak near 48.5°. The measured intensity in the region 46° to 49° was completely flat for all samples, with no evidence of ϵ-martensite (Figure 9.16).

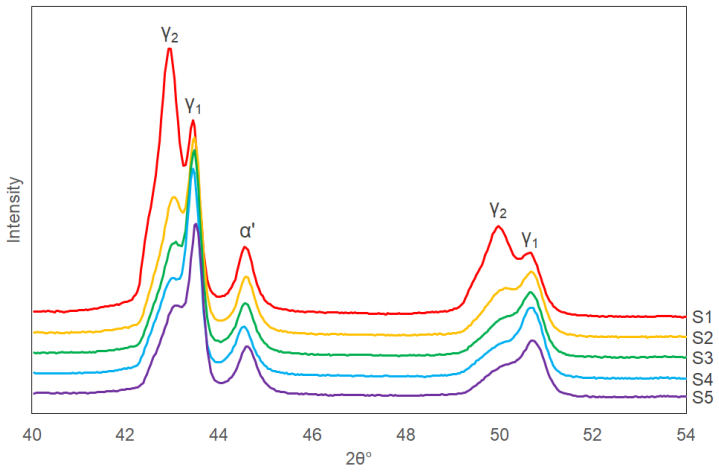

Figure 9.16: Slow scan XRD through 40° to 60°

The peak positions of the two austenite phases were used to calculate their respective lattice parameters for each of the Square Series samples. This showed the γ_1 phase (higher 2θ) to have a consistent lattice parameter of 3.60 Å across the range of energy density. The γ_2 phase (lower 2θ) had slightly more variation between samples but no consistent trend, with an average lattice parameter of 3.64 Å, a shift of 1.2 %.

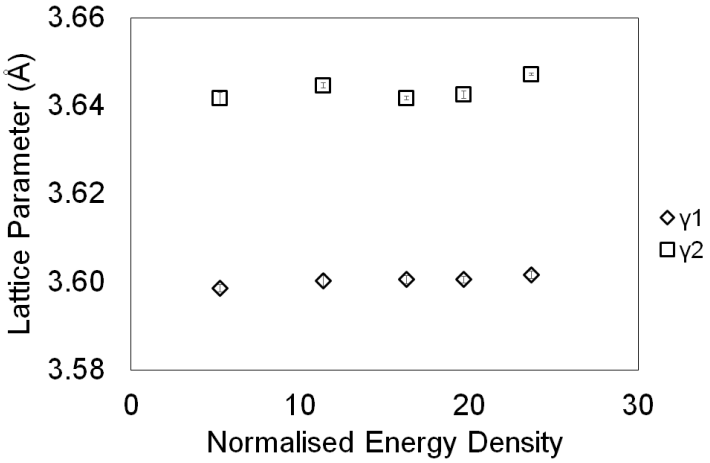

Figure 9.17: Lattice parameter of γ_1 and γ_2 peaks by energy density. Error bars show standard error.

Recalling the stress-strain curves for SLM-built 316L and 17-4PH (Figure 9.6), this lattice shift is greater than the strain to reach yield. The austenite would be expected to have transformed to martensite before this point, so the γ_2 phase is unlikely to be strained untransformed austenite.

9.5 Discussion

Additively manufactured components commonly suffer from thermal strain, in some cases to levels that can distort the component during build. Investigations have shown that stress is primarily in the build direction (vertical) and increases with distance from the base plate. There is also evidence of tensile vertical stresses around the edges of AM-built components, balanced by compressive vertical stresses in the middle.

In the earlier chapters it was determined that thermally-activated martensite was completely suppressed in SLM-built 17-4PH by the fine grain/cell size resulting from rapid solidification. Yet, the highest energy density samples showed up to 28 wt% martensite, raising the possibility that it was deformation-driven martensite caused by thermal strain during the build.

Melt pool modelling predicted that it was possible to vary ϵ^*, a normalised thermal strain parameter, by up to 500× through control of power, exposure time, point spacing and hatch spacing. However, being an uncalibrated, normalised parameter, it was not possible to predict whether this would be sufficient to drive martensitic transformation.

Reviewing the earlier experimental data identified that the Square and Hatch series had a good correlation between ϵ^* and martensite content, although the Point Series did not match the same trend. The Point Series samples had low build quality with high levels of porosity which may have influenced the strain profile through the sample, affecting the extent of martensitic transformation.

The spatially resolved Feritscope data from a high energy density (S1) cuboid showed martensite content increasing with build height, corresponding with the increased strain reported in the literature. Additional samples, manufactured using the high energy density parameters but with different cross sectional areas, again confirmed the variation in martensite content with build height, with most samples showing the martensite content reaching a maximum over the first few millimetres of build height.

The strain caused by the expansion and contraction of the melt pool acts over a relatively limited depth, around 10× the melt pool depth. For the initial layers this includes the baseplate, which is much larger than the sample geometry and therefore significantly increases rigidity, reflected in the thermal strain parameter by the second moment of area, I. High rigidity minimises the thermal strain caused by deflection of the top surface (Fig-

ure 9.1). As layers are added, the region over which the strain acts moves upwards, away from the baseplate and the rigidity dramatically reduces. This allows more deflection, so strain and deformation-martensite content both increase.

There was found to be variation in martensite content between samples of different cross-sectional aspect ratio and different cross-sectional area, even when manufactured using the same build parameters. The larger sample, 20 mm length, had generally higher martensite, even though the pyrometer data indicated the average temperature was lower. Recalling the equation for the thermal strain parameter (Equation 9.7), for builds with the same material and same build parameters, there is a balance between temperature range ΔT, deposition time per layer t and second moment of area I.

$$\epsilon^* = \frac{\beta\,\Delta T}{E\,I}\frac{t_{dep}}{F\sqrt{\rho}}\,H^{3/2} \tag{9.7}$$

A lower average temperature suggests a smaller temperature range ΔT, and a larger surface area indicates higher rigidity I, both of which would reduce ϵ. But this is countered by a larger area driving a longer deposition time T_{dep}, which would increase ϵ. It is the relative strengths of these which determine the overall strain, and therefore martensite content, of a particular geometry.

The absence of ϵ-martensite, which is associated with stacking faults, does not preclude deformation-driven transformation to a'_s-martensite. Stress-assisted transformation uses existing nucleation sites, rather than stacking faults, and has been observed both before and after yield. Additionally, material with a fine austenite grain size, comparable with that of the SLM-built samples, has been reported to transform to α'-martensite directly without any ϵ-martensite being observed [87].

In summary, having suppressed thermally-activated martensite, transformation to deformation martensite has occurred due to thermal strain accrued during the SLM build. The magnitude of thermal strain, and therefore martensite phase fraction, has been controlled through energy density for a fixed geometry, or through geometry for a fixed energy density.

Chapter 10

Second Austenite Phase

10.1 Background

In the earlier chapters, XRD data was presented showing the presence of two austenite phases, with slightly different lattice parameters (Figure 10.1). The phase at higher 2θ was designated γ_1, and the phase at lower 2θ was designated γ_2.

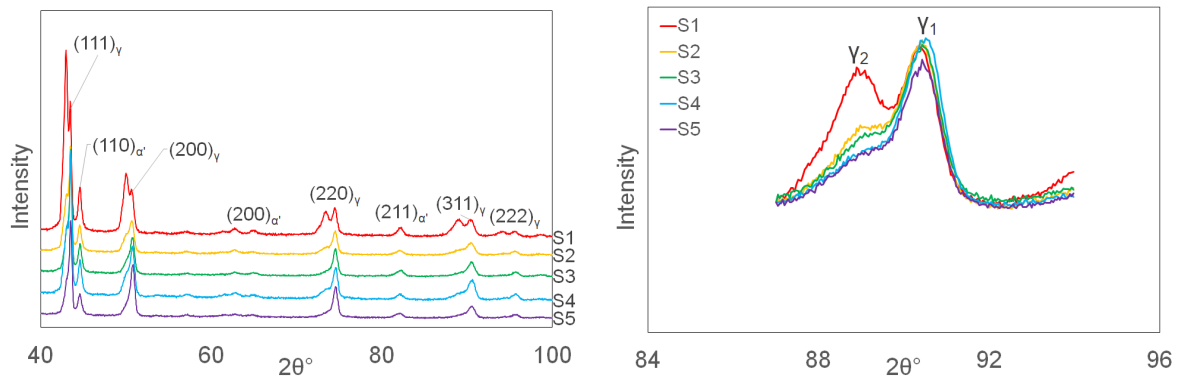

(a) **(b)**

Figure 10.1: XRD showing two austenite phases at different 2θ. a) Full scan from 40° to 100°, 0.039° step size, 1120 s per step. b) Detailed scan from 87° to 94°,0.039° step size, 5000 s per step.

The peak positions were used to determine lattice parameter for the two phases individually. The γ_1 phase had a lattice parameter of 3.60 Å, and the γ_2 phase had a lattice parameter of 3.64 Å (Figure 10.2a). The difference between the two corresponded to a

lattice shift of 1.2 %, which was stable across the range of energy densities in the Square Series (Figure 10.2b).

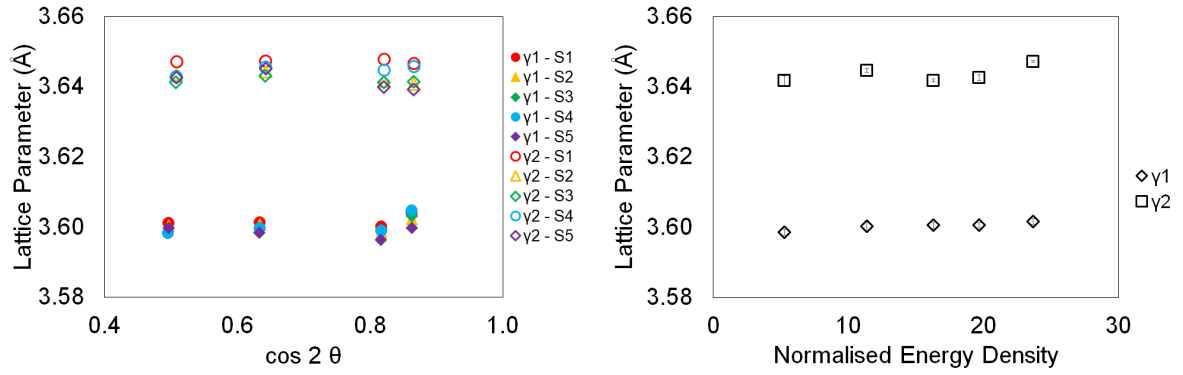

(a) **(b)**

Figure 10.2: a) Determination of lattice parameter for γ_1 and γ_2 in each Square Series condition. b) Lattice parameter by energy density, error bars show standard error from (a).

The XRD data was deconvoluted in Origin to calculate peak areas for the two phases (Figure 10.3a). Assuming both phases have the same structure factor, the ratio of γ_1 to γ_2 was calculated from the ratio of their peak areas, summed over the four peaks in the 40° to 100° range. Using the VSM data presented earlier to obtain the γ-austenite to α'-martensite phase fraction, this was then used to determine the phase fraction of α', γ_1 and γ_2 across the Square Series samples (Figure 10.3b).

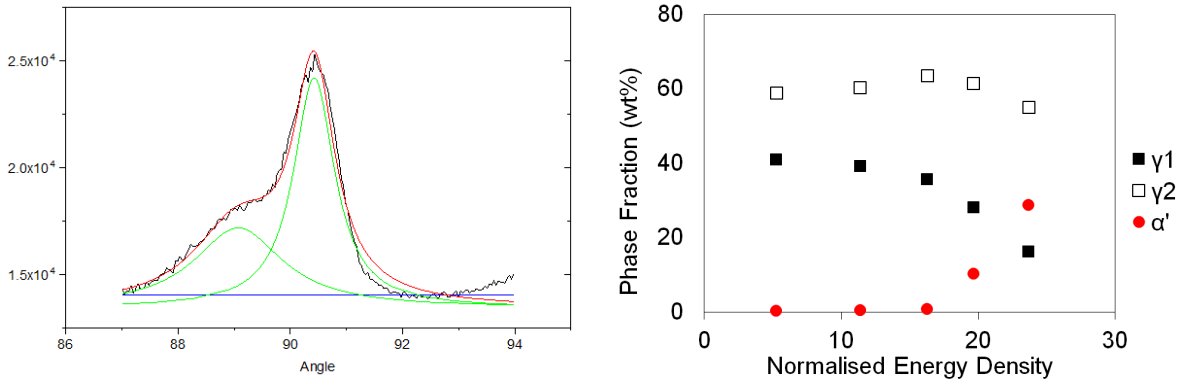

(a) **(b)**

Figure 10.3: a) Example Origin peak deconvolution for low energy density (S5) sample from Square Series. b) Phase fraction of α', γ_1 and γ_2 across the Square Series samples.

This showed the fraction of γ_2-austenite to be constant around 55 % to 65 %, while the

γ_1-austenite reduced as α'-martensite phase fraction increased.

A further observation was that the γ_2 peak disappeared completely when the surface was manually polished with 600-grit SiC paper. This occurred for both the high and low energy density samples.

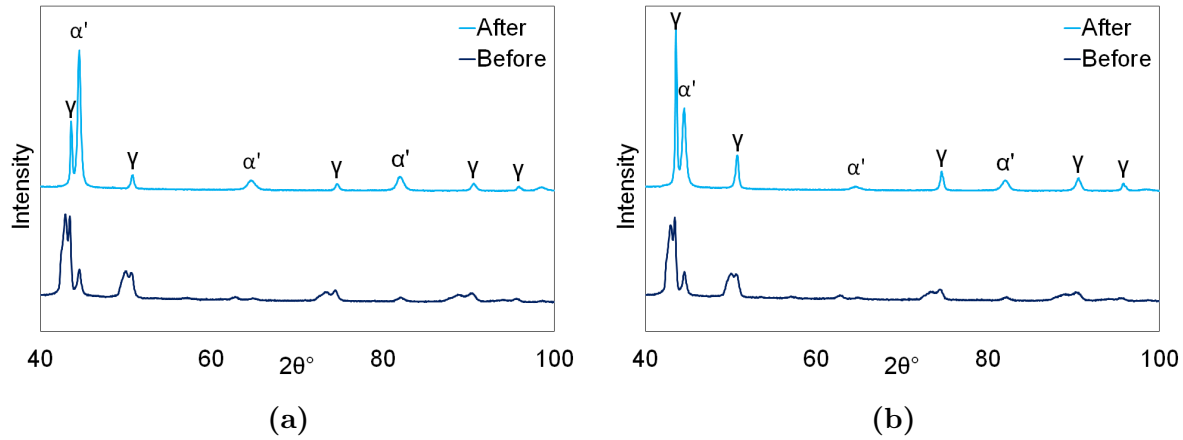

Figure 10.4: XRD for 17-4PH before and after manual polishing, showing change in phase fraction of γ_1, γ_2 and α'.

Investigation of this split austenite considered a number of areas, which are presented below with their respective discussion points.

10.2 Monochromated Beam

The copper source used in the XRD analysis was not monochromated, both $K_{\alpha 1} = 1.5406\,\text{Å}$ and $K_{\alpha 2} = 1.5444\,\text{Å}$ wavelengths were used to generate data.

For the austenite (111) plane, assuming a lattice parameter of 3.60 Å, the peak from $K_{\alpha 1}$ would be at 43.51° of 2θ, and from $K_{\alpha 2}$ at 43.62° of 2θ. This shift is far smaller than that observed between γ_1 and γ_2, so it cannot explain the peak split although the use of both wavelengths would have contributed to overall peak broadening.

Further, there were no split peaks for the α'-martensite which would be expected if the use of both wavelengths were responsible for the split austenite peaks.

10.3 Mechanical Strain

The SLM-built material is known to have sufficient levels of thermal strain to have caused deformation-driven martensitic transformation in the higher energy density (higher thermal strain) samples.

The lattice shift between γ_1 and γ_2 was 1.2 %. Stress-strain data for SLM-built 17-4PH (Figure 10.5a) shows this to be beyond the yield point, although the data in this instance was from a dual phase structure, so there may be an influence from martensite in the mechanical behaviour.

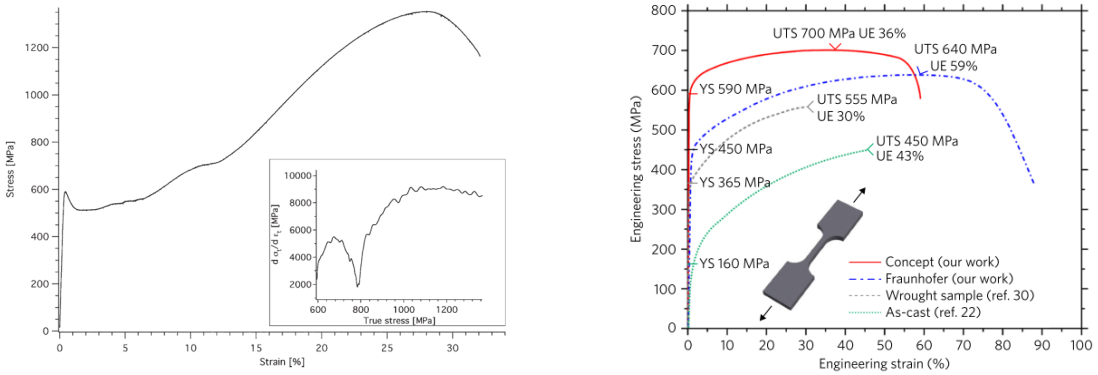

(a) **(b)**

Figure 10.5: Stress-strain data for SLM-built material a) 17-4PH [5] b) 316L [165].

316L stainless steel has a similar composition to 17-4PH but is fully austenitic. For SLM-built 316L with a grain size comparable to that demonstrated in this work, the yield stress was 590 MPa (Figure 10.5b) [165]. Taking the Young's modulus of 316L to be 200 MPa [180], a fully elastic strain of 1.2 % would require a stress of 2400 MPa, far beyond the yield stress . This indicates that the γ_1-austenite would have yielded long before achieving the level of elastic strain necessary to account for the lattice shift.

Even if the stress-strain data for 316L were not representative for these samples, and it was possible to reach 1.2 % strain elastically, there are further issues with a mechanical explanation:

1. The retained austenite in SLM-built 17-4PH is metastable, this amount of strain should have driven transformation to martensite.

2. To avoid martensite formation, γ_2 austenite would need to be mechanically sta-

bilised, where the dislocation density is sufficiently high to block movement of the $\alpha' - \gamma$ interface [105]. This is observed for engineering strains of $> 80\,\%$, much greater than the $1.2\,\%$ in this instance.

3. Thermal strain increased with energy density, as seen by the increasing proportion of martensite, yet the phase fraction of γ_2 was constant. For the low energy density (S5) condition there was insufficient strain to drive martensitic transformation, yet there was still $60\,\text{wt\%}$ γ_2.

4. A significant proportion of austenite has remained at the original lattice parameter, apparently unstrained, and there are no intermediate conditions.

10.4 Solidification Segregation

The rapid solidification caused by the SLM build process is far from equilibrium, although not necessarily fast enough to result in solute trapping.

Table 10.1: 17-4PH Simplified Composition (wt%)

Fe	Cr	Ni	Cu	Mn	Si	C	Nb	Mo	V	W	P	S	Al
balance	15.51	4.56	4.31	0.79	0.71	0.05	0.26	0.09	0.03	0.02	0.014	0.07	0.03

Using Thermocalc [160, 161], a Scheil-Guliver simulation was carried out on a simplified composition (Table 10.1), to identify the potential for segregation during solidification. This predicted that both chromium and carbon would significantly partition into the liquid phase, such that the final $20\,\%$ of liquid would have $26.8\,\text{wt\%}$ Cr and $0.88\,\text{wt\%}$ C.

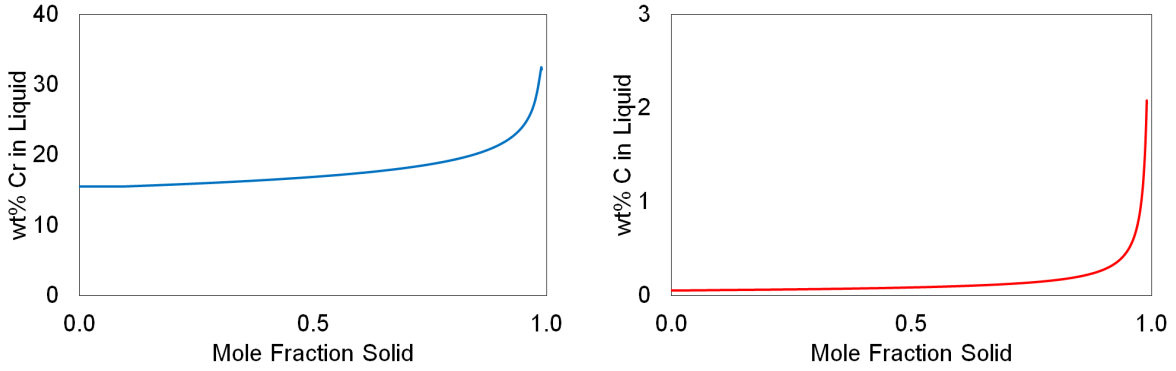

(a) Chromium **(b)** Carbon

Figure 10.6: Scheil-Guliver segregation during solidification

From the composition, Equation 10.1 was used to calculate expected lattice parameters for the bulk and final liquid, where w_x is the weight fraction of each element [63–65]. The bulk composition was predicted to have a lattice parameter of 3.589 Å, 0.3 % below the 3.60 Å measured from the XRD data for γ_1. The final liquid composition was predicted to have a lattice parameter of 3.624 Å, 0.5 % below the 3.64 Å measured from the XRD data for γ_2.

$$\begin{aligned} a_\gamma = {} & 0.3578 + 0.33\, w_C + 0.0095\, w_{Mn} - 0.002\, w_{Ni} \\ & + 0.006\, w_{Cr} + 0.056\, w_{Al} + 0.031\, w_{Mo} + 0.018\, w_V \end{aligned} \tag{10.1}$$

However, the phase fraction analysis shows there to be a constant 55 % to 65 % of γ_2 across all Square Series conditions. This is not consistent with γ_2 being the final 20 % of liquid to solidify.

Further, the Scheil-Guliver simulation shows the composition of the last liquid changing gradually, rather than as a sharp cut-off. XRD data should therefore show asymmetric peak broadening, in the direction appropriate for the elements being partitioned into the liquid. Then if the composition reached a eutectic, the broadening effect would be curtailed. Segregation would not result in solidification at one composition, then a gap, followed by solidification at a different composition.

Examination of Equation 10.1 also shows that the majority of the lattice shift is driven by carbon. The Scheil-Guliver approach assumes no back diffusion into the solid, however

carbon is an interstitial element and will diffuse relatively easily, so some back diffusion may occur, reducing the level of segregation.

10.5 Carbon Partitioning from Martensite

It has been reported for other alloys that transformation from austenite to bainitic ferrite has been accompanied by growth of a secondary austenite phase with a larger lattice parameter than the original material (Figure 10.7a) [65, 181].

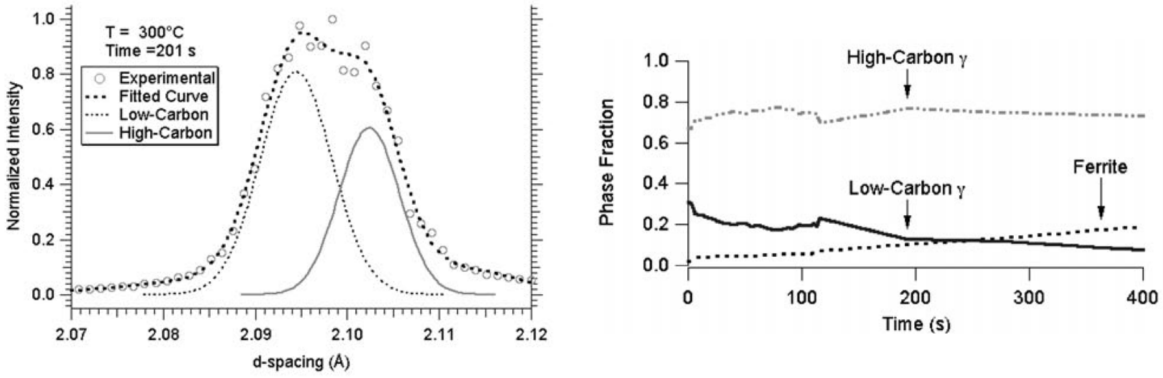

(a) **(b)**

Figure 10.7: Formation of high-carbon austenite by carbon partitioning from bainitic ferrite. a) (111) diffraction peak from FCC austenite, showing two austenite phases with different lattice parameters. b) Impact of increasing phase fraction of bainitic ferrite on phase fraction of low-carbon austenite and high-carbon austenite. [65]

It has been proposed in the literature that bainitic ferrite, forming by a displacive mechanism from the parent austenite, is initially supersaturated with carbon. The bainitic ferrite plates reject carbon into the austenite directly in contact with them, creating a new austenite phase of much higher carbon content. This causes an increase in austenite lattice parameter, according to Equation 10.1, where it can be seen that carbon has the strongest effect on the size of the austenite lattice.

The data showed this high-carbon austenite forming as soon as the bainitic transformation started, reaching 70 % phase fraction immediately, and then staying at that level for the duration of the experiment (Figure 10.7b). In contrast, the phase fraction of low-carbon austenite fell as that of the bainite increased.

This is a very similar pattern to that observed from the split austenite peaks in the Square Series data. Assuming both γ_1 and γ_2 to have the bulk composition with the exception of carbon, Equation 10.1 was used to calculate the carbon content necessary to achieve the individual lattice parameters determined from the XRD peaks. This indicated that γ_1, lattice parameter 3.60 Å, would require 0.38 wt% carbon and γ_2, lattice parameter 3.64 Å, would require 1.71 wt% carbon.

Considering the high energy density (S1) condition, there was 16 % γ_1 and 55 % γ_2. Even assuming no carbon in the martensite, to achieve the calculated carbon contents would require a bulk average of around 1 wt%, much higher than that measured in the chemical analysis of the raw powder.

One possibility was that carbon could have been picked up during the build, through an unidentified contamination route. To investigate this, solid post-build samples were sent for chemical analysis for comparison with the original powder chemistry. The results showed minimal shifts for carbon and the major alloying elements (Table 10.2).

Table 10.2: 17-4PH Powder & Solid Composition (wt%)

	Cr	Ni	Cu	Mn	Si	C	Nb	Mo	V
Powder	15.51	4.56	4.31	0.79	0.71	0.05	0.26	0.09	0.03
Solid	15.80	4.61	4.52	0.74	0.78	0.03	0.32	0.09	0.04

This suggests that while carbon partitioning fits the splitting of the austenite peaks observed in the XRD data, there is insufficient carbon to drive 60 wt% of γ_2 phase with the measured lattice parameter. The extra carbon would also stabilise the γ_2, making it less susceptible to martensitic transformation, which conflicts with the observation of γ_2 being preferentially transformed by manual polishing.

10.6 Summary

The XRD data identified the presence of two austenite phases, with distinctly different lattice parameters. The discussion above covers a number of mechanisms that could have caused this split in the austenite phases, however none of them have been capable of explaining all the experimental observations.

The presence of two austenite phases does not detract from the ability to control the austenite-martensite phase fraction of SLM-built 17-4PH and thereby achieve a magnetically graded material. The explanation for this split austenite is therefore judged to be the subject of future work, outside the scope of this study.

Possible avenues that would be worth considering are:

- Electron diffraction and EBSD studies, to identify the location of the γ_1, γ_2 and α' phases
- Glancing angle XRD, to identify whether γ_2 could be a surface effect caused by the EDM process

Chapter 11

Application

This work has focussed on exploiting the solid-state transformation from austenite to martensite to make a magnetically graded material from a single composition of stainless steel. One potential application for this type of material is in electrical machine architectures, where magnetic and non-magnetic materials are used to direct and contain magnetic flux. The specific application considered here is for synchronous reluctance motors, creating mechanical support struts without flux leakage [23, 24].

11.1 Manufacture

An off-the-shelf induction motor was purchased (TEC 0.12kW 4 pole 3 phase AV motor, model 56M4C-TECA), stripped down and the dimensions of the rotor recorded.

A new synchronous rotor of identical external dimensions was manufactured using the Renishaw SLM125 with 17-4PH powder. The ferromagnetic shells (flux guides) were manufactured using high energy density (S1) build parameters, while the support struts used low energy density (S5) build parameters (Table 11.1). All regions used the meander strategy with 67° rotation between layers and built under argon.

Table 11.1: Synchronous Motor Build Parameters

Sample ID	Power W	Exposure µs	Point Spacing µm	Hatch µm	Layer µm	E_0^*
S1	200	100	30	30	40	26.5
S5	200	100	90	90	40	3.3

The build was carried out as three sections, each 15 mm in length, built concurrently on a single baseplate. After building the sections were removed from the baseplate by EDM.

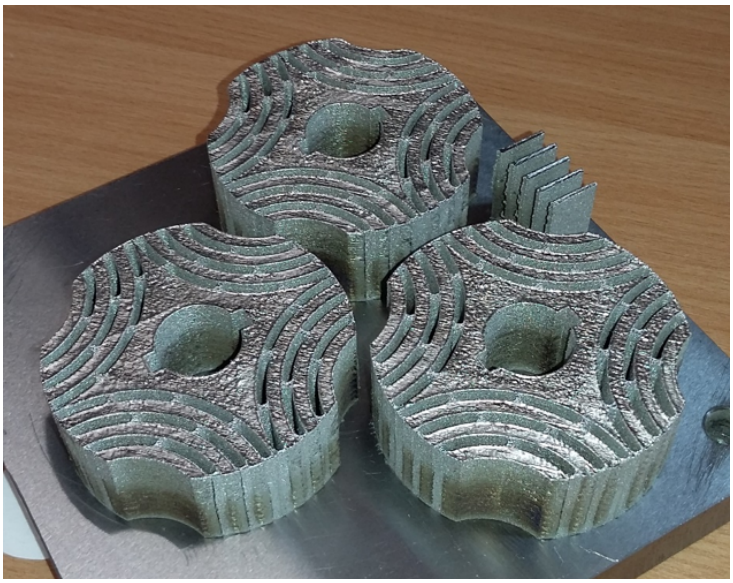

Figure 11.1: Rotor sections after build

The graded samples created in the previous chapters had one STL file for each build condition, which were then placed adjacent to each other. The STL files were overlapped by 0.1 mm to 0.2 mm to improve bonding. For the rotor, one STL file was created for the high energy density (S1) shells and one for the low energy density (S5) struts. It was not possible to overlap them in the same way due to the complexity of the geometry, and as a result the built rotor showed some cracking at the interfaces between the build conditions.

To improve mechanical stability around the cracking, the three sections of the rotor were clamped together and filled with magnetically insulating resin. The SLM-built rotor was then fitted to a new shaft and positioned inside the original stator windings before being run (Figure 11.2).

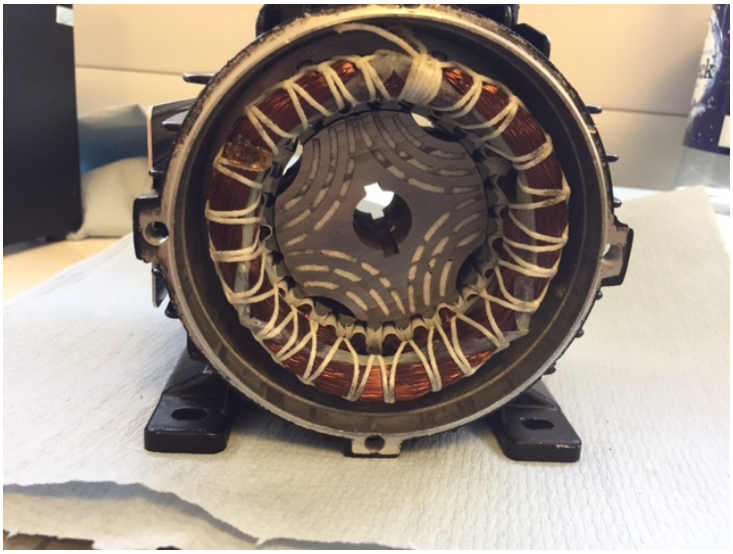

Figure 11.2: Off-the-shelf motor with SLM-built rotor fitted

11.2 Operation

The motor was operated at 100 rpm to 400 rpm with current probes to measure the 'pulse width modulated' supply from the drive electronics. Dynamometer speed and torque curves were not taken as this was a demonstrator motor rather than an optimised machine.

The output showed the rotor turning successfully, confirming that sufficient flux was retained within the ferromagnetic shells to allow the motor to operate (Figure 11.3).

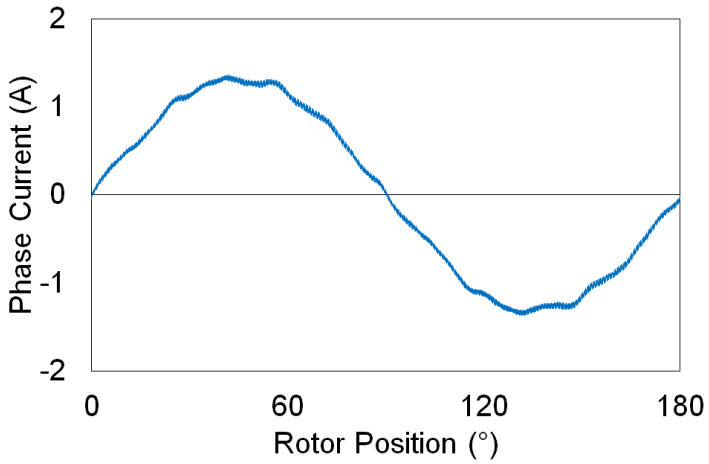

Figure 11.3: Current generated by synchronous motor using SLM-built magnetically graded rotor at 400 rpm

Chapter 12

Further Work

All the samples prepared in this study had higher energy density than normally used for SLM-builds. This caused them to exhibit keyhole-mode melting, with very deep narrow melt pools and associated keyhole pores. The result was that while the microstructural and magnetic properties achieved the intended objective, the build quality was poor compared with a normal SLM build. It would therefore be useful to investigate whether similar control of microstructure could be achieved at lower energy density and with lower porosity.

The thermal strain parameter was used to compare the levels of strain predicted for a particular set of build parameters and geometry. However this is a normalised and uncalibrated parameter, which could not be directly related to the onset or progress of martensitic transformation. In addition, the normalised thermal strain parameter gives a single value for a whole build/geometry, whereas the Feritscope data clearly showed variation in martensite phase fraction across different regions of the samples. To allow this type of magnetically graded material to be fully engineered, it would be beneficial to develop a model for predicting the actual strain achieved in different regions of a build, and then relating that directly to the extent of martensitic transformation.

This study achieved the objective of a fabricating a microstructurally and magnetically graded material because 17-4PH has a thermal martensite start temperature that is capable of being suppressed below room temperature by the grain/cell sizes achievable by SLM, and the resulting retained austenite has a sufficiently low stacking fault energy to be highly susceptible to deformation-driven transformation. However, 17-4PH is a steel designed for structural applications, rather than electrical machines. Looking towards ap-

plications for electrical machine architectures, it would be necessary to identify an alloy composition with good electrical performance that was also capable of being microstructurally controlled in this way.

Alternatively, a microstructurally graded material with controllable austenite:martensite phase fraction may have useful mechanical properties. For example, it could be possible to build a single-composition component where the onset and extent of transformation induced plasticity was spatially controlled. Development of this concept would require fabrication, mechanical testing and modelling of samples with a range of phase compositions.

Finally, aside from the original objective of a graded material, the XRD data showed the presence of two austenite phases of different lattice parameters. It has not been possible to explain this observation so far, and further analysis is required through a combination of EBSD, electron diffraction and glancing angle XRD.

Chapter 13

Conclusions

The aim of this work was to use additive manufacturing processes to create a magnetically graded material from a single composition of stainless steel, exploiting the solid-state transformation between paramagnetic austenite and ferromagnetic martensite. The specific objectives were:

- Can thermally-driven martensitic transformation be suppressed in SLM-built 17-4PH to yield a fully austenitic material?
- Can martensitic transformation be triggered and controlled (thermally or mechanically) in-situ to give variation in phase fraction in the as-built material?
- Do these materials show different magnetic properties?
- Can these materials be combined to produce a microstructurally and magnetically graded material?
- Can this approach be used to fabricate a magnetically graded rotor for a synchronous motor?
- Can a model be created to predict the melt pool geometry, cooling rate and other associated parameters?

17-4PH was chosen as the target alloy because the literature showed a variation in the ratio of austenite:martensite reported from different studies, suggesting the transformation was sensitive to SLM build parameters.

The early chapters covered the development of a Matlab model capable of predicting the melt pool geometry, cooling rate and duration of in-situ heat treatment. This was validated by a series of melt tracks, which initially showed good correlation between the melt tracks and the melt pool geometry predicted using a fixed absorption efficiency. However, comparison with microstructural data from actual builds showed that absorption efficiency was dependent on energy density. The model was modified to allow for a variable absorption efficiency, the value of which was determined for each energy density condition individually.

Other studies on 17-4PH had shown that the level of retained austenite was higher in SLM-built samples than in conventionally manufactured material. This had been attributed to the effect of rapid solidification driving a fine austenite grain size, suppressing the martensite start temperature. This was investigated in Chapter 7, where it was shown that all SLM-built 17-4PH would have a hierarchical microstructure, with grains of 10 µm to 100 µm capable of suppressing the majority of martensitic transformation. These grains contain cells only 0.5 µm to 2 µm in diameter, which would further suppress the martensite start temperature, giving a fully austenitic structure at room temperature.

Experimental observation confirmed this, with the low energy density (S5) build having a fine cellular microstructure while a combination of magnetic characterisation and XRD confirming the sample to be fully austenitic with < 0.5 wt% martensite. The higher energy density (S1) build did show some martensitic transformation, but with a comparably fine cellular microstructure, indicating that there must be a secondary mechanism overriding the effect of grain/cell size.

The next chapter considered the role of in-situ heat treatment, as a potential mechanism for driving dislocation recovery, which might allow the cell structure to coarsen sufficiently for transformation to occur. However, a combination of Matlab modelling and experimental work determined that, even for extremely high energy density builds with small hatch spacings and thin layers, the duration of in-situ heat treatment would be insufficient to enable the amount of coarsening required. Further, electron microscopy showed no difference in cell size with energy density or between the surface and bulk of individual builds.

With thermally-driven martensitic transformation suppressed, Chapter 9 investigated the potential for deformation-driven transformation. The normalised thermal strain parameter was used to quantify the variation in strain achievable with SLM and across the

experimental samples, which showed that the phase fraction of martensite could be correlated with the amount of thermal strain. This was supported by spatially resolved data within individual samples, which showed higher martensite content where higher thermal strain was expected. Additionally, samples were built with fixed build parameters but different geometries, which showed variation in martensite content, which would not be expected if the martensite were thermally driven. This demonstrated that, while thermal martensite may have been suppressed, it was possible to trigger and control the transformation to deformation martensite in-situ during an SLM-build.

Magnetic characterisation by both VSM and Feritscope was used throughout the study to assess magnetic behaviour and carry out quantitative phase analysis. This confirmed that there had been a graduation in magnetic properties caused by the graduation in microstructure from fully austenitic to dual-phase. Further, these conditions were used to build both a magnetically graded cuboid presented in Chapter 7, and the magnetically graded rotor that was tested in Chapter 11.

Chapter 10 covered a short parallel investigation into a secondary austenite phase which was apparent from the XRD data. The mechanism behind this second phase has not been identified and will be the subject of further work.

The technique was used to build a magnetically graded rotor, which was demonstrated in a synchronous motor. While was a successful outcome for the trial, this type of magnetically graded motor built from 17-4PH would not actually be an efficient direct replacement for the current laminated rotor stacks built from electrical steels. This is due to the high coercivity and low permeability of 17-4PH compared with electrical steels, as demonstrated by the VSM hysteresis loops presented in Chapter 7. However, the ability to control the solid-state transformation from austenite to martensite, and allow scope for further strain-driven transformation post-build, means that this may have mechanical applications as a technique for fabricating graded TRIP materials.

The work presented has shown it is possible to control the microstructure, and therefore magnetic properties, of 17-4PH stainless steel by exploiting the deformation-driven transformation from paramagnetic austenite to ferromagnetic martensite. Firstly, the thermally-driven martensitic transformation is suppressed by the fine austenite grain structure resulting from the high solidification rates, then the extent of deformation-driven transformation is controlled through the magnitude of thermal strain, which is itself sensitive to build parameters and component geometry.

The residual austenite is highly metastable, and is susceptible to additional unintended transformation as a result of surface preparation. This must be taken into account when carrying out quantitative phase analysis to avoid over-measurement of the martensite phase fraction.

Appendix A

Glossary

Table A.1: Definition of Symbols

Symbol	Description	Value	Units	Reference
a_l	Thermal diffusivity of liquid	$k/(\rho C_{pliq})$	$\mathrm{m^2\,s^{-1}}$	
a_s	Thermal diffusivity of solid	$k/(\rho C_{psol})$	$\mathrm{m^2\,s^{-1}}$	
c	Laser travel velocity between points		$\mathrm{m\,s^{-1}}$	
$f_{\alpha'}$	Phase fraction of martensite		vol% or wt%	
f_γ	Phase fraction of austenite		vol% or wt%	
$hatch$	Hatch spacing		m	
i	Number of points in simulation			
j	Number of hatches in simulation			
k	Thermal conductivity (482 °C)	22.6	$\mathrm{W\,m^{-1}\,K^{-1}}$	[141]
$layer$	Layer thickness		m	
m_s	Saturation magnetisation		$\mathrm{emu\,g^{-1}}$	
$m_{s\alpha'}$	Saturation magnetisation of martensite	164.2	$\mathrm{emu\,g^{-1}}$	[138]
n	Laser efficiency	n_{abs}/n_τ		
n_{abs}	Absorption efficiency			
n_τ	Ramp-up efficiency			
$point$	Point spacing		m	
$r_{\alpha'}$	Aspect ratio of martensite plate	0.05		[74]
t	Time (elapsed during simulation)		s	
t_{dep}	Deposition Time		s	
v	Average travel velocity		$\mathrm{m\,s^{-1}}$	
w	Melt pool length		m	
A	Deposition area		$\mathrm{m^2}$	
C_{psol}	Specific heat capacity of solid (0 °C to 100 °C)	460	$\mathrm{J\,kg^{-1}\,K^{-1}}$	[141, 182]

Table A.1: Definition of Symbols (continued)

Symbol	Description	Value	Units	Reference
C_{pliq}	Specific heat capacity of liquid	541*	$\mathrm{J\,kg^{-1}\,K^{-1}}$	[183]
D_t	Solute diffusion coefficient in liquid	4.91×10^{-9}†	$\mathrm{m^2\,s^{-1}}$	[184]
E	Elastic modulus		Pa	
E_0^*	Normalised energy density			[148]
F	Fourier number	a_s/vw		
G	Thermal gradient		$\mathrm{K\,m^{-1}}$	
G^α	Gibbs free energy of ferrite (martensite)		$\mathrm{J\,mol^{-1}}$	
G^γ	Gibbs free energy of austenite		$\mathrm{J\,mol^{-1}}$	
H	Heat input per unit length	Q/v	$\mathrm{J\,m^{-1}}$	
I	Second moment of inertia		$\mathrm{m^4}$	
L_γ	Austenite grain size		m	
LH_m	Latent heat of melting	272.5‡	$\mathrm{kJ\,kg^{-1}}$	[185]
M_s	Martensite start temperature		°C	
M_s^0	Theoretical 'large grain' M_s		°C	
Q	Laser power		W	
Q_{act}	Activation energy for dislocation recovery	309§	$\mathrm{kJ\,mol^{-1}}$	[169]
Q_{eff}	Laser power adjusted for pulsed laser duty cycle		W	
R	Gas constant	8.314	$\mathrm{J\,mol^{-1}\,K^{-1}}$	
R_y	Fraction of recovery			
S	Sample size in laser travel direction		m	
$\dot{T}$	Cooling rate		$\mathrm{K\,s^{-1}}$	
T^*	Temperature for heat treatment comparison	800	°C	
T_0	Ambient temperature		°C	
T_b	Boiling temperature	3100¶	°C	[33]
T_c	Curie temperature		°C	
T_{liq}	Liquidus temperature	1440	°C	[140, 182]
T_{sol}	Solidus temperature	1404	°C	[140, 182]
V	Solidification front velocity		$\mathrm{m\,s^{-1}}$	
V_γ	Austenite grain volume	$\frac{4\pi}{3}(\frac{L_\gamma}{2})^3$	$\mathrm{m^3}$	
X	Position in direction of laser travel		m	
Y	Position transverse to laser travel		m	
Z	Position in build direction		m	
β	Coefficient of thermal expansion		$\mathrm{K^{-1}}$	
ϵ^*	Normalised thermal strain parameter			[179]

*Estimated based on ratio between C_{psol} and C_{pliq} for 304 stainless steel
†Diffusion coefficient for pure Fe at 1873 K
‡Average value for 316 stainless steel
§Average value for low-carbon steel
¶Value for 304SS

Table A.1: Definition of Symbols (continued)

Symbol	Description	Value	Units	Reference
κ	Partition coefficient	0.83[‖]		[186]
λ_1	Primary dendrite arm spacing		m	
μ	Magnetic permeability			
ρ	Density	7780	$\mathrm{kg\,m^{-3}}$	[141, 187]
σ	Beam radius		m	
τ	Exposure time		s	
χ	Magnetic susceptibility			
$\Delta G^{\gamma\alpha}$	Free energy change from austenite to ferrite		$\mathrm{J\,mol^{-1}}$	
$\Delta G_C^{\gamma\alpha}$	Critical free energy change at M_s^0		$\mathrm{J\,mol^{-1}}$	
ΔT	Temperature gradient (peak to ambient)		°C	
ΔT_0	Equilibrium freezing range	$T_{liq} - T_{sol}$	°C	
Γ	Gibbs-Thomson coefficient	$2{\times}10^{-7}$	K m	[188]

Table A.2: Definition of Terms

Exposure Time:	Duration of a laser pulse
Hatch Spacing:	Distance between adjacent lines of pulses, perpendicular to direction of laser travel
Layer Thickness:	Thickness of powder layer added
Meander:	Rotation of scan direction between layers of a build
Melt Pool:	Molten volume defined by isotherm at solidus temperature
Point Spacing:	Distance between laser pulses in direction of laser travel
STL file:	Digital file of component geometry

[‖] Partition coefficient for Cr in Fe-20Cr-1C

Table A.3: Definition of Acronyms

Acronym	Full Name
AM:	Additive Manufacture
BCC:	Body Centred Cubic
BCT:	Body Centred Tetragonal
BF:	Bright Field
COSHH:	Control of Substances Hazardous to Health
CTE:	Coefficient of Thermal Expansion
DF:	Dark Field
DOE:	Design of Experiments
EBSD:	Electron Backscatter Diffraction
EBW:	Electron Beam Welding
EDM:	Electro-Discharge Machining
EDS / EDX:	Energy-Dispersive X-ray Spectroscopy
FCC:	Face Centred Cubic
FG:	Functional Grading
FN:	Ferrite Number
FOD:	Focal Offset Distance
HAZ:	Heat Affected Zone
HCP:	Hexagonal Close Packed
HRTEM:	High Resolution TEM
HVEM:	High-Voltage Electron Microscopy
IPF:	Inverse Pole Figure
LENS:	Laser Engineered Net Shaping
OM:	Optical Microscopy
SEM:	Scanning Electron Microscopy
SFE:	Stacking Fault Energy
SLM:	Selective Laser Melting
STEM:	Scanning Transmission Electron Microscopy
TEM:	Transmission Electron Microscopy
TRIP:	Transformation Induced Plasticity
VSM:	Vibrating Sample Magnetometer
XRD:	X-Ray Diffraction

Appendix B

Health & Safety

Metallic powders are known for having significant heath and safety implications. The stainless steel powder used in this study had a COSHH assessment to identify the hazards and appropriate precautions, using the manufacturer's material safety data sheets for reference. The hazards included: skin sensitization, carcinogenicity, organ toxicity (repeated exposure), harm to aquatic life and flammability. The precautions included wearing of appropriate personal protective equipment (ventilated air mask, safety glasses, gloves, lab coat).

In addition, there were risk assessments in place for use of the additive manufacture machines and for some specific manual handling activities associated with the processes (fitting the powder hopper, emptying the wet vacuum cleaner), which identified the requirement to wear safety shoes.

Two etchant approaches were used. The main etchant was Kallings #2 reagent, which was mixed as required from 5 g copper II chloride, 100 ml ethanol and 100 ml hydrochloric acid.

The COSHH assessment for Kallings #2 reagent identified that it is highly flammable, is harmful if swallowed, causes severe skin burns and eye damage, causes respiratory irritation and is toxic to aquatic life. Etching was carried out using freshly mixed reagent contained within a fume cupboard, wearing PPE including nitrile gloves, safety glasses and lab coat. Used reagent was disposed of into a marked container within the laboratory fume cupboard for waste chemical collection.

Appendix C

Experimental Detail

All users of the SLM125 are trained in accordance with the local work instruction. The key stages in operation are:

Machine Set Up:

1. Check dosing mechanism on hopper is moving freely
2. Fill hopper with powder and load into back of upper build chamber (heavy item - 2 person lift)
3. Load baseplate into base of upper chamber, screwing down in all four corners
4. Fit silicon rubber bead into wiper blade
5. Load wiper blade into machine, use slip gauge to set wiper blade level with chamber floor
6. Gently brush powder into gaps around the edges of the baseplate
7. Adjust ram to move baseplate until the wiper blade just removes all powder
8. Clean the glass lens using lens wipes and lens cleaning fluid
9. Load build file
10. Check there is sufficient argon
11. Open the valves on the safe-change filter cartridge

12. Select automatic build and press start

Build:

1. Machine will pump down to vacuum, then back fill with argon
2. Argon will be pumped through until oxygen sensor reads less than 1000 ppm oxygen
3. After a 120 s hold time, the first dose of powder will be released
4. The wiper will move forward, distributing powder across the baseplate
5. The laser will load and process the first layer
6. This will be repeated (dose powder, wiper moves, laser) until all layers have been processed
7. The machine will then run a 5 min cool down before indicating that the build is complete

Clean Down:

1. Close the valves on the filter cartridge
2. Open the chamber door
3. Vacuum any burnt or discoloured powder from the chamber
4. Brush remaining excess powder into the overflow container
5. Unload the baseplate, wiper blade, hopper and overflow container
6. Remove the covers from the sides of the machine
7. Vacuum all surfaces of both upper and lower build chambers and the door
8. Thoroughly clean all surfaces of both upper and lower build chambers using blue roll and isopropanol

Clean Filter:

1. Check valves are closed and remove cartridge from the machine
2. Open the top valve on the filter cartridge, fill with water and allow to soak for 10 min
3. Drain and open the filter cartridge, remove the filter and dispose appropriately
4. Clean and fully dry the filter cartridge before fitting a new filter and replacing in the machine

Common Issues:

1. Powder ingress into the ram mechanism can lead to wear which causes increased backlash when moving the baseplate between layers, which can in turn result in variable layer thickness.
2. Gaps around the seals in the powder hopper can lead to powder leaking from the hopper, this does not affect build quality directly, but can cause the build to run out of powder early.
3. If the baseplate is not sufficiently flat, the first layer of powder can be too thick, resulting in poor adhesion between the first layer and the baseplate which can cause the part to peel off the baseplate during the build.
4. If a region of the part lifts up, often due to swelling (too much energy put in) or peeling (poor adhesion to lower layers), it can cut into the silicon bead in the wiper blade leading to uneven powder distribution.

Appendix D

Matlab Code

The Matlab code described below has been stored on the GitHub repository.

```
%Laser parameters
Qmax=200;                       %Laser power (W)
point=0.000030;                 %Point spacing (m)
hatch=0.000200;                 %Hatch spacing (m)
layer=0.000040;                 %Layer thickness (m)
tau=0.000100;                   %Laser ON time (s) pulse exposure
Samplesize=0.003;               %Sample size in beam travel direction (m)
c=4.1;                          %Laser travel speed between points (m/s)
n_abs=0.45;                     %Absorbtivity factor
sigma=0.000035;                 %Spot radius at half maximum (m)
v=(point)./(tau+(point./c));    %Apparent speed
nabla=(200./0.000013);          %Gradient of ramp up to maximum laser power, determined experimentally by Alistair Lyle
tau_ramp=(Qmax./nabla);         %Time to reach maximum power
Q=@(t) ((nabla.*t).*(t<=tau_ramp))+(Qmax.*(t>tau_ramp));    %Time dependent power

%Material properties (17-4PH Stainless Steel)
T0=(25+273);                    %Initial temperature (K)
Tliq=(1440+273);                %Liquidus Temperature (K)
Tsol=(1404+273);                %Solidus Temperature (K)
Tboil=3100;                     %Boiling Temperature (K)
rho=7780;                       %Density (kg/m3)
cp_sol=460;                     %Specific Heat by mass for solid 17-4PH (J/kgK)
cp_liq=(cp_sol).*(0.2/0.17);    %Specific Heat for liquid 17-4PH (J/kgK)
k=22.6;                         %Thermal Conductivity (W/mK)
LHm=272500;                      %Latent Heat of Fusion (J/kg)
a_sol=(k)./(rho.*cp_sol);       %Thermal Diffusivity of Solid (m2/s)
a_liq=(k)./(rho.*cp_liq);       %Thermal Diffusivity of Liquid (m2/s)
cp_v_sol=(cp_sol*rho);          %Specific Heat by volume for solid 17-4PH (J/m3K)
THAZ=(0.5).*Tsol;               %Heat affected zone temperature (K)

%Simulation size
step=0.000005;                   %Step size for simulation (m)
x=(-0.002000):step:(0.000200);          %Horizontal extent for simulation - travel direction
y=(-0.000400):step:(0.000400);          %Horizontal extent for simulation - across width
z=(-0.000400):step:0;                   %Vertical extent for simulation - depth
[X,Y,Z]=meshgrid(x,y,z);

%3D steady state Rosenthal, multiplied by 2 for semi-infinite solid
P_actual = integral(Q,0,tau,'ArrayValued',true);
P_ideal = Qmax.*tau;
n_tau=P_actual./P_ideal;
n=n_abs.*n_tau;

Q_eff=Qmax.*((tau)./(tau+(point./c)));

T=T0+(((n.*Q_eff)./(2.*pi.*k.*(sqrt((X.^2)+(Y.^2)+(Z.^2))))).*(exp((-v.*(X+(sqrt((X.^2)+(Y.^2)+(Z.^2)))))/(2.*a_sol))));
```

Figure D.1: Matlab code for Rosenthal

```
%Steady state temperature calculation
P_actual = integral(Q,0,tau,'ArrayValued',true);
P_ideal = Qmax.*tau;
n_tau=P_actual./P_ideal;
n=n_abs.*n_tau;

Q_eff=Qmax.*((tau)./(tau+(point./c)));
pulse=(tau+(point./c));          %Total pulse duration (s)
Meltsize1=0;

F=@(t) ((Q_eff.*n)./(pi.*rho.*cp_sol.*((4.*pi.*a_sol).^(1/2)))).*((t.^(-1/2))./((2.*a_sol.*t)+(sigma.*sigma)))...
    .*(exp(((-1).*(((X.^2)+(2.*X.*v.*t)+((v.^2).*(t.^2))+(Y.^2))./((4.*a_sol.*t)+(2.*(sigma.*sigma)))))-((Z.^2)/(4.*a_sol.*t))));

dT1=integral(F,0,pulse,'ArrayValued',true);

for tmax=(10*pulse):(pulse):100
    dT2=integral(F,0,tmax,'ArrayValued',true);
    shift=max(max(max(dT2-dT1)));
    if shift>0.1
        dT1=dT2;
    else
        break
    end
end

T=T0+dT2;
```

Figure D.2: Matlab code for Eagar

```
%Steady state temperature calculation
T=(X.*0)+T0;

%Hatch 1 - beam centreline
for il=0:round((-1)*((Samplesize./(-2))./point),0)
    if il==0
        F=@(t) ((Q(t).*n_abs)./(pi.*rho.*cp_sol.*((4.*pi.*a_sol).^(1/2)))).*((t.^(-1/2))./((2.*a_sol.*t)+(sigma.*sigma)))...
            .*(exp(((-1).*(((X.^2)+(Y.^2))./((4.*a_sol.*t)+(2.*(sigma.*sigma)))))...
            -((Z.^2)/(4.*a_sol.*t))));
        dT=integral(F,0,(tau),'ArrayValued',true);
    else
        tmax=(tau)+((il.*(tau+(point./c))));
        i2=(il*(-1));
        F=@(t) ((Q(t).*n_abs)./(pi.*rho.*cp_sol.*((4.*pi.*a_sol).^(1/2)))).*(((tmax+(t-tau)).^(-1/2))./((2.*a_sol.*(tmax+(t-tau)))+(sigma.*sigma)))...
            .*(exp(((-1).*((((X-(i2.*point)).^2)+(Y.^2))./((4.*a_sol.*(tmax+(t-tau)))+(2.*(sigma.*sigma)))))...
            -((Z.^2)/(4.*a_sol.*(tmax+(t-tau))))));
        dT=integral(F,0,tau,'ArrayValued',true);
    end
    T=T+dT;
end
```

Figure D.3: Matlab code for Pulsed

```
%Steady state temperature calculation
T=(X.*0)+T0;

%Hatch 1 - beam centreline
for il=0:round((-1)*((Samplesize./(-2))./point),0)
    if il==0
        tmax=(tau);
        F=@(t) ((Q(t).*n_abs)./(pi.*rho.*cp_sol.*((4.*pi.*a_sol).^(1/2)))).*((t.^(-1/2))./((2.*a_sol.*t)+(sigma.*sigma)))...
            .*(exp(((-1).*((X.^2)+(Y.^2))./((4.*a_sol.*t)+(2.*(sigma.*sigma)))))...
            -((Z.^2)/(4.*a_sol.*t))));
        dT=integral(F,0,tau,'ArrayValued',true);
    else
        tmax=(tau)+(il.*(tau+(point./c)));
        i2=(il*(-1));
        F=@(t) ((Q(t).*n_abs)./(pi.*rho.*cp_sol.*((4.*pi.*a_sol).^(1/2)))).*(((tmax+(t-tau)).^(-1/2))./((2.*a_sol.*(tmax+(t-tau)))+(sigma.*sigma)))...
            .*(exp(((-1).*((((X-(i2.*point)).^2)+(Y.^2))./((4.*a_sol.*(tmax+(t-tau)))+(2.*(sigma.*sigma)))))...
            -((Z.^2)/(4.*a_sol.*(tmax+(t-tau))))));
        dT=integral(F,0,tau,'ArrayValued',true);
    end
    T=T+dT;
end

% %Previous Hatches
for jl=1:round((-1)*((Samplesize./(-2))./hatch),0)
    for i2=((-1)*il):il
        if mod(jl,2)==0
            i3=i2*(-1);
        else
            i3=i2;
        end
        tmax=(tau)+((Samplesize./v).*jl)+((i3+jl)*(tau+(point./c)));
        F=@(t) ((Q(t).*n_abs)./(pi.*rho.*cp_sol.*((4.*pi.*a_sol).^(1/2)))).*(((tmax+(t-tau)).^(-1/2))./((2.*a_sol.*(tmax+(t-tau)))+(sigma.*sigma)))...
            .*(exp(((-1).*((((X-(i2.*point)).^2)+((Y+(jl.*hatch)).^2))./((4.*a_sol.*(tmax+(t-tau)))+(2.*(sigma.*sigma)))))...
            -((Z.^2)/(4.*a_sol.*(tmax+(t-tau))))));
        dT=integral(F,0,tau,'ArrayValued',true);
        T=T+dT;
        if i2==0
            maxdT=max(max(max(dT)))
        end
    end
    if maxdT<dtmax
        break
    end
end
```

Figure D.4: Matlab code for Hatches

```
%Steady state temperature calculation
for count=1:2
    T=(X.*0)+T0;

    %Hatch 1 - beam centreline
    for il=0:round((-1)*((Samplesize./(-2))./point),0)
        if il==0
            tmax=(tau);
            F=@(t) ((Q(t).*n_abs)./(pi.*rho.*cp_sol.*((4.*pi.*a_sol).^(1/2)))).*((t.^(-1/2))./((2.*a_sol.*t)+(sigma.*sigma)))...
                .*(exp(((-1).*((X.^2)+(Y.^2))./((4.*a_sol.*t)+(2.*(sigma.*sigma))))))...
                -(((Z./scaling).^2)/(4.*a_sol.*t))));
            dT=integral(F,0,tau,'ArrayValued',true);
        else
            tmax=(tau)+(il.*(tau+(point./c)));
            i2=(il*(-1));
            F=@(t) ((Q(t).*n_abs)./(pi.*rho.*cp_sol.*((4.*pi.*a_sol).^(1/2)))).*(((tmax+(t-tau)).^(-1/2))./((2.*a_sol.*(tmax+(t-tau)))+(sigma.*sigma)))...
                .*(exp(((-1).*((((X-(i2.*point)).^2)+(Y.^2))./((4.*a_sol.*(tmax+(t-tau)))+(2.*(sigma.*sigma))))))...
                -(((Z./scaling).^2)/(4.*a_sol.*(tmax+(t-tau))))));
            dT=integral(F,0,tau,'ArrayValued',true);
        end
        T=T+dT;
    end

    %Previous Hatches
    for jl=1:round((-1)*((Samplesize./(-2))./hatch),0)
        for i2=((-1)*il):il
            if mod(jl,2)==0
                i3=i2*(-1);
            else
                i3=i2;
            end
            tmax=(tau)+((Samplesize./v).*jl)+((i3+jl)*(tau+(point./c)));
            F=@(t) ((Q(t).*n_abs)./(pi.*rho.*cp_sol.*((4.*pi.*a_sol).^(1/2)))).*(((tmax+(t-tau)).^(-1/2))./((2.*a_sol.*(tmax+(t-tau)))+(sigma.*sigma)))...
                .*(exp(((-1).*((((X-(i2.*point)).^2)+((Y+(jl.*hatch)).^2))./((4.*a_sol.*(tmax+(t-tau)))+(2.*(sigma.*sigma))))))...
                -(((Z./scaling).^2)/(4.*a_sol.*(tmax+(t-tau))))));
            dT=integral(F,0,tau,'ArrayValued',true);
            T=T+dT;
            if i2==0
                maxdT=max(max(max(dT)))
            end
        end
        if maxdT<dtmax
            break
        end
    end

    %Size above boiling point
    Qsol=(rho.*cp_sol.*(Tsol-T0).*(step.^3));                   %Heat input for a cell to reach solidus
    Qmelt=(rho.*(step.^3)).*LHm;                                %Heat input for a cell to melt
    Qboil=(rho.*cp_liq.*(Tboil-Tsol).*(step.^3));               %Heat input for a cell to reach boiling point
    Qsum=Qsol+Qmelt+Qboil;                                      %Total heat for a cell to get from T0 to boiling point

    DeltaT=T-T0;
    DeltaQ=(rho.*cp_sol.*DeltaT.*(step.^3));                    %Heat input to each cell, model assumes no phase change so use cp_sol
    maxDQ=max(max(max(DeltaQ)));

    if max(max(max(DeltaQ)))>Qsum
        DeltaQ_side=transpose(squeeze(DeltaQ(find(~y),:,:)));
        [C1,~]=contour(x,z,DeltaQ_side,[Qsum,Qsum]);            %Contour where heat in cell sufficient to reach boiling point
        [~, Aboil]=convhull(transpose(C1(1,2:end)),transpose(C1(2,2:end)));
        A3_VBoil=(2/3)*pi()*(((2.*Aboil./pi())^(0.5))^3);        %Volume of melt pool at or above boiling point
    else
        A3_VBoil=0;
    end

    if count==1
        if A3_VBoil<VBoil_Limit_Low
            break
        else
            if A3_VBoil<VBoil_Limit_High
                scaling=(2E12 * A3_VBoil)+1;
            else
                scaling=2;
            end
        end
    else
        break
    end
end
```

Figure D.5: Matlab code for Scaled

```
%Calculate heat treatment profile
maxlayer=floor(abs(min(z))./layer);     %maxmimum number of layers within calculation space
maxhatch=floor(max(y)./hatch);          %maxmimum number of hatches within calculation space
offlayer=floor(layer./step);            %number of matrix elements for a layer
offhatch=floor(hatch./step);            %number of matrix elements for a hatch

HT1=[];
for ga=1:maxlayer
    for gb=(-1*maxhatch):1:maxhatch
        hatchid=(find(~y))+(gb.*offhatch);
        layerid=(size(T,3))-(ga*offlayer);
        HT2=T(hatchid,:,layerid);     %extract temperature profile along laser travel direction
        HT2=fliplr(HT2);
        HT2=transpose(HT2);
        HT1=cat(1,HT1,HT2);
        if hatchid==(find(~y))
            max_HT=max(HT2);
        end
    end
    if max_HT<THAZ
        break;                          %stop when temperature immediately below laser drops below THAZ (50% Tsol)
    end
end

for gc=size(HT1,1):-1:1
    if HT1(gc,1)>Tsol
        HT1=HT1((gc+1):end,:);
        break
    end
end

HT3=(transpose(0:1:(size(HT1,1)-1))).*(step./v);           %calculate time step for plot of temperature v. time
HT4=((step./v).*(exp((Qstar./R).*((1./Teq_HT)-(1./HT1))))); %calculate equivalent time at specified equivalent temperature
A3_HeatTreat=sum(HT4);
HT1=cat(2,HT3,HT1,HT4);
```

Figure D.6: Matlab code for Heat Treatment

Bibliography

1. Freeman, F. S. *et al.* Exploiting thermal strain to achieve an in-situ magnetically graded material. *Materials & Design* **161,** 14–21. ISSN: 02641275 (2019).
2. ASTM. *ISO/ASTM 52900:2015(E). Standard Terminology for Additive Manufacturing General Principles Terminology* tech. rep. (2016), 9.
3. CFM International Jet Engines. *The LEAP Engine* `https://www.cfmaeroengines.com/engines/leap/` (2018).
4. Arcam AB. *EBM for Orthopedic Implants* 2018. `www.arcam.com/solutions/orthopedic-implants/` (2018).
5. Facchini, L *et al.* Metastable austenite in 17-4 precipitation-hardening stainless steel produced by selective laser melting. *Advanced Engineering Materials* **12,** 184–188. ISSN: 14381656 (2010).
6. Rafi, H. K. *et al.* Microstructure and mechanical behavior of 17-4 precipitation hardenable steel processed by selective laser melting. *Journal of Materials Engineering and Performance* **23,** 4421–4428. ISSN: 15441024 (2014).
7. Vora, P *et al.* AlSi12 in-situ alloy formation and residual stress reduction using anchorless selective laser melting. *Additive Manufacturing.* ISSN: 22148604. doi:`10.1016/j.addma.2015.06.003` (2015).
8. Mercelis, P & Kruth, J. P. Residual stresses in selective laser sintering and selective laser melting. *Rapid Prototyping Journal* **12,** 254–265 (2006).
9. King, W. E. *et al.* Observation of keyhole-mode laser melting in laser powder-bed fusion additive manufacturing. *Journal of Materials Processing Technology* **214,** 2915–2925 (2014).
10. Sames, W. J. *et al.* Thermal effects on microstructural heterogeneity of Inconel 718 materials fabricated by electron beam melting. *Journal of Materials Research* **29,** 1920–1930 (2017).
11. Gibson, I. *et al. Additive manufacturing technologies : 3D printing, rapid prototyping, and direct digital manufacturing* 453. ISBN: 978-1-4419-1119-3. doi:`10.1007/978-1-4419-1120-9`. arXiv: `arXiv:1011.1669v3` (2010).
12. Wang, F. *et al.* Laser fabrication of Ti6Al4V/TiC composites using simultaneous powder and wire feed. *Materials Science and Engineering A* **445-446,** 461–466. ISSN: 09215093 (2007).
13. Tammas-Williams, S & Todd, I. Design for additive manufacturing with site-specific properties in metals and alloys. *Scripta Materialia* **135,** 105–110 (2017).
14. Oxman, N. *Material-based Design Computation* PhD thesis (2010), 330.
15. Silva, E. C. N. *et al.* Modeling bamboo as a functionally graded material: Lessons for the analysis of affordable materials. *Journal of Materials Science* **41,** 6991–7004. ISSN: 00222461 (2006).
16. Van Grunsven, W. *et al.* Fabrication and Mechanical Characterisation of Titanium Lattices with Graded Porosity. *Metals* **4,** 401–409. ISSN: 2075-4701 (2014).
17. Rajan, T. P. D. *et al.* Developments in solidification processing of functionally graded aluminium alloys and composites by centrifugal casting technique. *Transactions of the Indian Institute of Metals* **65,** 531–537. ISSN: 09751645 (2012).
18. Hofmann, D. C. *et al.* Developing gradient metal alloys through radial deposition additive manufacturing. *Scientific Reports* **4,** 5357. ISSN: 2045-2322 (2015).

19. Mumtaz, K. A. & Hopkinson, N. Laser melting functionally graded composition of Waspaloy and Zirconia powders. *Journal of Materials Science* **42,** 7647–7656. ISSN: 00222461 (2007).

20. Hofmann, D. C. *et al.* Compositionally graded metals: A new frontier of additive manufacturing. *Journal of Materials Research* **29,** 1899–1910 (2014).

21. Inoue, T. Tatara and the Japanese sword: The science and technology. *Acta Mechanica* **214,** 17–30. ISSN: 00015970 (2010).

22. Niendorf, T. *et al.* Functionally graded alloys obtained by additive manufacturing. *Advanced Engineering Materials* **16,** 857–861. ISSN: 15272648 (2014).

23. Hofmann, H & Sanders, S. R. High-speed synchronous reluctance machine with minimized rotor losses. *IEEE Transactions on Industry Applications* **36,** 531–539. ISSN: 00939994 (2000).

24. Duke, A. *Brushless doubly-fed reluctance machines for aerospace electrical power generation systems* PhD thesis (2015).

25. Calverley, S. *et al.* Aerodynamic losses in switched reluctance machines. *IEE Proceedings - Electric Power Applications* **147,** 443. ISSN: 13502352 (2000).

26. Reiter, F. B. *et al. Method of making a powder metal rotor for a synchronous reluctance machine* 2004. `https://www.google.com/patents/US6675460`.

27. Jerrard, P. G. E. *et al.* Experimental investigation into selective laser melting of austenitic and martensitic stainless steel powder mixtures. *Proceedings of the Institution of Mechanical Engineers, Part B: Journal of Engineering Manufacture* **223,** 1409–1416. ISSN: 0954-4054 (2009).

28. Watanabe, Y & Momose, I. Magnetically graded materials fabricated by inhomogeneous heat treatment of deformed stainless steel. *Ironmaking & Steelmaking* **31,** 265–268. ISSN: 0301-9233 (2004).

29. Watanabe, Y *et al.* Fabrication of magnetically graded material by rolling deformation of wedge-shaped 304 stainless steel. *Materials Transactions, JIM* **40,** 961–966. ISSN: 0916-1821 (1999).

30. Keskitalo, M *et al.* Laser welding of duplex stainless steel with nitrogen as shielding gas. *Journal of Materials Processing Technology* **216,** 381–384. ISSN: 09240136 (2015).

31. Trapp, J *et al.* In situ absorptivity measurements of metallic powders during laser powder-bed fusion additive manufacturing. *Applied Materials Today* **9,** 341–349 (2017).

32. Hann, D. B. *et al.* A simple methodology for predicting laser-weld properties from material and laser parameters. *Journal of Physics D* **44,** 445401–9 (2011).

33. Rai, R *et al.* Heat transfer and fluid flow during keyhole mode laser welding of tantalum, Ti6Al4V, 304L stainless steel and vanadium. *Journal of Physics D: Applied Physics* **40,** 5753–5766. ISSN: 0022-3727 (2007).

34. Boley, C. D. *et al.* Metal powder absorptivity: modeling and experiment. *Applied Optics* **55,** 6496–6500. ISSN: 21553165 (2016).

35. Bidare, P *et al.* Fluid and particle dynamics in laser powder bed fusion. *Acta Materialia* **142,** 107–120 (2018).

36. Léonard, F. *et al. CT for Additive Manufacturing Process Characterisation: Assessment of melt strategies on defect population* in *6th Conference on Industrial Computed Tomography* (2016), 8.

37. Darvish, K. *et al.* Reducing lack of fusion during selective laser melting of CoCrMo alloy: Effect of laser power on geometrical features of tracks. *Materials & Design* **112,** 357–366. ISSN: 0264-1275 (2016).

38. Seto, N *et al.* Porosity formation mechanism and reduction method in CO 2 laser welding of stainless steel. *Welding International Quarterly Journal of the Japan Welding Society Reference QJ* **1601,** 451–460 (2002).

39. Kaplan, A. F. H. *et al.* Unbounded keyhole collapse and bubble formation during pulsed laser interaction with liquid zinc. *Journal of Physics D: Applied Physics* **35,** 319. ISSN: 00223727 (2002).

40. Gong, H. *et al. Melt Pool Characterization for Selective Laser Melting of Ti-6Al-4V Pre-alloyed Powder* in *Solid Freeform Fabrication Symposium* (2014), 256–267.

41. Stefanescu, D. M. *Science and Engineering of Casting Solidification* 2nd, 353. ISBN: 978-0-387-74609-8. doi:`10.1007/978-3-319-15693-4` (Springer London, 2002).

42. Porter, D. A. *et al. Phase transformations in metals and alloys* 3rd, 500. ISBN: 1439883572 (2016).

43. Brooks, J. A. & Thompson, A. W. Microstructural development and solidification cracking susceptibility of austenitic stainless steel welds. *International Materials Reviews* **36,** 16–44 (1991).

44. Kurz, W & Trivedi, R. Rapid solidification processing and microstructure formation. *Materials Science and Engineering A* **179,** 46–51. ISSN: 09215093 (1994).

45. Saeidi, K *et al.* Transformation of austenite to duplex austenite-ferrite assembly in annealed stainless steel 316L consolidated by laser melting. *Journal of Alloys and Compounds* **633,** 463–469. ISSN: 09258388 (2015).

46. Cheruvathur, S *et al.* Additive manufacturing of 17-4 PH stainless steel: post-processing heat treatment to achieve uniform reproducible microstructure. *JOM* **68,** 930–942 (2016).

47. Mukherjee, T *et al.* Mitigation of thermal distortion during additive manufacturing. *Scripta Materialia* **127,** 79–83 (2017).

48. Gnäupel-Herold, T *et al.* Neutron measurements of stresses in a test artifact produced by laser-based additive manufacturing. *AIP Conference Proceedings Journal of Applied Physics* **1581,** 1205–1212 (2014).

49. Wang, Z. *et al.* Residual stress mapping in Inconel 625 fabricated through additive manufacturing: Method for neutron diffraction measurements to validate thermomechanical model predictions. *Materials and Design* **113,** 169–177 (2017).

50. Moat, R. J. *et al.* Residual stresses in laser direct metal deposited Waspaloy. *Materials Science & Engineering A* **528,** 2288–2298 (2010).

51. Prime, M. B. Cross-Sectional Mapping of Residual Stresses by Measuring the Surface Contour After a Cut. *Journal of Engineering Materials and Technology* **123,** 162. ISSN: 00944289 (2001).

52. ASTM. *E837 13a Standard Test Method for Determining Residual Stresses by the Hole-Drilling Strain- Gage Method 1* tech. rep. (2013), 16. doi:10.1520/E0837-13A.

53. Casavola, C *et al.* Preliminary investigation on distribution of residual stress generated by the selective laser melting process. *The Journal of Strain Analysis for Engineering Design* **44,** 93–104 (2009).

54. Deffley, R. J. *Development of processing strategies for the additive layer manufacture of aerospace components in Inconel 718* PhD thesis (University of Sheffield, 2012).

55. Catchpole-Smith, S *et al.* Fractal scan strategies for selective laser melting of 'unweldable' nickel superalloys. *Additive Manufacturing* **15,** 113–122 (2017).

56. Griffith, M. *et al.* Understanding thermal behavior in the LENS process. *Materials and Design* **20,** 107–113 (1999).

57. Kirka, M. M. *et al.* Microstructure Development in Electron Beam-Melted Inconel 718 and Associated Tensile Properties. *JOM* **68,** 1012–1020 (2016).

58. Xu, W. *et al.* Additive manufacturing of strong and ductile Ti6Al4V by selective laser melting via in situ martensite decomposition. *Acta Materialia* **85,** 74–84. ISSN: 1359-6454 (2015).

59. Folkhard, E. *Welding Metallurgy of Stainless Steels* 279. ISBN: 3709189659 (Springer Vienna, 1988).

60. Li, Z. *et al.* Metastable high-entropy dual-phase alloys overcome the strengthductility trade-off. *Nature* **534,** 227–230 (2016).

61. ASM International. *ASM Handbook Vol 1. Properties and Selection: Irons, Steels and High-Performance Alloys* 10th ed. (ed ASM International Handbook Committee) ISBN: 0-87170-377-7 (ASM International, 1990).

62. ASM International. *ASM Handbook Vol 3. Alloy Phase Diagrams* (eds Okamoto, H. *et al.*) ISBN: 978-1-62708-070-5 (ASM International, 2016).

63. Bhadeshia, H. K.D. H. *et al.* Stress induced transformation to bainite in FeCrMoC pressure vessel steel. *Materials Science and Technology* **7,** 686–698 (1991).

64. Dyson, D. J. & Holmes, B. Effect of alloying additions on the lattice parameter of austenite. *Journal of the Iron and Steel Institute* **208,** 469–473 (1970).

65. Babu, S. S. *et al.* In-situ observations of lattice parameter fluctuations in austenite and transformation to bainite. *Metallurgical and Materials Transactions A* **36A,** 3281–3289 (2005).

66. Bain, E. The nature of martensite. *Transactions of the American Institute of Mining* **70,** 25–46 (1924).

67. Kurdjumov, G & Sachs, G. Über den Mechanismus der Stahlhärtung. *Zeitschrift für Physik* **64,** 325–343 (1930).

68. Nishiyama, Z. X-ray investigation of the mechanism of the transformation from face-centred cubic lattice to body-centred cubic. *Science Reports of the Thoku University* **23,** 637–664 (1934).

69. Wassermann, G. Uber den Mechanismus der alpha-gamma Umwandlung des Eisens. *Mitt. Kaiser Wihelm Inst. Eisenforsch* **17,** 149–155 (1935).

70. Morito, S. *et al.* The morphology and crystallography of lath martensite in alloy steels. *Acta Materialia* **51,** 1789–1799. ISSN: 13596454 (2003).

71. Olson, G. B. & Cohen, M. A mechanism for the strain-induced nucleation of martensitic transformations. *Journal of Less-Common Metals* **28,** 107–118 (1972).

72. Bhadeshia, H. K.D. H. & Honeycombe, R. W. K. *Steels : microstructure and properties.* 4th ed., 461. ISBN: 9780081002704 (Butterworth-Heinemann, 2017).

73. Bhadeshia, H. K.D. H. Thermodynamic extrapolation and martensite-start temperature of substitutionally alloyed steels. *Metal Science* **15,** 178–180 (1981).

74. Yang, H.-S. & Bhadeshia, H. K.D. H. Austenite grain size and the martensitestart temperature. *Scripta Materialia* **60,** 493–495 (2009).

75. Bhadeshia, H. K.D. H. Driving force for martensitic transformation in steels. *Metal Science* **15,** 175–177 (1981).

76. Schaeffler, A. L. Constitution diagram for stainless steel weld metal. *Metal Progress* **56,** 680–680B (1949).

77. Kotecki, D. J. & Siewert, T. A. WRC-1992 Constitution Diagram for Stainless Steel Weld Metals: A Modification of the WRC-1988 Diagram. *Welding Research Supplement* **71,** 171s–178s (1992).

78. Long, C. J. & Delong, W. T. The Ferrite Content of Austenitic Stainless Steel Weld Metal. *Welding Research Supplement,* 281s–297s (1973).

79. Inokuti, Y & Cantor, B. Splat-quenched Fe-Ni alloys. *Scripta Metallurgica* **10,** 655–659. ISSN: 00369748 (1976).

80. García-Junceda, A *et al.* Dependence of martensite start temperature on fine austenite grain size. *Scripta Materialia* **58,** 134–137. ISSN: 13596462 (2008).

81. Takaki, S *et al.* Effect of grain refinement on thermal stability of metastable austenitic steel. *Materials Transactions* **45,** 2245–2251 (2004).

82. Johnson, E *et al.* Microstructure of rapidly solidified stainless steel. *Materials Science and Engineering* **98,** 301–303. ISSN: 00255416 (1988).

83. Fischer, F. D. *et al.* A new view on transformation induced plasticity (TRIP). *International Journal of Plasticity* **16,** 723–748 (2000).

84. Sherif, M. Y. *et al.* Stability of retained austenite in TRIP-assisted steels. *Materials Science and Technology* **20,** 319–322 (2004).

85. Chatterjee, S & Bhadeshia, H. K.D. H. Transformation induced plasticity assisted steels: stress or strain affected martensitic transformation? *Materials Science and Technology ISSN:* **23,** 1101–1104 (2007).

86. Geijselaers, H. J. M. & Perdahcoglu, E. S. Mechanically induced martensitic transformation as a stress-driven process. *Scripta Materialia* **60,** 29–31 (2009).

87. Maréchal, D. *Linkage between mechanical properties and phase transformations in a 301LN austenitic stainless steel* PhD thesis (University of British Columbia, 2011), 228. doi:10.14288/1.0071814.

88. Bracke, L *et al.* Transformation mechanism of α'-martensite in an austenitic FeMnCN alloy. *Scripta Materialia* **57,** 385–388 (2007).

89. Misra, R. D. K. *et al.* Nanoscale deformation experiments on the strain rate sensitivity of phase reversion induced nanograined/ultrafine-grained austenitic stainless steels and comparison with the coarse-grained counterpart. *Materials Science & Engineering A* **548,** 161–174 (2012).

90. Inamura, T *et al.* Crystallography of nanometre-sized α-martensite formed at intersections of mechanical γ-twins in an austenitic stainless steel. *Philosophical Magazine* **83,** 9350954 (2003).

91. Kikuchi, T & Kajiwara, S. HVEM in situ Observation of Isothermal MT under Applied Stress. *Transactions of the Japan Institute of Metals* **26,** 861–868 (1985).

92. Spencer, K *et al.* The strain induced martensite transformation in austenitic stainless steels: Part 1 Influence of temperature and strain history. *Materials Science and Technology* **25,** 7–17 (2009).

93. Tamura, I. Deformation-induced martensitic transformation and transformation-induced plasticity in steels. *Metal Science* **16,** 245–253 (1982).

94. Das, A *et al.* Analysis of deformation induced martensitic transformation in stainless steels. *Materials Science and Technology* **27,** 366–370 (2011).

95. Shirzadi, A. A. *et al.* Bainite Orientation in Plastically Deformed Austenite. *International Journal of Materials Research* **100,** 40–45 (2009).

96. Patel, J. R. & Cohen, M. Criterion for the action of applied stress in the martensitic transformation. *Acta Metallurgica* **1,** 531–538 (1953).

97. Iwamoto, T *et al.* Investigation on deformation mode dependence of strain-induced martensitic transformation in trip steels and modelling of transformation kinetics. *International Journal of Mechanical Sciences* **40,** 173–182 (1998).

98. Angel, T. Formation of martensite in austenitic stainless steels. *Journal of the Iron and Steel Institute,* 165–174 (1954).

99. Wang, Z & Beese, A. M. Effect of chemistry on martensitic phase transformation kinetics and resulting properties of additively manufactured stainless steel. *Acta Materialia* **131,** 410–422. ISSN: 13596454 (2017).

100. Nohara, K. *et al. Composition and Grain Size Dependencies of Strain-induced Martensitic Transformation in Metastable Austenitic Stainless Steels* 1977. doi:10.2355/tetsutohagane1955.63.5_772.

101. ASTM International. *E112-13 Standard Test Methods for Determining Average Grain Size* tech. rep. (), 28. doi:10.1520/E0112-13.

102. Allain, S *et al.* Correlations between the calculated stacking fault energy and the plasticity mechanisms in FeMnC alloys. *Materials Science and Engineering A* **387-389,** 158–162 (2004).

103. Reick, W *et al.* Determination of stacking fault energy of austenite in a duplex stainless steel. *Steel Research International* **67,** 253–256 (1996).

104. Shigeta, T. *et al.* The Effects of Ausforming on Variant Selection of Martensite in CrMo Steel. *Quarterly Journal of the Japan Welding Society* **31,** 178–182 (2013).

105. Chatterjee, S *et al.* Mechanical stabilisation of austenite. *Materials Science and Technology* **22,** 641–644 (2006).

106. Wang, H. S. *et al.* Characterisation of severely deformed austenitic stainless steel wire. *Materials Science and Technology ISSN:* **21,** 1323–1328 (2013).

107. Apple, C. A. & Krausst, G. The effect of heating rate on the martensite to austenite transformation in Fe-Ni-C alloys. *Acta Metallurgica* **20,** 849–856 (1972).

108. Kapoor, R. & Batra, I. On the α to γ transformation in maraging (grade 350), PH 13-8 Mo and 17-4 PH steels. *Materials Science and Engineering: A* **371,** 324–334. ISSN: 0921-5093 (2004).

109. Lee, S.-J. *et al.* Reverse transformation mechanism of martensite to austenite in a metastable austenitic alloy. *Materials Science and Engineering: A* **515,** 32–37. ISSN: 0921-5093 (2009).

110. Tomimura, K. *et al.* Reversion mechanism from deformation induced martensite to austenite in metastable austenitic stainless steels. *ISIJ International* **31,** 1431–1437 (1991).

111. Leem, D.-S. *et al.* Amount of retained austenite at room temperature after reverse transformation of martensite to austenite in an Fe13%Cr7%Ni3%Si martensitic stainless steel. *Scripta Materialia* **45,** 767–772. ISSN: 1359-6462 (2001).

112. Forouzan, F. *et al.* Production of nano/submicron grained AISI 304L stainless steel through the martensite reversion process. *Materials Science and Engineering: A* **527,** 7334–7339. ISSN: 0921-5093 (2010).

113. Poulon-Quintin, A. *et al.* Fine Grained Austenitic Stainless Steels: The Role of Strain Induced a' Martensite and the Reversion Mechanism Limitations. *ISIJ International* **49,** 293–301 (2009).

114. Misra, R. D. K. *et al.* Nanograined/Ultrafine-Grained Structure and Tensile Deformation Behavior of Shear Phase Reversion-Induced 301 Austenitic Stainless Steel. *Metallurgical and Materials Transactions A: Physical Metallurgy and Materials Science* **41A,** 2162–2174 (2010).

115. LPW Technology. *Powder Range* 2017. `https://www.lpwtechnology.com/wp-content/uploads/2016/11/LPW{\_}PowderRange{\_}Brochure{\_}web{\_}pdf.pdf` (2018).

116. Saeidi, K *et al.* Hardened austenite steel with columnar sub-grain structure formed by laser melting. *Materials Science and Engineering: A* **625,** 221–229. ISSN: 09215093 (2015).

117. Jägle, E. A. *et al.* Precipitation and austenite reversion behavior of a maraging steel produced by selective laser melting. *Journal of Materials Research* **29,** 2072–2079 (2014).

118. Mertens, R *et al.* Influence of Powder Bed Preheating on Microstructure and Mechanical Properties of H13 Tool Steel SLM Parts. *Physics Procedia* **83,** 882–890 (2016).

119. Divya, V. D. *et al.* Microstructure of selective laser melted CM247LC nickel-based superalloy and its evolution through heat treatment. *Materials Characterization* **114,** 62–74 (2016).

120. Hunziker, O *et al.* On the formation of a centreline grain boundary during fusion welding. *Acta Materialia* **48,** 4191–4201 (2000).

121. Buchbinder, D *et al.* High Power Selective Laser Melting (HP SLM) of Aluminum Parts. *Physics Procedia* **12,** 271–278. ISSN: 1875-3892 (2011).

122. Kurz, W & Fisher, D. F. *Fundamentals of solidification* 3rd, 305. ISBN: 0878495223 (Trans Tech Publications, 1989).

123. Kurz, W & Frenk, A. Microstructure formation in laser materials processing. *Lasers in Engineering* **1,** 193–212 (1992).

124. Gilath, I *et al.* A comparison of methods for estimating the weld-metal cooling rate in laser welds. *Journal of Materials Science* **29,** 3358–3362 (1994).

125. El-Bealy, M & Thomas, B. G. Prediction of dendrite arm spacing for low alloy steel casting processes. *Metallurgical and Materials Transactions B* **27,** 689–693 (1996).

126. Jacobi, H. & Schwerdtfeger, K. Dendrite morphology of steady state unidirectionally solidified steel. *Metallurgical Transactions A* **7,** 811–820. ISSN: 0360-2133 (1976).

127. Spaldin, N. A. *Magnetic Materials: Fundamentals and Applications* ISBN: 9780511781599. doi:`10.1017/CBO9780511781599` (Cambridge University Press, Cambridge, 2010).

128. Cullity, B. D. & Graham, C. D. *Introduction to magnetic materials* 544. ISBN: 0471477419 (IEEE/Wiley, 2009).

129. Bai, G. *et al.* Study of high-coercivity sintered NdFeB magnets. *Journal of Magnetism and Magnetic Materials* **308,** 20–23. ISSN: 0304-8853 (2007).

130. Akhter, M. A. *et al.* Thickness and grain-size dependence of the coercivity in permalloy thin films. *Journal of Applied Physics* **81,** 4122–4124 (1997).

131. Carpenter. *CarTech® Silicon Core Iron "B-FM"* `http://cartech.ides.com/datasheet.aspx?i=103{\&}e=190{\&}c=techart` (2019).

132. Jiles, D. *Introduction to magnetism and magnetic materials* 440. ISBN: 9780412386404 (Chapman and Hall, 1991).

133. Bader, S. D. & Moog, E. R. Magnetic properties of novel epitaxial films. *Journal of Applied Physics* **61,** 3729 (1987).

134. Bhadeshia, H. K.D. H. Bessemer Memorial Lecture: The dimensions of steel. *Ironmaking & Steelmaking* **34,** 194–199 (2007).

135. Christien, F *et al.* A comparison of dilatometry and in-situ neutron diffraction in tracking bulk phase transformations in a martensitic stainless steel. *Materials Characterization* **82,** 50–57. ISSN: 10445803 (2013).

136. Ino, H. *et al.* Appearance of ferromagnetism in f.c.c. solid solutions of binary and ternary FeCu-based systems prepared by mechanical alloying technique. *Materials Science and Engineering: A* **304-306,** 972–974. ISSN: 0921-5093 (2001).

137. Zhao, L. *et al.* Magnetic detection of small fractions of ferromagnetic martensite within the paramagnetic austenite matrix of TWIP steel. *Journal of Materials Science* **48,** 1474–1479. ISSN: 0022-2461 (2013).

138. Tavares, S. S. M. *et al.* Influence of sulfur content on the corrosion resistance of 17-4PH stainless steel. *Journal of Materials Engineering and Performance* **26,** 2512–2519. ISSN: 1059-9495 (2017).

139. Crangle, J & Goodman, G. M. The magnetization of pure iron and nickel. *Proceedings of the Royal Society of London A: Mathematical, Physical and Engineering Sciences* **321** (1971).

140. Sandmeyer Steel. *Specification Sheet: Alloy 17-4PH* 2014. `https://www.sandmeyersteel.com/17-4PH.html{\#}PhysicalProperties` (2017).

141. AK Steel Corporation. *Specification 17-4PH Stainless Steel* 2007. `http://www.aksteel.com/pdf/markets{\_}products/stainless/precipitation/17-4{\_}ph{\_}data{\_}sheet.pdf` (2017).

142. Gu, H. *et al. Influences of Energy Density on Porosity and Microstructure of Selective Laser Melted 17- 4PH Stainless Steel* in *Solid freeform fabrication symposium* (2013), 474–489.

143. Murr, L. E. *et al.* Microstructures and properties of 17-4 PH stainless steel fabricated by selective laser melting. *Journal of Materials Research and Technology* **1,** 167–177 (2012).

144. Renishaw. *Renishaw Additive Manufacturing Systems* tech. rep. (2017), 157.

145. CEN. *BS EN ISO 2178 : 2016* tech. rep. (Standardization, European Committee for, 2016), 48.

146. Fischer Technology. *Feritscope® MP30 User Guide* 212 (Fischer Technology, 2001).

147. Cullity, B. D. & Weymouth, J. W. Elements of X-Ray Diffraction. *American Journal of Physics* **25,** 394–395. ISSN: 0002-9505 (1957).

148. Thomas, M *et al.* Normalised model-based processing diagrams for additive layer manufacture of engineering alloys. *Acta Materialia* **108,** 26–35 (2016).

149. Lyle, A. *SLM125 Exposure Ram-Up* 2018. `PrivateCommunication(25/01/2018)`.

150. Panwisawas, C. *et al.* Mesoscale modelling of selective laser melting: Thermal fluid dynamics and microstructural evolution. *Computational Materials Science* **126,** 479–490. ISSN: 0927-0256 (2017).

151. Smith, C. W. *Laser Travel Speed* 2016. `PrivateCommunication(28/11/2016)`.

152. London, G. *Renishaw SLM125 Spot Size* 2016. `PrivateCommunication(27/09/2016)`.

153. Eagar, T. W. & Tsai, N. S. Temperature fields produced by traveling distributed heat sources. *Welding Journal* **62,** 346–355. ISSN: 00432296 (1983).

154. Scott, G. D. & Kilgour, D. M. The density of random close packing of spheres. *Journal of Physics D: Applied Physics* **2,** 863–866. ISSN: 00223727 (1969).

155. Rosenthal, D. The Theory of Moving Sources of Heat and Its Application of Metal Treatments. *Transactions of ASME* **68,** 849–866 (1946).

156. Moat, R. J. *et al.* Crystallographic texture and microstructure of pulsed diode laser-deposited Waspaloy. *Acta Materialia.* ISSN: 13596454. doi:`10.1016/j.actamat.2008.11.004` (2009).

157. Higginson, R. L. & Sellars, C. M. *Worked examples in quantitative metallography* 116. ISBN: 1902653807 (Maney, 2003).

158. Cool, T & Bhadeshia, H. K.D. H. Prediction of martensite start temperature of power plant steels. *Materials Science and Technology ISSN:* **12,** 40–44 (1996).

159. Hsiao, C. N. *et al.* Aging reactions in a 17-4 PH stainless steel. *Materials Chemistry and Physics* **74,** 134–142. ISSN: 02540584 (2002).

160. Andersson, J. O. *et al.* Thermo-Calc and DICTRA, Computational tools for materials science. *Calphad* **26,** 273–312 (2002).

161. Thermo-Calc Software AB. *Thermo-Calc Software TCFE Steels/Fe-alloys database version 8*

162. AMG Superalloys UK Ltd. *17-4PH Powder Chemistry* tech. rep. (2016), 1.

163. Ghosh, G & Olson, G. B. Kinetics of FCC BCC heterogeneous martensitic nucleationI. The critical driving force for athermal nucleation. *Acta Metallurgica et Materialia* **42,** 3361–3370 (1994).

164. Koistinen, D. P. & Marburger, R. E. A general equation prescribing the extent of the austenite-martensite transformation in pure iron-carbon alloys and plain carbon steels*. *Acta Metallurgica* **7,** 59–60 (1959).

165. Wang, Y. M. *et al.* Additively manufactured hierarchical stainless steels with high strength and ductility. *Nature Materials* **17,** 63–70 (2018).

166. Humphreys, F. J. & Hatherly, M. *Recrystallization and related annealing phenomena* 497. ISBN: 0080426859 (Pergamon, 1996).

167. Hull, D. & Bacon, D. J. *Introduction to dislocations* 257. ISBN: 9780080966724 (Butterworth-Heinemann, 2011).

168. Kuo, C.-M. & Lin, C.-S. Static recovery activation energy of pure copper at room temperature. *Scripta Materialia* **57,** 667–670 (2007).

169. Martinez-de Guerenu, A *et al.* Recovery during annealing in a cold rolled low carbon steel. Part II: Modelling the kinetics. *Acta Materialia* **52,** 3665–3670 (2004).

170. Martinez-de Guerenu, A *et al.* Recovery during annealing in a cold rolled low carbon steel. Part I: Kinetics and microstructural characterization. *Acta Materialia* **52,** 3657–3664 (2004).

171. Brown, A. M. & Ashby, M. F. Correlations for diffusion constants. *Acta Metallurgica* **28,** 1085–1101 (1980).

172. Poddar, D. *et al.* Evolution of strain-induced precipitates in a model austenitic Fe-30Ni-Nb steel and their effect on the flow behaviour. *Acta Materialia* **80,** 1–15 (2014).

173. Becker, T. H. & Dimitrov, D. The achievable mechanical properties of SLM produced Maraging Steel 300 components. *Rapid Prototyping Journal* **22,** 487–494 (2016).

174. Yasa, E *et al.* The investigation of the influence of laser re-melting on density, surface quality and microstructure of selective laser melting parts. *Rapid Prototyping Journal* **17,** 312–327 (2011).

175. Williamson, G. K. & Hall, W. H. Discussion of the theories of line broadening. *Acta Metallurgica* **1,** 22–31 (1953).

176. Ma, L. & Bin, H. Temperature and stress analysis and simulation in fractal scanning-based laser sintering. *International Journal of Advanced Manufacturing Technology* **34,** 898–903 (2007).

177. Rangaswamy, P *et al.* Residual stresses in LENS ® components using neutron diffraction and contour method. *Materials Science and Engineering A* **399,** 72–83 (2005).

178. Rangaswamy, P *et al.* Residual stresses in components formed by the laser- engineered net shaping (LENS) process. *The Journal of Strain Analysis for Engineering Design* **38,** 519–527 (2003).

179. Mukherjee, T *et al.* Printability of alloys for additive manufacturing. *Scientific Reports* **6.** doi:10.1038/srep19717 (2016).

180. Sandmeyer Steel. *Specification Sheet: Alloy 316/316L* 2014. `https://www.sandmeyersteel.com/images/316-316L-317L-Spec-Sheet.pdf` (2018).

181. Stone, H. J. *et al.* Synchrotron X-ray Studies of Austenite and Bainitic Ferrite. *Proceedings of the Royal Society A* **464,** 1009–1027 (2008).

182. Huang, P.-H & Guo, M.-J. A study on the investment casting of 17-4PH stainless steel helical impeller of centrifugal pump. *Materials Research Innovations* **19,** S9–77–S9–81 (2015).

183. He, X *et al.* Heat transfer and fluid flow during laser spot welding of 304 stainless steel. *Journal of Physics D: Applied Physics J. Phys. D: Appl. Phys. J. Phys. D: Appl. Phys* **36,** 1388–1398 (2003).

184. Protopapas, P *et al.* Theory of transport in liquid metals. I. Calculation of self-diffusion coefficients Theory of transport in liquid metals. I. Calculation of self-diffusion coefficients*. *The Journal of Chemical Physics Journal of Chemical Physics The Journal of Chemical Physics* **59,** 4507–518 (1973).

185. AZO Materials. *Properties: Stainless Steel - Grade 316* 2017. `https://www.azom.com/properties.aspx?ArticleID=863` (2017).

186. Rickinson, B. A. & Kirkwood, D. H. Equilibrium partition coefficients for ferrite/liquid and austenite/liquid in Fe-Cr-C alloys. *Metal Science* **12,** 138–146 (1978).

187. EOS. *Material Data Sheet - GP1 (www.eos.info/material-m)* 2009. `https://cdn1.scrvt.com/eos/public/5f84f5d2c88ac900/05fb1582834a38c85ef6dd859733a230/EOS{\_}StainlessSteel-GP1{\_}en.pdf` (2017).

188. Jacot, A *et al.* Modelling of Reaustenitisation from the Pearlite Structure in Steel. *Acta Materialia* **46,** 3949–3962 (1998).